Springer Tracts in Modern Physics
174

T. Schäpers

# Superconductor/ Semiconductor Junctions

Springer

# Springer Tracts in Modern Physics
# Volume 174

Managing Editor: G. Höhler, Karlsruhe

Editors: J. Kühn, Karlsruhe
Th. Müller, Karlsruhe
A. Ruckenstein, New Jersey
F. Steiner, Ulm
J. Trümper, Garching
P. Wölfle, Karlsruhe

Honorary Editor: E. A. Niekisch, Jülich

Now also Available Online

Starting with Volume 165, Springer Tracts in Modern Physics is part of the Springer LINK service. For all customers with standing orders for Springer Tracts in Modern Physics we offer the full text in electronic form via LINK free of charge. Please contact your librarian who can receive a password for free access to the full articles by registration at:

http://link.springer.de/series/stmp/reg_form.htm

If you do not have a standing order you can nevertheless browse through the table of contents of the volumes and the abstracts of each article at:

http://link.springer.de/series/stmp/

There you will also find more information about the series.

Springer
*Berlin*
*Heidelberg*
*New York*
*Barcelona*
*Hong Kong*
*London*
*Milan*
*Paris*
*Singapore*
*Tokyo*

**Physics and Astronomy** ONLINE LIBRARY
http://www.springer.de/phys/

# Springer Tracts in Modern Physics

Springer Tracts in Modern Physics provides comprehensive and critical reviews of topics of current interest in physics. The following fields are emphasized: elementary particle physics, solid-state physics, complex systems, and fundamental astrophysics.
Suitable reviews of other fields can also be accepted. The editors encourage prospective authors to correspond with them in advance of submitting an article. For reviews of topics belonging to the above mentioned fields, they should address the responsible editor, otherwise the managing editor.
See also http://www.springer.de/phys/books/stmp.html


## Managing Editor

Gerhard Höhler

Institut für Theoretische Teilchenphysik
Universität Karlsruhe
Postfach 69 80
76128 Karlsruhe, Germany
Phone: +49 (7 21) 6 08 33 75
Fax: +49 (7 21) 37 07 26
Email: gerhard.hoehler@physik.uni-karlsruhe.de
http://www-ttp.physik.uni-karlsruhe.de/

## Elementary Particle Physics, Editors

Johann H. Kühn

Institut für Theoretische Teilchenphysik
Universität Karlsruhe
Postfach 69 80
76128 Karlsruhe, Germany
Phone: +49 (7 21) 6 08 33 72
Fax: +49 (7 21) 37 07 26
Email: johann.kuehn@physik.uni-karlsruhe.de
http://www-ttp.physik.uni-karlsruhe.de/~jk

Thomas Müller

Institut für Experimentelle Kernphysik
Fakultät für Physik
Universität Karlsruhe
Postfach 69 80
76128 Karlsruhe, Germany
Phone: +49 (7 21) 6 08 35 24
Fax: +49 (7 21) 6 07 26 21
Email: thomas.muller@physik.uni-karlsruhe.de
http://www-ekp.physik.uni-karlsruhe.de

## Fundamental Astrophysics, Editor

Joachim Trümper

Max-Planck-Institut für Extraterrestrische Physik
Postfach 16 03
85740 Garching, Germany
Phone: +49 (89) 32 99 35 59
Fax: +49 (89) 32 99 35 69
Email: jtrumper@mpe-garching.mpg.de
http://www.mpe-garching.mpg.de/index.html

## Solid-State Physics, Editors

Andrei Ruckenstein
*Editor for The Americas*

Department of Physics and Astronomy
Rutgers, The State University of New Jersey
136 Frelinghuysen Road
Piscataway, NJ 08854-8019, USA
Phone: +1 (732) 445 43 29
Fax: +1 (732) 445-43 43
Email: andreir@physics.rutgers.edu
http://www.physics.rutgers.edu/people/pips/Ruckenstein.html

Peter Wölfle

Institut für Theorie der Kondensierten Materie
Universität Karlsruhe
Postfach 69 80
76128 Karlsruhe, Germany
Phone: +49 (7 21) 6 08 35 90
Fax: +49 (7 21) 69 81 50
Email: woelfle@tkm.physik.uni-karlsruhe.de
http://www-tkm.physik.uni-karlsruhe.de

## Complex Systems, Editor

Frank Steiner

Abteilung Theoretische Physik
Universität Ulm
Albert-Einstein-Allee 11
89069 Ulm, Germany
Phone: +49 (7 31) 5 02 29 10
Fax: +49 (7 31) 5 02 29 24
Email: steiner@physik.uni-ulm.de
http://www.physik.uni-ulm.de/theo/theophys.html

Thomas Schäpers

# Superconductor/ Semiconductor Junctions

With 91 Figures

Springer

Dr. Thomas Schäpers
Forschungszentrum Jülich
Institut für Schichten und Grenzflächen (ISG)
52425 Jülich, GERMANY
E-mail: th.schaepers@fz-juelich.de

Library of Congress Cataloging-in-Publication Data applied for.

Die Deutsche Bibliothek - CIP-Einheitsaufnahme

Schäpers, Thomas:
Superconductor, semiconductor junctions/Thomas Schäpers. -
Berlin; Heidelberg; New York; Barcelona; Hong Kong; London; Milan; Paris;
Singapore; Tokyo: Springer, 2001
(Springer tracts in modern physics; Vol. 174)
(Physics and astronomy online library)
ISBN 3-540-42220-X

Physics and Astronomy Classification Scheme (PACS): 74.50.+r, 74.80.Fp, 74.40.+k, 73.23.-b, 73.61.Ey

ISSN print edition: 0081-3869
ISSN electronic edition: 1615-0430
ISBN 3-540-42220-X Springer-Verlag Berlin Heidelberg New York

This work is subject to copyright. All rights are reserved, whether the whole or part of the material is concerned, specifically the rights of translation, reprinting, reuse of illustrations, recitation, broadcasting, reproduction on microfilm or in any other way, and storage in data banks. Duplication of this publication or parts thereof is permitted only under the provisions of the German Copyright Law of September 9, 1965, in its current version, and permission for use must always be obtained from Springer-Verlag. Violations are liable for prosecution under the German Copyright Law.

Springer-Verlag Berlin Heidelberg New York
a member of BertelsmannSpringer Science+Business Media GmbH

http://www.springer.de

© Springer-Verlag Berlin Heidelberg 2001
Printed in Germany

The use of general descriptive names, registered names, trademarks, etc. in this publication does not imply, even in the absence of a specific statement, that such names are exempt from the relevant protective laws and regulations and therefore free for general use.

Typesetting: Camera-ready copy from the author using a Springer LaTeX macro package
Cover design: *design & production* GmbH, Heidelberg

Printed on acid-free paper SPIN: 10791132 57/3141/tr 5 4 3 2 1 0

# Preface

The present book covers the transport properties of superconductor/two-dimensional-electron-gas Josephson junctions. Starting with the basic element, a superconductor/two-dimensional-electron-gas interface, phase-coherent Andreev reflection in hybrid Josephson junctions is introduced and further on, multiterminal structures are discussed. Special care is taken on explaining the underlying theoretical concepts related to the transport mechanisms. Employing a two-dimensional electron gas in a semiconductor as a normal conductor opens up the possibility to observe effects not found in purely metallic junctions. One example is the light sensitivity of the semiconductor, which has a direct impact on the supercurrent in the Josephson junction.

Many of the effects reported here rely on the fast technological progress in the epitaxial growth of III–V semiconductor heterostructures. By using these layer systems, fascinating quantum effects have been found. Two examples out of many are the quantized conductance in a point contact and electron optics using ballistic electron beams. By combining heterostructures with superconductors, many of the effects found in purely semiconductor systems can in a sense, be transferred to the superconducting state. A prominent example is the quantization of the critical current in a superconducting quantum point contact.

The present book is based on the *Habilitationsschrift* that the author submitted to the Rheinisch-Westfälische Technische Hochschule (RWTH) Aachen. A large portion of the experimental results reported here are from measurements performed in Jülich. By including results of other groups active in this research field, the author attempted to obtain a more or less complete coverage of the present status of the physics of superconductor/two-dimensional electron gas structures. Since most of the phenomena are described in a detailed fashion, this book should suit not only specialists active in the field but also interested students and scientists not familiar with these structures.

The author wishes to express his gratitude to former and present colleagues in Jülich who were involved in the superconductor/semiconductor hybrid project: J. Appenzeller, A.I. Braginski, G. Crecelius, A. Förster, V.A. Guzenko, H. Hardtdegen, A. Kaluza, J. Kaufmann, T. Klocke, S.G.

Lachenmann, J. Malindretos, K. Neurohr, D. Uhlisch and A.V. Ustinov. Valuable discussions on the theory of superconductor/semiconductor structures with A.A. Golubov (Twente University, The Netherlands), P. Samuelsson (Chalmers University of Technology) and M.Yu. Kupriyanov (Moscow State University) as well as the hospitality of the NTT Basic Research Laboratory during the final stage of the preparation of the manuscript are gratefully acknowledged. I am indebted to H. Lüth for his support of the hybrid activities in Jülich. Above all, I would like to thank my wife Gitta for her patience and understanding during the time when this manuscript was being written.

Jülich, May 2001 *Thomas Schäpers*

# Contents


**1. Introduction** ..... 1

**2. Carrier Transport Through a Superconductor/Normal-Conductor Interface** ..... 5
2.1 The Bogoliubov Equation ..... 5
2.2 Quasiparticle Transport Through a Superconductor/Normal-Conductor Interface ..... 8
2.2.1 Andreev Reflection ..... 8
2.2.2 Blonder–Tinkham–Klapwijk Model ..... 9
2.2.3 Inclusion of the Proximity Effect ..... 14

**3. Fabrication of Superconductor/ Two-Dimensional-Electron-Gas Structures** ..... 21
3.1 Two-Dimensional Electron Gases ..... 21
3.1.1 Two-Dimensional Electron Gases in Inversion Layers .. 21
3.1.2 Two-Dimensional Electron Gases in Heterostructures . 24
3.2 Fabrication of Superconductor/ Two-Dimensional-Electron-Gas/ Superconductor Junctions ..... 26
3.2.1 Junctions Based on a Surface Inversion Layer ..... 27
3.2.2 Junctions Based on a Buried Two-Dimensional Electron Gas ..... 28

**4. Transport Studies on Single Superconductor/ Two-Dimensional-Electron-Gas Interfaces** ..... 31
4.1 Effect of the Surface Treatment ..... 31
4.1.1 Preparation of Single S/2DEG Contacts ..... 31
4.1.2 Samples Cleaned by Wet Chemical Etching ..... 33
4.1.3 $Ar^+$ Sputter Cleaning ..... 36
4.1.4 Electron Cyclotron Resonance Plasma Cleaning ..... 41
4.2 Point Contact Spectroscopy ..... 43

**5. Superconductor/Two-Dimensional-Electron-Gas/ Superconductor Junctions: Voltage-Carrying State** ..... 47
5.1 Subharmonic Gap Structures: Theoretical Models ..... 47
5.1.1 Kümmel–Gunsenheimer–Nicolsky Model ..... 47
5.1.2 Inclusion of Normal Reflection at the SN Interface .... 49
5.1.3 Octavio–Tinkham–Blonder–Klapwijk Model ..... 51
5.1.4 Inclusion of the Proximity Effect ..... 53
5.2 Measurement of the Voltage-Carrying State ..... 56
5.2.1 Andreev Current in S/2DEG/S Structures ..... 56
5.2.2 Subharmonic Gap Structures ..... 57
5.2.3 Subharmonic Gap Structures and the Proximity Effect 60
5.3 Resonant Structures and Interference Effects ..... 61

**6. Josephson Current in Superconductor/ Two-Dimensional-Electron-Gas Junctions** ..... 65
6.1 Theoretical Description of the Supercurrent in an S/2DEG/S Junction ..... 65
6.1.1 Supercurrent in an Ideal One-Dimensional SNS Junction 66
6.1.2 Supercurrent in a General One-Dimensional SNS Junction ..... 68
6.1.3 Supercurrent in a Junction with a Two-Dimensional Electron Gas ..... 75
6.1.4 Supercurrent in a Junction with Proximity Layers ... 76
6.2 Measurements of the Superconductive State ..... 77
6.2.1 Current–Voltage Characteristics ..... 78
6.2.2 Effect of a Magnetic Field ..... 83
6.2.3 Hysteresis ..... 86
6.2.4 Self-Detection of Josephson Radiation ..... 88
6.2.5 Light Exposure ..... 89

**7. Gate-Controlled Superconductor/ Two-Dimensional-Electron-Gas Junctions** ..... 95
7.1 The Josephson Field Effect Transistor ..... 95
7.2 Interference Effects ..... 100
7.2.1 Critical-Current Oscillations ..... 100
7.2.2 Mesoscopic Fluctuations and Localization Effects ..... 102
7.3 Superconducting Quantum Point Contacts ..... 105

**8. Nonequilibrium Josephson Current** ..... 111
8.1 Supercurrent Control by Nonequilibrium Carriers: Theoretical Concepts ..... 111
8.1.1 Carrier Injection in a Three-Terminal Structure ..... 112
8.1.2 Carrier Injection in a Four-Terminal Junction ..... 117
8.2 Supercurrent Control by Nonequilibrium Carriers: Experiments ..... 121

8.2.1 Carrier Injection in an InAs Step Junction ..... 121
8.2.2 Multiterminal Josephson Junctions ..... 123
8.2.3 Local Suppression of the Josephson Current ..... 130

**9. Conclusion** ..... 133

**References** ..... 135

**Index** ..... 143

# 1. Introduction

Introducing a semiconductor as a normal conducting layer in a weak-link structure [1] has induced a vast variety of new potential applications and unique physical effects [2, 3, 4, 5]. One motivation behind this approach is of course the aim of combining superconducting electronics, e.g. rapid single flux logic (RSFQ) [6], with state-of-the-art semiconductor circuits. The key element is the so-called Josephson field effect transistor (JoFET) [7], where the Josephson supercurrent can be controlled by a gate. JoFET operation has been demonstrated in the past by using several different semiconducting materials [8, 9, 10, 11]. However, since the voltage necessary to control the supercurrent is relatively large compared with the output voltage, voltage gain is difficult to obtain. A possible way towards better performance might be to use interference effects, i.e. Fabry–Pérot resonances [12, 13, 14].

As a promising alternative to a JoFET, nonequilibrium carriers injected into the normal-conducting area can also be used to control the supercurrent in a weak-link structure [15, 16, 17, 18, 19, 20, 21, 22, 23]. Here, the underlying mechanism is that the occupation of the Andreev levels, which determine the supercurrent flow, is altered by the injected carriers. It was shown that relatively small injection currents are sufficient for an efficient supercurrent control [22].

The application of superconducting three-terminal structures such as JoFETs or injection-type devices in real electronic circuits is still an open question. Many technological obstacles have to be overcome before this is done. Nevertheless, superconductor/two-dimensional-electron-gas structures can serve as an almost ideal system when fundamental questions about supercurrent flow are to be addressed. Novel quantum effects can be observed, which rely on the large Fermi wavelength found in semiconductors compared with purely metallic structures. A prominent example is the superconducting quantum point contact, where a quantized supercurrent was predicted [24, 25] and experimentally observed [26].

Superconductor/two-dimensional-electron-gas structures can be classified into two groups. First, an inversion layer, e.g. on the surface of InAs, can be employed as a two-dimensional electron gas (2DEG). In this case the transport through the structure usually has to be described in the so-called *dirty limit*, where the coherence length $\xi$ is larger than the elastic mean

Thomas Schäpers: Superconductor/Semiconductor Junctions, STMP 174, 1–3 (2001)
© Springer-Verlag Berlin Heidelberg 2001

free path. The carrier transport is diffusive in this case. In the alternative regime, the *clean limit*, the coherence length is smaller than the elastic mean free path $l_{el}$. In order to have access to the latter regime, two-dimensional electron gases in semiconductor heterostructures are used. Here, the spatial separation of the donors from the electrons in the quantum well leads to an efficient suppression of the mobility-reducing ionized-impurity scattering. As a result, an elastic mean free path of several microns can be obtained easily at low temperatures. Since the relevant dimensions in a superconductor/2DEG structure are mostly smaller than $l_{el}$, the carrier transport can be considered as *ballistic*. In this regime, interesting quantum effects have been predicted theoretically [24, 25] and confirmed experimentally [26, 27, 28].

Concerning the choice of an appropriate semiconductor, the height and thickness of the Schottky barrier at the interface is one of the most important parameters. In order to obtain a good coupling between the superconductor and the semiconductor, the transparency of the interface barrier should be as large as possible. In this respect InAs is an ideal candidate, since the Fermi level is pinned above the conduction band edge. In addition, the large electron concentration of the 2DEG at the surface and the low effective electron mass lead to a large coherence length in the normal-conducting material [8, 29, 30, 31]. A drawback is that the conductance of the 2DEG at the surface can result in insufficient isolation between adjacent junctions. However, if the InAs surface is covered with an additional InAlAs layer, this surface conductance can be suppressed, as shown by Lachenmann et al. [32]. In addition to InAs, Si [9] and InGaAs [33] have been used as a semiconducting material in hybrid weak-link structures.

In order to contact a superconductor to a 2DEG embedded in a semiconductor heterostructure, two different approaches can be pursued. If, ultimately, a high mobility is needed, AlGaAs/GaAs heterostructures are the material of choice [34, 35]. However, a drawback of this system is that owing to the diffusion process necessary for the formation of the superconductive Sn contact, the junction geometry is not precisely defined. This problem can be circumvented if the heterostructure is etched down to or below the 2DEG so that, subsequently, the superconductor can be contacted from the top or from the side to the channel layer [14, 36, 37, 38]. The latter method is only applicable if the Schottky barrier is sufficiently low, e.g. in InAs-based channel layers.

For many of the effects discussed here, results on structures based on InAs surface layers as well as on $In_{0.57}Ga_{0.43}As/In_{0.77}Ga_{0.23}As/InP$ heterostructures have been reported [39, 40]. For the latter, the 2DEG is located in a strained $In_{0.77}Ga_{0.23}As$ channel layer. Owing to the high mobility, even ballistic transport through a quantum point contact could be demonstrated [41, 42, 43]. Because of the high indium content, the Fermi level pinning occurs approximately at the conduction band edge. This property leads to a low-resistance coupling to the superconductor [44, 45].

This book is organized as follows. The basic principles of carrier transport through a single superconductor/normal-conductor interface are discussed in Chap. 2. The properties of two-dimensional electron gases and the preparation steps necessary to fabricate a junction are described in Chap. 3. The following chapter deals with the characterization of single superconductor/two-dimensional-electron-gas interfaces. Special care was taken here in optimizing the superconductor/normal-conductor interface properties by employing several alternative methods to clean the semiconductor surface before the deposition of the superconducting material. In Chap. 5 the voltage-carrying state of superconductor/two-dimensional-electron-gas junctions structures is investigated, whereas the next chapter is dedicated to the superconductive state. As outlined above, gate control of the carrier concentration is one of the unique features of a semiconducting channel. In Chap. 7, first, the Josephson field effect transistor is introduced, while in the second part more fundamental effects, e.g. quantization or fluctuations of the critical current, are described. The effect of nonequilibrium carriers on the Josephson supercurrent is presented in Chap. 8.

# 2. Carrier Transport Through a Superconductor/Normal-Conductor Interface

In this chapter the carrier transport through the simplest structure, a superconductor/semiconductor bilayer is, discussed. A detailed understanding of this key structure is essential for the study of more sophisticated structures, i.e. Josephson junctions or three-terminal structures, as presented in the following chapters. First, we shall introduce Andreev reflection as a fundamental mechanism related to transport through a superconductor/semiconductor interface. Next, the Blonder–Tinkham–Klapwijk (BTK) model [46] is explained, which treats the carrier transport through a non-ideal interface with a barrier in between. Because of its simplicity, the BTK model is referred to frequently to describe transport through a superconductor/semiconductor interface. However, the experimental results obtained on single interfaces suggest that some extensions, e.g. the inclusion of the proximity effect, are necessary in order to obtain a better theoretical description of the experimental findings.

For the discussion of the basic transport phenomena it is often sufficient to use an *ideal* normal conductor (N), which means that this normal conductor consists of the same material as the superconductor (S). This simplifies the theoretical description considerably, since all material parameters, e.g. electron concentration, are identical. However, as we shall see later, the coupling of a semiconductor to a superconductor can differ significantly from the above-mentioned idealized case, i.e. the effective electron mass or the electron concentration can be much smaller than the corresponding values for the superconductor. Therefore, in some cases it is necessary to extend the description of an S/N interface in order to take the specific properties of the superconductor/semiconductor interface into account.

## 2.1 The Bogoliubov Equation

In 1957, Bardeen, Cooper and Schrieffer (BCS) [47] succeeded in explaining the appearance of the superconductive state at an atomistic level. They found that two electrons with opposite wave vector and spin form a Cooper pair $(\boldsymbol{k}\uparrow, -\boldsymbol{k}\downarrow)$. The electron pairing is mediated by a weak electron–phonon coupling, the Fröhlich interaction. Owing to this attractive interaction, Cooper pairs, which are bosonic particles, condense to an energetically lower ground

Thomas Schäpers: Superconductor/Semiconductor Junctions, STMP 174, 5–19 (2001)
© Springer-Verlag Berlin Heidelberg 2001

state. Despite the lower ground state energy, the kinetic energy of the electrons is increased compared with a noninteracting Fermi gas. However, this is overcompensated by the pairing energy, which is gained owing to the attractive electron–phonon interaction. Because of the increased kinetic energy, the probability $v_0^2$ to find a Cooper pair $(\boldsymbol{k}\uparrow, -\boldsymbol{k}\downarrow)$ at $T = 0$ is not step-like as for a noninteracting Fermi gas, but rather is smeared out around the Fermi wave vector $k_\mathrm{F}$, as shown in Fig. 2.1.

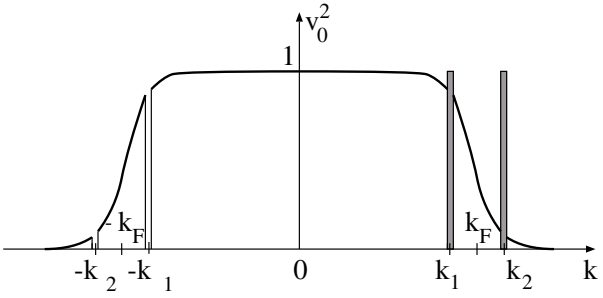


**Fig. 2.1.** Probability $v_0^2$ that a pair state $(\boldsymbol{k}\uparrow, -\boldsymbol{k}\downarrow)$ is occupied along a particular $\boldsymbol{k}$ axis. Two single-particle exitations are shown, with electrons placed at $k_1$ and $k_2$. Since these electrons do not form a Cooper pair, the states at $-k_1$ and $-k_2$ must be empty

The vanishing resistance of a superconductor is closely related to the opening of an energy gap $\Delta_0$ between the ground state of the Cooper pair condensate and the spectrum of excited single-electron states. Owing to this energy gap, scattering processes, which are responsible for the resistance of a conductor, are suppressed. In order for an electron to occupy a single-particle state, the electron energy must be larger than the gap $\Delta_0$.

Let us have a closer look at what happens if a state is occupied by a single electron. In Fig. 2.1 this situation is depicted for an electron with a wave number $k_1$ below $k_\mathrm{F}$ and for a wave number $k_2$ above $k_\mathrm{F}$. In this case, the corresponding states are occupied with probability one. Since these electrons must not form a Cooper pair, the corresponding states at the opposite side of $\boldsymbol{k}$ space $-k_1$ and $-k_2$ must be empty. As can be seen in Fig. 2.1, at $k_1$ the system gains a small portion of additional electron character, which can be quantified by $1 - v_0^2$. Owing to the empty state at $-k_1$, the additional hole character, expressed by $v_0^2$, is larger. Thus, as a net result, an excitation with a wave vector below $k_\mathrm{F}$ can be regarded as hole-like. The opposite situation is found for a wave vector located above $k_\mathrm{F}$. As shown in Fig. 2.1, the system gains more electron character at $k_2$ than hole character at $-k_2$, thus this excitation can be regarded as an electron-like quasiparticle.

The quasiparticle states introduced above can be described by the Bogoliubov equation [48],

$$\begin{pmatrix} H(\boldsymbol{r}) & \Delta(\boldsymbol{r}) \\ \Delta^*(\boldsymbol{r}) & -H(\boldsymbol{r}) \end{pmatrix} \begin{pmatrix} u_{\boldsymbol{k}}(\boldsymbol{r}) \\ v_{\boldsymbol{k}}(\boldsymbol{r}) \end{pmatrix} = E \begin{pmatrix} u_{\boldsymbol{k}}(\boldsymbol{r}) \\ v_{\boldsymbol{k}}(\boldsymbol{r}) \end{pmatrix} . \tag{2.1}$$

The solutions of the Bogoliubov equation are electron-like or hole-like quasiparticles represented by the vector $(u_{\boldsymbol{k}}, v_{\boldsymbol{k}})$. Here, $H(\boldsymbol{r})$ is the one-electron Hamiltonian, defined as

$$H(\boldsymbol{r}) = -\frac{\hbar^2}{2}\nabla^2 \frac{1}{m^*} + U(\boldsymbol{r}) - \mu \, , \tag{2.2}$$

where $\mu$ is the electrochemical potential, $m^*$ is the effective electron mass and $U(\boldsymbol{r})$ is a scalar potential. The coupling between the two components of the vector $(u_{\boldsymbol{k}}, v_{\boldsymbol{k}})$ is provided by the superconducting pair potential $\Delta(\boldsymbol{r})$. In a metallic superconductor $m^*$ is identical to the free electron mass $m_\mathrm{e}$. Following the discussion above, the component $v_{\boldsymbol{k}}$ represents the probability amplitude for a hole-like state, while $u_{\boldsymbol{k}}$ represents the probability of an electron-like state. The two are coupled by the pair potential $\Delta(\boldsymbol{r})$. The character of the quasiparticle, electron-like ($|u_{\boldsymbol{k}}|^2 > |v_{\boldsymbol{k}}|^2$) or hole-like ($|u_{\boldsymbol{k}}|^2 < |v_{\boldsymbol{k}}|^2$), is determined by the predominant component of the vector $(u_{\boldsymbol{k}}, v_{\boldsymbol{k}})$.

In many cases, the common spatial component $g(\boldsymbol{r})$ can be split off from $(u_{\boldsymbol{k}}, v_{\boldsymbol{k}})$:

$$\begin{pmatrix} u_{\boldsymbol{k}}(\boldsymbol{r}) \\ v_{\boldsymbol{k}}(\boldsymbol{r}) \end{pmatrix} = g(\boldsymbol{r}) \begin{pmatrix} u_0 \\ v_0 \end{pmatrix} \; ; \tag{2.3}$$

e.g., for a homogeneous superconductor with $\Delta(\boldsymbol{r}) = \Delta_0$, plane wave solutions $\exp(\mathrm{i}\boldsymbol{k}\cdot\boldsymbol{r})$ can be assumed for $g(\boldsymbol{r})$. In this case $u_0$ and $v_0$ are given by

$$u_0^2 = \frac{1}{2}\left(1 + \frac{\sqrt{E^2 - \Delta_0^2}}{E}\right) , \tag{2.4a}$$

$$v_0^2 = 1 - u_0^2 \, , \tag{2.4b}$$

where the energy eigenvalues are

$$E = \pm \left[ \left( \frac{\hbar^2 k^2}{2m_\mathrm{e}} - \mu \right)^2 + \Delta_0^* \Delta_0 \right]^{1/2} . \tag{2.5}$$

The quantity $v_0^2$ in (2.4b) is identical to the above-discussed probability of finding a Cooper pair in the BCS theory. Thus, for the case where $|\boldsymbol{k}|$ is larger than the Fermi wave vector, the quasiparticle is electron-like, since $|u_0|^2 > |v_0|^2$, while for $|\boldsymbol{k}| < k_\mathrm{F}$ the character of the particle is hole-like ($|u_0|^2 < |v_0|^2$). As can be seen in (2.5), a gap of $\Delta_0$ exists in the excitation spectrum. Within this gap no single-particle states exist in the superconductor.

For a normal conductor, the superconducting pair potential is zero. This implies that the two components of (2.1) are decoupled and pure electrons (1,0) and holes (0,1) exist. For a hole state (0,1), the energy eigenvalues are positive for $|\boldsymbol{k}| < k_\mathrm{F}$ and negative for $|\boldsymbol{k}| > k_\mathrm{F}$. This can easily be seen if the Bogoliubov equation is solved for a hole state with $\Delta_0 = 0$. As an important consequence, the direction of the group velocity

$$\boldsymbol{v_k} = \frac{1}{\hbar}\nabla_{\boldsymbol{k}} E \tag{2.6}$$

is, for a hole, opposite to its wave vector $\boldsymbol{k}$. This is in contrast to the case of an electron, where $\boldsymbol{v_k}$ and $\boldsymbol{k}$ are oriented in the same direction.

In addition to its application to homogeneous systems, as discussed above, the Bogoliubov equation can also be used as a very powerful tool to describe inhomogeneous systems like superconductor/normal conductor interfaces.

## 2.2 Quasiparticle Transport Through a Superconductor/Normal-Conductor Interface

Here, the models describing carrier transport through a superconductor/normal-conductor interface are introduced. The Andreev reflection process is the basic ingredient of the theoretical description. However, in order to be able to model nonideal interfaces, normal scattering and the proximity effect have to be included also.

### 2.2.1 Andreev Reflection

If a normal conductor is coupled to a superconductor a unique reflection process, namely Andreev reflection, can be observed [49]. This reflection mechanism is depicted in Fig. 2.2. Let us assume an electron with an energy $E < \Delta_0$ slightly above the Fermi level $\mu$ moving towards the normal conductor/superconductor interface. Since no quasiparticle states are provided in the superconductor, transmission is excluded. Furthermore, no normal reflection is allowed, because there is no barrier present at the interface, which can absorb the momentum difference. However, a Cooper pair can be formed in the superconductor, with the consequence that an additional electron is taken from the completely filled Fermi sea of the normal conductor. In a degenerate electron gas this electron vacancy can be interpreted as a hole carrying a positive charge.

For the generation of a Cooper pair in the superconductor, the wave vector of the electron taken from the Fermi sea needs to have a direction opposite to the wave vector of the incident electron. Since in a completely filled Fermi sea the total wave vector is zero, the remaining wave vector of the system after one electron has been removed for the Cooper pair has the same direction as the incident electron. The wave vector of the system is identical to the wave vector of the hole. Thus, the incident electron and the created hole have a wave vector in the same direction. However, as mentioned above, the wave vector and the group velocity of a hole are in opposite directions. Consequently, the hole takes the same path as the incident electron in the reverse direction; therefore this process is called *retroreflection*. Owing to the opposite charge and opposite group velocity of electrons and holes, this

also implies that the conductance is twice as large as for an ideal normal transmission through the interface.

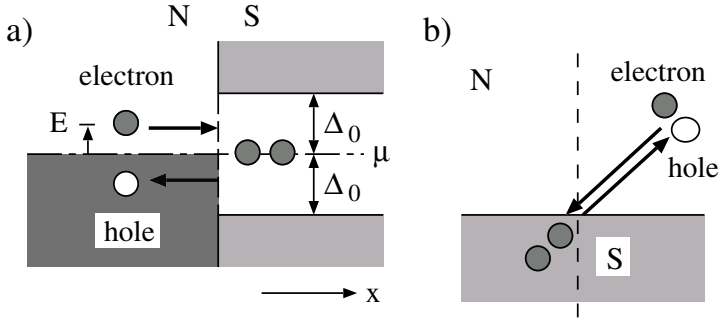


**Fig. 2.2.** (**a**) Energy diagram of the Andreev reflection process: an incident electron from the normal-conductor side is retroreflected as a hole, while a Cooper pair is formed in the superconductor. (**b**) In real space: in contrast to the normal reflection process, the retroreflected hole takes the same path as the incident electron in reverse

For an incident electron with $|E| > \Delta_0$, quasiparticles, electron- or hole-like, are excited in the superconductor. In this case not only Andreev reflection but also normal specular electron reflection take place with a certain probability. An Andreev reflection probability less than one is found even for $|E| < \Delta_0$ if a potential barrier is introduced at the superconductor/normal-conductor interface, because now normal reflection at the barrier is allowed.

### 2.2.2 Blonder–Tinkham–Klapwijk Model

A model which describes Andreev and normal reflection at a superconductor/ normal-conductor (SN) interface, as well as the transmission of particles through this interface, was first developed by Blonder, Tinkham and Klapwijk (BTK) [46]. A rigorous microscopic derivation of this model was presented a few years later by Zaitsev [50] and Arnold [51]. In the BTK model a potential barrier at the SN interface, e.g. an oxide layer or a Schottky barrier, is approximated by a $\delta$-shaped barrier as depicted in Fig. 2.3a. In the original BTK model no difference of the Fermi energy between the superconductor and the normal conductor was assumed. However, in the case of a semiconductor in contact with a superconductor, the Fermi energies can differ significantly, since the electron concentration in the semiconducting material is usually much lower than in the superconductor. Therefore, if these materials are brought together, the alignment of the Fermi energy leads to a potential step of height $U_0$ at the bottom of the conduction band at the interface (Fig. 2.3a). Similarly to the case of a $\delta$-shaped barrier, this also leads to enhanced normal reflection at the normal-conductor/superconductor interface.

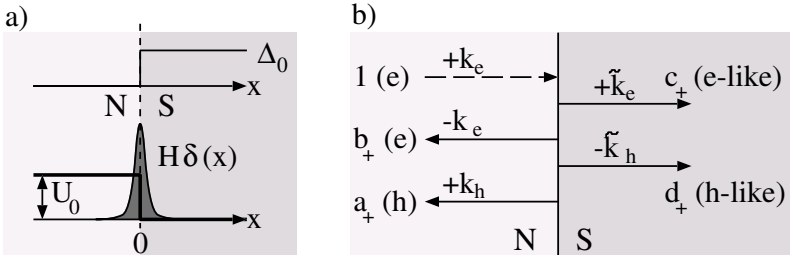


**Fig. 2.3.** (**a**) Model of a normal-conductor/superconductor interface. A step-like increase of the pair potential $\Delta(x)$ is assumed at the NS boundary. The potential step between the superconductor and the normal conductor is $U_0$. In addition, a $\delta$-shaped barrier is assumed at the interface. (**b**) Andreev reflection process where an electron (e) enters the normal-conductor/superconductor interface. The orientation of the *arrows* represent the direction of the group velocity

For simplicity, a step-like increase of the superconducting pair potential is assumed at the interface: $\Delta(x) = \Theta(x)\Delta_0$. The potential $U(x)$ contains the step $U_0$ as well as the $\delta$-shaped barrier at the interface:

$$U(x) = U_0\Theta(-x) + \frac{\hbar^2 k_{\mathrm{FS}}}{m_{\mathrm{e}}} Z\delta(x) \;, \tag{2.7}$$

where $k_{\mathrm{FS}} = \sqrt{2m_{\mathrm{e}}\mu/\hbar^2}$ is the Fermi wave number in the superconductor. The height $H$ of the $\delta$-shaped barrier is expressed by the dimensionless $Z$ parameter

$$Z = Hm_{\mathrm{e}}/\hbar^2 k_{\mathrm{FS}} \;. \tag{2.8}$$

The scattering process of an incident electron wave

$$\psi_{\mathrm{in}}(x) = \begin{pmatrix} 1 \\ 0 \end{pmatrix} \mathrm{e}^{\mathrm{i}k_{\mathrm{e}}x} \tag{2.9}$$

from the normal-conductor side N is depicted in Fig. 2.3b. As a result, electron-like $(u_0, v_0)$ and hole-like $(v_0, u_0)$ quasiparticles are transmitted into the superconductor:

$$\psi_{\mathrm{trans}}(x) = c_+ \begin{pmatrix} u_0 \\ v_0 \end{pmatrix} \mathrm{e}^{+\mathrm{i}\tilde{k}_{\mathrm{e}}x} + d_+ \begin{pmatrix} v_0 \\ u_0 \end{pmatrix} \mathrm{e}^{-\mathrm{i}\tilde{k}_{\mathrm{h}}x} \;. \tag{2.10}$$

At the same time a fraction of the incoming wave is reflected as an electron $(1, 0)$ and a hole $(0, 1)$:

$$\psi_{\mathrm{refl}}(x) = b_+ \begin{pmatrix} 1 \\ 0 \end{pmatrix} \mathrm{e}^{-\mathrm{i}k_{\mathrm{e}}x} + a_+ \begin{pmatrix} 0 \\ 1 \end{pmatrix} \mathrm{e}^{+\mathrm{i}k_{\mathrm{h}}x} \;. \tag{2.11}$$

The corresponding wave numbers in the normal conductor and superconductor are

$$k_{\mathrm{e}} = \sqrt{k_{\mathrm{FN}}^2 + (2m^*/\hbar^2)E}\,, \tag{2.12a}$$

$$k_{\mathrm{h}} = \sqrt{k_{\mathrm{FN}}^2 - (2m^*/\hbar^2)E}\,, \tag{2.12b}$$

and

$$\tilde{k}_{\mathrm{e}} = \sqrt{k_{\mathrm{FS}}^2 + (2m_{\mathrm{e}}/\hbar^2)(E^2 - \Delta_0^2)^{1/2}}\,, \tag{2.13a}$$

$$\tilde{k}_{\mathrm{h}} = \sqrt{k_{\mathrm{FS}}^2 - (2m_{\mathrm{e}}/\hbar^2)(E^2 - \Delta_0^2)^{1/2}}\,, \tag{2.13b}$$

respectively; $k_{\mathrm{FN}} = \sqrt{(2m^*/\hbar^2)(\mu - U_0)}$ is the Fermi wave number in the normal conductor. All particles involved in the scattering process are depicted in the $E(k)$ dispersion relation, shown in Fig. 2.4. From the continuity of the

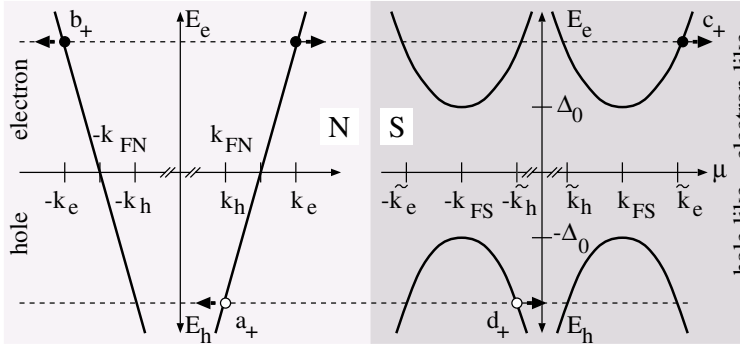


**Fig. 2.4.** Schematic illustration of the $E(k)$ dispersion relation in the normal conductor (N) and in the superconductor (S). The *filled circles* denote electrons and electron-like particles, the *open circles* holes and hole-like particles. The *arrows* indicate the direction of the group velocity. The axis of the hole energy $E_{\mathrm{h}}$ points downwards

wave function at the normal-conductor/superconductor interface ($x = 0$),

$$\psi_{\mathrm{in}}(0) + \psi_{\mathrm{refl}}(0) = \psi_{\mathrm{trans}}(0)\,, \tag{2.14}$$

and the boundary condition for the derivative,

$$\psi'_{\mathrm{in}}(0^-) + \psi'_{\mathrm{refl}}(0^-) - \psi'_{\mathrm{trans}}(0^+) = 2k_{\mathrm{FS}}Z\psi(0)\,, \tag{2.15}$$

the coefficients $a_+$ ,..., $d_+$ can be determined:

$$a_+ = \frac{u_0 v_0}{\gamma}\,, \tag{2.16a}$$

$$b_+ = \frac{(v_0^2 - u_0^2)(\mathrm{i}Z + q)}{\gamma}\,, \tag{2.16b}$$

$$c_+ = \frac{u_0\,[(1+r)/2 - \mathrm{i}Z]}{\gamma}\,, \tag{2.16c}$$

$$d_+ = -\frac{v_0\,[(r-1)/2 - \mathrm{i}Z]}{\gamma}\,. \tag{2.16d}$$

Here, we define $\gamma = u_0^2(p+1) - v_0^2 p$, $q = Z^2/r + (1-r^2)/4r$ and $p = Z^2/r + (r-1)^2/4r$. The ratio

$$r = \frac{v_{\mathrm{FN}}}{v_{\mathrm{FS}}} \tag{2.17}$$

is the Fermi velocity mismatch between the normal-conductor and the superconductor. In case of $|E| < \Delta_0$ the quasiparticle waves are exponentially damped since $\tilde{k}_{\mathrm{e}}$ and $\tilde{k}_{\mathrm{h}}$ contain an imaginary component.

For a hole injected from the normal-conductor side, the reflection coefficients $a_-$ ,..., $d_-$ can be calculated from the coefficients determined above by simply replacing $Z$ by $-Z$, i.e. $a_-(Z) = a_+(-Z)$. In case of injection of an electron-like particle from the superconductor into the normal-conductor, time reversal symmetry leads to the following transmission coefficients:

$$\begin{aligned} c'_\pm &= c_\pm(u_0^2 - v_0^2)/r\,, \\ d'_\pm &= d_\pm(u_0^2 - v_0^2)/r\,. \end{aligned} \tag{2.18}$$

The set of coefficients $a_\pm$,..., $d_\pm$, $c'_\pm$ and $d'_\pm$ will be used explicitly for the calculation of the supercurrent in a superconductor/two-dimensional-electron-gas/superconductor junction in Sect. 6.1.2.

The electrical current $I(V)$ through a single SN interface can be calculated from the probability currents [46]. In order to find an expression for $I(V)$ it is sufficient to consider the contributions on the normal-conductor side, i.e. the Andreev-reflected contribution $A(E)$ and the normal-reflected contribution $B(E)$:

$$I(V) = \frac{e k_{\mathrm{FN}} W}{\pi^2 \hbar} \int_{-\infty}^{\infty} [f_0(E+eV) - f_0(E)][1 + A(E) - B(E)]\,\mathrm{d}E\,. \tag{2.19}$$

Here, $f_0(E)$ is the equilibrium Fermi distribution function, $V$ is the voltage drop at the interface and $W$ is the contact width. The Andreev reflection coefficient is defined as $A(E) = a_+^* a_+$, which is the probability current $J_{\mathrm{P}}^A$ of the Andreev reflected quasiparticles divided by $v_{\mathrm{FN}}$ [46]. Similarly, the normal reflection coefficient $B(E)$ is given by $b_+^* b_+$.

A unique feature of the Andreev reflection is that the total current and thus the conductance are enhanced by this process. This is due to fact that the Andreev-reflected quasiparticle moves with the opposite group velocity to the incident quasiparticle but possesses the opposite charge at the same time. The contribution of the Andreev reflection can result in a so-called excess current $I_{\mathrm{exc}}$, which is the current added to the normal current $I_{\mathrm{N}} = V/R_{\mathrm{N}}$ at $eV \gg \Delta_0$ [46]. $R_{\mathrm{N}}$ is the normal-state resistance in the absence of superconductivity.

For an isolated SN junction the Fermi velocity mismatch $r$ can be exactly reproduced by shifting the $Z$ parameter to a higher effective value, $Z_{\mathrm{eff}} = \sqrt{p} = [Z^2 + (1-r)^2/4r]^{1/2}$ [52]. If we define $\eta = v_0/u_0$, the Andreev and

normal reflection coefficients $A(E)$ and $B(E)$ used in (2.19) can be written as [53]

$$A(E) = \frac{|\eta|^2}{|1 + Z_{\text{eff}}^2(1-\eta^2)|^2}\,, \tag{2.20a}$$

$$B(E) = \frac{Z_{\text{eff}}^2(1+Z_{\text{eff}}^2)|1-\eta^2|^2}{|1+(1-\eta^2)Z_{\text{eff}}^2|^2}\,. \tag{2.20b}$$

In Fig. 2.5, the coefficients $A(E)$ and $B(E)$ are plotted for $Z_{\text{eff}} = 0$ and $Z_{\text{eff}} = 0.5$.

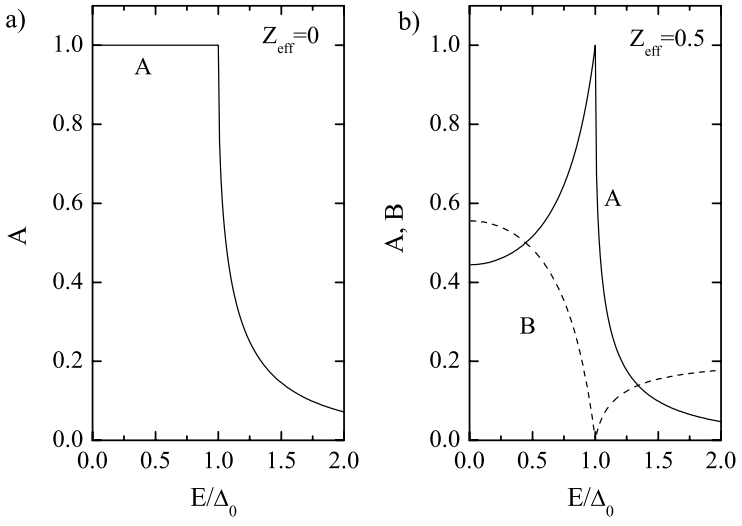


**Fig. 2.5.** (**a**) Andreev reflection coefficient $A$ as a function of $E/\Delta_0$ for $Z_{\text{eff}} = 0$; (**b**) Andreev reflection coefficient $A$ and normal reflection coefficient $B$ for $Z_{\text{eff}} = 0.5$

In the expression for the current through the interface (2.19), only normal incidence of the quasiparticles was considered. The dependence of the Andreev reflection coefficient on the angle of incidence $\theta$ was calculated by Hoonsawat and Tang [54]. Mortensen et al. [55] could show in an extended model, which also includes the Fermi velocity mismatch, that the Andreev reflection process is forbidden when $\theta$ is larger than a critical angle. Extensions of the BTK model concerning a finite-thickness barrier or a superconductive interlayer have been developed by Kupka [56] and by Sánchez-Cañizares and Sols [57].

### 2.2.3 Inclusion of the Proximity Effect

One key assumption of the BTK model is the step-like superconductive pair potential $\Delta(x)$ at the superconductor/normal-conductor interface, where $\Delta(x)$ is usually set to the value of the bulk superconductor. However, in many cases it can be necessary to assume a modified pair potential at the boundary with the normal-conducting layer in order to obtain a consistent interpretation of the measured results [45, 58, 59]; i.e., if a superconducting material is deposited on a normal-conductor, the properties of the first atomic layers can be degraded owing to residual atoms or molecules on the surface. Hence, for a more realistic description of the superconductor/normal-conductor system, it can be worthwhile to assume an additional normal-conductive interlayer (N) in between. The normal-conducting electrode can, in our case be specified to be a semiconductor (Sm). Owing to the additional N layer, the semiconductor is in this case not in direct contact with the superconductor anymore. The complete layer sequence would thus be SN/Sm. However, if the N layer is sufficiently thin, the superconducting properties will be preserved to a certain degree. The underlying mechanism is the proximity effect [60]. Here, Cooper pairs from the superconductor can leak into the normal-conductor and diffuse a certain distance before they decay. This decay takes place on a length scale given by the coherence length $\xi_{\mathrm{N}}$.

For the discussion of the basic principle of the proximity effect, an SN sandwich in the *dirty limit* will be considered first. The dirty limit means that the coherence lengths $\xi_{\mathrm{S}}$ and $\xi_{\mathrm{N}}$ are much larger than the corresponding elastic mean free paths $l_{\mathrm{el,S}}$ and $l_{\mathrm{el,N}}$ in the superconductor and normal-conductor, respectively. The coherence lengths $\xi_{\mathrm{S,N}}$ in the dirty limit are given by

$$\xi_{\mathrm{S,N}} = \sqrt{\hbar \mathcal{D}_{\mathrm{S,N}} / 2\pi k_{\mathrm{B}} T_{\mathrm{c}}}\,, \tag{2.21}$$

where $\mathcal{D}_{\mathrm{S,N}}$ is the corresponding diffusion constant and $T_{\mathrm{c}}$ is the critical temperature of the superconductor. As mentioned above, the N layer will usually be composed of a degraded superconductor material. The metallic superconducting films used for superconductor/semiconductor structures contain a large number of scattering centers. Therefore, the dirty-limit case is justified for the S as well as for the N layer. Independently, the semiconductor attached to this SN sandwich can be either in the clean or in the dirty limit. In the former case the coherence length is much smaller than the elastic mean free path.

The large number of scattering centers in the SN sandwich makes it virtually impossible to apply the Bogoliubov equation directly, in order to describe the system. A theoretical tool that allows one to handle the dirty-limit case in the S and N layers is provided by the Usadel equation [61], which follows from the Eilenberger equations [62] under momentum averaging:

$$\xi_{\mathrm{N,S}}^2 \theta''_{\mathrm{N,S}}(x) + \mathrm{i}\frac{E}{\pi k_{\mathrm{B}} T_{\mathrm{c}}} \sin\theta_{\mathrm{N,S}}(x) + \frac{\Delta_{\mathrm{N,S}}(x)}{\pi k_{\mathrm{B}} T_{\mathrm{c}}} \cos\theta_{\mathrm{N,S}}(E,x) = 0\,. \tag{2.22}$$

Here, the system is described by a formally introduced complex angle $\theta_{\mathrm{N,S}}(E,x)$, where $\cos\theta_{\mathrm{N,S}}(E,x)$ is the normal angle-averaged Green's function $G(E,x)$ and $\sin\theta_{\mathrm{N,S}}(E,x)$ represents the anomalous angle-averaged Green's function $F(E,x)$. The pair potential $\Delta_{\mathrm{S}}(x)$ in the superconductor has to be determined from the self-consistency equation

$$\frac{\Delta_{\mathrm{S}}(x)}{\pi k_{\mathrm{B}} T_{\mathrm{c}}} \ln\frac{T}{T_{\mathrm{c}}} + 2\frac{T}{T_{\mathrm{c}}} \sum_{\omega_n>0} \left[ \frac{\Delta_{\mathrm{S}}(x)}{\pi\omega_n k_{\mathrm{B}} T_{\mathrm{c}}} - \sin\theta_{\mathrm{S}}(E=\mathrm{i}\omega_n, x) \right] = 0\,. \quad (2.23)$$

Here, $\omega_n$ is the normalized Matsubara frequency given by $(2n+1)T/T_{\mathrm{c}}$. In the normal-conductor the pair potential $\Delta_{\mathrm{N}}(x)$ is assumed to be zero. The Green's functions $G(E,x)$ and $F(E,x)$ contain a direct physical meaning. The real part of $G(E,x)$ can be interpreted as the quasiparticle density of states (DOS)

$$\mathrm{DOS}(E,x) = \mathrm{Re}[G(E,x)]\,, \quad (2.24)$$

while $\mathrm{Re}[F(E,x)]$ may be interpreted as the DOS of correlated particles.

The proximity effect in an SN sandwich was treated theoretically by Kupriyanov and Lukichev [63]. They succeeded in deriving boundary conditions for the normal and anomalous Green's functions $G(E,x)$ and $F(E,x)$ at the SN interface [64, 65]. Since the Usadel equations are not valid at distances of the order of $l_{\mathrm{el,S}}$ and $l_{\mathrm{el,N}}$ from the interface, the boundary conditions, as given below, had to be derived from the more general Eilenberger equations [62]:

$$\gamma_{\mathrm{B}}\xi_{\mathrm{N}}\theta'_{\mathrm{N}}(0^+) = \sin\left[\theta_{\mathrm{N}}(0^+) - \theta_{\mathrm{S}}(0^-)\right]\,, \quad (2.25)$$

$$\gamma\xi_{\mathrm{N}}\theta'_{\mathrm{N}}(0^+) = \xi_{\mathrm{S}}\theta'_{\mathrm{S}}(0^-)\,, \quad (2.26)$$

$$\theta_{\mathrm{S}}(-\infty) = \arctan[\mathrm{i}\Delta_0(T)/E]\,, \quad (2.27)$$

$$\theta'_{\mathrm{N}}(d_{\mathrm{N}}) = 0\,. \quad (2.28)$$

The parameter

$$\gamma_{\mathrm{B}} = \frac{2}{3}\frac{l_{\mathrm{el,N}}}{\xi_{\mathrm{N}}}\left\langle\frac{1-D}{D}\right\rangle \quad (2.29)$$

in the first boundary condition (2.25) is a measure of the barrier strength at the interface. This is plausible, since the normal-transmission coefficient $D$ at the SN interface in (2.29) is connected to the $Z$ parameter in the BTK model by $D^{-1} = 1 + Z^2$. In the expression for $\gamma_{\mathrm{B}}$, $< ... >$ denotes angle averaging. The pair-breaking parameter

$$\gamma = \frac{\varrho_{\mathrm{S}}\xi_{\mathrm{S}}}{\varrho_{\mathrm{N}}\xi_{\mathrm{N}}}\,, \quad (2.30)$$

in the second boundary condition (2.26), is a measure of the suppression of the order parameter in the superconductor due to the proximity effect; $\varrho_{\mathrm{N}}$ and $\varrho_{\mathrm{S}}$ are the specific normal-state resistances of the normal and superconducting

material, respectively. For a thin N layer of thickness $d_N$ with $d_N/\xi_N \ll 1$, $\gamma$ can be replaced by

$$\gamma_m = \gamma \frac{d_N}{\xi_N} \,. \tag{2.31}$$

The remaining two boundary conditions (2.27) and (2.28) match the solution at $-\infty$ to a bulk superconductor at $-\infty$ and at the free interface of the N layer at $d_N$, respectively.

The effect of the proximity effect on the Cooper pair density $F(x)$ in an SN sandwich is depicted schematically in Fig. 2.6. As can be seen here, $F(x)$ decreases in the vicinity of the interface on the superconductor side. On the normal-conductor side, $F(x)$ is not zero but rather decreases monotonically. As shown in Fig. 2.6, $\gamma_B$ determines the step in the Cooper pair density $F(x)$, while $\gamma$ is a measure of the suppression of $F(x)$ in the superconductor near the interface.

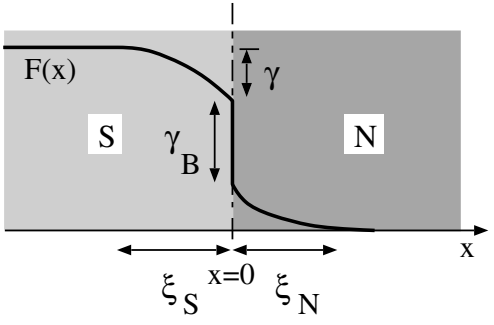


**Fig. 2.6.** Schematic illustration of the spatial dependence of the Cooper pair density $F(x)$ for a representative, fixed energy $E = E_0$ at an SN boundary

As can be seen in Fig. 2.7, the density of states in an SN sandwich, calculated according to (2.24), differs significantly from the DOS of a bulk superconductor. At the SN interface, the maximum of the density of states around $\Delta_S$ is widened and lowered if the coupling between the layers is enhanced by decreasing $\gamma_B$. At the free surface of the N layer ($x = +d_N$) a gap $\Delta_N$ is developed in the density of states owing to the coupling to the superconductor.[1] This energy gap approaches the gap of the superconductor $\Delta_0$ if $\gamma_B$ is decreased. No gap is expected if the N layer is very thick. This situation was considered by Belzig et al. [66]. Near the SN interface the DOS in the N layer has an induced maximum below the gap of the superconductor. This maximum is shifted towards zero if the distance from the interface is

[1] The gap $\Delta_N$ should not confused with the spatially dependent pair potential $\Delta_N(x)$.

increased. For very long distances the DOS approaches the Fermi-level DOS in the normal state.

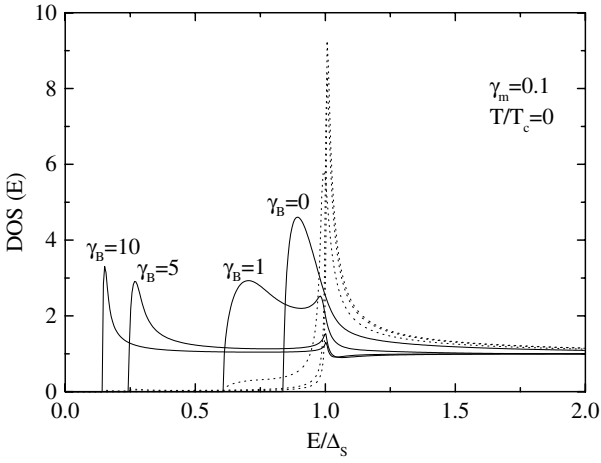


**Fig. 2.7.** Density of states in a thin N layer ($d_N \ll \xi_N$) of an SN sandwich normalized to the normal-state value at the free surface (*solid lines*) and at the SN boundary (*dashed lines*) for $\gamma_m = \gamma d_N/\xi_N = 0.1$ and for various values of $\gamma_B$. Data taken from [58] (© (1996) by the American Physical Society)

In an SN sandwich with a thin layer and a small ratio $\gamma_m/\gamma_B$, the spatial gradients in S can be neglected, and $\Delta_S(x) = \Delta_0$. Then the temperature dependence of the energy gap in the N layer can be determined from [58]

$$\Delta_N(T) = \frac{\Delta_0(T)}{1 + \gamma_B \sqrt{\Delta_0^2(T) - \Delta_N^2(T)}/\pi T_c} \,. \tag{2.32}$$

The two gaps $\Delta_N$ and $\Delta_0$ merge if the temperature is increased towards $T_c$.

Golubov and Kupriyanov [53, 67] succeeded in generalizing the BTK model by including the proximity effect. Instead of an SN bilayer, they assumed an SN/c/N′ structure. Here c is a constriction, which ensures that the proximity effect in the SN sandwich does not extend to the N′ layer. For the structures discussed later, N′ is identical to the semiconductor layer (Sm). The constriction c is naturally given by the reduced dimensions of the conducting channel in the semiconductor. In contrast to the BTK model, the semiconductor is not in direct contact with the superconductor via the constriction but rather with a normal-conducting layer (N), which is modified by the proximity effect. Owing to the proximity effect, the density of states at the interface with the semiconductor is altered, whereas in the BTK model, the quasiparticle density of states of the superconductor at the interface corresponds to its bulk value $DOS(E) = E/\sqrt{E^2 - \Delta_0^2}$.

Owing to the modified density of states in the N layer, the Andreev reflection coefficient $A(E)$ and the normal-reflection coefficient $B(E)$ of the BTK model, as given by (2.20b), have to be replaced by

$$A(E) = \frac{|F(E, x = 0^-)|^2}{|1 + 2Z^2 + G(E, x = 0^-)|^2} , \tag{2.33}$$

$$B(E) = \frac{4Z^2(1 + Z)^2}{|1 + 2Z^2 + G(E, x = 0^-)|^2} . \tag{2.34}$$

In these expressions the Green's functions $G(E, x)$ and $F(E, x)$ have to be taken at the N/c boundary in the N region. The $Z$ factor is determined by the barrier in the constriction between the N and the Sm layers. In Fig. 2.8, $A(E)$, $B(E)$ and the transmission probability $T(E)$ are plotted as a function of energy. In accordance with the lower gap at the free interface of the N

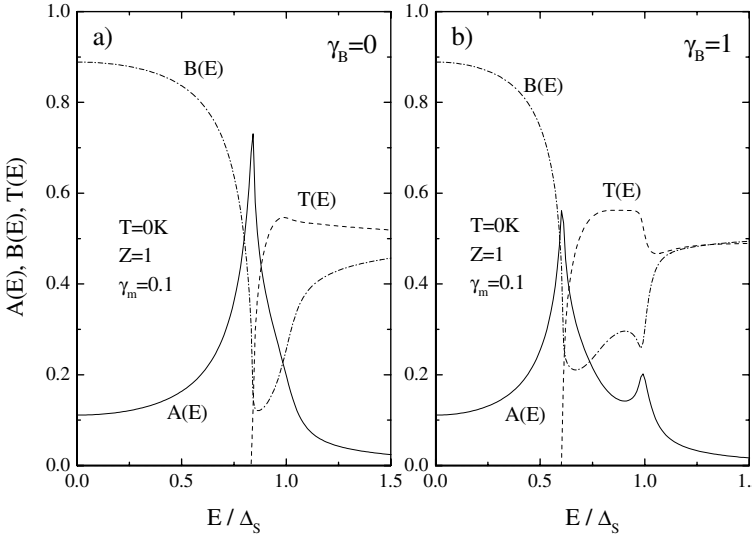


**Fig. 2.8.** Coefficients for Andreev reflection $A(E)$, normal $B(E)$ reflection and transmission $T(E)$ for $Z = 1$ and $\gamma_m = 0.1$. In (**a**) $\gamma_B = 0$ and in (**b**) $\gamma_B = 1$ was assumed. Data taken from [58] (© (1996) by the American Physical Society)

layer due to the proximity effect, the peak position in the Andreev reflection coefficient as a function of energy is found at $E = \Delta_N$. For large values of $\gamma_B$, a second peak near $\Delta_S$ is found in the Andreev reflection coefficient, e.g. for $\gamma_B = 1$ (Fig. 2.8b). This originates from the second maximum in the density of states (see Fig. 2.7).

So far, it has been assumed that in the SN junctions the superconductor is decoupled sufficiently from the normal-conductor that no proximity effect has to be considered between these layers. The proximity layer appeared

exclusively on the side of the superconductor, where an additional nonsuperconducting interlayer was assumed. However, if the coupling between the superconducting and normal-conducting electrodes is sufficiently strong, the proximity effect between these layers has to be considered. As a result the interface pair potential in the superconductor can be reduced compared with its bulk value $\Delta_0$ [68]. The Andreev reflection probability for an SN junction including the proximity effect was calculated by van Son et al. [69]. It was shown that, owing to the decrease of the pair potential in the superconductor at the interface, the Andreev reflection probability is decreased for $E > \Delta_0$ compared with the BTK result.

# 3. Fabrication of Superconductor/ Two-Dimensional-Electron-Gas Structures

Two-dimensional electron gases in semiconductors have some interesting properties, which differ significantly from those of the bulk material, e.g. the electron mobility of a two-dimensional electron gas can be larger by orders of magnitude at low temperatures compared with a bulk semiconductor. Here, a brief overview of different realizations of two-dimensional electron gases and their physical properties is given. After that, the principal fabrication steps required to fabricate a superconductor/semiconductor junction are outlined for a junction based on a surface inversion layer, as well as for a junction with a buried two-dimensional electron gas in a heterostructure.

## 3.1 Two-Dimensional Electron Gases

In a two-dimensional electron gas the electrons can move freely within a plane, while in the direction perpendicular to this plane they are confined by a potential well. Two-dimensional electron gases in semiconductors can be classified into two groups. First, a 2DEG can be formed at the surface of some semiconductors, e.g. InAs. Second, a 2DEG can be located at the interface between two different semiconductor materials, e.g. GaAs and AlGaAs. Since both kinds of structures are employed in superconductor/two-dimensional-electron-gas hybrid structures, the properties of both will be discussed briefly, below. Detailed information on 2DEGs can be found, for example, in [70, 71].

### 3.1.1 Two-Dimensional Electron Gases in Inversion Layers

In some semiconducting materials two-dimensional electron gases are formed directly at the surface of the crystal. Here, a downward bending of the conduction band at the surface leads to a potential well in which the electrons are trapped. This downward bending has its origin in the modified atomic bonds at the surface. Owing to the broken periodicity of the crystal, the electron structure at the surface differs considerably from the structure in the bulk semiconductor. The free valences left at the surface atoms are saturated either by a reconstruction of the surface structure or by adsorption of atoms or molecules. In order to describe these modified surface bonds, discrete energy

Thomas Schäpers: Superconductor/Semiconductor Junctions, STMP 174, 21–30 (2001)
© Springer-Verlag Berlin Heidelberg 2001

levels, so-called surface states, within the band gap of the semiconductor are introduced [72]. The downward bending of the valence band at the surface is a result of the balancing of the Fermi level between the charged surface states and the space-charge region in the semiconductor crystal.

A surface two-dimensional electron gas, as described above, is found in p-doped InAs [73, 74]. Here, the filling of surface states leads to a depletion of holes near the surface and thus to the downward bending of the valence and conduction bands (Fig. 3.1) [75]. Directly at the surface, an inversion layer with accumulated electrons is formed. Inversion means that, in contrast to the bulk crystal, where holes are the majority carriers, the majority carriers are now electrons. Between the inversion layer and the bulk material, a depletion region exists. The electrons are spatially confined in the inversion layer and thus cannot move perpendicular to the surface. The width of the inversion layer is in the order of 10 nm and therefore comparable with the Fermi wavelength. As a result the electron energy is quantized in discrete levels (Fig. 3.1). Since free electron motion is only possible along the surface, a two-dimensional electron gas is formed.

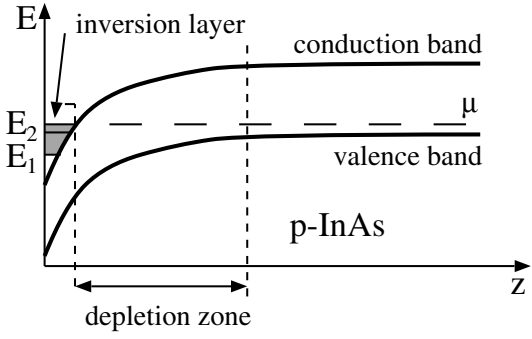


**Fig. 3.1.** Schematic band profile of p-doped InAs at the surface. Directly at the surface, an inversion layer is formed. The electrons are confined in a quantum well with discrete energy levels $E_1$ and $E_2$

The basic properties of a two-dimensional system can be derived from the Schrödinger equation. For a confinement potential $eV(z)$ along the $z$ direction, as shown in Fig. 3.1, the Schrödinger equation can be written as

$$\left[-\frac{\hbar^2}{2m^*}\left(\frac{\partial^2}{\partial x^2}+\frac{\partial^2}{\partial y^2}+\frac{\partial^2}{\partial z^2}\right)+eV(z)\right]\psi(\boldsymbol{r})=E\psi(\boldsymbol{r})\,. \tag{3.1}$$

Here, $m^*$ is the effective electron mass in the semiconductor, which can differ considerably from the free electron mass. Owing to the free motion in the $xy$ plane, the following ansatz can be used for the wave function:

$$\psi(\boldsymbol{r}) = \varphi(z)\exp(\mathrm{i}k_x x + \mathrm{i}k_y y) = \varphi(z)\exp(\mathrm{i}\boldsymbol{k}_\parallel \cdot \boldsymbol{r}) \; . \tag{3.2}$$

The Schrödinger equation can thus be separated into an equation for the free motion along $\boldsymbol{k}_\parallel$ in the $xy$ plane,

$$-\frac{\hbar^2}{2m^*}\left(\frac{\partial^2}{\partial x^2}+\frac{\partial^2}{\partial y^2}\right)\exp(\mathrm{i}k_x x + \mathrm{i}k_y y) = E_\parallel \exp(\mathrm{i}k_x x + \mathrm{i}k_y y) \; , \tag{3.3}$$

and an equation for the bound states within the potential well,

$$\left(-\frac{\hbar^2}{2m^*}\frac{\partial^2}{\partial z^2} + eV(z)\right)\varphi_i(\boldsymbol{r}) = E_i\varphi_i(\boldsymbol{r}) \; . \tag{3.4}$$

$E_i$, where $i = 1, 2, ...$, are the discrete energy levels of the quantum well. As depicted in Fig. 3.2, the energy dispersion relation has the form of parabolas, representing the kinetic motion within the $xy$ plane, shifted by the confinement energy $E_i$. The density of states of each subband $D_i(E)$ is constant,

$$D_i(E) = \frac{m^*}{\pi\hbar^2} \; , \tag{3.5}$$

so that the total density of states increases stepwise each time the next energy level $E_i$ is reached (Fig. 3.2). Owing to the small band gap of InAs, a non-

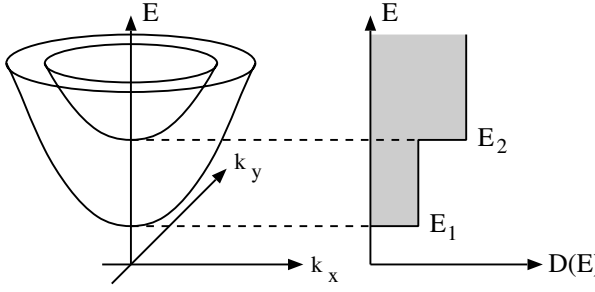


**Fig. 3.2.** Energy dispersion relation of a two-dimensional electron gas. The parabolas of the the kinetic energy are shifted by the energy of the quantized levels in the quantum well. The corresponding density of states is shown on the *right*

parabolic energy dispersion has to be taken into account at higher energies. In this case $D_i(E)$ is not constant anymore [76].

For the case when only one subband is occupied, the sheet electron concentration $n_{2\mathrm{D}}$ can be calculated by using (3.5):

$$n_{2\mathrm{D}} = \int_{E_1}^{\mu} D_1(E)\,\mathrm{d}E = \frac{m^*}{\pi\hbar^2}(\mu - E_1) \; , \tag{3.6}$$

where $\mu$ is the Fermi energy. Since $\mu - E_1 = \hbar^2 k_{\mathrm{FN}}^2/2m^*$, the Fermi wave vector of the two-dimensional electron gas can be expressed as

$$k_{\mathrm{FN}} = \frac{m^* v_{\mathrm{FN}}}{\hbar} = \sqrt{2\pi n_{\mathrm{2D}}} \,. \tag{3.7}$$

The confinement potential for a two-dimensional electron gas in InAs can be approximated by a triangular well [70]. Typical electron concentrations are in the order of $n_{\mathrm{2D}} = 10^{12}$ cm$^{-2}$ [74]. At low temperatures the electron mobility $\mu_{\mathrm{e}}$ is limited by scattering on ionized impurities and by surface roughness scattering. A typical value at low temperature (4.2 K) is $\mu_{\mathrm{e}} = 10\,000$ cm$^2$/V s [74, 77].

The elastic mean free path $l_{\mathrm{el}}$ for carriers in the two-dimensional electron gas is given by

$$l_{\mathrm{el}} = v_{\mathrm{FN}} \tau_{\mathrm{el}} \,. \tag{3.8}$$

Here, $\tau_{\mathrm{el}}$ is the elastic scattering time, which can be extracted from the mobility by using $\tau_{\mathrm{el}} = m^* \mu_{\mathrm{e}} / e$. Taking the typical values for InAs of $\mu_{\mathrm{e}}$ and $n_{\mathrm{2D}}$ results in an elastic mean free path of less than one micrometer.

As we shall see in Sect. 3.2.1, low-resistance contacts to the two-dimensional channel can be prepared by evaporating a superconductor directly on the surface [8]. In order to improve the contact resistance the semiconductor surface is usually cleaned prior to the metal deposition, e.g. by Ar sputtering. The two-dimensional electron gas on the surface of p-InAs is difficult to suppress, with the consequence that adjacent structures are not sufficiently isolated. Isolation can be gained by growing an additional AlInAs layer on top of the p-InAs layer by molecular beam epitaxy [32]. Owing to the band offset between AlInAs and InAs, the band bending in InAs is reduced so that no electrons are accumulated. By simply removing the AlInAs layer by wet chemical etching, the two-dimensional electron gas in the inversion layer can be recovered.

### 3.1.2 Two-Dimensional Electron Gases in Heterostructures

In a semiconductor heterojunction two different semiconducting materials with different band gaps are combined. The band profile for a typical heterostructure is shown in Fig. 3.3. Here, GaAs is used as the lightly n-doped material with the smaller band gap, while the highly n-doped AlGaAs possesses the wide band gap. At the interface the conduction band $E_{\mathrm{c}}$ and valence band $E_{\mathrm{v}}$ change abruptly on an atomic length scale by $\Delta E_{\mathrm{c}}$ and $\Delta E_{\mathrm{v}}$, respectively. Furthermore, the alignment of the Fermi level leads to a charge transfer between the two materials. As a result electrons are trapped at the interface within the lower-band-gap semiconductor. The electrons are supplied by the donors of the wide-gap material. Similarly to the inversion layer at the InAs surface, the electrons can move freely along the interface within the GaAs layer. The scattering of electrons on ionized impurities can be suppressed almost completely if the electrons in the well are separated from the

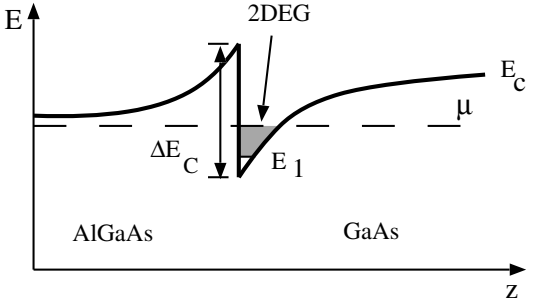


**Fig. 3.3.** Two-dimensional electron gas in a GaAs/AlGaAs heterostructure. The electrons are accumulated at the GaAs/AlGaAs interface in the low-gap material

ionized donors by an undoped spacer layer. By employing this so-called modulation doping technique, the electron mobility is increased and thus very long electron mean free paths $l_{el}$ can be obtained [78].

Electron mobilities as high as $10^7$ cm$^2$/V s have been reported for two-dimensional electron gases in GaAs/AlGaAs modulation-doped heterojunctions [79, 80]. In principle, these structures would be an ideal basis for ballistic superconductor/2DEG structures owing to the extremely large elastic mean free path of several micrometers. "Ballistic" means that the carriers can pass through the structure without any scattering. However, a serious obstacle concerning the coupling of a superconductor to the 2DEG in a GaAs/AlGaAs heterostructure is the high Schottky barrier at the interface. Owing to this barrier, the carrier transfer from the metallic superconductor into the 2DEG is considerably hindered. Nevertheless, superconductor/2DEG contacts based on GaAs/AlGaAs have been successfully prepared by using either annealed indium or tin contacts or by epitaxial growth of aluminum [35, 81, 82].

With regard to a high interface transparency, heterostructures where the two-dimensional electron gas is located in an InAs layer are ideal candidates, since in this case no Schottky barrier is formed. In these structures, AlSb or $Al_{0.2}Ga_{0.8}Sb$ is used as a barrier material for the quantum well (Fig. 3.4a) [83, 84, 85]. Typical electron concentrations and mobilities at low temperatures ($< 50$ K) are in the order of $1 \times 10^{12}$ cm$^{-2}$ and 60 000 cm$^2$/V s, respectively [84]. In order to make contact between the 2DEG and the superconductor, the heterostructure has to be etched down to the top of the InAs channel and covered subsequently by the superconductor layer. By this method a larger contact area and thus a low interface resistance are obtained [28, 36, 86, 87]. Alternatively, the layer system can be etched below the InAs channel so that the superconductor layer is contacted at the sidewall of the semiconductor mesa [23]. The latter method leads to a better geometrical definition of the contact at the cost of a larger interface resistance.

Heterostructures with an InAs-based channel layer can also be realized by using $Al_{0.48}In_{0.52}As$ as a barrier material if the structure is grown by

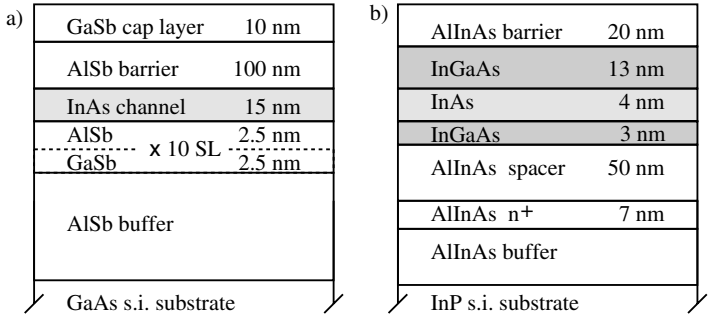


**Fig. 3.4.** (**a**) Typical layer structure of an AlSb/InAs heterostructure (on a GaAs semi-insulating substrate). The lower barrier is formed by an AlSb/GaSb superlattice terminated by AlSb. The top GaSb cap layer prevents oxidation of the AlSb layer [88]. (**b**) A two-dimensional electron gas in an AlInAs/In(Ga)As/InP heterostructure. The electrons are located in the InGaAs/InAs/InGaAs sandwich. The carriers are supplied by the AlInAs $n^+$ dopant layer [89]

molecular beam epitaxy (MBE), or by using an InP barrier if low-pressure metal-organic vapor phase epitaxy is employed. However, the large lattice mismatch between the channel and the barrier restricts the maximum allowed thickness of the InAs layer before strain causes dislocations in the crystal. In order to obtain a sufficiently low bound state so that electrons are accumulated in the quantum well, the quantum well width can be extended effectively by sandwiching the InAs layer between two $In_{0.53}Ga_{0.47}As$ layers (Fig. 3.4b) [89, 90]. The latter is lattice matched to InP. Another feasible way is to use a strained InGaAs channel layer with a higher indium content, with respect to $In_{0.53}Ga_{0.47}As$ [39, 40]. By this method the quantum well can be grown sufficiently thick to accumulate enough electrons. For a channel layer with an indium content of 77%, very high mobilities of up to $4.5 \times 10^5$ cm$^2$/V s at a sheet carrier concentration of $6.0 \times 10^{11}$ cm$^{-2}$ were obtained. The layer sequence of this type of heterostructure is shown in Fig. 4.1 in Sect. 4.1.1.

## 3.2 Fabrication of Superconductor/ Two-Dimensional-Electron-Gas/ Superconductor Junctions

The different locations of the two-dimensional electron gas in a surface inversion layer and in a heterostructure require different methods to contact the 2DEG to a superconducting electrode. Only the basic principles concerning the fabrication of superconductor/two-dimensional-electron-gas/superconductor junctions will be discussed in the following two sections. Of course, fabricating these elements is only a first step for the experiments

described in the subsequent chapters, and additional fabrication processes are required.

### 3.2.1 Junctions Based on a Surface Inversion Layer

In the case of a semiconductor structure with an inversion layer, the superconductor can be deposited directly on the surface in order to make contact to the two-dimensional electron gas. Josephson coupling can be obtained if the two superconducting electrodes are linked by a small semiconducting bridge with a length of a few hundreds of nanometers. One possible way to obtain such small dimensions is to use electron beam lithography [8, 14, 91]. However, the use of electron beam lithography can be circumvented by using simple optical lithography in conjunction with some special preparation techniques in order to obtain a small separation of the superconducting electrodes.

The first method is based on a step edge, which is used as a shadow mask for the definition of the superconducting contacts [30, 92]. The concept of a step edge junction was first introduced by Serfaty et al. [93]. A schematic illustration of this type of junction based on p-type InAs is depicted in Fig. 3.5a. In the first preparation step the upper Nb electrode is defined by optical lithography and lift-off. Prior to the deposition, the semiconductor surface is cleaned either by a water solution of $NH_3$ or by $Ar^+$ sputtering to remove oxides from the surface. After the first Nb layer is deposited, the step, which defines the channel length, is wet chemically etched ($H_2O_2$:$H_3PO_4$:$H_2O$), using the first Nb layer as an etch mask. Typical step heights are around 100 nm. Next, the second Nb layer is deposited. In order to avoid shorts between the electrodes, the sample is tilted during the deposition. The two-dimensional channel at the InAs surface follows the step from the top Nb electrode to the bottom electrode. In order to obtain a well-defined two-dimensional electron gas, a low-p-doped ($< 10^{17}$ cm$^{-3}$) InAs layer is grown by molecular beam epitaxy on an InAs substrate, which is usually highly p-doped. By this method, the two-dimensional channel is sufficiently insulated from the substrate.

As an interesting feature, additional semiconducting layers embedded in the InAs can be inserted by using molecular beam epitaxy. These layers can, for example, serve as barriers in the channel along the step [20]. In other structures, a p-doped layer used to form the channel at the surface is sandwiched between two n-doped layers, which serve as a contact layer to the Nb electrodes [30].

Another very interesting method to fabricate Nb–InAs–Nb junctions was developed by Chrestin et al. [29, 59]. The structure is shown in Fig. 3.5b. After the first Nb electrode has been defined by sputter deposition and lift-off, the front edge of the Nb electrode is anodically oxidized. The insulating $Nb_2O_5$ layer serves as a spacer for the second Nb layer. The geometry for this second Nb layer is defined by optical lithography. Before the Nb film can be deposited, the oxidized InAs has to be removed by a selective wet chemical etch ($H_2SO_4$:$H_2O$), which does not etch the $Nb_2O_5$ layer. Owing to

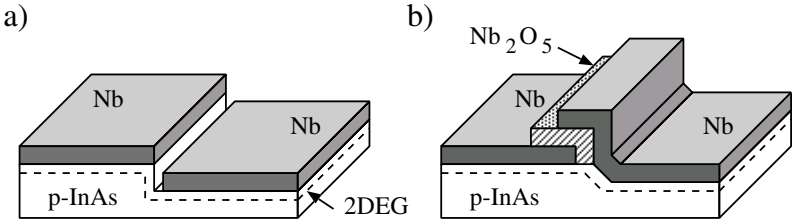


**Fig. 3.5.** Two alternative methods which can be used to prepare Nb–InAs–Nb junctions. (**a**) Step edge junction, where the Nb electrode separation is determined by a step etched into the InAs substrate. (**a**) Nb–InAs junction, where the channel length is given by an anodic oxidized Nb layer

the overlapping Nb layers separated by the $Nb_2O_5$ layer, a relatively large capacitance is connected in parallel with the junction, which has a large influence on the current–voltage characteristics.

### 3.2.2 Junctions Based on a Buried Two-Dimensional Electron Gas

In order to prepare junctions with a buried two-dimensional electron gas in a heterostructure, electron beam lithography is mostly employed in order to obtain a superconductor electrode separation of a few hundred nanometers. Nevertheless, advanced self-aligned optical lithography processes can also be used to obtain electrode separations of less than half a micron [94].

In order to give an impression of how a typical junction with a buried two-dimensional electron gas is fabricated, the preparation steps required for a Nb–InGaAs/InP–Nb junction are described in detail. For the fabrication of these junctions, a two-step electron beam lithography process is employed. The junctions are based on the heterostructure introduced in Sect. 3.1.2. In the first step an InGaAs/InP wire structure is defined by electron beam lithography and subsequent reactive ion etching (RIE) with $CH_4/H_2$, as depicted in Fig. 3.6. A Ti layer is used as an etching mask to fabricate wire structures having a width of a few hundreds of nanometers.

After the etching procedure, the samples are mounted in an ultrahigh-vacuum chamber, where $Ar^+$ sputtering is used to clean the semiconductor surface. Subsequently, a 100 nm thick Nb layer is evaporated in situ. Depositing the Nb layer directly on the semiconductor and thus avoiding any lithography step after the RIE process ensures that no residual organic contamination from the resist remains on the surface.

The geometry of the Nb electrodes is defined by a second electron beam lithography step aligned with the first pattern. Again a Ti etching mask is employed for the reactive-ion-etching process ($SF_6$) of the Nb layer. A scanning electron micrograph of a complete sample is shown in Fig. 3.7. It

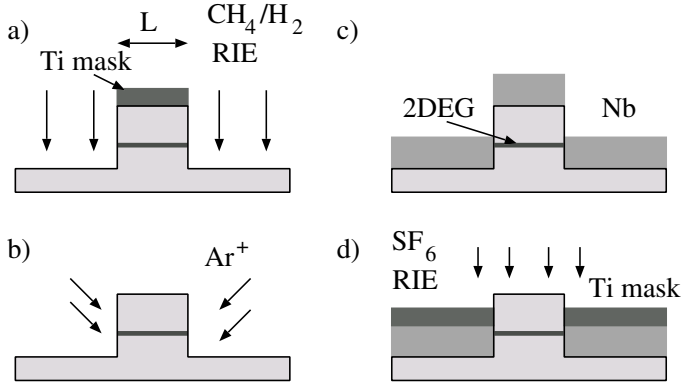


**Fig. 3.6.** Preparation steps used for the fabrication of a Nb–InGaAs/InP–Nb junction: (**a**) $CH_4/H_2$ reactive ion etching of the semiconductor wire structure, (**b**) $Ar^+$ sputter cleaning before Nb deposition, (**c**) Nb deposition, (**d**) geometrical definition of the Nb electrodes by electron beam lithography and $SF_6$ RIE

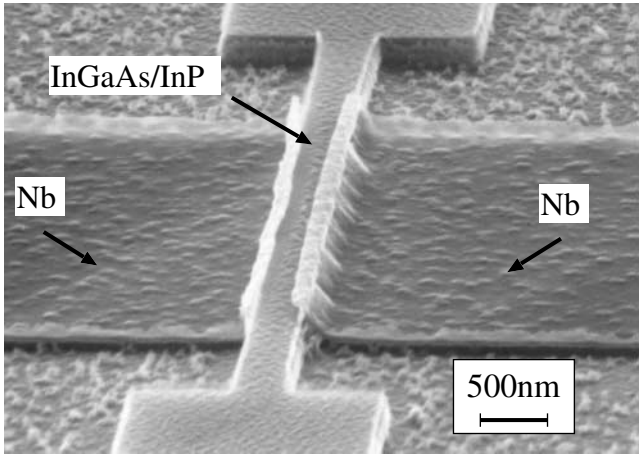


**Fig. 3.7.** Scanning electron micrograph of a typical Nb–InGaAs/InP–Nb junction with a length $L$ of 450 nm and a width $W$ of 2 µm [165]

can be seen that the InP surface is covered by In droplets. During the $Ar^+$ sputtering, the phosphorus component is removed from the lattice so that the remaining surplus indium forms droplets on the surface [95, 96]. In order to prevent a conductive bypass channel on the surface, the samples are etched in an acetic acid solution [94, 97].

As an alternative to the fabrication methods described above, the width of the semiconducting channel can be defined by wet chemical etching [38, 98] or by wet chemical etching combined with $Ar^+$ milling [14]. For some types of junctions, the semiconductor is only etched down to the top of the conductive

layer [38, 98]. By this technique, the contact area between the superconductor and the semiconductor is enlarged. The definition of the channel by etching can be completely omitted if the superconducting electrodes are fabricated by alloying, as has been demonstrated for AlGaAs/GaAs-based junctions [35, 81].

# 4. Transport Studies on Single Superconductor/ Two-Dimensional-Electron-Gas Interfaces

A detailed knowledge of single superconductor/two-dimensional-electron-gas structures is very important in order to understand more complex systems like the S/2DEG/S junctions treated in the following chapters. First, we shall focus on the effect of different surface treatments prior to the deposition of the Nb electrodes. Measurements of the differential resistance as a function of the voltage drop at the interface give direct information about the Andreev reflection probability and thus about the transparency of the interface. Only two-dimensional electron gases in heterojunctions are covered here. However, most of the findings also apply to inversion layer structures. Several alternative fabrication methods for S/2DEG contacts which have been investigated and evaluated will be reported. By using a point contact to inject carriers into a superconductor/two-dimensional-electron-gas interface, the Andreev reflection probability can be measured, directly. In addition, point contacts can also be used to obtain information about the angular distribution of the Andreev reflection.

## 4.1 Effect of the Surface Treatment

The transparency of a superconductor/2DEG interface depends crucially on the surface treatment of the semiconductor prior to the deposition of the superconductor layer. Here, different cleaning methods for InGaAs/InP heterostructures will be compared. For the electrical characterization of the differential conductance, $\mathrm{d}I/\mathrm{d}U$ was measured by using a lock-in technique. This approach has been chosen earlier also for other superconductor/semiconductor structures e.g. for Nb–Si [99, 100], Nb-$In_{0.53}Ga_{0.47}As$ [33, 101, 102], Sn–GaAs/AlGaAs [103] and Nb–(Al,Ga)Sb systems [86, 104].

### 4.1.1 Preparation of Single S/2DEG Contacts

In order to study of the transparency of an S/2DEG interface prepared by different methods, it is sufficient to fabricate relatively large samples by optical lithography [45]. In contrast to the 2DEG at the surface of InAs, the 2DEG in a heterostructure is covered by a nonconductive cap layer. Therefore, it is necessary to contact the two-dimensional channel from the side. For

Thomas Schäpers: Superconductor/Semiconductor Junctions, STMP 174, 31–46 (2001)
© Springer-Verlag Berlin Heidelberg 2001

the following studies InGaAs/InP structures were used. Of course, the results reported here can be transferred to the preparation of superconductor/two-dimensional-electron-gas structures based on a different type of heterostructure.

The $In_{0.53}Ga_{0.47}As/In_{0.77}Ga_{0.23}As/InP$ heterostructure was grown by low-pressure metal-organic vapor phase epitaxy (LP-MOVPE) [39, 40]. In Fig. 4.1, the layer sequence together with a schematic conduction band profile is shown. The electrons of the 2DEG, which is located in the strained $In_{0.77}Ga_{0.23}As$ layer, are supplied from a 10 nm thick InP dopant layer, which is separated by a 20 nm thick InP spacer layer. The dopant concentration was $4.9\times10^{17}$ cm$^{-3}$. On top of the strained $In_{0.77}Ga_{0.23}As$ channel, a 150 nm thick $In_{0.53}Ga_{0.47}As$ layer, lattice matched to InP, was grown. Since the quality of the InGaAs/InP interface is not as good as that of the inverse InP/InGaAs interface if grown by MOVPE, $In_{0.53}Ga_{0.47}As$ instead of InP was used as a top barrier in order to obtain maximum electron mobilities. Shubnikov–de Haas and quantum Hall measurements at 1.4 K yield mobilities of about 370 000 cm$^2$/V s and a carrier concentration of $7 \times 10^{11}$ cm$^{-2}$. An effective electron mass of $m^* = 0.04\, m_e$ was extracted from temperature-dependent Shubnikov–de Haas measurements.

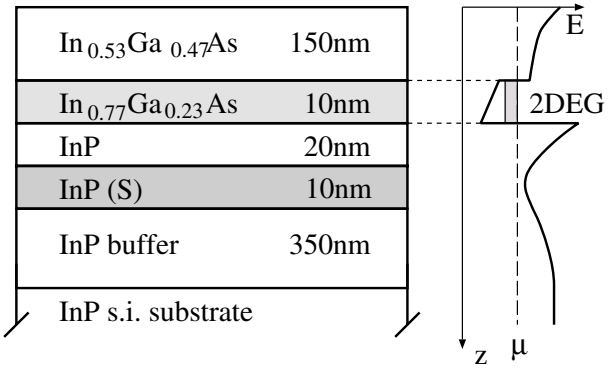


**Fig. 4.1.** Layer system of the $In_{0.53}Ga_{0.47}As/In_{0.77}Ga_{0.23}As/InP$ heterostructure. The conduction band profile is drawn schematically

In order to contact the 2DEG laterally to the superconductor, the heterostructure is partially removed by a $CH_4/H_2$ reactive-ion-etching process (Fig. 4.2). Subsequently, alloyed Ni/AuGe/Ni ohmic contacts are prepared in order to measure the voltage drop at the interface between the superconductor and the 2DEG. The crucial step for the preparation of transparent Nb/2DEG interfaces is the cleaning procedure, which has to be carried out immediately before the evaporation of the Nb layer. Either wet chemical

etching, ion sputter cleaning or a plasma treatment can be performed for this purpose. Details of the surface cleaning procedure are described in conjunction with the corresponding measurements. The 100 nm thick Nb film is deposited by sputtering or by electron beam evaporation. The width of the contact is $W = 100$ µm. The Nb film has an overlap of a few microns with the $In_{0.53}Ga_{0.47}As$ cap layer. However, the possible leakage current can be neglected, as shown by a comparative study of top and side contacts [105].

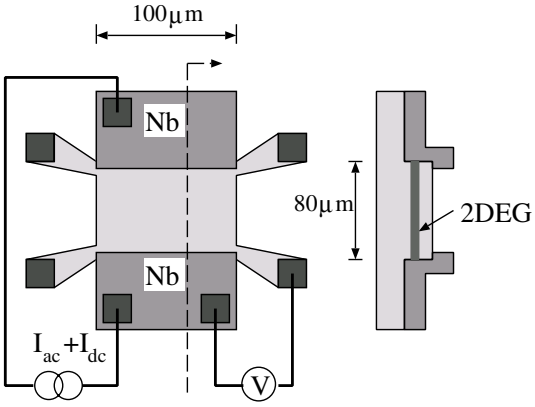


**Fig. 4.2.** Schematic top view and cross section of the lateral contact from the Nb layer to the 2DEG. In order to obtain a homogeneous current distribution, the current flows from one Nb electrode to the opposite one

### 4.1.2 Samples Cleaned by Wet Chemical Etching

Wet chemical cleaning has an advantage over ion sputter methods because the semiconductor crystal is not degraded by the impact of ions. Especially for InP, this can be a serious problem [95, 96, 106]. For the wet chemical cleaning, the samples were etched in 1 HF : 20 $H_2O$ [45]. HF was chosen since oxides are expected on the surface owing to an $O_2$ treatment after the $CH_4/H_2$ RIE and owing to exposure of the structures to air before the Nb deposition. As an alternative to HF, $NH_4OH$ [30] or $HCl/CH_4COOH/H_2O_2/H_2$ [107] can be used to remove oxides from the surface before Nb deposition. For the HF-cleaned samples reported here, the Nb film was deposited by sputtering.

The normalized differential conductance $R_N dI/dV$ of the sample cleaned by HF wet chemical etching is plotted as a function of $eV/\Delta_0$ in Fig. 4.3. The normal-state resistance for this sample was 1 kΩ and $\Delta_0$ had a value of 1.38 meV, corresponding to $T_c = 9.1$ K. The experimental curve reveals two evident features. First, $\sigma_{SN}(0) = dI/dV_{(V=0)}$ is reduced to only 14% of its normal-state value $\sigma_{NN}$. Second, maxima are observed near $eV = \pm\Delta_0$. From

the drop of the differential conductance at low bias voltage, it can be concluded that a barrier is present at the interface. This barrier could partially originate from the Fermi velocity mismatch between the superconductor and the 2DEG. Furthermore, adsorbates on the surface such as fluoride and water could give rise to an additional contribution to the barrier.

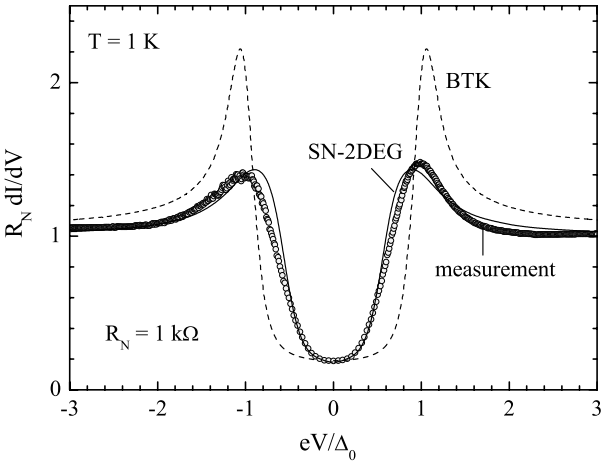


**Fig. 4.3.** Normalized differential conductance as a function of $eV/\Delta_0$ (○). The BTK curve for $Z_{\mathrm{BTK}} = 2$ is plotted for comparison (*dashed line*). The fit assuming an SN/2DEG layer system with $\gamma_1 = 1.6$, $\gamma_2 = 0.2$, $\gamma_{\mathrm{B}_2} = Z^2 = 6$, $d_{\mathrm{N}} = 0.06\,\xi_{\mathrm{N}}$ and $\Gamma_{\mathrm{SN}} = 0.07$ is plotted as a *solid line* [45] (© (1996) by the American Physical Society)

The overall shape of the $R_{\mathrm{N}}\mathrm{d}I/\mathrm{d}V$ curve can be explained by the BTK model if a finite barrier ($Z > 0$) is assumed at the interface. Owing to normal reflection processes, a decrease of the differential conductance is expected for $|eV| < \Delta_0$, while the singular density of states near $\Delta_0$ causes an enhancement of $\mathrm{d}I/\mathrm{d}V$. A $Z$ parameter of 2.0, which gives rise to the observed drop of $\sigma_{\mathrm{SN}}(0)$, was determined from $\sigma_{\mathrm{SN}}(0)/\sigma_{\mathrm{NN}} = 2(1 + Z^2)/(1 + 2Z^2)^2$ [46]. As can be seen in Fig. 4.3, the curve calculated from the BTK model does not agree very well with the measured one. The peaks in the BTK model are found at a larger bias voltage and have a substantially higher peak value.

Obviously, the BTK model does not describe the experimental findings sufficiently. The shift of the conduction maxima towards lower voltages can be explained if a normal-conducting film (N) between the Nb layer (S) and the 2DEG is assumed [45]. This normal-conducting film consists most likely of $\mathrm{NbO}_x$ compounds. Owing to the strong gettering of the Nb film, the first atomic layers in particular contain oxygen, which originates from residual gas atoms in the sputter chamber and also from water molecules which resided

on the surface after the wet chemical treatment. $NbO_x$ ($x \sim 1$) has metallic properties but is not superconducting [108].

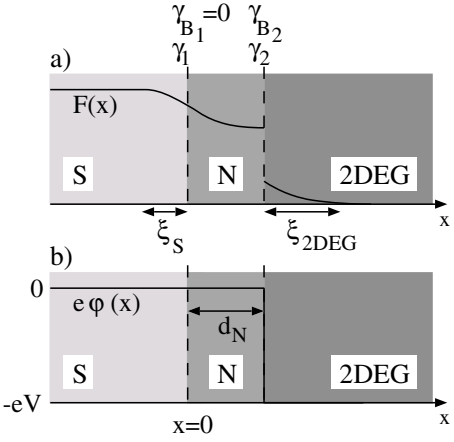


**Fig. 4.4.** (**a**) Schematic illustration of the Cooper pair density $F(x)$ and (**b**) potential drop $e\varphi(x)$ in an SN/2DEG layer sequence. $\gamma_{1,2}$ describe the suppression of $F(x)$ at the SN and N–2DEG interfaces, while $\gamma_{B_{1,2}}$ are a measure of the discontinuity of $F(x)$ at the corresponding interfaces

Since it seems to be reasonable to include an additional normal-conducting layer, the extended model introduced in Sect. 2.2.3, which incorporates the proximity effect in the SN layer, can be applied. The slope of the Cooper pair density $F(x)$, as well as the electrical potential $e\varphi(x)$, is depicted schematically in Fig. 4.4. Owing to the proximity effect, $F(x)$ decreases in the N layer. The lower value of $F(x)$ at the N/2DEG interface in comparison with its value in the bulk superconductor is responsible for the shift of the conductance maxima towards lower voltages. No barrier was assumed between the S and N layers ($\gamma_{B_1} = 0$), because of the good electrical contact between the two metals. Owing to the comparable conductances of N and S, $\gamma_1$ must be in the order of one. Since the N layer is connected to a *clean* 2DEG, the definition of $\gamma_2$, as given by (2.30), cannot be applied directly. However, $\gamma_2$ can be estimated from $\gamma_2 \approx (3k_{F,2DEG}/k_{FN}l_{el,N})\xi_N/\xi_{2DEG}$, as shown in [109]. $\xi_{2DEG} = (\hbar^2/k_B T m^*)\sqrt{n_{2D}/2\pi}$ is the coherence length of the 2DEG in the clean limit. For a 2DEG as used here, the upper limit for $\gamma_2$ can be set at 0.2 [45]. As can be seen in Fig. 4.3, the best fit to the measured data was obtained by assuming a barrier at the N/2DEG interface with $\gamma_{B_2} = 6$. If the clean limit applies, this value is connected directly with the $Z$ parameter of the BTK model by the relation $\gamma_{B_2} = Z^2$, so that $Z \approx 2.5$ [45]. It can thus be concluded that the barrier strength needed to obtain a good fit is larger than that estimated from the BTK model ($Z = 2$), with the consequence

that the amount of Andreev reflection is overestimated. Even if the shift of the maxima in the differential conductance can be explained by the model given above, inelastic scattering, represented by $\Gamma_{\mathrm{SN}}$, has to be incorporated additionally in order to explain the damping of the conductance peaks. For this structure an inelastic mean free path in Nb of 1.4 μm was taken, which was extrapolated from a value given for Nb at 10 K [110].

The experimental curve is fitted well by the model which considers a proximity layer (N). By using the BTK model and the extended model, a high barrier at the interface is found. In addition, the normal-state resistance $R_{\mathrm{N}} = 1\ \mathrm{k\Omega}$ is also very large, which can be explained by an inhomogeneous Nb–2DEG interface.

### 4.1.3 $Ar^+$ Sputter Cleaning

As an alternative to wet chemical etching, the surface of the semiconductor can be cleaned by $Ar^+$ sputtering. For the set of structures discussed first, RF $Ar^+$ sputtering (800 V, 90 s) was performed in the same chamber where the 100 nm thick Nb film was deposited subsequently to sputtering [45]. The resulting normalized differential conductance as a function of bias voltage is given in Fig. 4.5. Two striking differences can be made out. First, the drop of $R_{\mathrm{N}}\mathrm{d}I/\mathrm{d}V$ is significantly lower than for the wet-chemically-cleaned sample. Second, the conductance maxima are damped out more strongly. Even more important is the normal-state resistance, which is, with a value of only 8 Ω, two orders of magnitude smaller than $R_{\mathrm{N}}$ for the wet-chemically-cleaned sample.

The ratio of the differential conductances $\sigma_{\mathrm{SN}}(0)/\sigma_{\mathrm{NN}}$ can be used to determine the $Z$ parameter within the BTK model. For this sample $Z = 0.8$ is obtained, which is significantly lower than the value calculated for the wet-chemically-cleaned sample. However, the general shape of the measured differential-resistance curve does not fit at all to the BTK curve for $Z = 0.8$. In order to obtain a more realistic description of the experimental situation, the degradation of the semiconductor surface by the $Ar^+$ ions must be included in the model [45].

As depicted in Fig. 4.6, the previously presented model has to be extended by an additional diffusive N′ layer, which represents the degraded region in the 2DEG. The semiconductor has lost its ballistic properties owing to crystal defects near the surface [95, 96, 106]. The inclusion of the nonballistic N′ layer makes it necessary to assume a voltage drop not only at the metal/semiconductor interface but also within the N′ layer itself. A theoretical model, which accounts for a nonequilibrium proximity effect in the N′ layer, was developed by Volkov et al. [111]. An extended model including this theory, which applies to the SN/N′2DEG layer structure, is described in detail in [45]. The major difference compared with the model used for the SN/2DEG structure is that now the current through the structure has to be calculated from the transmission probability $T(E)$ through the N′ layer

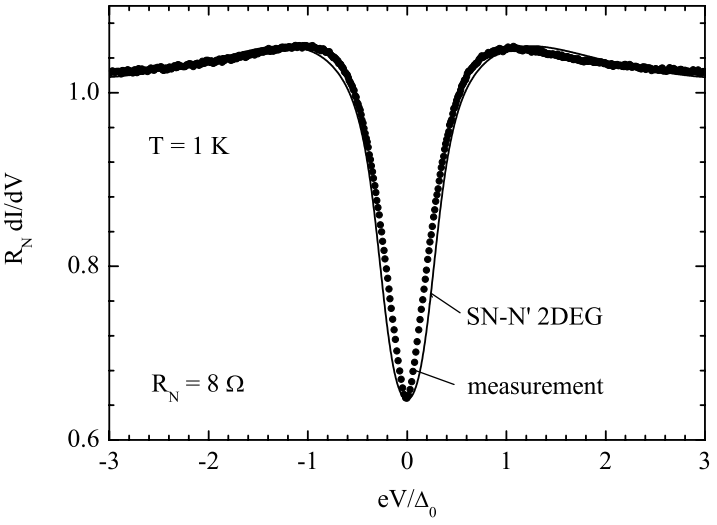


**Fig. 4.5.** Normalized differential conductance as a function of $eV/\Delta_0$ with $\Delta_0 = 1.38$ meV (•). The curve calculated using an SN–N′2DEG model with $\gamma_{m_1} = 0.15$, $\gamma_{B_2}$, $L_{N'} = 7\,\xi_{N'}$ and $\Gamma_{N'} = \Gamma_{SN} = 0.26$ is plotted as the *solid line*. $\Gamma_{N'}$ and $\Gamma_{SN}$ are the parameters for the inelastic scattering in the corresponding layers [45] (© (1996) by the American Physical Society)

and not of the coefficients for Andreev reflection $A(E)$ and normal reflection $B(E)$. This is necessary since here the voltage drop in the N′ layer must be taken into account. The set of parameters which leads to a good fit to the experimental data is given in Fig. 4.5. Details of the simulation are given in [45]. Within this model, the parameter $\gamma_{B_2} = Z^2$ provides only a lower bound for the $Z$ parameter. Here, a $Z$ parameter of 2.3 is obtained, which is considerably larger than the corresponding value for the BTK model ($Z_{BTK} = 0.8$).

For the $Ar^+$-sputtered (800 V) sample it can be concluded that, although the BTK model suggests a lower barrier at the interface, the actual barrier is comparable to the barrier obtained for wet-chemically-cleaned structures. The underestimation of the $Z$ parameter in the BTK model is due to the fact that the voltage drop in the degraded semiconductor layer is not included. Nevertheless, $Ar^+$ sputter cleaning will be one of the preferred cleaning methods for Nb–2DEG junctions, since the normal-state resistance of 8 Ω is significantly lower than $R_N$ for wet-chemically-cleaned samples.

In order to reduce the surface degradation, an $Ar^+$ ion beam source with a lower acceleration voltage (300 V) can be employed [112]. In Fig. 4.7, the normalized differential conductance of samples cleaned for 1 h, 3 h and 6 h with a low ion current of 2 μA is plotted as a function of the voltage drop $V$. The most striking feature is that, with increasing sputtering time, the zero-bias conductance increases, while the maxima near $\pm\Delta_0$ are damped out

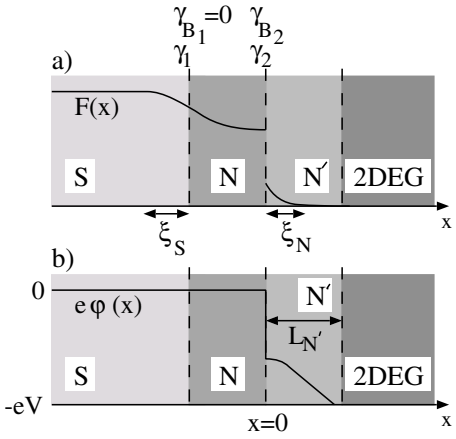


**Fig. 4.6.** (**a**) Schematic illustration of the Cooper pair density $F(x)$ and (**b**) the potential drop $e\varphi(x)$ in an SN/N′2DEG layer system. $\gamma_{1,2}$ is a measure of the suppression of $F(x)$ at the SN and NN′ interfaces. The barrier at the NN′ interface is described by $\gamma_{B_2}$. At the SN interface, no barrier is assumed ($\gamma_{B_1} = 0$)

more strongly. Apart from that, the normal-state resistance also decreases with increasing sputtering time. For the samples sputtered for 1 h, 3 h and 6 h normal-state resistances of 60 Ω, 13 Ω and 8 Ω, respectively, were measured. The set of samples sputtered for 1 h showed a large spread of $R_N$ between 32 Ω and 500 Ω [112]. This is presumably due to an incomplete removal of residual atoms, which therefore leads to a large variation of the transmission probability. For the samples sputtered for 3 h and 6 h, this was not the case. Here, a variation in the range of 10% was measured. For the sample sputtered for 1 h, $Z_{BTK}$ has a value of 1.14, while values of 0.7 and 0.56 were obtained for the structures sputtered for 3 h and 6 h, respectively. For increasing sputtering times the $R_N dI/dV$ vs. $V$ curves resemble more and more the damped curve measured for the 800 V $Ar^+$-cleaned samples. At least partially, this tendency can again be attributed to the formation of a degraded semiconductor layer at the surface.

An interesting question is to what extent the 2DEG is degraded by the $Ar^+$ sputter cleaning. This information is especially important for the Josephson junctions discussed in the following chapters, where the Nb electrodes are only a few hundreds of nanometers apart. In order to address the problem of degradation by $Ar^+$ sputtering, wire structures were prepared. The underlying idea is that owing to the small width of the wire, the effect of $Ar^+$ sputtering on the 2DEG should be directly visible in magnetotransport measurements. In order to separate this effect from other effects a comparative study was performed, where the voltage drop at the $Ar^+$-ion-treated part of the wire was compared with the voltage drop at a nontreated section of the

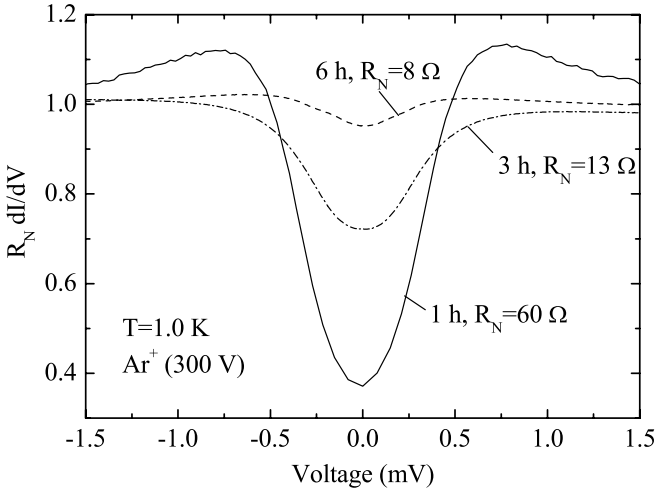


**Fig. 4.7.** Normalized differential conductance as a function of bias voltage at $T = 1$ K for samples cleaned by $Ar^+$ (300 V) sputtering. The cleaning times were 1 h (*solid line*), 3 h (*dash-dotted line*) and 6 h (*dashed line*)

wire. Selective sputtering was performed by opening a window in an electron beam lithography resist layer. The covered area of the semiconductor is not affected by the $Ar^+$ sputtering. The 400 nm wide wires were prepared by electron beam lithography and $CH_4/H_2$ reactive ion etching. A schematic of the geometry and measurement setup can be found in Fig. 4.8b (inset).

In Fig. 4.8a, the magnetoresistance $R_{xx}$ of a wire cleaned with $Ar^+$ for 3 h is plotted together with $R_{xx}$ of the reference wire. The latter curve shows pronounced Shubnikov–de Haas oscillations for $B > 1$ T. The decrease of $R_{xx}(B)$ for $B < 1$ T can be explained by diffusive interface scattering in two-dimensional wire structures [113]. The wire cleaned for 3 h contains a conductive bypass channel. This is deduced from the lower zero-field resistance $R_{xx}(B = 0)$ in comparison with the nonsputtered wire and from the overall increase of $R_{xx}$ with $B$. The local maximum at $B \approx 0.3$ T can be attributed to diffusive interface scattering [113].

From the magnetoresistance measurements, it can be concluded that the two-dimensional character of the transport in the InGaAs/InP wire is not destroyed by the $Ar^+$ sputter cleaning, because the oscillations in $R_{xx}$ still remain after $Ar^+$ sputtering. However, the sputtered part of the wire possesses a higher electron concentration, which can be attributed to an altered pinning of the Fermi level at the surface due to the sputtering. The bypass channel can be explained by conduction in the sputtered semiconductor surface. Especially on an InP surface, $Ar^+$ sputtering has the effect that the phosphorus component is removed selectively, leaving a rough, In-rich sur-

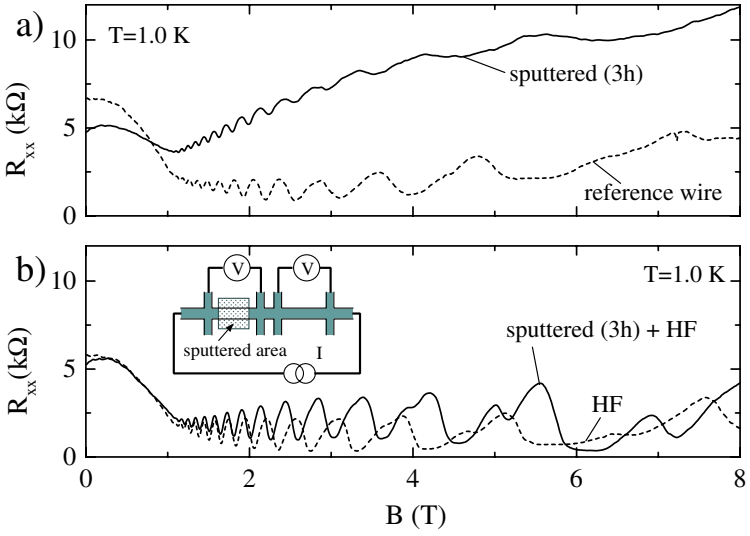


**Fig. 4.8.** (**a**) Magnetoresistance $R_{xx}$ of the wire section cleaned for 3 h by $Ar^+$ ions and of the non-sputtered wire section. (**b**) Magnetoresistance after a wet-chemical-etching step using HF. The *inset* shows the geometry of the sample and the measurement configuration

face, as shown in Fig. 4.9. On exposure to air, a conductive $In_2O_3$ layer is formed, which is measured as a bypass channel. From the observation that the conductance of the bypass channel increases with increasing sputtering time, it can be inferred that the oxidation process is supported by the $Ar^+$-induced roughness of the surface [95]. For InGaAs, the oxidation is probably much less pronounced, since here the surface is more stable against $Ar^+$ sputtering [114].

The proof that oxidation of the surface is responsible for the conductive bypass was delivered by a subsequent HF etching of the wires. Fig. 4.8b shows the magnetoresistance of the sample after an HF dip, which was performed immediately before the wire structure was mounted into the cryostat again. Obviously, the bypass channel of the $Ar^+$-sputtered wire section has vanished, because the overall resistance does not increase with $B$ anymore. In addition, the zero-field resistance is now almost the same for the $Ar^+$-sputtered and nonsputtered sections of the wire. For structures sputtered for 6 h at 300 V and sputtered for 90 s at 800 V, the bypass channel could not be removed completely by the HF dip. Possibly the degradation of the semiconductor surface is in this case deeper than the oxidized layer. Only the latter is removed by HF.

As shown above, the study of the wire structures gives valuable information concerning the choice of the cleaning procedure. The measurements on $Ar^+$-cleaned wires show that the 2DEG in the wire is effectively not degraded

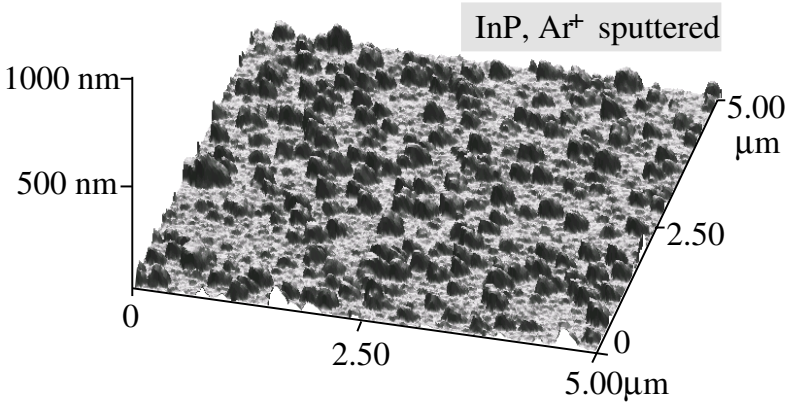


**Fig. 4.9.** Scanning atomic force microscope picture of an InP surface sputtered for 6 h with 300 V $Ar^+$ ions. On the surface In droplets are found, which are formed after a selective removal of the phosphorus component

by sputtering. This is a crucial result concerning the S/2DEG/S Josephson junctions. The InP surface is especially affected by the cleaning procedure, which can be deduced from the conductive oxide layer. Of course, in case of in-situ cleaning and Nb deposition, this oxidation does not occur. Nevertheless, the degraded InP affects the transmissivity through the Nb/semiconductor interface in any case. The oxidation of the surface can also be prevented if the sample is passivated directly after etching of the semiconductor mesa, by using $(NH_4)_2S$ [115]. Here, one or two monolayers of sulfur cover the surface. If a brief $Ar^+$ sputter cleaning is employed, this coverage can be removed before the Nb layer is deposited.

### 4.1.4 Electron Cyclotron Resonance Plasma Cleaning

Although $Ar^+$ cleaning is a viable way to produce transparent superconductor/semiconductor junctions, it is still worthwhile to search for more gentile cleaning procedures. A very promising alternative cleaning method is an electron cyclotron resonance plasma treatment of the semiconductor surface, which is based on the well-established cleaning method prior to the regrowth of semiconductor layers by molecular beam epitaxy [116, 117, 118]. In most cases a hydrogen plasma is used, which removes surface oxides, hydrocarbons and other contaminants. However, it was shown for a phosphorus-based III–V semiconductor, i.e. InP, that a hydrogen electron cyclotron resonance plasma can lead to a group-III-enriched surface owing to the formation of P hydrids [118]. Therefore, a mixture of He/H or even pure He was used for the cleaning of the InGaAs/InP surface. The underlying idea is that owing to the lower mass of the helium or hydrogen atoms compared with Ar atoms, the momentum transfer at the semiconductor surface is considerably smaller.

After the $CH_4/H_2$ etching process for the definition of the semiconductor mesa, the samples were treated in the He plasma for 2 h and subsequently completely covered in situ by a 100 nm thick electron-beam-evaporated Nb layer. The final geometry of the Nb electrodes was defined by electron beam lithography and an $SF_6$ RIE process. The junctions had a width of 20 µm. In the plasma source employed for the cleaning, the gas is excited to a plasma in a tunable microwave cavity by a microwave source at 2.45 GHz.

InP is known to be the less stable material and thus the surface of a semi-insulating InP wafer was exposed to the plasma. The effect on the surface morphology can be investigated by using an atomic force microscope (AFM). For an He/H (50 : 50) mixture, the surface topology measured by an AFM reveals the formation of droplets with a size of the order of 50 nm (Fig. 4.10a). This result shows the same effect as reported in studies on InP surfaces exposed to a pure H plasma [116, 118]. Here, the exposure of an InP surface to hydrogen led to the formation of volatile $PH_3$ and to an indium-rich surface covered with In droplets. As can be seen in Fig. 4.10b, the formation of indium droplets is prevented if pure He gas is used for the plasma source. The InP surface remains smooth after the He plasma treatment [119].

The effect of the plasma cleaning on the interface transparency of the Nb–InGaAs/InP interface can be investigated by measuring the differential conductance as a function of the voltage drop. In Fig. 4.11 $R_N \mathrm{d}I/\mathrm{d}V$ is plotted as a function of the voltage drop. The temperature was increased from 1.0 K to 8.0 K in steps of 1.0 K. As can be seen here, the normal-state resistance $R_N$ has a value of about 21 Ω at 1 K, which would correspond to a value of 4 Ω for a 100 µm wide junction. Obviously, the normal-state resistance is noticeably smaller than for moderately $Ar^+$-cleaned samples. As shown in Fig. 4.11 (inset), the He/H treatment leads to a much larger normal-state resistance of about 115 Ω, which is attributed to the surface deterioration (Fig. 4.10a).

Below 7 K, the curves plotted in Fig 4.11 show a minimum at zero bias voltage and maxima at about $\pm\Delta_0$. The critical temperature of this Nb layer was 8 K, which results in a superconducting gap of 1.2 meV. A comparison with the measurements reveals that the maxima are found at voltages below $\Delta_0(T)$. This can be explained by the proximity effect at the interface. The increase of $\mathrm{d}I/\mathrm{d}V$ at zero bias for increasing temperature can be attributed to the broadening of the distribution function. For temperatures near $T_c$ the lowering of $\Delta_0$ with temperature leads to a further damping of the structure.

From the normalized differential conductance $R_N \mathrm{d}I/\mathrm{d}U$ at zero bias, a $Z$ parameter of 0.85 was deduced by following the BTK model. It is remarkable that this $Z$ parameter is larger than, for example, the $Z$ parameter of the 3 h $Ar^+$-sputtered sample, although the interface resistance per micron is considerably smaller, 400 Ω µm$^{-1}$ for the He-cleaned sample in contrast to 1300 Ω µm$^{-1}$ for the $Ar^+$ sputter-cleaned sample. This result can be interpreted as showing that for the He-cleaned surface, the area where transmission through

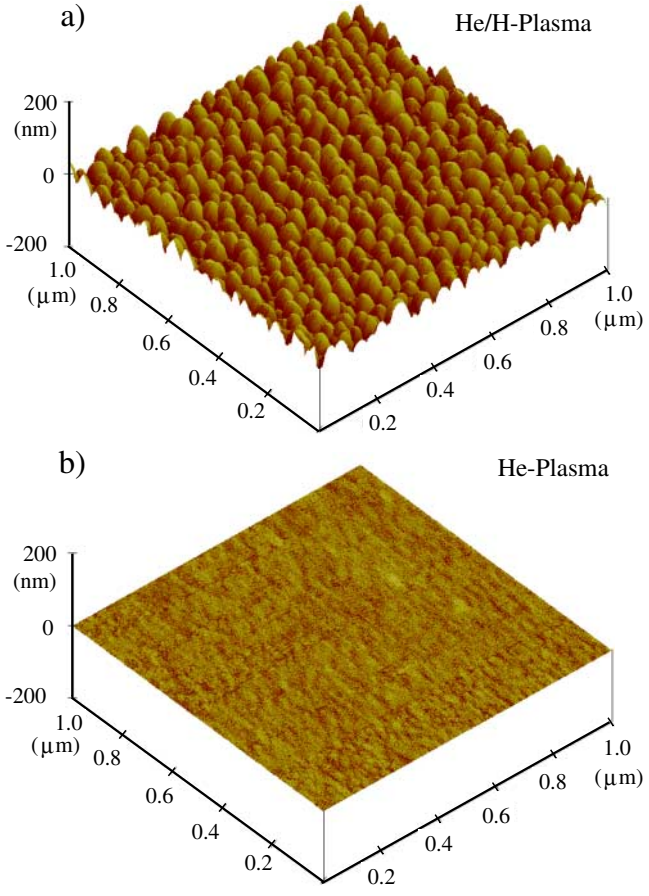


**Fig. 4.10.** (**a**) Atomic force microscope picture of an InP surface treated in an He/H electron cyclotron resonance plasma. The effect of an He plasma is shown in (**b**) [119]

the interface takes place is larger than for the $Ar^+$-treated sample. The barrier at the interface seems to be higher at the interface for the He-cleaned sample, since the $Z$ parameter is larger. Finally, it can be stated that the He plasma cleaning is a very promising method, since here a clean and homogeneous interface is prepared without deteriorating the semiconductor surface.

## 4.2 Point Contact Spectroscopy

Point contacts are a versatile tool for studying transport through a normal-conductor/superconductor interface [99]. When a point contact is employed,

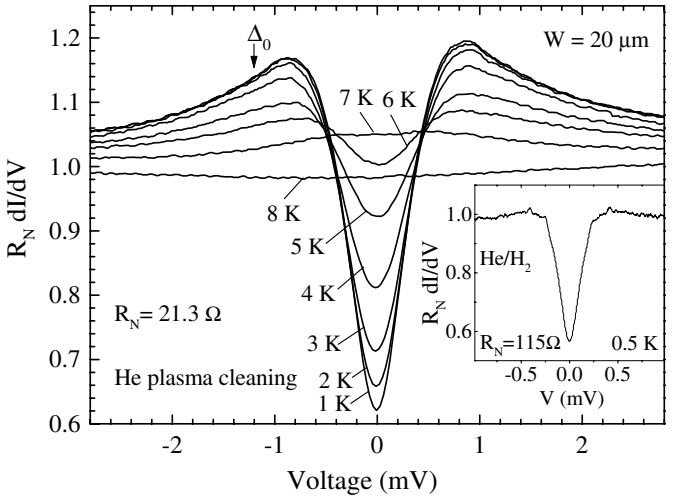


**Fig. 4.11.** Normalized differential conductance as a function of bias voltage at various temperatures for a sample cleaned in an He plasma. The *inset* shows the differential conductance for an He/H plasma-cleaned sample [119]

carriers are injected or collected via a very small opening. In conjunction with a superconductor/two-dimensional-electron-gas interface, it is even possible to directly separate normal-reflected electrons and Andreev-reflected holes.

An experiment where a superconductor/two-dimensional-electron-gas interface was analyzed by a point contact was reported by Jakob et al. [120]. A scanning electron beam micrograph of the structure used for point contact spectroscopy is shown in Fig. 4.12a. Again, the two-dimensional electron gas is located in a strained InGaAs/InP heterostructure. The point contact geometry was defined by reactive ion etching. Separated by a distance of $L = 1$ µm, an Nb electrode is attached to the sidewalls of the semiconductor mesa. As depicted in Fig. 4.12, a current is driven through the point contact to the superconducting electrode. In the case of normal reflection, the electron is specularly reflected and thus does not reach the point contact opening. On the other hand, if Andreev reflection occurs, so that an electron is retroreflected as a hole, the hole trajectory follows the path of the incident electron and passes through the point contact opening.

The effect of the retroreflected holes passing through the point contact can be seen in Fig. 4.13, where the differential conductance $G_{\mathrm{Nb}}$ of the point contact is shown as a function of the excess energy. As can be seen, at excess energy zero the conductance is enhanced by 20% compared with $G_{\mathrm{Nb}}$ at excess energies exceeding the superconducting gap of Nb. The enhanced conductance can be attributed to the additional contribution of the retroreflected holes. The modification of the point contact conductance $G_{\mathrm{PC}}$ if a

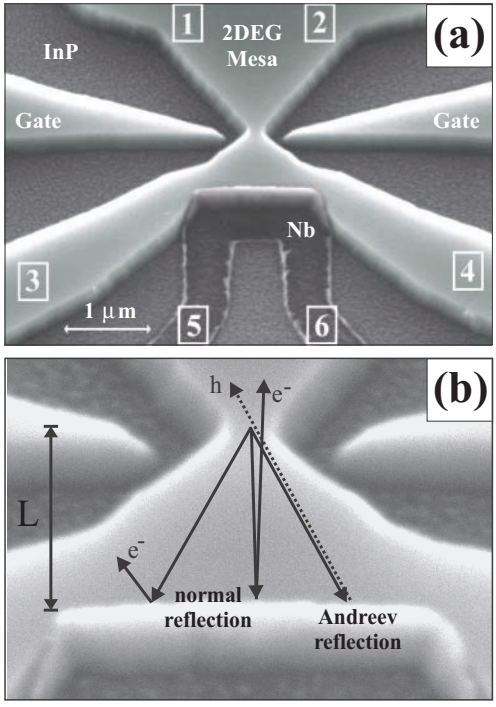


**Fig. 4.12.** (**a**) Scanning electron micrograph of a point contact with an Nb electrode in front. The separation between the point contact and the Nb electrode is 1 µm. (**b**) A normal-reflected electron can only pass through the point contact opening if it is almost incident almost perpendicular to the interface. Owing to the retroreflection property, an Andreev-reflected hole reaches the point contact opening for all angles of reflection [120]

superconducting electrode is placed in front can be expressed as

$$G_{\mathrm{Nb}} = G_{\mathrm{PC}} \left[ 1 + A(E) \exp\left( -\frac{2L}{l_{\mathrm{in,h}}(E)} \right) - B(E)\eta_{\mathrm{e}} \exp\left( -\frac{2L}{l_{\mathrm{ball,e}}(E)} \right) \right] . \tag{4.1}$$

The Andreev reflection $A(E)$ leads to an increase of the conductance, which is reduced only by inelastic scattering, characterized by the scattering length $l_{\mathrm{in,h}}(E)$, whereas the normal reflection $B(E)$ leads to a decrease. Only a very small fraction $\eta_{\mathrm{e}} \approx 0.02$ of the electrons, which are incident almost perpendicular to the two-dimensional-electron-gas/superconductor interface, can in principle reach the point contact on their way back [120]. This amount is further decreased by elastic scattering ($l_{\mathrm{ball,e}}$); hence the normal-reflection contribution can be neglected in (4.1). As a consequence (4.1) can be rewritten

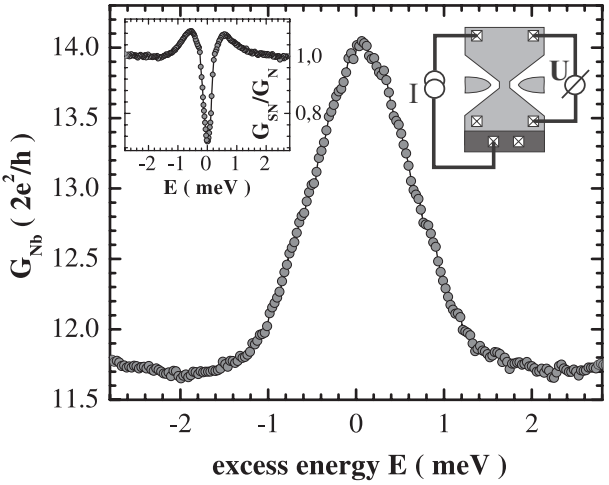


**Fig. 4.13.** Differential conductance $G_{\mathrm{Nb}}$ as a function of the excess energy. The *inset* shows the normalized differential conductance of the Nb–InGaAs/InP interface [120]

as an expression where the Andreev reflection probability can be determined directly from $G_{\mathrm{Nb}}(E)$:

$$A(E) \approx \left( \frac{G_{\mathrm{Nb}}(E)}{G_{\mathrm{PC}}} - 1 \right) \exp\left( \frac{2L}{l_{\mathrm{in,h}}(E)} \right) . \tag{4.2}$$

A comparison of the experimentally determined Andreev reflection probability with the BTK model [46] showed that this model was not able to explain the experimental results. In particular, the conductance peaks at $\pm\Delta_0$ in the BTK model are not found in the experiment. A better agreement is obtained if the proximity effect is taken into account, as in the model by Golubov et al. [121] (see also Sect. 2.2.3). Besides the energy dependence of the Andreev reflection probability, Andreev reflection can also be studied as a function of temperature by using the measurement setup depicted in Fig. 4.12. It could be shown that the Andreev reflection probability $A(T)$ at zero excess energy decreases with increasing temperature, which is in contradiction to the constant value of $A$ expected from the BTK model [122]. The decrease of $A(T)$ with temperature was explained here by inelastic scattering at the superconductor/two-dimensional-electron-gas interface, which leads to an energetic smearing of the quasiparticle states.

The angular dependence of Andreev reflection can be studied if two very small superconducting electrodes ($\approx$ 200 nm) are employed, separated by a small angle [123]. In order to adjust the angle of the trajectories which couple the two superconducting electrodes, a reflecting barrier induced by a gate electrode was used.

# 5. Superconductor/ Two-Dimensional-Electron-Gas/ Superconductor Junctions: Voltage-Carrying State

If two S/2DEG interfaces are brought into close proximity, fascinating effects can be observed. In this chapter, only the voltage-carrying state of S/2DEG/S structures will be discussed. In this regime, subharmonic gap structures at voltages equal to $2\Delta_0/n$, $n = 1, 2, 3, ...$, and excess currents, for example, can be measured; these are due to multiple Andreev reflections. The different theoretical models explaining these effects will be introduced first. Subsequently, the experimental results will be presented and compared with these models. Effects related to the superconductive state of S/2DEG/S structures will be covered in the next chapter.

## 5.1 Subharmonic Gap Structures: Theoretical Models

Two alternative models will be introduced here in order to explain the subharmonic gap structures as well as the excess currents found in the current–voltage ($I$–$V$) characteristics. The first model is based on the motion of Gaussian wave packets within the normal conductor [124]. The second model, which will also be employed to interpret the experimental data, deals with ballistic particles in a Boltzmann equation approach [125]. For the latter model, the inclusion of the proximity effect will also be discussed briefly [58].

### 5.1.1 Kümmel–Gunsenheimer–Nicolsky Model

Kümmel, Gunsenheimer and Nicolsky (KGN) [124] developed a model, where the $I$–$V$ characteristics of a SNS junction are calculated by considering the trajectories of single electrons or holes. No barrier at the interface is included ($Z = 0$). The particles, described as Gaussian wave packets, are accelerated or decelerated by the electric field $\boldsymbol{E}$ in the normal conductor depending on their initial momentum. Between the Andreev reflection events at the interface the particles climb or descend the Andreev ladder as depicted in Fig. 5.1a. As long as the energy of the particles at the SN interface is within the superconducting gap, ideal Andreev reflection occurs. If the applied voltage is decreased, more and more Andreev reflections are necessary to gain or lose enough energy before the particle can enter the superconductor as a quasiparticle above

Thomas Schäpers: Superconductor/Semiconductor Junctions, STMP 174, 47–64 (2001)
© Springer-Verlag Berlin Heidelberg 2001

$\Delta_0$ or below $-\Delta_0$. The increase of the particle contribution to the electrical current by multiple Andreev reflections is balanced by inelastic scattering processes. The latter limit the number of Andreev reflections.

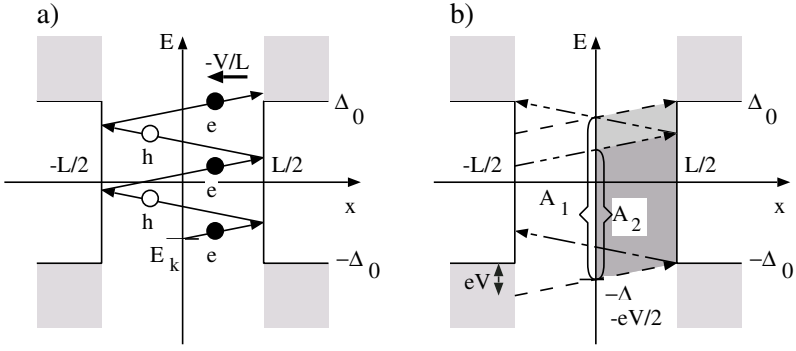


**Fig. 5.1.** (**a**) Electrons e and holes h accelerated by an electric field $\boldsymbol{E} = -\boldsymbol{e}_x V/L$. As long as the particle energy is within the gap $\pm\Delta_0$, Andreev reflections occur at the SN interfaces. $E_k$ is the initial energy of the particles. (**b**) Energy range of electrons which can undergo one ($A_1^+$) or two ($A_2^+$) Andreev reflections. The electrons start at $x = 0$

The total current through the SNS junction results from a competition between two opposite currents carried by electron and hole wave packets; the electrons and holes moving with the field make a positive contribution, while the corresponding particles moving against the field make a negative contribution. Calculating the time and spatial average of the Gaussian wave packets and using the symmetry properties of the Andreev reflection coefficients leads finally to the following expression for the Andreev current density [124]:

$$\begin{aligned} \mathbf{j}_{\mathrm{AR}} &= -\boldsymbol{e}_x \frac{e}{m}\frac{\hbar}{\Omega_{\mathrm{N}}} \sum_k P_{\mathrm{N}}(E_k)\{f_0(E_k)k_{\mathrm{e}} - [1-f_0(E_k)]k_{\mathrm{h}}\} \\ &\quad \times \sum_{n=1}^{\infty} \mathrm{e}^{-(n+1/2)L/l_{\mathrm{in}}} \left[A_n^+(E_k) - A_n^-(E_k)\right] \ . \end{aligned} \tag{5.1}$$

Here, $k_{\mathrm{e}}$ and $k_{\mathrm{h}}$ are the initial electron and hole wave vectors, respectively. $\Omega_{\mathrm{N}}$ is the volume of the normal conductor and $P_{\mathrm{N}}(E_k)$ is the probability to find the particle in the N layer. $L$ is the distance between the superconducting electrodes, while $l_{\mathrm{in}}$ is the inelastic mean free path. In the first sum all possible initial $k$ vectors are considered. The second sum adds up the steps in the Andreev ladder. The Andreev coefficients $A_n^{\pm}(E_k)$ represent the probability that at least $n$ Andreev reflections (see Fig. 5.1) are possible:

$$A_n^{\pm}(E) = \prod_{i=1}^{n} A\left[E + \left(i - \frac{1}{2}\right) eV\right]$$
$$\approx \Theta\left(\Delta \pm E + \frac{eV}{2}\right) \Theta\left(\Delta \mp E - neV + \frac{eV}{2}\right) . \quad (5.2)$$

Here, $A(E)$ is approximated by $A(E) = 1$ for $|E| < \Delta$ and 0 elsewhere [124]. The (+) and (−) signs represent particles moving with and against the field, respectively. A direct consequence of the form of $A_n^{\pm}$ is the appearance of subharmonic gap structures at voltages

$$V_n = 2\Delta_0/en, \quad n = 1, 2, 3, ... \quad (5.3)$$

At $V_n$ a transition from $n-1$ to $n$ Andreev reflection processes takes place.

In (5.1), only the additional current due to Andreev reflection is considered. For the total current density, the normal-state current density has to be added. The excess current $I_{\mathrm{exc}}$ is defined as the Andreev current accumulated at voltages far above $2\Delta_0$.

In order to calculate the current density $\boldsymbol{j}_{\mathrm{AR}}$, information about the density of Andreev states $g(E)$ is needed. Information about $g(E)$ can in principle be gained from the sum over $k$ if one knows the dispersion of the Andreev states $E(k_{\mathrm{F}x})$ as a function of the $x$ component of the Fermi wave vector [124]. For an ideal SNS junction, an expression for the energy levels $E(k_{\mathrm{F}x})$ was given by Kulik [126], for example. Pereira et al. [127, 128] showed that for a fit of an experimental $I$–$V$ characteristic, it can be sufficient to assume a simplified analytical Andreev density of states.

One prediction of the KGN model is that for a large $l_{\mathrm{in}}/L$ ratio a negative differential conductance ($\mathrm{d}I/\mathrm{d}V < 0$) should be observable. The current increase with decreasing bias voltage is due to the increasing number of Andreev reflections. The only limiting process is the inelastic scattering. For a current-biased junction, the negative differential conductance will lead to a hysteresis in the $I$–$V$ characteristics. In addition, the steep rise of the current density at low bias voltages, the characteristic *foot* of weak-link structures, can also be explained within the KGN model. Recently, a more rigorous treatment of inelastic scattering processes was provided by Gunsenheimer and Zaikin [129].

### 5.1.2 Inclusion of Normal Reflection at the SN Interface

In the Kümmel–Gunsenheimer–Nicolsky model, no barrier at the interface was assumed, and therefore ideal Andreev reflection occurs for particle energies within the superconductive gap. If a $\delta$-shaped barrier is introduced at the interfaces, the particle wave packets are partially normal-reflected at the interface even for $|E| < \Delta_0$, as shown in Fig. 5.2. We shall now introduce a simple extension of the KGN model, where in (5.1) the sum over $\exp[-(n+1/2)L/l_{\mathrm{in}}][A_n^+(E_k) - A_n^-(E_k)]$ will be replaced by a term which also

includes normal reflection processes [130]. Interference effects are neglected in this model.

The probability to find an electron or a hole at $x = 0$ with energy $E$ is defined as $C_{\mathrm{e}}^{\pm}$ or $C_{\mathrm{h}}^{\pm}$, respectively. The $(+)$ sign represents motion with the field, the $(-)$ sign motion against the field. As shown in Fig. 5.2, a hole

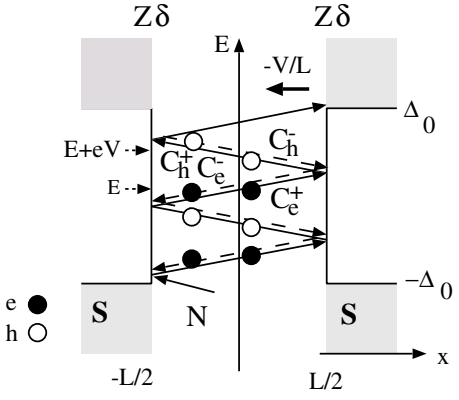


**Fig. 5.2.** Trajectories of Andreev and normal-reflected particles in an SNS structure. $C_{\mathrm{e}}^{\pm}$ and $C_{\mathrm{h}}^{\pm}$ are the electron and hole probabilities, respectively, at $x = 0$; $(+)$ denotes motion with the field, while $(-)$ denotes motion against the electric field

with probability $C_{\mathrm{h}}^{+}(E + eV)$, with energy $E + eV$ at $x = 0$, which left the interface at $x = L/2$, moving with the field, can originate either from an Andreev-reflected electron with probability $C_{\mathrm{e}}^{+}(E)$, of energy $E$, or from a normal-reflected hole with probability $C_{\mathrm{h}}^{-}(E + eV)$, of energy $E + eV$, at $x = 0$:

$$C_{\mathrm{h}}^{+}(E + eV) = \mathrm{e}^{-L/l_{\mathrm{in}}} \left[ A(E + eV/2) C_{\mathrm{e}}^{+}(E) + B(E + eV/2) C_{\mathrm{h}}^{-}(E + eV) \right] . \tag{5.4}$$

$A(E + eV/2)$ and $B(E + eV/2)$ are the BTK coefficients for Andreev and normal reflection. A corresponding process can be found for an electron with probability $C_{\mathrm{e}}^{-}(E)$, at energy $E$ moving against the field:

$$C_{\mathrm{e}}^{-}(E) = \mathrm{e}^{-L/l_{\mathrm{in}}} \left[ B(E + eV/2) C_{\mathrm{e}}^{+}(E) + A(E + eV/2) C_{\mathrm{h}}^{-}(E + eV) \right] . \tag{5.5}$$

The factor $\exp(-L/l_{\mathrm{in}})$ accounts for losses by inelastic scattering in the normal conductor. The equations given above show that $C_{\mathrm{e}}^{+}$ and $C_{\mathrm{e}}^{-}$ at energy $E$ can be deduced from the values of $C_{\mathrm{h}}^{+}$ and $C_{\mathrm{h}}^{-}$ at the energy $E + eV$ one step higher:

$$C_{\mathrm{e}}^{+}(E) = \frac{\mathrm{e}^{L/l_{\mathrm{in}}} C_{\mathrm{h}}^{+}(E + eV/2) - B(E + eV/2) C_{\mathrm{h}}^{-}(E + eV)}{A(E + eV/2)} , \tag{5.6a}$$

$$C_{\mathrm{e}}^{-}(E) = \frac{B(E+eV/2)}{A(E+eV/2)} C_{\mathrm{h}}^{+}(E+eV) + \mathrm{e}^{-L/l_{\mathrm{in}}} \frac{\left[A^2(E+eV/2) - B^2(E+eV/2)\right] C_{\mathrm{h}}^{-}(E+eV)}{A(E+eV/2)} . \tag{5.6b}$$

One step further down, $C_{\mathrm{h}}^{+}(E-eV)$ and $C_{\mathrm{h}}^{-}(E-eV)$ can be written as functions of $C_{\mathrm{e}}^{+}(E)$ and $C_{\mathrm{e}}^{-}(E)$.

Since electrons and holes have the same reflection and transmission probabilities at the SN interface, two series $C^{+}(E+neV)$ and $C^{-}(E+neV)$ can be defined, which describe the motion of a particle with and against the electric field, respectively. Suppose that the initial particle has been an electron with energy $E_k$, then the even terms $C^{\pm}(E_k+2neV)$ correspond to electrons, while the odd terms $C^{\pm}[E_k+(2n+1)eV)]$ belong to holes.

The boundary conditions are given by the fact that for particle energies $E_k+neV$ far beyond $\Delta_0$, the Andreev reflection process can be neglected. Only normal reflection has to be considered. For $E_k+neV \gg \Delta_0$, this means

$$C^{-}(E_k+neV) = B(E_k+neV+eV/2)C^{+}(E_k+neV) , \tag{5.7}$$

while for the lower side ($E_k+neV \ll -\Delta_0$), one obtains

$$C^{+}(E_k+neV) = B(E_k+neV+eV/2)C^{-}(E_k+neV) . \tag{5.8}$$

The total solution is given by a linear combination of two solutions $(C_1^{+}, C_1^{-})$, satisfying the boundary conditions above $\Delta_0$, and of a solution $(C_0^{+}, C_0^{-})$ with nonzero values only for $E < E_k$ and with a step in $C_0^{+}$ or $C_0^{-}$ equal to one at $E_k$ for an initial particle moving with or against the field, respectively. The linear combination is chosen in such a manner that the boundary condition for energies far beyond $-\Delta_0$ is satisfied:

$$C^{\pm}(E) = C_1^{\pm}(E) \frac{C_0^{+}(E_-) - B(E_- - eV/2)C_0^{-}(E_-)}{C_1^{+}(E_-) - B(E_- - eV/2)C_1^{-}(E_-)} - C_0^{\pm}(E) , \tag{5.9}$$

where $E_- = E_k + neV \ll -\Delta_0$. The step at $E_k$ is normalized to 1. The Andreev current $\boldsymbol{j}_{AR}$ is obtained by substituting $\sum_n \mathrm{e}^{-(2n+1)L/l_{\mathrm{in}}}[A_n^{+}(E_k) - A_n^{-}(E_k)]$ in (5.1) by

$$\sum_{p=\mathrm{w,a}} \sum_{n} \left[C_p^{+}(E_k+neV)A(E_k+neV+eV/2) - C_p^{-}(E_k+neV)A(E_k+neV-eV/2)\right] .$$

$P = \mathrm{w}, \mathrm{a}$ denotes generation of a particle at $E_k$ moving with (w) or against (a) the field.

### 5.1.3 Octavio–Tinkham–Blonder–Klapwijk Model

The Octavio–Tinkham–Blonder–Klapwijk (OTBK) model [125] is based on a Boltzmann equation approach. As in the modified KGN model, normal

scattering at the SN interface is included by introducing a $\delta$-shaped barrier, whose strength is expressed by the $Z$ parameter. In contrast to the previously discussed model, inelastic scattering processes are not considered here. The OTBK model can be regarded as a generalization of a preceding model with no barriers at the SN interface developed by Klapwijk et al. [131].

In order to calculate the current as a function of the applied voltage $V$ between the superconducting electrodes, the electrons are divided into two subpopulations $f_{\rightarrow}(E,x)$, $f_{\leftarrow}(E,x)$ representing the two directions of motion. The nonequilibrium distributions at the left-hand SN interface ($x=0$) and at the right-hand NS interface ($x=L$) are calculated from the boundary conditions

$$f_{\rightarrow}(E,0) = A(E)[1-f_{\leftarrow}(-E,0)] + B(E)f_{\leftarrow}(E,0) + T(E)f_0(E)\,, \tag{5.2010a}$$

$$f_{\leftarrow}(E,L) = A(E)[1-f_{\rightarrow}(-E,L)] + B(E)f_{\rightarrow}(E,L) + T(E)f_0(E)\,. \tag{5.2010b}$$

Here, $A(E)$, $B(E)$ and $T(E)$ are the coefficients for Andreev reflection, normal reflection and transmission through the interface, respectively. For the transmission from the superconductor, a Fermi distribution function $f_0(E)$ is assumed. Since no inelastic scattering within the normal conductor is assumed, the reference point for all distribution functions can be shifted to $x=0$; for example an electron starting at $x=L$ with energy $E$ will arrive at $x=0$ with energy $E-eV$:

$$f_{\rightleftharpoons}(E,L) = f_{\rightleftharpoons}(E-eV,0) = f_{\rightleftharpoons}(E-eV)\,. \tag{5.2011}$$

The net current for a two-dimensional structure as a function of the applied voltage is determined by the difference between the distribution functions $f_{\rightleftharpoons}(E)$:

$$I = \frac{ek_{\mathrm{FN}}W}{\pi^2\hbar}\int_{-\infty}^{\infty} \mathrm{d}E\,[f_{\rightarrow}(E) - f_{\leftarrow}(E)]\,. \tag{5.2012}$$

Here, $W$ is the width of the contact. The distribution functions themselves are calculated self-consistently [125, 132]. As an example, $f_{\rightarrow}(E)$ and $f_{\leftarrow}(E)$ are plotted in Fig. 5.3 for $Z=0.5$, $T/T_{\mathrm{c}}=0.6$ and $V=0.4\,\Delta_0/e$. The appearance of subharmonic gap structures in the form of pronounced steps at $V_n = e\Delta_0/(en)$ are clearly seen in Fig. 5.4 for a structure with $Z=1$.

The OTBK model for a two-dimensional structure can be extended by considering an angle-dependent scattering probability. Here, it must be taken into account that only the wave vector component normal to the interface is altered by the scattering at the barrier. The component parallel to the interface is preserved. As can be seen in (2.8), the $Z$ parameter is defined with respect to the Fermi wave vector $k_{\mathrm{FS}}$. In order to account for the fact that only the wave vector component normal to the interface is affected, the $Z$ parameter has to be replaced by an angle-dependent factor $Z(\theta) = Z/\cos\theta$

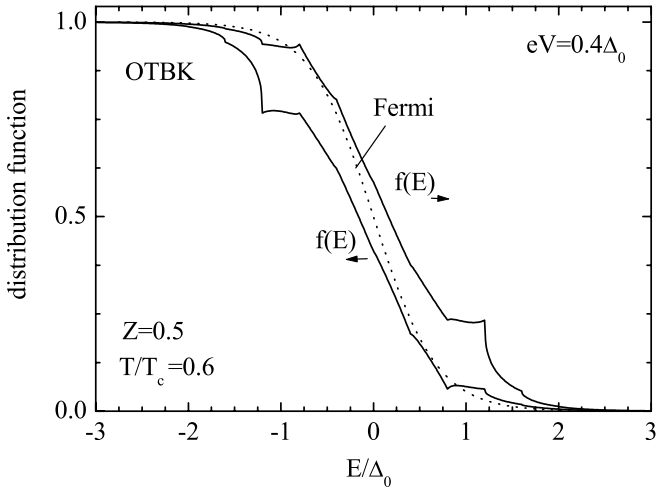


**Fig. 5.3.** Distribution functions $f_{\rightarrow}$ and $f_{\leftarrow}$ for $Z = 0.5$ and a Fermi distribution function at $T/T_c = 0.6$. The applied voltage is $V = 0.4\,\Delta_0/e$

[54]. Here, $\theta$ is the angle of incidence at the interface with reference to the axis normal to the interface. For particles with nonnormal incidence on the interface, an effectively larger $Z$ parameter is taken into account now. The expression for the current including $Z(\theta)$ is given by

$$I = \frac{eW}{2\pi^2\hbar}\int_{-\infty}^{\infty} \mathrm{d}E \int_{-\pi/2}^{\pi/2} \mathrm{d}\theta \cos\theta \times \sqrt{\frac{2m_e(E+\mu)}{\hbar^2}} \{f_{\rightarrow}[E, Z(\theta)] - f_{\leftarrow}[E, Z(\theta)]\} \,. \tag{5.2013}$$

The $I$–$V$ characteristics calculated from this expression with a given $Z$ parameter will correspond qualitatively to the $I$–$V$ characteristics calculated from (5.2012) with a a slightly larger $Z$ parameter.

The OTBK model can be generalized by considering superconductors with different energy gaps on the two sides (SNS′) [131, 133, 134] or by assuming different barriers ($Z$ parameters) at the SN interfaces [135, 136]. Ineleastic scattering processes were included in the OTBK model by Heslinga et al. [137].

### 5.1.4 Inclusion of the Proximity Effect

In Sect. 2.2.3 the effect of the proximity effect on the Andreev reflection process was discussed. Here, the semiconductor (Sm) is not in direct contact with the superconductor (S) but rather with a normal conductor (N), which

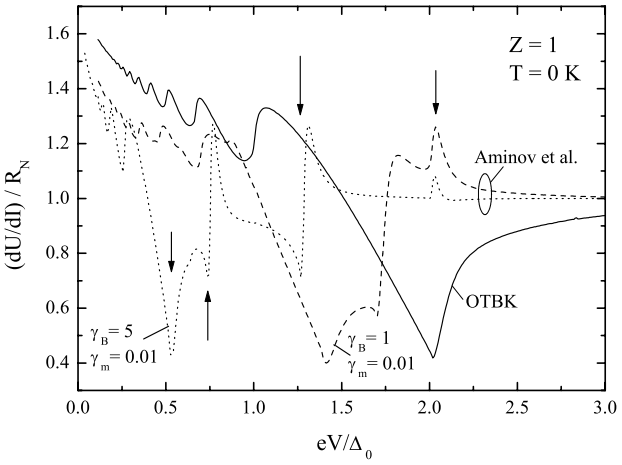


**Fig. 5.4.** Normalized differential resistance $(\mathrm{d}V/\mathrm{d}I)R_\mathrm{N}$ as a function of the bias voltage $eV/\Delta_0$ calculated from the OTBK model for $Z = 0$ and $T = 0$ (*solid line*). The *dashed* and *dotted lines* show $(\mathrm{d}V/\mathrm{d}I)R_\mathrm{N}$ if the proximity effect is included, for $\gamma_\mathrm{B} = 1$ and $\gamma_\mathrm{B} = 5$, respectively. The *arrows* indicate the first subharmonic gap structures of the $V_n = 2\Delta_\mathrm{N}/(en)$, $V_n = (\Delta_\mathrm{S} - \Delta_\mathrm{N})/(en)$, $V_n = (\Delta_\mathrm{S} + \Delta_\mathrm{N})/(en)$, and $V_n = 2\Delta_\mathrm{S}/(en)$ series (from *left* to *right*). The data was taken from [58] (© (1996) by the American Physical Society)

is modified owing to the proximity effect. In order to suppress the proximity effect between the semiconductor and the N layer, the two layers are connected via a small constriction c. As a result, the density of states (DOS) of the N layer at the interface with the Sm layer possesses two peaks, one at the induced gap $\Delta_\mathrm{N}$ and one at $\Delta_\mathrm{S} = \Delta_0$ (Fig. 2.7), in contrast to the bulk DOS of a superconductor, which has only a single singularity at $\Delta_0$ [53, 67]. Consequently, the Andreev reflection coefficient $A(E)$ has also a two peak structure, as was shown in Fig. 2.8.

Of course, the additional structures in the Andreev reflection coefficient $A(E)$ have a direct consequence for the subharmonic gap structures. A more complex structure can be expected in the differential resistance $\mathrm{d}V/\mathrm{d}I$, which may be due either to the gap of the superconductor $\Delta_\mathrm{S}$, to the induced gap $\Delta_\mathrm{N}$ or to a combination of the two, $\Delta_\mathrm{S} \pm \Delta_\mathrm{N}$. A generalization of the OTBK model in this respect was provided by Aminov et al. [58]. Here, an SN/c/NS structure, instead of the S/c/S structure in the OTBK model, is considered. The quasiparticle trajectories which lead to the structures in the differential resistance are shown schematically in Fig. 5.5.

The $(\mathrm{d}V/\mathrm{d}I)/R_\mathrm{N}$ vs. $eV/\Delta_\mathrm{S}$ curves calculated by applying the extended model of Aminov et al. [58] are plotted in Fig. 5.4 for a discontinuity parameter between the S and N layers of $\gamma_\mathrm{B} = 1$ and $\gamma_\mathrm{B} = 5$. The suppression parameter $\gamma_\mathrm{m}$ was set to 0.01, while the $Z$ parameter between the N layer

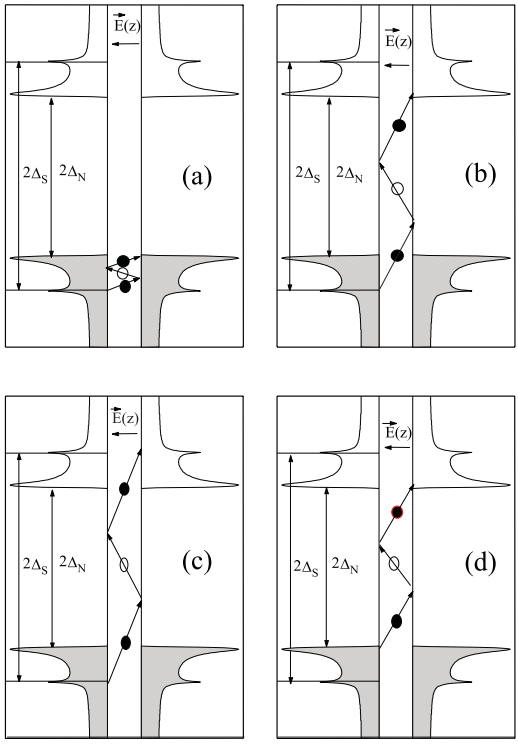


**Fig. 5.5.** Schematic illustration of the quasiparticle trajectories in the constriction region suffering multiple Andreev reflection at $T = 0$ K, at bias voltages of (**a**) $eV = (\Delta_S - \Delta_N)/3$, (**b**) $eV = (\Delta_S + \Delta_N)/3$ (**c**) $eV = 2\Delta_S/3$ and (**d**) $eV = 2\Delta_N/3$ [58] (© (1996) by the American Physical Society)

and the constriction was equal to one. Compared with the curve calculated from the OTBK model, also shown in Fig. 5.4, the curves calculated from the extended model show many additional features. These structures can be explained by referring to the diagram shown in Fig. 5.5. At $V_n = 2\Delta_S/(en)$, the structures already known from the OTBK model are found (Fig. 5.5c), as indicated for $n = 1$ (arrow) at $eV/\Delta_S = 2$ for $\gamma_B = 5$. This structure is very weak, since only a small peak at $\Delta_S$ remains in the density of states at the N/c boundary. The much more pronounced structures at $eV/\Delta_0 \approx 1.6$ and 0.75 belong to the series $V_n = (\Delta_S + \Delta_N)/(en)$ and $V_n = (\Delta_S - \Delta_N)/(en)$ with $n = 1$, respectively (Figs. 5.5b, a). Note that, in contrast to the diagram, for the calculated curve $\Delta_N$ is smaller than $\Delta_S/2$ for $\gamma_B = 5$ (Fig. 2.7). The most pronounced dip in the differential resistance is found for $eV/\Delta_N = 2$ at $eV/\Delta_S \approx 0.5$. This structure corresponds to the enhanced differential conductance at $eV/\Delta_0 = 2$ in the OTBK model, since the induced DOS at the N/c boundary has its maximum at $\Delta_N$.

## 5.2 Measurement of the Voltage-Carrying State

### 5.2.1 Andreev Current in S/2DEG/S Structures

The fact that the Andreev reflection process can indeed lead to an additional current contribution is visualized in Fig. 5.6. Here, the Andreev current $I_{\mathrm{AR}}$ of a 450 nm long and 6 µm wide Nb–InGaAs/InP–Nb junction, prepared as described in Sect. 3.2.2, is plotted as a function of the voltage drop. The sheet electron concentration of the heterostructures used here was $7.05 \times 10^{11}$ cm$^{-2}$ at 0.3 K, with a mobility of 270 000 cm$^2$/Vs. An elastic mean free path $l_{\mathrm{el}}$ of 3.7 µm is deduced from these values. The Nb layer had a critical temperature of $T_{\mathrm{c}} = 8.9$ K, related to a superconducting gap of $\Delta_0 = 1.35$ meV.

$I_{\mathrm{AR}}$ is calculated from the total current $I$ by subtracting the contribution of the normal current: $I_{\mathrm{AR}} = I - V/R_{\mathrm{N}}$, see Fig. 5.6 (inset). $R_{\mathrm{N}}$ has a value of 50 Ω. The measured $I_{\mathrm{AR}}$–$V$ characteristics reveal a negative differential conductance at small voltages $V < 0.1$ mV. Since the measurement was performed in a current bias mode, a shunt resistor of 6.8 Ω was connected in parallel with the junction in order to gain access to the negative-differential-conductance range. Details of the measurement setup are given in Sect. 6.2.3.

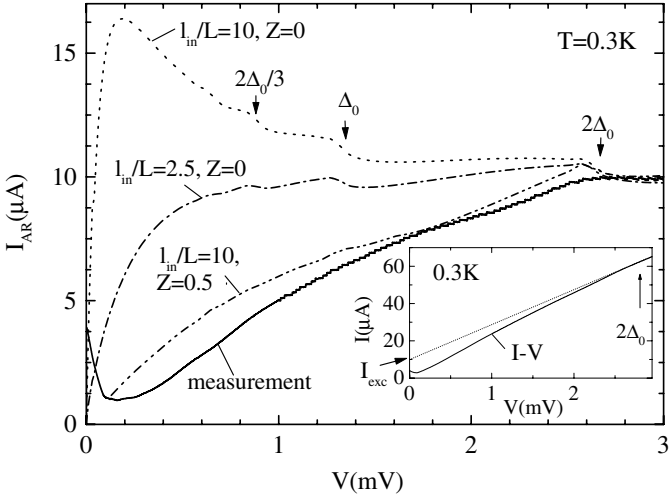


**Fig. 5.6.** Measured Andreev current as a function of $V$ (*solid line*). Also plotted are the calculated $I_{\mathrm{AR}}$–$V$ curves obtained from the KGN model for $l_{\mathrm{in}}/L = 10$ (*dashed line*) and $l_{\mathrm{in}}/L = 2.5$ (*dash-dotted line*) and from the modified KGN model for $l_{\mathrm{in}}/L = 10$, $Z = 0.5$ (*dash-dot-dotted line*). The *inset* shows the measured total current (*solid line*) and the ohmic characteristics (*dashed line*) extrapolated from $V > 2\Delta_0$. The intersection with the current axis is the excess current $I_{\mathrm{exc}}$

It should be remarked that in this S/2DEG/S junction, a finite excess current $I_{\mathrm{exc}}$ of 10 μA is found. The excess current is taken here as the Andreev current $I_{\mathrm{AR}}$ obtained for voltages far above $2\Delta_0$. The fact that an excess current, in contrast to a deficit current [135], is observed means that in this structure the current gain due to the Andreev reflection is larger than the current loss due to the normal reflection process.

The occurrence of a negative differential conductance could lead to the conclusion that this is an effect of current enhancement by multiple Andreev reflections as predicted by the KGN model [124]. In order to compare the measurement with the results of the KGN model, two calculated curves based on this model are also plotted in Fig. 5.6. For a large inelastic mean free path ($l_{\mathrm{in}}/L = 10$) the theoretical curve shows the predicted negative differential conductance. However, the overall shape of this curve does not fit very well to the experimental results. First, the negative differential conductance is observed for $0.1\ \mathrm{mV} < V < 2.6\ \mathrm{mV}$, whereas in the experiment a positive differential conductance is measured in this range. Second, the so-called "foot" appears for $V < 0.1$ mV in the calculated curve. In contrast, no foot structure but, rather, a negative slope is found in the experimental curve. A further analysis shows that it is impossible to obtain theoretically an increase of $I_{\mathrm{AR}}$ with increasing $V$ in the voltage range where this was observed in the experiments and to maintain a negative differential conductance at low voltages. This is demonstrated by the curve for $l_{\mathrm{in}}/L = 2.5$ in Fig. 5.6. It can thus be concluded that the experimentally observed negative differential conductance cannot be explained within the KGN model. In addition, as shown by Uhlisch et al. [138], the inelastic mean free path for this kind of heterostructure is larger than $l_{\mathrm{in}} = 2.5\,L$, which supports the assumption that the experimentally obtained Andreev current must be restricted by an additional process.

As can be seen in Fig. 5.6, the overall shape of the experimental $I_{\mathrm{AR}}(V)$ curve can be better reproduced by applying the modified KGN model. Here, $\delta$-shaped barriers at the SN interfaces are assumed. A good fit to the experimental data is obtained by assuming a $Z$ parameter of 0.5 with $l_{\mathrm{in}}/L = 10$. Nevertheless, the additional normal-reflection contribution also prevents a negative differential conductance, so that this experimentally observed feature cannot be explained within this framework either. In Sect. 6.2.3 the discussion on the negative differential conductance will be continued by including the Josephson effect.

### 5.2.2 Subharmonic Gap Structures

Subharmonic gap structures can best be resolved by measuring the differential resistance $\mathrm{d}V/\mathrm{d}I$ as a function of the voltage drop. In Nb–InGaAs/InP–Nb junctions, pronounced subharmonic gap structures are found in the $\mathrm{d}V/\mathrm{d}I(V)$ measurements as shown in Fig. 5.7 for a 450 nm long, and 6 μm wide Nb–InGaAs/InP–Nb junction.

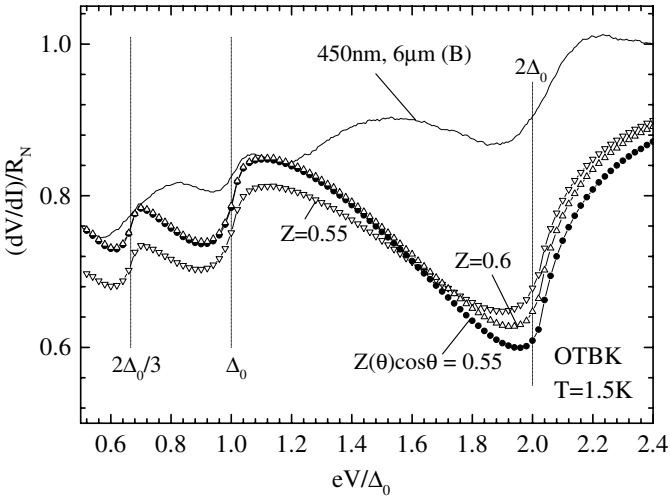


**Fig. 5.7.** Normalized differential resistance as a function of $eV/\Delta_0$ (*solid line*) at $T = 1.5$ K. The theoretical curves obtained from the OTBK model were calculated for $Z = 0.55$ ($\bigtriangledown$) and $Z = 0.6$ ($\bigtriangleup$) and in addition for $Z = 0.55$ ($\bullet$), taking the angle-dependent $Z$ parameter into account

From the discussion in the preceding section it was concluded that the barriers at the interface mainly determine the magnitude of the Andreev current, while the influence of the inelastic scattering is less pronounced. This is the reason why, in the following discussion the OTBK model, which neglects inelastic scattering, is referred to.

In Fig. 5.7, curves calculated using (5.2012) for $Z = 0.55$ and $Z = 0.6$ are added. The features of the calculated subharmonic gap structures at $eV = 2\Delta_0$, $\Delta_0$ and $2\Delta_0/3$ agree reasonably well with the measured structures. For $Z = 0.6$ the local maximum near $\Delta_0$ fits the measured maximum. However, the $\mathrm{d}V/\mathrm{d}I$ modulations in the calculated curves are generally more pronounced than the experimentally obtained variations of the differential resistance. If the $\mathrm{d}V/\mathrm{d}I$–$V$ characteristics are calculated from (5.2013), which considers the angle dependence of the Andreev reflection, the values of the differential resistance for $eV$ smaller than $\approx 1.6\Delta_0$ are larger than the corresponding values calculated from (5.2012). This is demonstrated in Fig. 5.7, where the characteristic for $Z = 0.55$ calculated from the extended OTBK model is plotted. Again, the $\mathrm{d}V/\mathrm{d}I$ modulation is more pronounced than in the experiment. The less developed minima in the experimental curve might be due to scattering processes within the normal conductor or due to diffusive scattering at the interface. The OTBK model considers only the ballistic case with ideal Andreev and normal reflection at the interface. From studies of single S/2DEG junctions, it is known that the interface has a certain roughness due to the $Ar^+$ sputter cleaning. This roughness can lead to diffusive

scattering at the interface. Furthermore, the scattering of carriers at residual donors in the channel can also lead to damping of the $\mathrm{d}V/\mathrm{d}I$ modulations.

An additional minimum at $eV = 1.2\Delta_0$, together with a broad maximum at $1.55\Delta_0$, is found in the measured curve, which is not predicted by the OTBK model. A possible origin of the minimum could be a difference in the gaps in the superconductive electrodes [131, 133, 134] but since both Nb electrodes were prepared simultaneously, this effect could be excluded for our samples. Probably these additional structures are due to the influence of the proximity effect [58], where the maximum at $1.55\Delta_0$ can be attributed to $2\Delta_\mathrm{N}$, where $\Delta_\mathrm{N}$ is the proximity-induced energy gap.

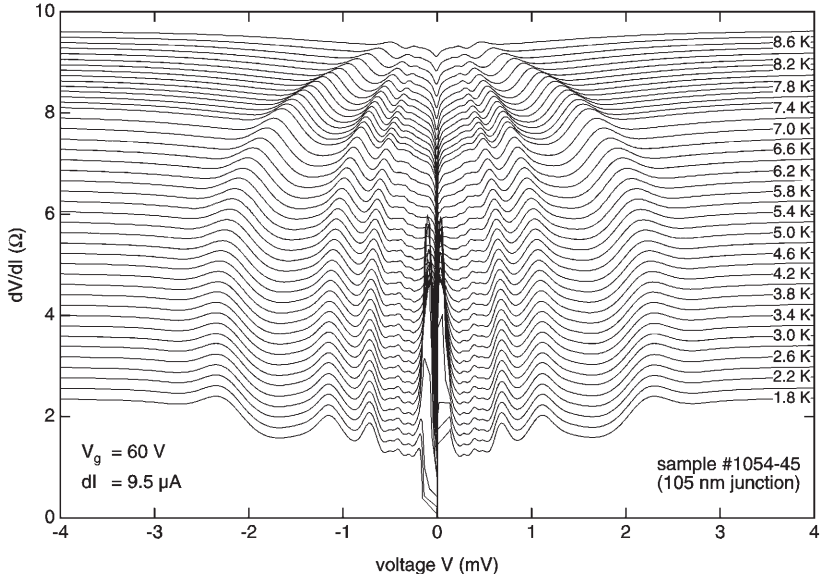


**Fig. 5.8.** Differential resistance of a planar Nb–InAs junction as a function of voltage, with the temperature varied as a parameter [139]

The occurrence of an excess current $I_\mathrm{exc}$ can be deduced directly from the fact that the major part of the normalized differential resistance for $eV/\Delta_0 < 2$ is smaller than 1. From the normalized excess current $eI_\mathrm{exc}R_\mathrm{N}/\Delta_0$ the $Z$-parameter can be estimated following the approach introduced by Flensberg et al. [132]. For $I_\mathrm{exc} = 10$ µA and $R_\mathrm{N} = 50$ Ω, a $Z$ parameter of 0.9 is estimated. This factor is larger than the $Z$ parameter used for the modified KGN model. In the OTBK model $I_\mathrm{exc}$ is mainly determined from the minima of the oscillations, which are deeper than the experimentally observed minima. If the angle-dependent Andreev reflection is taken into account, a slightly smaller $Z$ parameter results for a given excess current.

The differential resistance of a planar Nb–InAs junction is plotted in Fig. 5.8 as a function of the voltage drop, with the temperature varied as a parameter. It can be clearly seen that the subharmonic gap structures shift towards smaller voltages if the temperature is increased. The temperature dependence follows $\Delta_0(T)$ of the BCS theory.

In Fig. 5.9 the subharmonic gap structures are plotted for samples with different geometries (samples A–F). The length of the junctions varied from 300 nm up to 800 nm. Even for large separations of the Nb electrodes, an excess current is observed indicated by the lowering of $\mathrm{d}I/\mathrm{d}V$ below $2\Delta_0 = 2.7$ meV. For larger electrode spacings the subharmonic gap structures are less pronounced. This can be attributed to an increasing scattering probability of the particles when they move through the 2DEG. The pronounced structures at low voltages observed for samples A and C are not due to multiple Andreev reflections but rather due to the Josephson effect, as explained in Sect. 6.2.4. The absence of these structures for the 800 nm and 600 nm long samples is due to a small magnetic field ($< 1$ mT), which suppresses the Josephson effect.

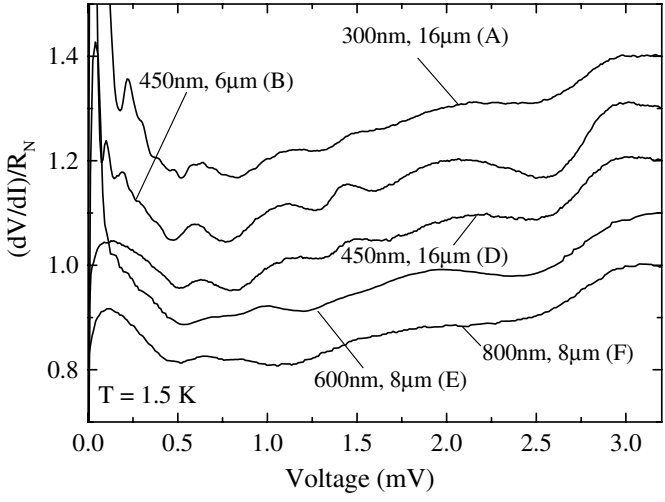


**Fig. 5.9.** Normalized differential resistance for different junction geometries as a function of the voltage drop. The corresponding lengths and widths are given in the graph. The curves are shifted upwards in steps of 0.1

### 5.2.3 Subharmonic Gap Structures and the Proximity Effect

In some junctions the proximity effect has to be taken into account in order to interpret the subharmonic gap structures. Here, the SN/c/NS model in-

troduced in Sect. 5.1.4 can be applied instead of the OTBK model. A typical example of a sample showing evidence for a proximity layer is an Nb/p-InP/Nb junction, as depicted in Fig. 3.5b [59]. The proximity layer (N) is formed in the InAs inversion layer directly underneath the superconducting Nb electrodes, as illustrated in Fig. 5.10 (inset). Because of the strong coupling to the superconductor due to the absence of a barrier, a gap in the density of states is induced in the inversion layer (N) below the Nb electrode. The two N layers are connected via a short bridge, constituted from the two-dimensional electron gas in the surface inversion layer of the p-InAs. This bridge serves as the constriction c in the SN/c/NS model.

As can be seen in Fig. 5.10, the measured subharmonic gap structures cannot be explained consistently by the OTBK model. In order to obtain a reasonable agreement with the OTBK model at low temperatures (1.8 K), a lower gap $\Delta_S$ of 1.2 meV compared with the value determined from the critical temperature $T_c$ has to be assumed. However, a look at the measured curve at a higher temperature of 6.6 K shows that the subharmonic gap structures calculated from the OTBK model appear at bias voltages that are much too low. The reason for this discrepancy is the gap value calculated from the BCS theory, which is too small at 6.6 K.

A much better agreement between experiment and theory is obtained if a proximity layer with an induced gap $\Delta_N$ is assumed. In this case, it is possible to take a gap value of 1.45 meV in the superconductor (S), deduced from the measured $T_c$ of the Nb layer. According to the SN/c/NS model, a reduced gap $\Delta_N$ is found at the boundary with the bridge c formed by the two-dimensional electron gas at the surface of the InAs. In the calculated curves the subharmonic gap structures at $V_n = 2\Delta_N/(en)$ due to the induced gap $\Delta_N$ are much more pronounced than the remaining structures at $V_n = 2\Delta_S/(en)$ or $V_n = (\Delta_S \pm \Delta_N)/(en)$ [59]. This is probably due to the fact that for the parameter set taken here, the peak at $E = \Delta_S$ in the induced density of states is only weak. According to theory, the induced gap $\Delta_N$ approaches the gap of the superconductor layer $\Delta_S$ as $T \to T_c$ [58]. This is the reason why the subharmonic gap structures in the SN/c/NS model are found at larger voltages than in the OTBK model and thus agree better with the experiment.

## 5.3 Resonant Structures and Interference Effects

In some junctions the differential resistance reveals features which cannot explained by the subharmonic gap structures discussed above. A typical example is shown in Fig. 5.11a, where the differential resistance $\mathrm{d}V/\mathrm{d}I$ of a p-InAs step edge junction (Fig. 3.5a) is plotted [140]. For voltages below the first subharmonic gap structure at $2\Delta_N/e$ (upward arrow), distinct subgap peaks are observed, which cannot be explained either by the BTK or by the SN/c/NS model. These subgap peaks are much more pronounced than the

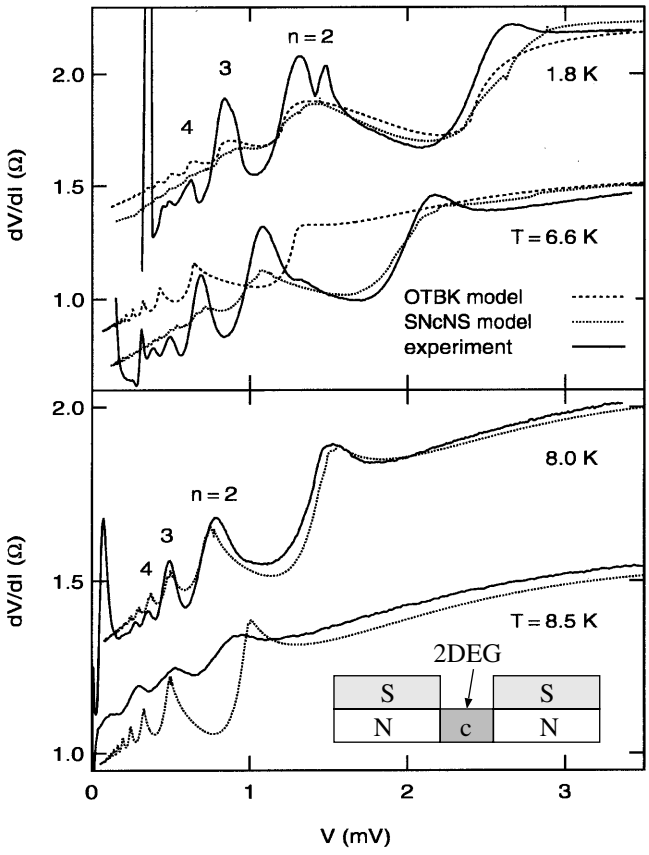


**Fig. 5.10.** Comparison of the measured differential resistances (*solid lines*) of a Nb/p-InAs/Nb junction at four temperatures with the SN/c/NS model (*dotted lines*) and the OTBK model (*dashed lines*). The parameters for the SN/c/NS model are $\Delta_S(T=0) = 1.45$ meV, $R_N = 1.55\ \Omega$, $\gamma_B = 0.65$ and $Z = 0.45$. For the OTBK model, the following parameters were used: $\Delta_S(T=0) = 1.20$ meV, $R_N = 1.55\ \Omega$ and $Z = 0.45$. The curves for 1.8 K and 8.0 K are shifted by 0.7 and 0.5 $\Omega$, respectively. The *inset* shows the realization of the SN/c/NS junction in a planar Nb/p-InAs/Nb junction [59] (© (1997) by the American Physical Society)

subharmonic gap structures. If the temperature is increased, the peak positions shift towards lower voltages. In Fig. 5.11b the position of the dominant peak (◇) is plotted versus temperature. It can be seen that the peak position does not scale with the induced gap $2\Delta_N/e$ but, rather, maintains a constant distance from $2\Delta_N/e$. Comparable resonances have also been observed in other types of junctions, e.g. junctions based on InAs/AlSb [28, 36].

A qualitative explanation of the sharp resonances was suggested by Bastian et al. [28]. According to their interpretation, the peak is caused by quasi-

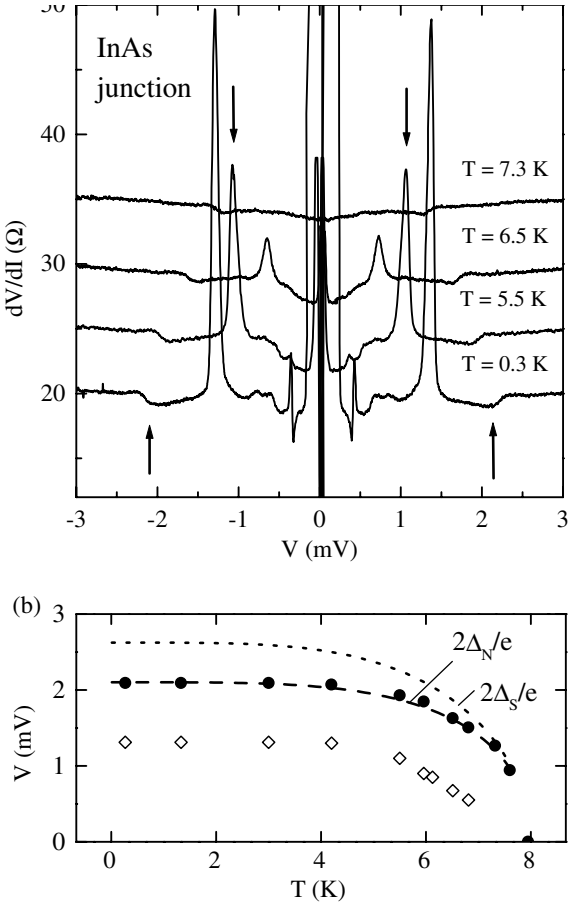


**Fig. 5.11.** (**a**) Differential resistance d$V$/d$I$ of a 2.5 μm wide p-InAs step junction at different temperatures as a function of bias voltage. For clarity, the curves are shifted in steps of 5 Ω. The *arrows* at the *bottom* indicate the induced energy gap $2\Delta_N/e$. The *arrows* at the *top* point to a giant subgap peak. (**b**) Temperature dependence of $2\Delta_N/e$ (•) and the giant subgap peak (◇) The *dotted line* is the calculated value of $2\Delta_S/e$ (BCS theory). The *dashed line* is the calculated value of $2\Delta_N/e$, according to (2.32), with $\Delta_N/\Delta_0 = 0.8$ at $T = 0$ and an interface transparency parameter $\gamma_B = 0.25$ (SN/c/NS model) [140]

particle interference. In Fig. 5.2 the electron and hole trajectories in an SNS junction are shown. Owing to the finite barrier at the interface ($Z > 0$), there is a certain probability for normal reflection. By this normal reflection process, a quasiparticle can return to the same energy and position where it started from. For those voltage drops which satisfy the condition for constructive interference, a standing wave is formed. Since the particle is trapped in the cavity, the differential resistance is increased, as observed in the experiment.

The interpretation given above is supported by measurements on junctions with different separations of the superconducting electrodes. With an increasing width of the cavity, the number of spikes is increased as expected [28]. The shift of the peaks towards smaller voltages with increasing temperature can be explained by the fact that the effective width of the cavity is increased. The cavity is bounded by two induced proximity layers (for details see Sect. 5.2.3). With increasing temperature the width of these proximity layers decreases, leading to an effective widening of the cavity and thus to a shift of the spikes to lower voltages.

# 6. Josephson Current in Superconductor/ Two-Dimensional-Electron-Gas Junctions

During the discussion of the subharmonic gap structures, the phase of the superconducting electrodes was neglected. We shall see in this chapter that phase coherence is crucial for the occurrence of a Josephson supercurrent. In the first part of this chapter, the theoretical concepts will be discussed, starting with the simplest model of an ideal one-dimensional junction, without any barriers at the SN interface and with no Fermi velocity mismatch. Later on, more elaborate models will be introduced, which describe the experimental situation more appropriately.

In the second part of the chapter, measurements of the superconductive state are discussed. After analyzing the current–voltage characteristics of various types of Josephson junctions and comparing them with the theoretical models, the interference effect due to an applied magnetic field is discussed. The light sensitivity of the sheet resistance in a semiconductor heterostructure can be employed to control the supercurrent in a Josephson junction. This will be demonstrated in the last section.

## 6.1 Theoretical Description of the Supercurrent in an S/2DEG/S Junction

For the description of a Josephson supercurrent within the framework of Andreev reflection, it is essential to maintain the phase coherence between the two electrodes. In the clean-limit case ($\xi < l_{\mathrm{el}}$) it was shown that a significant portion of this supercurrent is carried by discrete energy levels, which are formed within the superconductive gap [126]. The second part contributing to the total supercurrent is due to the continuous energy spectrum at $|E| > \Delta_0$. For the ideal case, an expression for the discrete energy-level spectrum with no barriers at the interface and no Fermi velocity mismatch was derived for a one-dimensional structure by Kulik [126], Ishii [141] and by Bardeen and Johnson [142]. The next step towards a more realistic description of the experimental situation was provided by Bagwell [143], who discussed the effect of a single impurity within the normal conductor modeled by a $\delta$-shaped barrier. A further generalization was achieved by Tang et al. [144], where $\delta$-shaped barriers were assumed at the SN interface. In addition, a

Thomas Schäpers: Superconductor/Semiconductor Junctions, STMP 174, 65–94 (2001)
© Springer-Verlag Berlin Heidelberg 2001

Fermi velocity mismatch was also included here. It is sometimes interesting, especially for modeling structures with regard to potential applications, to introduce an arbitrary potential shape, e.g. tunnel barriers, in the normal conductor, as discussed in [13, 145, 146].

In order to describe the transport in a realistic device, the one-dimensional model has to be extended to two or three dimensions. A detailed model for an Nb/n-type-InAs/Nb junction was provided by Schüssler and Kümmel [76]. For a two-dimensional electron gas sandwiched between two superconducting electrodes, a model was developed for the ideal case with no barriers at the S/2DEG interface by Kresin [147]. Later this model was extended by Chrestin et al. [148] by including $\delta$-shaped barriers at the S/2DEG interfaces.

### 6.1.1 Supercurrent in an Ideal One-Dimensional SNS Junction

In order to understand the basic transport mechanisms in an SNS junction, it is instructive to discuss an ideal one-dimensional junction. "Ideal" means that neither barriers at the interface nor differences in the Fermi velocity between the superconductor and the normal conductor are considered [126]. In contrast to a single SN interface, now the phase difference $\phi$ of the pair potential between the two superconducting electrodes must be taken into account (Fig. 6.1). Similarly to the BTK model [46], a step-like superconducting pair potential $\Delta(x)$ is assumed, which is zero in the normal conductor:

$$\Delta(x) = \begin{cases} \Delta_0 \mathrm{e}^{-\mathrm{i}\phi/2} & , \quad x < 0 \\ 0 & , \quad 0 < x < L \\ \Delta_0 \mathrm{e}^{\mathrm{i}\phi/2} & , \quad x > L \end{cases} . \tag{6.1}$$

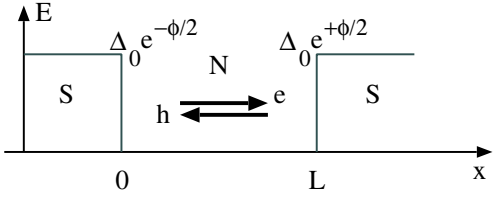


**Fig. 6.1.** Spatial dependence of the pair potential $\Delta(x)$ for an ideal one-dimensional SNS junction. The *arrows* represent the group velocities of an electron and a hole. The wave vectors of the two particles have the same direction

The energy spectrum of an ideal SNS junction, as a solution of the the Bogoliubov equation (2.1), can be separated into a continuous Andreev spectrum for $|E| > \Delta_0$ and discrete Andreev states for $|E| \leq \Delta_0$. The latter are due to the fact that states within the gap of the superconductor cannot exist. Here, the wave function attenuates exponentially in the superconductor. In a sense, the situation is comparable to a finite-depth quantum well for electrons, with

discrete states within and extended states outside the well. However, in contrast to a quantum well, the Andreev bound states in an SNS junction can carry a supercurrent.

Following the ansatz of Kulik [126], the wave functions $\psi_\pm$ for an excitation moving to the right (+) and to the left (−) for $|E| \leq \Delta_0$ can be expressed by

$$\psi_+(x) = \begin{cases} A_+ \begin{pmatrix} v_0 \mathrm{e}^{-\mathrm{i}\phi/2} \\ u_0 \end{pmatrix} \mathrm{e}^{+\mathrm{i}\tilde{k}_\mathrm{h} x} & , \; x < 0 \\ B_+ \begin{pmatrix} v_0 \mathrm{e}^{-\mathrm{i}\phi/2} \\ 0 \end{pmatrix} \mathrm{e}^{+\mathrm{i}k_\mathrm{e} x} + B_+ \begin{pmatrix} 0 \\ u_0 \end{pmatrix} \mathrm{e}^{+\mathrm{i}k_\mathrm{h} x} & , \; 0 < x < L \\ C_+ \begin{pmatrix} u_0 \mathrm{e}^{\mathrm{i}\phi/2} \\ v_0 \end{pmatrix} \mathrm{e}^{+\mathrm{i}\tilde{k}_\mathrm{e}(x-L)} & , \; x > L \end{cases} \quad (6.2)$$

and by

$$\psi_-(x) = \begin{cases} A_- \begin{pmatrix} u_0 \mathrm{e}^{-\mathrm{i}\phi/2} \\ v_0 \end{pmatrix} \mathrm{e}^{-\mathrm{i}\tilde{k}_\mathrm{e} x} & , \; x < 0 \\ B_- \begin{pmatrix} u_0 \mathrm{e}^{-\mathrm{i}\phi/2} \\ 0 \end{pmatrix} \mathrm{e}^{-\mathrm{i}k_\mathrm{e} x} + B_- \begin{pmatrix} 0 \\ v_0 \end{pmatrix} \mathrm{e}^{-\mathrm{i}k_\mathrm{h} x} & , \; 0 < x < L. \\ C_- \begin{pmatrix} v_0 \mathrm{e}^{\mathrm{i}\phi/2} \\ u_0 \end{pmatrix} \mathrm{e}^{\mathrm{i}\tilde{k}_\mathrm{h}(x-L)} & , \; x > L \end{cases} \quad (6.3)$$

Here, $k_\mathrm{e}$ and $k_\mathrm{h}$ are the wave vectors given by (2.12a) and (2.12b) for an electron (e) and a hole (h), respectively, in the normal conductor. Note that the group velocity of the hole has the reverse direction to its phase velocity. The latter is oriented along $k_\mathrm{h}$. $\tilde{k}_\mathrm{e}$ and $\tilde{k}_\mathrm{h}$ are the wave vectors of an electron-like (e) and a hole-like (h) particle in the superconducting electrodes, as given in (2.13a) and (2.13b), respectively. For the ideal case, as considered here, the Fermi wave vectors in the normal conductor and the superconductor are identical; $k_\mathrm{FN} = k_\mathrm{FS} = k_\mathrm{F}$. Since $|E| \leq \Delta_0$, $\tilde{k}_\mathrm{e}$ and $\tilde{k}_\mathrm{h}$ possess an imaginary component, which is responsible for the aforementioned exponential attenuation within the superconductor. Continuity at $x = 0$ and $x = L$ and use of the definition of $u_0$ and $v_0$, as given by (2.4a) and (2.4b), result in

$$\frac{u_0^2}{v_0^2} = \frac{2E^2 - \Delta_0^2}{\Delta_0^2} + \mathrm{i}\,2\frac{E}{\Delta_0^2}\sqrt{\Delta_0^2 - E^2} = \mathrm{e}^{\pm\mathrm{i}\phi}\mathrm{e}^{\mathrm{i}(k_\mathrm{e}-k_\mathrm{h})L} \,. \quad (6.4)$$

Here, $+\mathrm{i}\phi$ corresponds to the right-moving particles and $-\mathrm{i}\phi$ to the corresponding left-moving particles. Since $|E| \leq \Delta_0$, the absolute value of $u_0^2/v_0^2$ is 1, thus we can define $u_0^2/v_0^2 = \cos 2\gamma + \mathrm{i}\sin 2\gamma = \exp(\mathrm{i}2\gamma)$. Inserting this expression in (6.4), we arrive at

$$1 = \mathrm{e}^{-\mathrm{i}2\gamma}\mathrm{e}^{\pm\mathrm{i}\phi}\mathrm{e}^{\mathrm{i}(k_\mathrm{e}-k_\mathrm{h})L}. \quad (6.5)$$

For $|E| \ll \mu$, $(k_e - k_h)$ can be approximated by $k_F E/\mu = E/(\Delta_0 \xi_0)$, where $\xi_0 = \mu/(k_F \Delta_0)$ is the BCS coherence length. By equating the phase on the right-hand side to $2\pi n$, where $n = 0, \pm 1, \pm 2, ...$, and using $\cos\gamma = \sqrt{(1+\cos 2\gamma)/2} = E/\Delta_0$, we find that the energy eigenvalues are given by

$$\left(\frac{E}{\Delta_0}\right)\left(\frac{L}{\xi_0}\right) = 2\arccos\left(\frac{E}{\Delta_0}\right) \mp \phi - 2\pi n \; . \tag{6.6}$$

The energy eigenvalue spectrum has a phase periodicity of $2\pi$. In the limit of a short junction ($L \ll \xi_0$), the left-hand side of (6.6) can be approximated by zero. In this case the two bound states $E_0^+$ and $E_{-1}^-$ simply follow a cosine phase dependence:

$$\begin{aligned} E_0^+(\phi) &= +\Delta_0 \cos(\phi/2) \; , \\ E_{-1}^-(\phi) &= -\Delta_0 \cos(\phi/2) \; . \end{aligned} \tag{6.7}$$

The states are degenerate at $\phi = \pi$.

For a finite length $L$ comparable to $\xi_0$, the eigenvalue spectrum is as shown in Fig. 6.2a. Now, the discrete states are also degenerate at $\phi = 0$. If the phase difference is increased, the degeneracy is lifted. A typical eigenvalue spectrum as a function of the phase difference for a long junction ($L \gg \xi_0$) is given in Fig. 6.2b. Similarly to the eigenvalues for electrons in a quantum well, the number of states is increased, while the energetic separation between adjacent levels is lowered. At low energies ($E \ll \Delta_0$) the energy dispersion is approximately linear [126]:

$$E_n^{\pm}(\phi) = \frac{\xi_0 \Delta_0}{L}\left[\pi(2n+1) \mp \phi\right] \; . \tag{6.8}$$

As we shall see in the next section, the states $E_n^{\pm}(\phi)$ carry a supercurrent in an SNS junction. In equilibrium the contribution of each of these channels to the net supercurrent is determined by the Fermi distribution function $f_0(E)$. At zero temperature only the states with $E < 0$ contribute to the supercurrent, since they are fully occupied, whereas the states with $E > 0$ are empty. Besides the bound states $E_n^{\pm}(\phi)$, part of the net supercurrent is also carried by continuous states with $|E| > \Delta_0$. Details of how the Josephson supercurrent in an SNS junction is calculated are given in the following section.

### 6.1.2 Supercurrent in a General One-Dimensional SNS Junction

In this section we shall treat the more general case of a one-dimensional SNS junction with barriers at the interfaces and a Fermi velocity mismatch between the superconductor and the normal conductor. The Andreev-level spectrum and the supercurrent can be calculated very elegantly by a transmission matrix method, as presented by Tang et al. [144]. An alternative

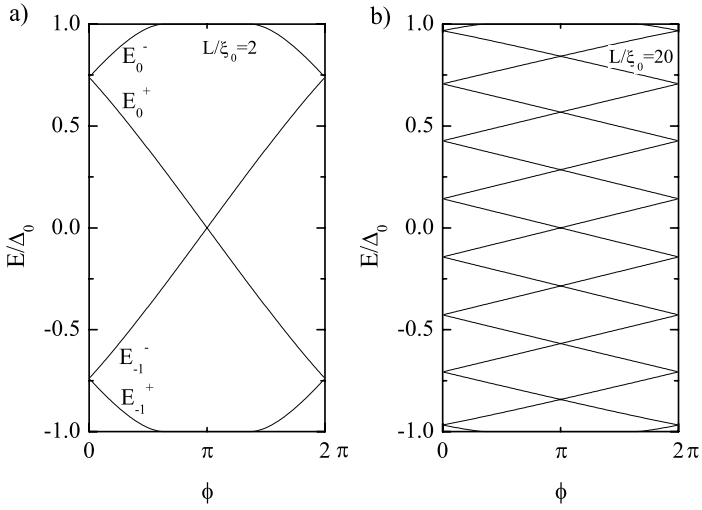


**Fig. 6.2.** Andreev levels of a short ($L/\xi_0 = 2$) (**a**) and long ($L/\xi_0 = 20$) (**b**) ideal SNS junction

method to calculate the supercurrent would be to use the scattering-matrix approach [149, 150, 151].

Once again, a step-like superconducting pair potential $\Delta_0$ and a phase difference $\phi$ between the two superconducting electrodes are assumed (Fig. 6.3). The potential $U(x)$ is given by the $\delta$-shaped barriers and by the step due to the difference $U_0$ between the Fermi energies between the normal conductor and the superconductor:

$$U(x) = U_0 \left[\Theta(x) - \Theta(x-L)\right] + \frac{\hbar^2 k_{\mathrm{FS}}}{m_{\mathrm{e}}} Z \left[\delta(x) + \delta(x-L)\right] \ . \tag{6.9}$$

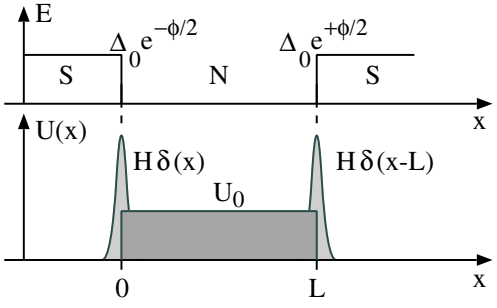


**Fig. 6.3.** Spatial dependence of the pair potential $\Delta(x)$ and the potential $U(x)$ in an SNS junction

For the calculation of the Josephson supercurrent, the transmission of incoming electron-like particles $\Psi_\mathrm{e}$ and hole-like particles $\Psi_\mathrm{h}$ through the junction is described by a transfer matrix $\mathbf{T}(\phi)$ [144]:

$$\begin{pmatrix} \widetilde{\Psi}_\mathrm{e} \\ \widetilde{\Psi}_\mathrm{h} \end{pmatrix} = \mathbf{T}(\phi) \begin{pmatrix} \Psi_\mathrm{e} \\ \Psi_\mathrm{h} \end{pmatrix} . \tag{6.10}$$

$\mathbf{T}(\phi)$ can be decomposed into matrices representing the different steps during the transport. The transmission through the left (SN) and right (NS) boundaries is represented by the following two matrices, which contain the transmission coefficients given by (2.16d) and (2.18) for the generalized BTK model introduced in Sect. 2.2.2:

$$\mathbf{I} = \begin{pmatrix} \mathrm{e}^{-\mathrm{i}\phi/4} c'_+ & \mathrm{e}^{-\mathrm{i}\phi/4} d'_- \\ \mathrm{e}^{\mathrm{i}\phi/4} d'_+ & \mathrm{e}^{i\phi/4} c'_- \end{pmatrix}, \quad x = 0 , \tag{6.11}$$

$$\mathbf{O} = \begin{pmatrix} \mathrm{e}^{-\mathrm{i}\phi/4} c_+ & \mathrm{e}^{\mathrm{i}\phi/4} d_- \\ \mathrm{e}^{-\mathrm{i}\phi/4} d_+ & \mathrm{e}^{i\phi/4} c_- \end{pmatrix}, \quad x = L . \tag{6.12}$$

After passing through the left SN interface, the electron and hole acquire phase shifts during the transfer through the normal conductor of $k_\mathrm{e}L$ and $-k_\mathrm{h}L$, respectively, which can be expressed by the matrix $\mathbf{P}$:

$$\mathbf{P} = \begin{pmatrix} \mathrm{e}^{\mathrm{i}k_\mathrm{e}L} & 0 \\ 0 & \mathrm{e}^{-\mathrm{i}k_\mathrm{h}L} \end{pmatrix} . \tag{6.13}$$

An electron or hole can either be transferred directly through the N layer or be multiply reflected inside the normal conductor as in a resonant cavity. Each of the cycles can be described by a reflection at the NS interface $\mathbf{S}(\phi/2)$, travel to the opposite interface $\mathbf{P}$, a reflection at this interface $\mathbf{S}(-\phi/2)$ and, finally, a transfer to the starting point $\mathbf{P}$, as can be seen in Fig. 6.4. If this single cycle is represented by a matrix $\mathbf{M}(\phi)$, the total transfer from the left to the right interface can be described by

$$\sum_{n=0}^{\infty} \mathbf{M}(\phi)^n = [1 - \mathbf{M}(\phi)]^{-1}. \tag{6.14}$$

$\mathbf{M}(\phi)$ is composed of the matrices for the above-mentioned single steps, where the scattering matrices $\mathbf{S}$ for the Andreev reflection $a_\pm$ and the normal reflection $b_\pm$ of an electron and a hole from the normal-conductor side are given by

$$\mathbf{S}(\pm\phi/2) = \begin{pmatrix} b_+ & \mathrm{e}^{\pm\mathrm{i}\phi/2} a_- \\ \mathrm{e}^{\mp\mathrm{i}\phi/2} a_+ & b_- \end{pmatrix} . \tag{6.15}$$

Combining all components leads to

$$\mathbf{M}(\phi) = \mathbf{P}\mathbf{S}(-\phi/2)\mathbf{P}\mathbf{S}(\phi/2) . \tag{6.16}$$

For the total transmission matrix $\mathbf{T}$ through the junction, the transmission through the SN interface (6.11) and through the opposite NS interface (6.12) have to be taken into account:

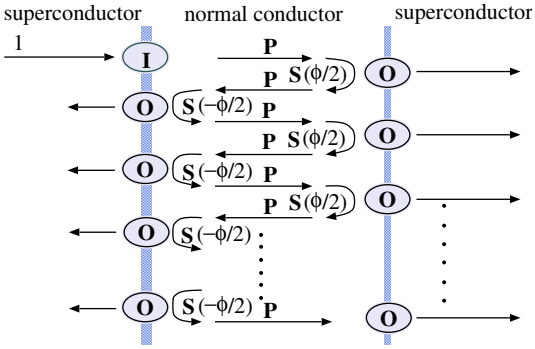


**Fig. 6.4.** Transmission and reflection processes in a superconductor/normal conductor/superconductor structure

$$\mathbf{T}(\phi) = \begin{pmatrix} C_+(\phi) & D_+(\phi) \\ D_-(\phi) & C_-(\phi) \end{pmatrix} = \mathbf{O}(\phi/2)[\mathbf{1} - \mathbf{M}(\phi)]^{-1}\mathbf{P}\,\mathbf{I}(-\phi/2). \quad (6.17)$$

The Josephson supercurrent $I(\phi)$ can be calculated by using the transmission matrix $\mathbf{T}$ directly. However, for the practical computation of $I(\phi)$ it is useful to separate the current into a component $I_{\rm dis}$, originating from the discrete Andreev levels inside the gap ($|E| \le \Delta_0$), and a component $I_{\rm cont}$, from the continuous spectrum outside the gap ($|E| > \Delta_0$). The discrete energy levels can be obtained from the poles of the transfer matrix $\mathbf{T}$. By writing

$$[\mathbf{1} - \mathbf{M}(\phi)]^{-1} = \frac{\mathbf{1} - \mathbf{M}(\phi)^{\rm t}}{\det[\mathbf{1} - \mathbf{M}(\phi)]} = \frac{\mathbf{1} - \mathbf{M}(\phi)^{\rm t}}{\Gamma}\,, \quad (6.18)$$

where $\mathbf{M}^{\rm t}$ is the adjoint of $\mathbf{M}$ and $\Gamma = \det(\mathbf{1} - \mathbf{M})$, it can be seen that the energy eigenvalues can be determined from the roots of $\Gamma$. Expanding $\Gamma$ leads to

$$\begin{aligned} \Gamma \;=\; & \gamma^2 \mathrm{e}^{\mathrm{i}\alpha}\Bigg\{\left(\frac{\Delta_0}{E}\right)^2\left[-\frac{1}{2}\cos\phi - \left(2p^2+2p+\frac{1}{2}\right)\cos\left(\alpha\frac{E}{\Delta_0}\right)\right. \\ & \left. +2(q^2-Z^2)\cos\beta - 4Zq\sin\beta\right] \\ & + \left[(2p^2+2p+1)\cos\left(\alpha\frac{E}{\Delta_0}\right) - 2(q^2-Z^2)\cos\beta + 4Zq\sin\beta\right] \\ & +(2p+1)\frac{\Delta_0}{E}\sqrt{1-\left(\frac{E}{\Delta_0}\right)^2}\sin\left(\alpha\frac{E}{\Delta_0}\right)\Bigg\}\,, \end{aligned} \quad (6.19)$$

where $\alpha = k_{\rm FN}L\Delta_0/(\mu - U_0)$ and $\beta = 2k_{\rm FN}L$. In $\alpha$ and $\beta$, $(k_{\rm e} - k_{\rm h})$ has been approximated by $2k_{\rm FN}E(\mu - U_0)$ and $(k_{\rm e} + k_{\rm h})/2$ by $k_{\rm FN}$; $p$ is defined as $Z^2/r + (r-1)^2/4r$ and $q$ as $Z^2/r + (1-r^2)/4r$; $r$ is the Fermi velocity mismatch given by (2.17).

At zero temperature ($T = 0$) only the discrete levels $E_n^{\pm}$ below the electrochemical potential $\mu$ are occupied and contribute to the net supercurrent. The current $I_{\rm dis}$ carried by the discrete levels, determined from (6.19), is obtained from

$$I_{\rm dis} = \sum_{n,\pm,E<0} \frac{2e}{\hbar} \frac{{\rm d}E_n^{\pm}(\phi)}{{\rm d}\phi} \,. \tag{6.20}$$

The supercurrent $I_{\rm cont}$ due to the continuous energy spectrum must be calculated directly from the transmission matrix $\mathbf{T}$:

$$\begin{aligned} I_{\rm cont} &= \frac{2e}{\hbar} \int_{-\infty}^{-\Delta_0} i(E,\phi)\,{\rm d}E \\ &= \frac{2e}{\hbar} \int_{-\infty}^{-\Delta_0} \frac{1}{|u_0^2 - v_0^2|} \big\{ [T^{\rm e}_{{\rm L}\to{\rm R}}(E,\phi) - T^{\rm e}_{{\rm L}\leftarrow{\rm R}}(E,\phi)] \\ &\quad - \big[T^{\rm h}_{{\rm L}\to{\rm R}}(E,\phi) - T^{\rm h}_{{\rm L}\leftarrow{\rm R}}(E,\phi)\big] \big\} {\rm d}E \\ &= \frac{2e}{\hbar} \int_{-\infty}^{-\Delta_0} \frac{1}{|u_0^2 - v_0^2|} \\ &\quad \times \big[ |C_+(\phi)|^2 - |C_+(-\phi)|^2 - |C_-(\phi)|^2 + |C_-(-\phi)|^2 \big] \, {\rm d}E \end{aligned} \tag{6.21}$$

The continuous current is composed of a current carried by both electron-like and hole-like particles. In the above expression we have made use of the fact that the current direction can be inverted simply by reversing the sign of $\phi$. The factors $C_{\pm}(\phi)$ are defined in (6.17).

The general expressions (6.19) and (6.21) for the calculation of the total Josephson supercurrent are relatively complex. However, for some special cases expression (6.19) can be simplified significantly; i.e., for a clean junction with no barriers at the interface ($Z = 0$) and no Fermi velocity mismatch ($U_0 = 0$), it reduces to (6.6). The general expression for bound states in a short junction ($L \ll (\mu - U_0)/k_{\rm FN}\Delta_0$), which can be obtained from (6.19), is

$$E_{\rm B}^{\pm}(\phi) = \pm\Delta_0 \sqrt{\frac{\cos^2(\phi/2) + 2p^2 + 2p - 2q^2 + 2Z^2}{2p^2 + 2p - 2q^2 + 2Z^2 + 1}} \,. \tag{6.22}$$

Here we have assigned $E_{\rm B}^{+} = E_0^{+}$ and $E_{\rm B}^{-} = E_{-1}^{-}$. Since $2p^2 + 2p - 2q^2$ is equal to $2Z^2$, this equation reduces to

$$E_{\rm B}^{\pm}(\phi) = \pm\Delta_0 \sqrt{\frac{\cos^2(\phi/2) + 4Z^2}{4Z^2 + 1}} \,, \tag{6.23}$$

which is the expression for the eigenvalues if a junction with $\delta$-shaped barriers but no Fermi velocity mismatch ($r = 1$) is considered. For the short-junction case the continuous current contribution is zero, so that only the current due to the discrete levels has to be considered for the calculation of the total supercurrent. In Fig. 6.5a the Andreev levels are plotted as a function of the phase difference $\phi$ for the case $Z = 0$, (6.7), as well as for $Z = 0.5$ and

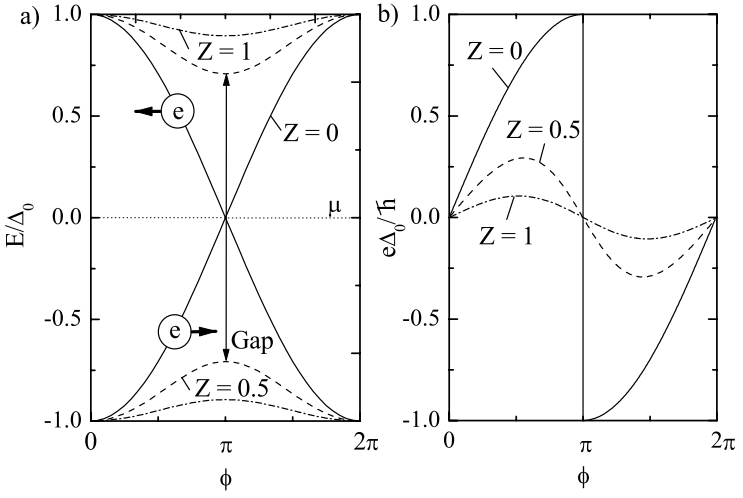


**Fig. 6.5.** (**a**) Normalized Andreev levels and (**b**) Josephson current of a short junction ($L \ll \xi_0$) as a function of the phase difference $\phi$ for $Z = 0$ (*solid lines*), $Z = 0.5$ (*dashed lines*) and $Z = 1.0$ (*dash-dotted lines*). The direction of the electron motion for the corresponding Andreev levels is denoted by *arrows*

1.0; these were obtained by using (6.23). Owing to the additional normal reflection process for $Z > 0$, the degeneracy at $\phi = \pi$ in the quasiparticle spectrum is lifted, with the consequence that an energy gap appears. As can be seen in Fig. 6.5b, the supercurrent is reduced by the presence of a barrier at the SN interface. The maximum value of the supercurrent which can be obtained before the junction switches into the normal state is called the critical current. In Fig. 6.5b it can be seen that $I(\phi)$ gradually transfers from the clean-limit point contact behavior [24, 152] to a tunnel junction characteristic [$I(\phi) \propto \sin\phi$] [153].

For a finite length of the normal-conducting region, more Andreev levels appear within the gap, as can be seen in Fig. 6.6a for a 450 nm long junction. The Andreev levels were determined by numerically calculating the roots of (6.19) for a given phase difference $\phi$. The degeneracy of the levels at $\phi = 0$, $\pi$ and $2\pi$ for $Z = 0$ and $r = 1$ is lifted if $Z > 0$ or if $r < 1.0$. Since the $E(\phi)$ dispersion is flattened for increasing $Z$ and $r$, the Josephson current due to these discrete levels is also lowered according to (6.20). Here, $r = 0.44$ was chosen, as a typical value for an Nb–InGaAs/InP junction, as introduced in Sect. 5.2.1, with a typical carrier concentration of $7.1 \times 10^{11}$ cm$^{-2}$ for the two-dimensional electron gas. In Fig. 6.6b, the discrete and the continuous contribution as well as the total supercurrent are plotted as a function of the phase difference $\phi$ for $Z = 0.5$ and $r = 0.44$. Since now the junction has a finite length, the continuous Andreev-level spectrum also contributes to the net supercurrent.

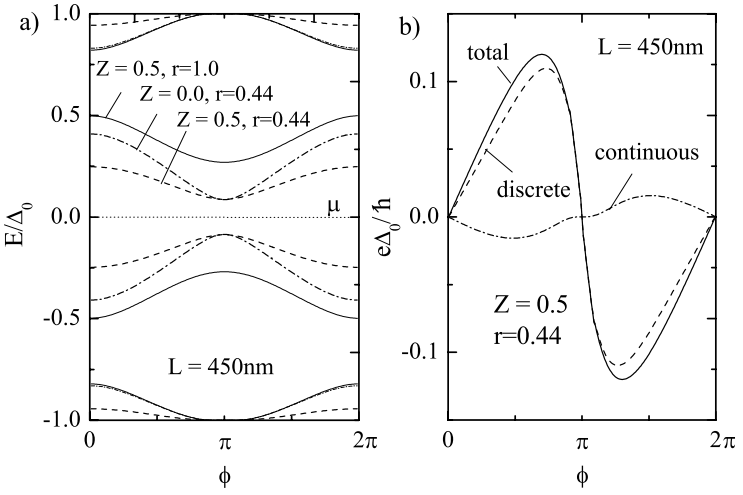


**Fig. 6.6.** (**a**) Andreev levels for a 450 nm long contact with $Z = 0.5$, $r = 1.0$ (*solid lines*), $Z = 0.0$, $r = 0.44$ (*dash-dotted lines*), and $Z = 0.5$, $r = 0.44$. (*dashed lines*). (**b**) Discrete, continuous and total Josephson supercurrent for a 450 nm long junction with $Z = 0.5$ and $r = 0.44$

At finite temperature the occupation of the Andreev levels is not simply determined by a step-like distribution function but rather by a Fermi distribution function $f_0(E)$ broadened around $\mu$. As a consequence, Andreev levels above $\mu$ become occupied and levels below $\mu$ are partially emptied. In this case the supercurrent carried by the discrete bound states is given by

$$I_{\mathrm{dis}} = \sum_{n,\pm} \frac{2e}{\hbar} \frac{\mathrm{d}E_n^{\pm}(\phi)}{\mathrm{d}\phi} f_0[E_n^{\pm}(\phi)] \; . \tag{6.24}$$

The current contribution originating from the imbalance $i(E,\phi)$ in the electrical current per unit energy of the quasiparticles flowing in the continuum levels is given by

$$I_{\mathrm{cont}} = \frac{2e}{\hbar} \left( \int_{-\infty}^{-\Delta_0} + \int_{\Delta_0}^{\infty} \right) i(E,\phi) f_0(E) \, \mathrm{d}E \; . \tag{6.25}$$

For a short junction with a two energy levels, as described by (6.23), the temperature dependence of the supercurrent can be calculated easily:

$$\begin{aligned} I_{\mathrm{dis}} &= \frac{2e}{\hbar} \frac{\Delta_0 \sin\phi}{4\sqrt{(4Z^2+1)(\cos^2\phi/2 + 4Z^2)}} [f_0(E_{\mathrm{B}}^-) - f_0(E_{\mathrm{B}}^+)] \\ &= \frac{e\Delta_0}{\hbar} \frac{\sin\phi}{2\sqrt{(4Z^2+1)(\cos^2\phi/2 + 4Z^2)}} \tanh(E_{\mathrm{B}}^+/2k_{\mathrm{B}}T) \; . \end{aligned} \tag{6.26}$$

The current direction of the upper states at $E_{\mathrm{B}}^{+}$ is opposite to that for the lower state at $E_{\mathrm{B}}^{-}$. As the temperature is increased $E_{\mathrm{B}}^{+}$ is filled more and more, while $E_{\mathrm{B}}^{-}$ is emptied at the same time. As a result the net supercurrent decreases with temperature. For junctions with a finite length, an exponential decrease of $I_{\mathrm{c}}$ with temperature, $I_{\mathrm{c}} \propto \exp(2\pi L)$, is derived.

### 6.1.3 Supercurrent in a Junction with a Two-Dimensional Electron Gas

The one-dimensional model, as introduced above, can be used very successfully to elucidate the fundamental transport mechanisms in a superconductor/normal-conductor Josephson junction. However, the experimentally investigated junctions contain a normal conductor between the superconducting electrodes which is extended in two dimensions. This implies that electrons and holes in the two-dimensional channel impinge at various angles onto the interface with the superconductor. Only the component of the wave vector normal to the interface is relevant for the phase-coherent transport mechanisms described in the preceding section. Thus, at a given Fermi wave number, a complete spectrum of wave vector components normal to the interface has to be taken into account.

A model for a two-dimensional semiconducting channel between two superconducting electrodes was first introduced by Kresin [147]. An extension of this model, which includes $\delta$-shaped barriers at the S/2DEG interface and a potential step due to the Fermi velocity mismatch (see Fig. 6.3), was developed by Chrestin et al. [148]. Here, the confining potential of the two-dimensional channel was modeled by a triangular well [70]. This shape approximates the potential of an inversion layer at the surface of InAs or in a heterojunction. If a single subband is occupied in this quantum well, the current through the junction can be expressed by

$$\langle i \rangle = -\frac{e k_{\mathrm{B}} T}{\hbar} \sum_{\omega_n} \frac{1}{2\pi} \int_{-\infty}^{+\infty} \frac{\sin\phi}{(1/2)\cos\phi + f(k_y, \omega_n)} \mathrm{d}k_y \,, \tag{6.27}$$

where

$$\begin{aligned} f(k_y, \omega_n) \;=\; & \eta_1^{-} \mathrm{e}^{\mathrm{i}(k^{+}-k^{-})L} + \eta_1^{+} \mathrm{e}^{-\mathrm{i}(k^{+}-k^{-})L} \\ & -\eta_2^{-} \mathrm{e}^{\mathrm{i}(k^{+}+k^{-})L} - \eta_2^{+} \mathrm{e}^{-\mathrm{i}(k^{+}+k^{-})L} \,, \end{aligned} \tag{6.28}$$

$$\begin{aligned} \eta_1^{\pm} \;=\; & \frac{1}{16} \frac{\sigma^2 p^2}{k^{+}k^{-}} \left\{ \frac{\Omega_n}{\Delta_0} \left[ 1 + \left( 2Z \frac{k_{\mathrm{FS}}}{p} \right)^2 + \frac{k^{+}k^{-}}{\sigma^2 p^2} \right] \right. \\ & \left. \pm \left( \frac{\omega_n}{\Delta_0} \frac{k^{+}+k^{-}}{\sigma p} - 2\mathrm{i}Z \frac{k_{\mathrm{FS}}}{p} \frac{\Omega_n}{\Delta_0} \frac{k^{+}-k^{-}}{\sigma p} \right) \right\}^2 \end{aligned} \tag{6.29}$$

and

$$\eta_2^{\pm} = \frac{1}{16}\frac{\sigma^2 p^2}{k^+ k^-}\left\{\frac{\Omega_n}{\Delta_0}\left[1+\left(2Z\frac{k_{\mathrm{FS}}}{p}\right)^2-\frac{k^+k^-}{\sigma^2p^2}\right]\right. \pm\left(\frac{\omega_n}{\Delta_0}\frac{k^+-k^-}{\sigma p}-2\mathrm{i}Z\frac{k_{\mathrm{FS}}}{p}\frac{\Omega_n}{\Delta_0}\frac{k^++k^-}{\sigma p}\right)\Bigg\}^2 . \tag{6.30}$$

Here, $\sigma$ is defined as $m^*/m_{\mathrm{e}}$ and $p=(k_{\mathrm{FS}}^2-k_y^2)^{1/2}$ is the wave vector in the superconductor perpendicular to the interface. $\Omega_n$ is given by $\sqrt{\omega_n^2+\Delta_0^2}$, where $\omega_n=(2n+1)\pi k_{\mathrm{B}}T$ are the Matsubara frequencies. The wave vector $k^{\pm}$ within the semiconductor is

$$k^{\pm}=\sqrt{k_{\mathrm{FN}}^2-k_y^2\pm\mathrm{i}\frac{2m^*}{\hbar^2}\omega_n}\,, \tag{6.31}$$

where $k_{\mathrm{FN}}=\sqrt{(2m^*/\hbar^2)(\mu-U_0-E_0)}$ is the Fermi wave vector in the semiconductor. $E_0$ is the energy level of the first subband in the 2DEG and $U_0$ is the conduction band offset between the superconductor and the semiconductor.

As we shall see in Sect. 6.2.1, the model of Chrestin et al. [148] can be employed to explain the temperature dependence of the critical current. In addition, this model is of interest if the characteristics of junctions with a gate on top of the two-dimensional electron gas are to be described. By applying a gate voltage, the carrier density $n_{2\mathrm{D}}$ in the channel can be adjusted. This directly affects the Fermi wave vector as given by (3.7) in (6.31) and therefore also the critical current. If the carrier concentration is increased, the critical current is on the average increased, if superimposed oscillations due to resonances are neglected [148].

The coherent transport of an SNS structure including a $\delta$ barrier at both interfaces was also discussed in the clean limit by Brinkman and Golubov [154]. The authors could show that for a thin normal layer, the junction is in the coherent regime, where the supercurrent is proportional to the angle-averaged transmission probability. This is expected for a thin interlayer (N), where the transmission resonances are broad. In contrast, for a wide interlayer the supercurrent was found to be proportional to the square of the angle-averaged transmission probability. This can be explained by sequential, incoherent tunneling through the two $\delta$ barriers. The results given by Brinkman and Golubov [154] were obtained for a three-dimensional structure but they can also easily applied to the two-dimensional case.

### 6.1.4 Supercurrent in a Junction with Proximity Layers

In Sect. 5.1.4 it was shown that a proximity layer (N) between the superconductor and a constriction (c) in a junction leads to additional features in the subharmonic gap structures. For the interpretation of the measured current–voltage characteristics of some particular superconducting junctions,

it is necessary to include a proximity layer between the superconductor and the 2DEG. Those models which are able to describe this situation usually consider the two-dimensional electron gas as a constriction. This is justified by the large difference in the number of states between the three-dimensional superconductor and the two-dimensional electron gas.

A superconducting junction with two superconducting electrodes connected by a constriction (ScS) was first discussed by Kulik and Omel'yanchuk (KO model) [152, 155]. The more general case with two different superconductors (ScS′), was considered by Zaitsev [50]. On the basis on this theory, Golubov and Kupriyanov succeeded in obtaining an expression for the supercurrent in an SNcNS junction with a constriction shorter than $\xi_N$ [156]. The Green's functions suitable for this problem have already been introduced in Sect. 2.2.3. Inserting these functions into the Zaitsev equation yields the following expression for the supercurrent:

$$I(\phi) = \frac{2\pi k_B T}{eR_N} \sum_{n=0}^{\infty} \frac{\Phi^2(\omega_n)\sin\phi}{\omega_n^2 + (1 - D\sin^2\phi/2)\Phi^2(\omega_n)} \,. \tag{6.32}$$

The function $\Phi$ is defined as $\Phi(\omega_n) = \Delta/[1 + (\Delta^2 + \omega_n^2)^{1/2}\gamma_B/\pi k_B T_c]$. $D$ is the normal transmission probability of the constriction and $\gamma_B$ represents the influence of the SN interface transparency as defined by (2.29).

In Fig. 6.7, the temperature dependence of $eI_cR_N/\pi T_c$ is shown for different values of the barrier strength at the SN boundary, $\gamma_B$, and of the suppression parameter $\gamma$ [156]. The temperature dependence is plotted in terms of the product $I_cR_N$, normalized to the critical temperature $T_c$. This $I_cR_N$ product, also referred to as the characteristic voltage $V_c$, is a measure of the superconducting coupling strength. The maximum value of $\approx 1.76$ is obtained for the ideal case of a ballistic ScS junction (KO model) [152], this is twice the value obtained for an ideal superconducting tunnel junction [153]. As can be seen in Fig. 6.7, the critical current is lowered if a proximity layer is introduced between the constriction and the superconductor. Furthermore, the shape of the curve changes from convex to concave as the superconducting electrodes are increasingly decoupled.

## 6.2 Measurements of the Superconductive State

In the following part of the chapter, experimental results on superconductor/two-dimensional-electron-gas Josephson junctions are discussed. First the $I$–$V$ characteristics are analyzed in detail. Subsequently, further properties, e.g. interference effects due to a magnetic field, which depend on the phase coherence are covered. The last part deals with the light sensitivity of the semiconducting material. As we shall see, this effect can be employed to control the critical current in the junction.

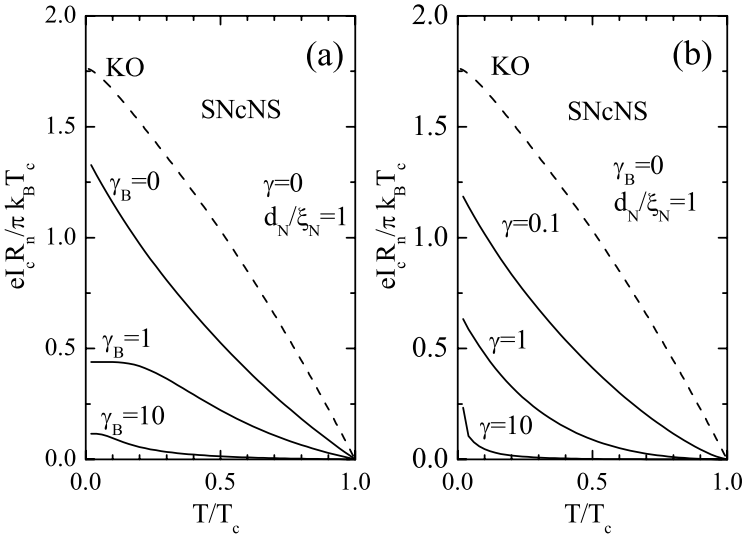


**Fig. 6.7.** Normalized critical current $eI_cR_N/\pi T_c$ of an SNcNS junction as a function of $T/T_c$ with $\gamma_B$ (**a**) and $\gamma$ (**b**) varied as a parameter [156]. The characteristics of an ScS junction obtained from the Kulik–Omel'yanchuk model are also shown (KO) for comparison [152]

### 6.2.1 Current–Voltage Characteristics

One of the basic methods to characterize a superconductor/two-dimensional-electron-gas junction is the measurement of the current–voltage characteristic. From these measurements, information on the junction properties can be obtained. Let us begin with a typical $I$–$V$ characteristic of a Nb/p-InAs step edge junction, as shown in Fig. 6.8 [140]. It can be clearly seen that a Josephson supercurrent flows through the junction with a maximum value of $I_c = 220$ μA. In contrast to Josephson tunnel junctions, the current–voltage characteristic is ohmic, which means linear, in the voltage-carrying state. At voltages above $2\Delta_0/e$ a normal-state resistance $R_N$ of 4.5 Ω is measured, which results in a characteristic voltage $V_c = I_cR_N$ of 990 μV. Compared with the earlier results on Nb/p-InAs junctions [8, 30, 92] the $I_cR_N$ product obtained here is larger by almost one order of magnitude and thus is relatively close to the maximum value $(4/\pi)e\Delta_0$ given by theory [152]. This improvement can be attributed to the optimized cleaning procedure prior to the deposition of the Nb electrode. An even larger $I_cR_N$ product of 1.35 meV at $T = 2$ K was obtained for an Nb/p-InAs junction fabricated by anodic oxidation, with a layout as shown in Fig. 3.5b [29]. The corresponding critical current has a value of 870 μA. The very large $I_cR_N$ product can be attributed to the small distance of only 20 nm between the Nb electrodes and the refined $Ar^+$ sputter cleaning. The latter leads to an improved cou-

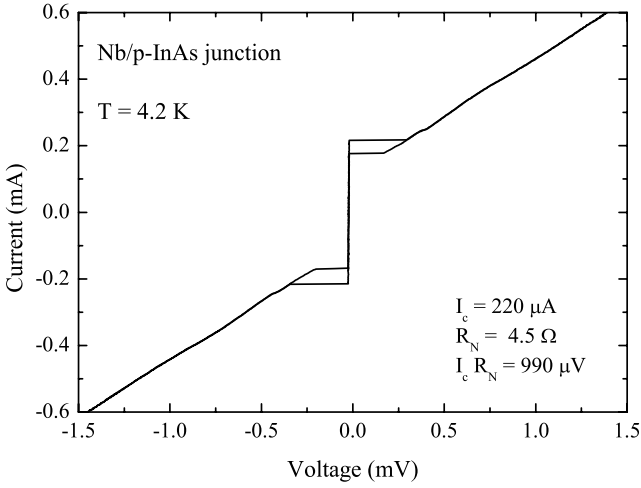


**Fig. 6.8.** Current–voltage characteristic of a 30 µm wide Nb/p-InAs step junction at a temperature of 4.2 K. The step height was ≈ 140 nm. The geometry of the junction is depicted in Fig. 3.5a [140]

pling of the superconductor to the two-dimensional channel at the surface. In Fig. 6.9, the temperature dependence of the critical current is plotted for a 20 nm and a 40 nm long junction. In order to explain the decrease of $I_c$ with temperature, the model for an SNcNS junction, as introduced in Sect. 6.1.4, can be referred to. The reason for doing so is that the two-dimensional channel underneath the Nb electrodes can be regarded as a diffusive normal conductor N, which serves as the proximity layer within this model. The assumption that this layer is indeed diffusive can be justified by the generation of defects due to the $Ar^+$ sputter cleaning prior to the deposition of the Nb electrodes. Owing to the proximity effect, a gap is induced in these N layers. The two-dimensional electron gas, serving as a bridge between the N layers covered by the Nb electrodes, is regarded here as the constriction. As can be seen in Fig. 6.9, the temperature dependence of the critical current can be very well explained by the SNcNS model, if a finite barrier between the superconducting electrodes and the 2DEG underneath ($\gamma_B > 0$) and a reduced transparency of the constriction ($D < 1$) are assumed [29].

The current–voltage characteristic of a typical junction with a buried two-dimensional electron gas in a strained InGaAs/InP heterojunction is plotted in Fig. 6.10. The junction has a length of 450 nm and a width of 6 µm (sample B in Table 6.1). At 0.3 K a critical current $I_c$ of 3.8 µA is obtained. For bias voltages larger than 3 mV, a normal-state resistance $R_N$ of 50 Ω is measured, which results in a characteristic voltage $V_c = I_c R_N$ of 190 µV.

At low temperatures ($\leq 1.3$ K) the $I$–$V$ characteristic shows a pronounced hysteresis. For sample B the return current $I_r$, which is the current where the

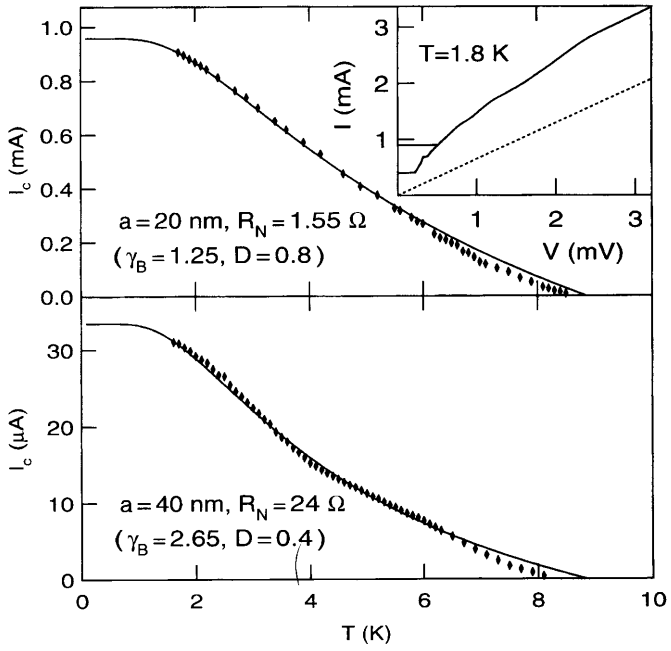


**Fig. 6.9.** Critical current as a function of temperature for a 20 nm and a 40 nm long planar Nb/p-InAs junction. The experimental values are compared with theoretical results (*solid line*) for the values of $T_c$ and $R_N$ given in the graph. The *inset* shows the $I$–$V$ characteristic of a 20 nm long junction at 1.8 K (*solid line*) and the ohmic line corresponding to $R_N = 1.55\ \Omega$ (*dotted line*). The hysteresis can be explained by the capacitance caused by the overlapping parts of the electrodes [29]

junction switches back from the normal-conducting to the superconducting state, is 2.4 μA (Fig. 6.10). In order to detect the hysteresis without any distortion, extensive filtering is required [38, 157]. Here, $\pi$ and $RC$ filters were used at 300 K and 4.2 K, respectively. Additional filtering was obtained from by Thermocoax Philips cables directly connected to the sample at low temperature [158].

In Table 6.1, $I_c$, $R_N$ and $V_c$ are given for a set of junctions with different geometries. Since the characteristic voltage is a measure of the superconducting coupling strength, it is reduced if a barrier is present at the S/2DEG interface or if the separation of the superconducting electrodes is enlarged. The latter effect can be observed here. For the larger separations, 600 nm (sample E) and 800 nm (sample F), the characteristic voltages are 139 μV and 112 μV, respectively, which are lower than the values obtained for the 450 nm long junctions. However, it can be seen in Table 6.1 that $V_c$ varies among the 450 nm long junctions. This is due to the fact that the average value of the transparency, as well as the transparency, along a particular S/2DEG interface, can vary. The characteristic voltages of the junctions discussed here

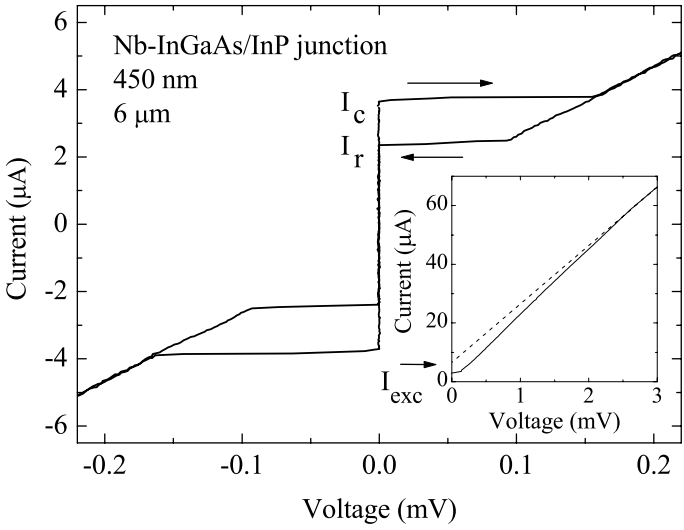


**Fig. 6.10.** Current–voltage characteristic of a 450 nm long, 6 µm wide Nb–InGaAs/InP junction at a temperature of 0.3 K. The upward and downward branches are marked by *arrows*. The *inset* shows the *I–V* characteristic for larger voltages. The excess current $I_{\mathrm{exc}}$ is obtained by a linear extrapolation (*dashed line*) [157]

**Table 6.1.** Characteristic data for a set of Nb–InGaAs/InP–Nb junctions with different geometries

| Sample | Length (nm) | Width (µm) | Nb electrode separation (nm) | $I_c$ (µA) | $R_N$ (Ω) | $I_cR_N$ (µV) |
|---|---|---|---|---|---|---|
| A | 300 | 6 | 300 | 3.3 | 43 | 142 |
| B | 450 | 6 | 350 | 3.8 | 50 | 190 |
| C | 450 | 6 | 450 | 2.7 | 69 | 186 |
| D | 450 | 16 | 350 | 13.0 | 20 | 260 |
| E | 600 | 8 | 400 | 4.1 | 34 | 139 |
| F | 800 | 8 | 600 | 3.4 | 33 | 112 |

are of the same order of magnitude as $V_c$ of comparable junctions with a heterostructure quantum well as the conductive channel [37, 38, 98].

In Fig. 6.11, the normalized critical current $I_c/I_{c0}$ and the normalized return current $I_r/I_{r0}$ of samples B and C are plotted as a function of temperature. $I_{c0}$ and $I_{r0}$ are the critical current and return current, respectively,

at 0.3 K. Although the absolute values of $I_c$ and $I_r$ differ for the two samples, the temperature dependence is almost identical. It can be seen that the critical current increases with decreasing temperature. However, at very low temperatures ($\leq$ 0.6 K) $I_c$ tends to saturate. The $I$–$V$ characteristic is hysteretic for temperatures below 1.3 K so that the junction returns to the resistive state at a lower current $I_r$ than the critical current. It is interesting to notice that $I_r/I_{r0}$ remains almost constant with temperature.

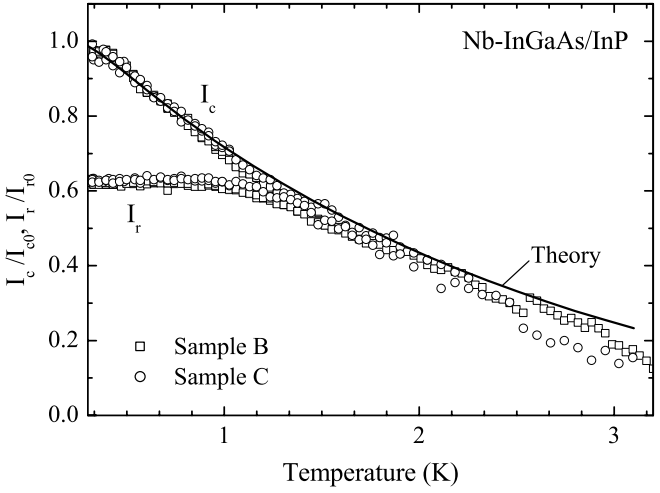


**Fig. 6.11.** Normalized critical current $I_c/I_{c0}$ and normalized return current $I_r/I_{r0}$ [157] as a function of temperature for samples B and C. The *solid line* shows the theoretical results obtained from the model of Chrestin et al. [148]

In order to explain the experimentally measured temperature dependence of $I_c$, the model of Chrestin et al. [148], as introduced in Sect. 6.1.3, can be used. The calculated critical current as a function of temperature is plotted in Fig. 6.11. For temperatures below $\approx$ 2.4 K, very good agreement with the experimentally determined critical current is obtained if a $Z$ parameter of 1.0 is assumed. For larger temperatures a minor deviation develops, which can be explained by uncertainties in the experimental determination of $I_c$ due to the thermal smearing of the $I$–$V$ characteristics. The $Z$ parameter was estimated from the normalized excess current $eI_{exc}R_N/\Delta_0$, following the approach introduced by Flensberg et al. [132]. For the sheet electron concentration, which determines the Fermi wave vector in the 2DEG, a value of $7.05 \times 10^{11}$ cm$^{-2}$ was assumed.

From the saturation of $I_c$ at low temperatures, the transport mechanism in the junction can be classified. In Sect. 6.1.2 the spectrum of the Andreev levels was calculated for an SNS structure which contains a barrier at the

interface and a potential step in the normal-conducting region. As a consequence, the degeneracy of the Andreev levels at the chemical potential is lifted and a gap is formed instead. At very low temperatures only the Andreev levels below the chemical potential are occupied, so that the critical current remains constant. Only if the temperature is raised to a value where Andreev levels above $\mu$ are thermally occupied will $I_c$ start to decrease with increasing temperature. The $I_c$ vs. $T$ characteristic discussed here shows exactly the behavior described above. It can thus be concluded that an energy gap is present in the Andreev level spectrum. A similar characteristic was also observed by Takayanagi and Akazaki [159]. In contrast, Mur et al. [38] found no saturation in the $I_c$ vs. $T$ measurements but rather an exponential law, $I_c(T) = I_c(0)\exp(-T/T_0)$, that match the experimental values. They attributed their finding to transport through a few resonant transport channels induced by disorder with almost ideal transmission probability [160, 161]. Although their semiconductor material is similar to the InGaAs/InP heterostructure discussed here, the technique of making contact between the Nb electrodes and the 2DEG differs substantially. In Mur et al.'s junctions the channel layer is contacted from the top, which might lead to contacts with a higher transmission probability owing to multiple Andreev reflections within the 2DEG channel layer.

### 6.2.2 Effect of a Magnetic Field

By means of $I_c$ measurements as a function of an external magnetic field $B$, more detailed information about the supercurrent transport in the junction may be gained. Owing to the effect of the magnetic flux penetrating the junction, an interference pattern develops in the critical current. For the simplest case, with a short junction, a regular Fraunhofer-like interference pattern is expected for a homogeneous supercurrent distribution [162, 163]:

$$I_c = I_{c0}\frac{\sin(\pi\Phi/\Phi_0)}{\pi\Phi/\Phi_0}\ . \tag{6.33}$$

Here, $I_{c0}$ is the critical current at zero magnetic field, $\Phi$ is the effective magnetic flux in the junction and $\Phi_0 = h/2e$ is the magnetic flux quantum. As can be seen in Fig. 6.12a, the assumption of such a constant supercurrent distribution for the simulation fits the $I_c$ vs. $B$ interference pattern of a 450 nm long, 6 µm wide Nb–InGaAs/InP junction (sample B, see Table 6.1) almost ideally.

For a 450 nm long, 16 µm wide junction (sample D), a step-shaped current density distribution (Fig. 6.12b, inset) has been assumed in order to explain the more complex measured interference pattern. As mentioned above, the variation in the current distribution is presumably due to an inhomogeneous interface. The experimental curve can be fitted reasonably by using the following expression [162]:

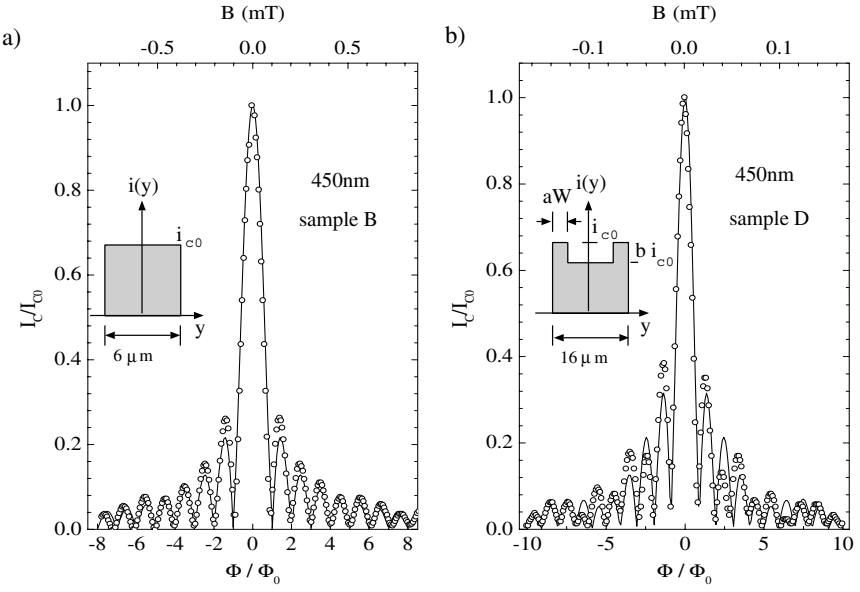


**Fig. 6.12.** $I_c$ at 0.5 K as a function of $B$ for samples B (**a**) and D (**b**) (○). The geometry of both samples is given in Table 6.1. The *full line* shows a fit as a function of $\Phi/\Phi_0$ using a current density distribution as depicted in the corresponding *insets*

$$I_c(\Phi/\Phi_0) = I_{c0}\frac{2a}{b-2ab+2a}\left|\frac{b-2ab}{2a}\frac{\sin[\pi(1-2a)\Phi/\Phi_0]}{[\pi(1-2a)\Phi/\Phi_0]} + \frac{\sin(\pi a\Phi/\Phi_0)}{\pi a\Phi/\Phi_0}\cos[\pi(1-a)\Phi/\Phi_0]\right| . \quad (6.34)$$

Here, the outer parts of width $aW$ carry the current density $i_{c0}$, whereas the inner part of width $(1-2a)W$ carries the current density $bi_{c0}$; $W$ is the total width of the sample. For junction D, a larger supercurrent density at both ends of the junction, expressed by the parameters $a = 0.2$ and $b = 0.62$, was assumed (Table 6.2). Considering the simplicity of the underlying model, the agreement is relatively good. In Table 6.2 the fitting parameters of two other samples, C and E, are summarized, in addition. As can be seen here, the current density $i_{c0}$ of junction D is considerably lower than for the 450 nm long sample. This can be explained by the smaller slope of the Andreev levels if the electrode separation is increased (see Sect. 6.1.2). According to (6.20), the Josephson current is determined partially by the slope of the Andreev levels as a function of $\phi$.

Because of the planar geometry of the junctions, the external magnetic field is focused into the semiconductor area owing to the shielding of the superconducting electrodes. Experimentally, the focusing factors $(B_{\text{eff}}/B)_{\text{exp}}$ were obtained by matching the minima of the measured interference pattern

**Table 6.2.** Results of the measurements in a magnetic field; $a$ and $b$ are the fitting parameters in (6.34) and $a = 0$ means that a homogeneous current distribution is present. $(B_{\text{eff}}/B)_{\text{exp}}$ and $(B_{\text{eff}}/B)_{\text{theo}}$ are the experimentally determined and theoretical focusing factors, respectively, of the magnetic field

| Sample | $a$ | $b$ | $i_{c0}$ (μA) | $\left(\frac{B_{\text{eff}}}{B}\right)_{\text{exp}}$ | $\left(\frac{B_{\text{eff}}}{B}\right)_{\text{theo}}$ |
|---|---|---|---|---|---|
| B | 0 | 1 | 80 | 7.05 | 8.55 |
| C | 0.23 | 0.3 | 62 | 6.66 | 8.55 |
| D | 0.20 | 0.62 | 82 | 16.85 | 16.44 |
| E | 0 | 1 | 44 | 8.27 | 8.21 |

with the corresponding multiples of $\Phi_0$. For the calculation of the effective magnetic field $B_{\text{eff}}$, the London penetration depth ($\approx$ 20 nm) was taken into account for the area penetrated by the magnetic field. A comparison of theoretically determined focusing factors $(B_{\text{eff}}/B_0)_{\text{theo}}$, calculated from an expression given by Gu et al. [164], shows good agreement with the experimentally obtained values (Table 6.2).

The magnetic field dependence of $I_c$ of Nb–InAs/AlSb junctions with a width $W$ comparable to the length $L$ has been investigated by Heida et al. [87]. These authors observed a large deviation from the $\Phi_0$ periodicity (6.33) and interpreted their results in terms of mesoscopic phase effects. In contrast to tunnel junctions or junctions with $L \ll W$, here all trajectories from one electrode (the left electrode in Fig. 6.13) to the opposite one have to be considered, rather than only the trajectories perpendicular to the interface ($x_1 \rightarrow x_2$ in Fig. 6.13) as in the case of a short junction or a tunnel junction. In a heuristic approach using a quasiclassical description, the following

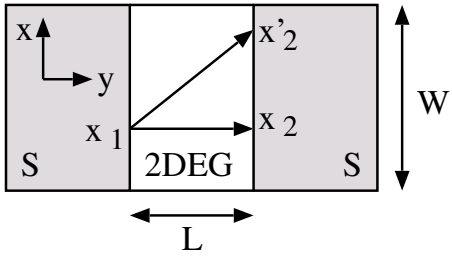


**Fig. 6.13.** Josephson junction with a width $W$ comparable to its length $L$. The supercurrent can flow from $x_1$ to any $x_2$ at the right electrode [87] (© (1998) by the American Physical Society)

expression was derived for the magnetic-field dependence of $I_c$ by averaging over all possible trajectories [87]:

$$I_c = I_{c0} \left( \frac{\sin(\pi\Phi/2\Phi_0)}{\pi\Phi/2\Phi_0} \right)^2 . \tag{6.35}$$

As can be inferred from this equation, a periodicity of $2\Phi_0$ is expected in this case, in contrast to the $\Phi_0$ periodicity of junctions with $L \ll W$. A period of $2\Phi_0$ was indeed experimentally observed for junctions where $L$ is comparable to $W$ [87].

### 6.2.3 Hysteresis

The $I$–$V$ characteristic plotted in Fig. 6.10 reveals that for low temperatures a hysteresis occurs. Furthermore, the temperature-dependent measurements show that the return current $I_r$ is almost constant for $T \leq 1.0$ K. The hysteresis originates from a negative differential conductance at low bias voltages. If an ohmic shunt resistor $R_s = 6.8\ \Omega$ [Fig. 6.14 (inset)] is connected to the junction, the range of negative conductance can be resolved. Apart from this shunt resistor, the contact resistances (10 Ω each) must also be taken into account, since $R_s$ is not directly connected to the junction but rather is fixed to the bond pads. The value of the resistance $R_s$ was chosen sufficiently low that a positive differential conductance was obtained for the complete circuit. The corrected $I$–$V$ characteristics, measured on the shunted junction (sample B) for various temperatures, are shown in Fig. 6.14 [165]. Here, a slightly larger critical current of 4.1 μA was measured, which can be attributed to changes due to the multiple thermal cycles the sample had to undergo before this measurement. Up to a temperature of 1.3 K a negative differential conductance is observed.

In contrast to Josephson tunnel junctions, the hysteresis cannot be explained by a shunt capacitance within the "resistively capacitively shunted junction" (RCSJ) model [162, 166, 167]. An estimation of the junction capacitance shows that it is two orders of magnitude smaller than the capacitance necessary to explain the hysteresis within the RCSJ model. In addition, $I_r$ is constant for temperatures $T \leq 1.0$, in contradiction to the predictions of the RCSJ model. For this type of junction the occurrence of the hysteresis can be explained by an effective heating of the electrons in the 2DEG, as pointed out by Heida [168]. This heating effect originates from a broadening of the electron distribution function in the 2DEG due to multiple Andreev reflections in the voltage-biased regime. The broadening of the distribution function can be seen, for example, in simulations using the OTBK model when compared with the corresponding equilibrium Fermi distribution function, as described in detail in Sect. 5.1.3. Following the approach discussed in Sect. 6.1, the resulting supercurrent in an S/2DEG/S junction is determined by the occupation of discrete and continuous Andreev levels. In the

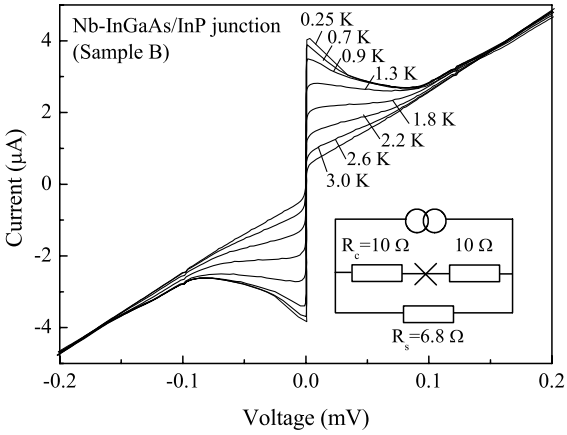


**Fig. 6.14.** Current–voltage characteristics measured at various temperatures. The *inset* shows the circuit with the shunt resistor $R_s$ and the contact resistances $R_c$ [165]

case of the discrete levels the corresponding part of the net Josephson current is provided by levels carrying a supercurrent alternately in the forward and the reverse direction. A broadening of the distribution function leads to occupation of formerly unoccupied discrete states and thus the maximum obtainable supercurrent is reduced to $I_r$. In the nonshunted case the $I$–$V$ characteristic switches back into the superconductive state at a current $I_r$, which corresponds to the critical current at this effective temperature. It is interesting to notice that the effective heating is relatively independent of the bath temperature, since the minimum in the $I$–$V$ characteristic, as shown in Fig. 6.14, is found at the same current for various temperatures.

In principle a negative differential conductance can also result from the conductance enhancement due to multiple Andreev reflections, as described within the KGN model [124]. For a decreasing bias voltage, more and more Andreev reflection processes occur. Since each Andreev reflection event increases the conductance, an increase of the total current and thus a negative differential conductance may be predicted for decreasing voltage. However, in order to obtain a noticeable conductance enhancement the interface transparency needs to be sufficiently large. This is in contradiction to our finding that a relatively large $Z$ parameter of about 1.0 had to be assumed in order to describe the temperature dependence of $I_c$. A further indication that the measured negative differential conductance cannot be explained adequately within the KGN model is given by measurements in a magnetic field (Fig. 6.15). A small magnetic field of 0.19 mT is sufficient to suppress the negative differential conductance completely. This is not expected in the KGN model, since here the transport is described by the nonphase-coherent motion

of Gaussian wave packets, which should be insensitive to a small magnetic field.

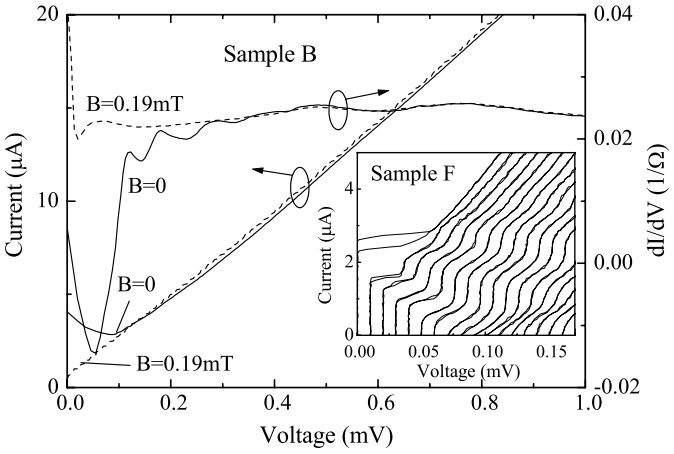


**Fig. 6.15.** Current and differential conductance of sample B as a function of voltage for $B = 0$ (*solid lines*) and $B = 0.19$ mT (*dashed lines*) [165]. The *inset* shows the Shapiro steps of an 800 nm long junction (sample F) for 12.7 GHz radiation at 0.7 K. The radiation power was increased step by step from an attenuation of −15.7 dB to −11.3 dB

### 6.2.4 Self-Detection of Josephson Radiation

A closer inspection of the differential conductance plotted in Fig. 6.15 shows that for $B = 0$, modulations are superimposed on the $\mathrm{d}I/\mathrm{d}V$ curve. From the absence of these modulations at $B = 0.19$ mT, it can be directly concluded that these features are not due to subharmonic gap structures. A more likely explanation is that these oscillations are due to the AC Josephson effect. This conclusion is supported by the measurement depicted in Fig. 6.16a.

At zero magnetic field the differential conductance shows peaks at 140 μV and at 230 μV, indicated by the concentric contour lines. If the magnetic field is increased these maxima vanish at first and then reappear at a field of 0.12 mT. In particular, at a fixed voltage of 140 μV the differential conductance oscillates periodically with the magnetic field. The plot of $\mathrm{d}V/\mathrm{d}I$ as a function of $B$ and $I$ (Fig. 6.16b) reveals that the structures are connected to the Josephson effect since they are only observable if the $I_\mathrm{c}(B)$ Fraunhofer pattern has a local maximum. The superconducting state corresponds in this plot to the black area, where $\mathrm{d}V/\mathrm{d}I = 0$.

A possible physical origin of the structures in the $\mathrm{d}I/\mathrm{d}V$ curves is a self-detection of Josephson radiation. Similarly to the coupling of an

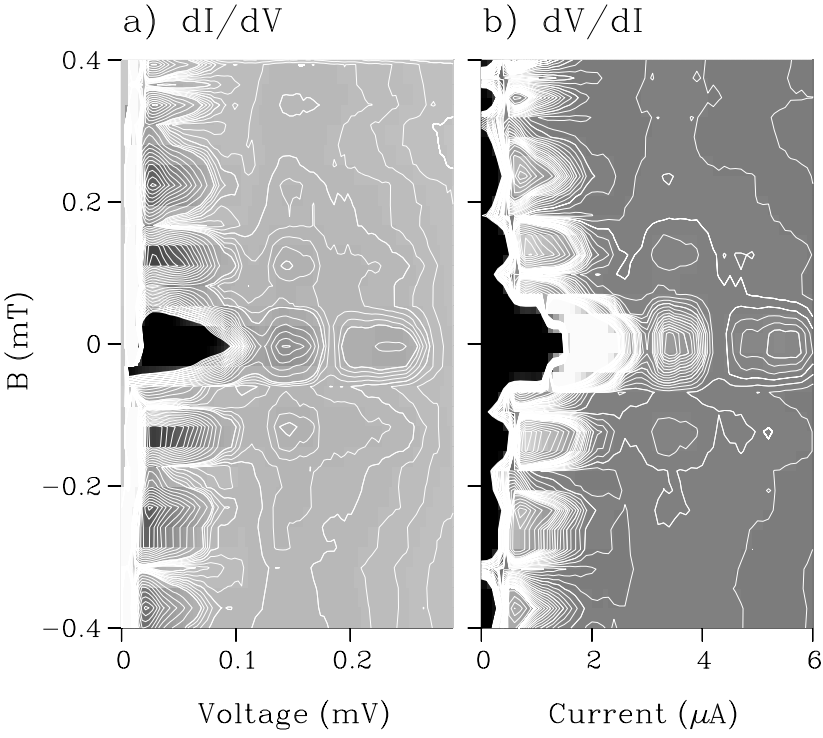


**Fig. 6.16.** (**a**) Differential conductance of sample B as a function of the applied voltage and the magnetic field [165]. The contour lines trace constant values of $\mathrm{d}I/\mathrm{d}V$, while the absolute value is represented by a gray scale. In (**b**) the differential resistance $\mathrm{d}V/\mathrm{d}I$ is plotted as a function of current and magnetic field. The *black area*, which represents a supercurrent, is identical to the Fraunhofer interference pattern

Nb/2DEG/Nb junction to an external microwave radiation, as shown by an example in Fig. 6.15 (inset), the junction can also couple resonantly to its own AC Josephson radiation [168]. From the $\mathrm{d}I/\mathrm{d}V$ plot for $B = 0$ in Fig. 6.15, a peak separation of about 90 μV can be extracted, which results in a frequency of $f = 2eV/h = 43.5$ GHz.

### 6.2.5 Light Exposure

A unique property of superconductor/semiconductor junctions is that $I_\mathrm{c}$ and $R_\mathrm{N}$ can be controlled by light exposure. The first measurements using this concept go back to the work of Giaever [169] and Andreozzi et al. [170], who studied junctions based on a CdS light-sensitive interlayer. Another normal-conductive material, which has also proved its suitability for light-sensitive weak-link junctions, is $\mathrm{Pb}_{1-x}\mathrm{Sn}_x\mathrm{Te}$ [171]. In many III–V semiconductor het-

erostructures a persistent photoconductance is observed at low temperatures [172, 173]. Persistent photoconductance means that the photogenerated carriers remain in the channel layer even after the light source is switched off.

The increase of $I_c$ relative to the initial value $I_{c0}$ of an Nb–InGaAs/InP junction after light exposure is shown in Fig. 6.17a. Here, a red (665 nm) GaAs light-emitting diode (LED) operating at room temperature was used as a light source, with a plastic fiber guiding the light down to the sample [174]. In order to increase the carrier concentration in the 2DEG stepwise, the LED was operated in a single-pulse mode with a pulse duration of 5 ms. The initial critical current $I_{c0}$ of the 300 nm long, 6 µm wide junction was 3.7 µA. First, the normalized critical current $I_c/I_{c0}$ increases very steeply for up to 15 light pulses. However, further exposure leads to a slower increase of $I_c/I_{c0}$ to a final relative increase of 12% after 90 accumulated light pulses. The critical current can be reset to its initial value by increasing the temperature above 100 K.

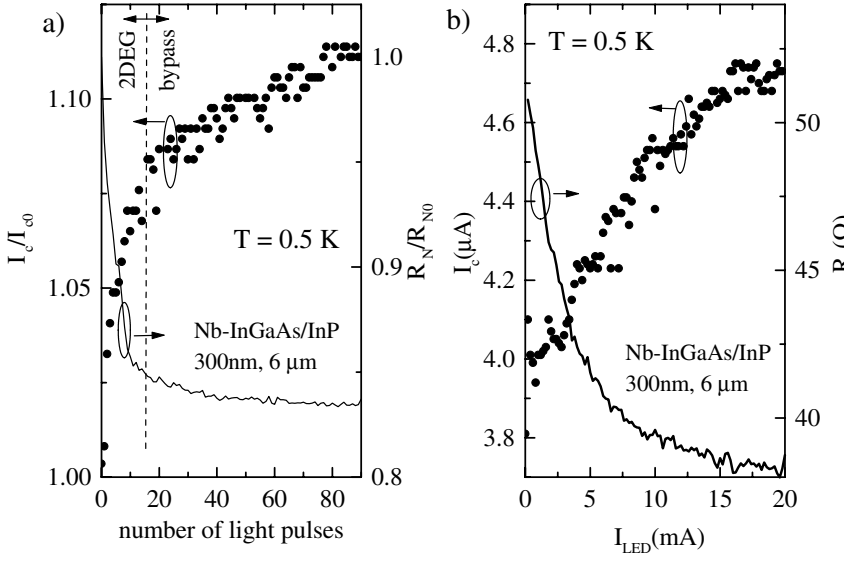


**Fig. 6.17.** (**a**) Relative increase of the critical current $I_c/I_{c0}$ and the normal-state resistance $R_N/R_{N0}$ of a 300 nm long, 6 µm wide Nb–InGaAs/InP junction as a function of the number of light pulses. (**b**) Critical current $I_c$ and normal-state resistance $R_N$ as a function of the LED bias current [174]

At the same time as the critical current increases, the normal-state resistance $R_N$ decreases with light exposure, as can be seen in Fig. 6.17a. Again the largest effect is measured for the first 15 pulses, while further light pulses lead to a slower decrease of $R_N$. A relative decrease of about 16% was observed after 90 pulses.

In order to relate the increase of $I_c$ and the decrease of $R_N$ to the properties of the two-dimensional channel layer, Shubnikov–de Haas measurements on Hall bars were performed under pulsed illumination. Since for these measurements at high magnetic fields a different sample holder had to be used, the dose per light pulse was different in this case. However, Shubnikov–de Haas effect measurements allowed us to determine the sheet electron concentration $n_{2D}$ and, at the same time, the sheet resistance $\varrho_{2D}$ at zero magnetic field as a function of the number of light pulses (Fig. 6.18). The sheet electron concentration increases from an initial value of $7.35 \times 10^{11}$ cm$^{-2}$ to a value of $8.45 \times 10^{11}$ cm$^{-2}$ after four light pulses. A further illumination does not change the sheet carrier concentration in the 2DEG. As can be seen in Fig. 6.18 (inset), a conductive bypass channel appears, indicated by the parabolic increase of the curve measured after seven light pulses. For less than four light pulses, no bypass channel was observed.

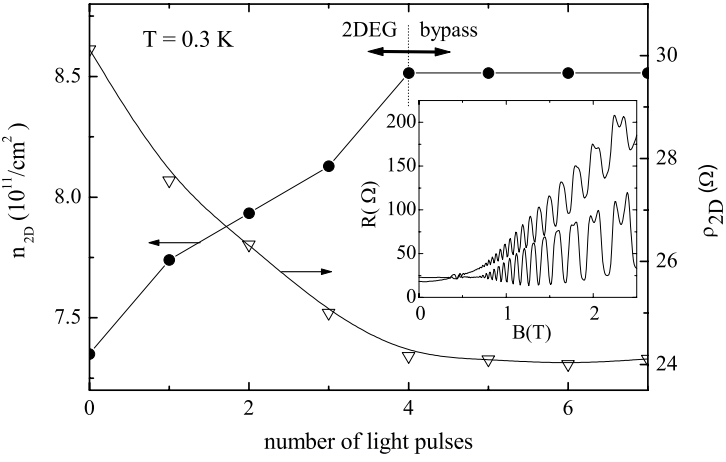


**Fig. 6.18.** Sheet electron concentration $n_{2D}$ (•) and specific sheet resistance $\varrho_{2D}$ ($\triangledown$) as a function of the number of light pulses. The measurement was performed at 0.3 K. In the *inset* the Shubnikov–de Haas oscillations are plotted before illumination (*lower curve*) and after seven light pulses (*upper curve*) [174]

The photogenerated carriers are due to an excitation across the band gap of InP, as found by Kane et al. [175], from the wavelength dependence of the persistent photoconductance. Electrons and holes are separated by the built-in electric field of the heterojunction. According to Kane et al. [175], the holes are trapped in the InP buffer layer. Up to a certain light dose the electrons are collected in the quantum well, whereas for even higher doses the electrons are found in the InP dopant layer. The latter effect is responsible

for the bypass channel. The sheet resistance $\varrho_{2D}$ plotted in Fig. 6.18 first shows a steeper decrease, followed by a saturation in accordance with the measurement of $R_N$ in Fig. 6.17a. By matching the measured drop of $\varrho_{2D}$ to the drop of the normal-state resistance $R_N$ of the junctions, it is now possible to gain information about the corresponding sheet electron concentration in the junction.

As mentioned above, the intensity of the light pulses was different for the measurements on the Hall bars and on the Josephson junctions. However, it is possible to match the measured drop of the normal-state resistance $R_N$ with that of the specific resistance $\varrho_{2D}$ by rescaling the intensity of the light pulses. By this method, information about the electron concentration $n_{2D}$ in the junction can be gained.

Referring to a simple picture, the increase of the critical current with increasing carrier concentration can be understood from the increase of the coherence length $\xi_N = \hbar v_F/(2\pi k_B T)$. If the number of carriers in the channel is increased, the Fermi velocity $v_F = \hbar\sqrt{2\pi n_{2D}}/m^*$ is increased, leading to a larger value of $\xi_N$. For a more detailed analysis, the model of Chrestin et al. [148] can be used (Sect. 6.1.3). However, owing to interference effects, the calculated critical current has an oscillating component as $n_{2D}$ is increased [27]. No clear indication for this oscillation is seen in the measurements, presumably because of fluctuations of the effective Nb electrode separation along the junction. Neglecting the oscillatory part of $I_c$ in the model, an increase of about 21% was estimated for a 300 nm wide junction when the carrier concentration was increased from $7.35 \times 10^{11}$ cm$^{-2}$ to $8.45 \times 10^{11}$ cm$^{-2}$. For the calculations, a $Z$ parameter of 1.0 was assumed in accordance with the simulations presented in Sect. 6.2.1. A possible explanation for this discrepancy in the increase of the critical current might be that a part of the 2DEG channel is covered by the superconducting electrodes so that the interface region is shadowed. The separation of the Nb electrodes is smaller than the distance $L$ between the Nb/2DEG interfaces. Therefore, fewer photogenerated carriers are present in this covered area. While the steep increase of the critical current can be explained by additional carriers in the channel layer, the bypass channel observed in the Shubnikov–de Haas measurements for more than four pulses is presumably responsible for the slower increase of $I_c/I_{c0}$.

The critical current can also be controlled by a continuous illumination, as shown in Fig. 6.17. Starting at an initial value of $I_c = 3.8$ μA, the critical current is increased by 24% to a final value of 4.7 μA. Similarly to the experiments with the pulsed light source, the normal-state resistance decreases. Since a conductive bypass channel is already observed after a few light pulses, the carriers excited under continuous light exposure will probably also be located in a bypass channel. The mechanism leading to a change of the critical current under continuous light exposure can in principle be used as a light-sensitive switch [174].

In an InGaAs/InP heterostructure, the carrier concentration can only be increased, not decreased, by illumination. If a GaSb/AlSb/InAs heterostructure is used as a two-dimensional electron gas instead, the critical current can be switched back and forth between two stable states by using two different photon wavelengths. The underlying mechanism can be explained by referring to the band profile shown in Fig. 6.19. The heterostructure used for

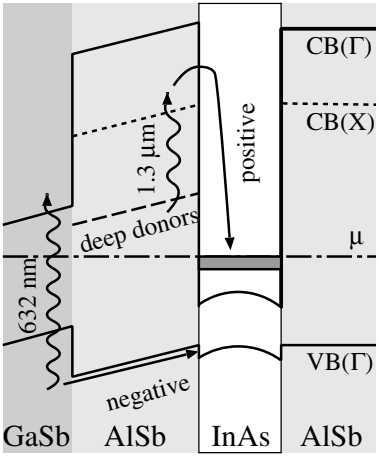


**Fig. 6.19.** Band profile of a GaSb/AlSb/InAs heterojunction. CB($\Gamma$) and CB($X$) are the conduction band edges at the $\Gamma$ and $X$ valleys, respectively. VB($\Gamma$) is the valence band edge at the $\Gamma$ point. If the layer system is illuminated by a 632 nm source, electron–hole pairs are generated in the GaSb layer. The holes are dragged to the InAs well by the built-in electric field. By illuminating with a 1.3 μm source, deep donors located in the AlSb barrier are activated [176]

this study is similar to the layer system depicted in Fig. 3.4a. In this case, the InAs channel layer has a thickness of 12.5 nm, while the upper AlSb barrier is only 50 nm thick.

As depicted in Fig. 6.19, illumination with infrared light with a wavelength of about 1.3 μm ionizes deep donors inside the AlSb barrier, which are transferred to the InAs quantum well. The carrier concentration in the quantum well is increased by this mechanism, similarly to the InGaAs/InP heterostructure discussed above. If the sample is illuminated by light of a wavelength shorter than 950 nm, electron–hole pairs are generated in the GaSb cap layer. As can be seen in Fig. 6.19, owing to the built-in electrical potential, the holes are dragged to the InAs well, where they recombine with part of the electrons accumulated in the quantum well [177]. As a result, the carrier concentration in the quantum well is decreased by this mechanism.

The effect of illumination with two different wavelengths on a Josephson junction can be seen in Fig. 6.20. During illumination with a wavelength of 632 nm, the critical current $I_c$ decreases from an initially higher value to

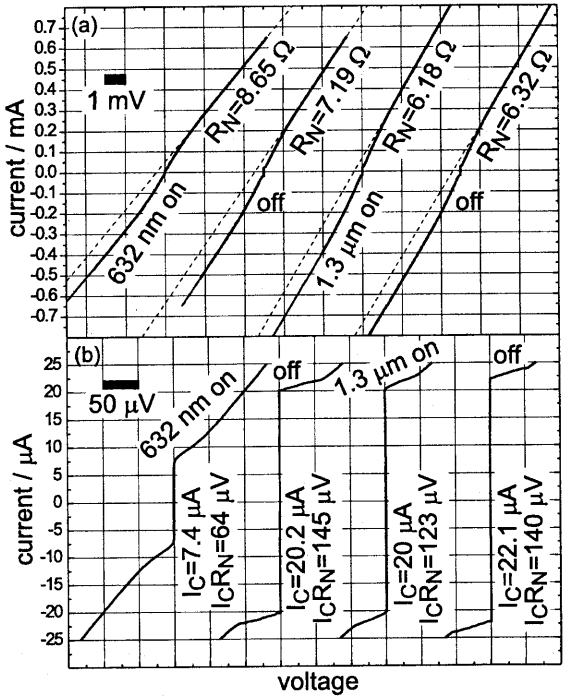


**Fig. 6.20.** Current–voltage characteristics for an illumination sequence with 632 nm and 1.3 μm wavelength light sources and intermediate stages where the light source is off. (**a**) $I$–$V$ characteristics for a large bias current range. (**b**) Details showing the characteristics close to zero voltage. Both the normal-state resistance, given by the slope in (**a**), and the critical current are changed persistently by light illumination [176]

7.4 μA. Simultaneously, the normal-state resistance $R_N$ increases. As mentioned above, this effect can be explained by a decrease of the carrier concentration in the InAs well due to hole transfer from the GaSb layer. After the light source is switched off, the normal-state resistance decrease slightly owing to some carriers trapped in the InAs layer, as can be seen in Fig. 6.20 (the second curve in each part of the figure) [176]. At the same time $I_c$ increases by almost a factor of three. When the 1.3 μm light source is switched on, $R_N$ is further decreased owing to an excitation of deep donors in the AlSb barrier. The carrier concentration in the well is increased by this effect. However, because of the detrimental effects of Cooper pair breaking and heating, the critical current remains approximately at the previous value. Only if the 1.3 μm source is finally switched off does $I_c$ increase (the fourth curve in each part of the figure). The sequence as described above can be employed as a switch that cycles between two stable states [176].

# 7. Gate-Controlled Superconductor/ Two-Dimensional-Electron-Gas Junctions

Compared with metals, semiconductors have the great advantage that the electron concentration can be changed very easily by means of a gate electrode. As we discussed in the preceding chapter, where light exposure was employed, a change of the electron concentration has an immediate effect on the superconducting properties, i.e. the critical current. The first structure discussed below, which utilizes this effect, is the Josephson field effect transistor (JoFET). This is a three-terminal device; the supercurrent of the superconductor/semiconductor Josephson junction can be switched on and off by applying a gate voltage. Besides questions related to the JoFET, which might be used in future electronic circuits, some more fundamental questions related to the wave nature of the particles can also be addressed by studying superconductor/semiconductor structures controlled by a gate. Typical examples, which will be discussed below, are interference effects due to Fabry–Pérot resonances, fluctuation and localization effects, and the quantization of the critical current.

## 7.1 The Josephson Field Effect Transistor

The possibility of controlling the electron concentration in a semiconductor by means of the field effect is one of the foundations of modern microelectronics. In a field effect transistor, the electron concentration and thus the resistance of the channel between the source and drain contacts are controlled by a gate electrode. Biasing the gate with a positive voltage leads to a higher electron concentration and, consequently, to a lower drain–source resistance. If a negative gate voltage is applied, the electron concentration is reduced, leading to an increase of the drain–source resistance.

The concept of a field effect transistor can be transferred to superconducting junctions. Here, the critical current in a superconductor/semiconductor junction is controlled by placing a gate electrode on top of the semiconductor channel, as depicted in Fig. 7.1a. This so-called Josephson field effect transistor was first proposed by Clark et al. [7]. The idea behind the JoFET is the control of the critical current $I_c$ by changing the coherence length $\xi_N$ in the semiconductor link. As discussed in Sect. 6.2.5, $\xi_N$ and the critical current $I_c$ are increased with increasing electron concentration. A JoFET can

Thomas Schäpers: Superconductor/Semiconductor Junctions, STMP 174, 95–110 (2001)
© Springer-Verlag Berlin Heidelberg 2001

be employed to switch between two output voltages between the drain and source contacts. Let us define the "on" state as the state, where the link between the source and drain is superconducting. The drain–source current is adjusted to a value below the critical current $I_c$ of the junction (Fig. 7.1b). In the "off" state a sufficiently negative gate voltage is applied that the electron concentration is reduced such that the critical current is suppressed. Now, a nonzero voltage $V^{\text{off}}$ appears between the drain and source contacts, which is determined by the load resistance $R_L$ and the drain–source resistance $R_N^{\text{off}}$.

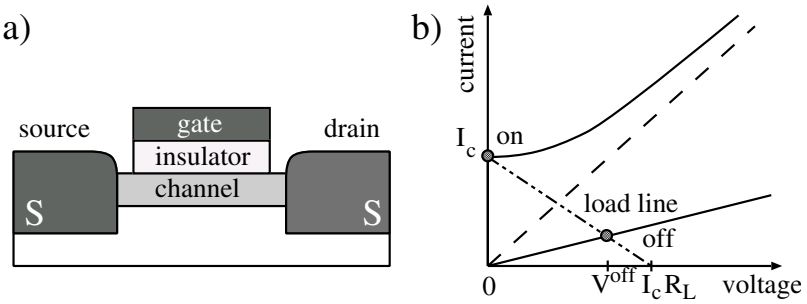


**Fig. 7.1.** (**a**) Schematic illustration of Josephson field effect transistor. The supercurrent flows through the channel between the source and drain contacts. The gate is separated by an insulator in order to suppress leakage currents. (**b**) Schematic current–voltage characteristics of a JoFET. In the "on" state the transistor is in the superconducting state. The *dashed line* represents the one state that occurs without superconductivity

A few years after the proposal by Clark et al. [7] JoFET operation was reported by Nishino et al. [9, 178] and by Takayanagi and Kawakami [8]. The first device was based on an inversion layer formed by an $SiO_2$/Si structure. For the second device, the native inversion layer of InAs was used as a channel. Owing to the lack of a Schottky barrier for InAs, the gate electrode was insulated by an $SiO_2$ layer from the channel in order to prevent gate leakage currents (Fig. 7.1a). In addition to these structures based on dielectric gate insulation, control of a Josephson supercurrent was gained in an InGaAs-based junction field effect transistor using a pn junction in order to insulate the gate from the channel layer [179].

The first JoFET with a two-dimensional electron gas in a semiconductor heterojunction was realized by employing a GaAs/AlGaAs layer system [10]. However, as outlined above, the large Schottky barrier suppresses the superconducting coupling and thus reduces the device performance. In contrast, InAs-based heterostructures are the material of choice for a transparent coupling to a superconductor, owing to the inversion layer at the surface, and are consequently well suited as a basis for a

JoFET device. The first JoFET based on this type of heterostructure, realized with an $In_{0.53}Ga_{0.47}As/InAs/In_{0.53}Ga_{0.47}As$ 2DEG channel (Fig. 3.4b), was fabricated by inserting an $SiO_2$ layer in order to insulate the Al gate electrode [180]. Unfortunately, the high density of interface states at the $SiO_2$/semiconductor boundary results in a relatively large gate voltage ($> 10$ V) being necessary to suppress the supercurrent between the drain and source contacts. Luckily, the AlInAs top layer by itself provides a sufficiently high Schottky barrier. Therefore, the gate electrode can be placed directly on top of the AlInAs cap layer, providing that the gate electrode can be aligned between the source and drain contacts, which are only a few hundreds of nanometers apart. A cross section of this most advanced type of JoFET, fabricated by Akazaki et al. [11], is shown in Fig. 7.2.

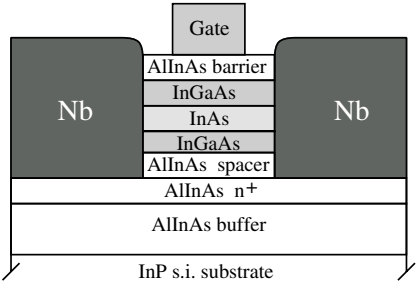


**Fig. 7.2.** Cross section of Josephson field effect transistor based on an InAs inserted-channel InAlAs/InGaAs heterojunction. The gate length is typically 100 nm, while the Nb electrode separation is a few hundreds of nanometers [11]

Figure 7.3 shows the current–voltage characteristics of an InAs inserted-channel InAlAs/InGaAs heterojunction Schottky gate JoFET, as depicted in Fig. 7.2 [11]. At zero gate voltage a critical current of about 5 μA and a normal-state resistance of 16 Ω are obtained for a 40 μm wide junction at a temperature of 1 K. Biasing the gate with a negative voltage results in a decrease of $I_c$ and, at the same time, an increase of $R_N$. A gate voltage of about 1 V is sufficient to suppress the Josephson supercurrent completely.

The decrease of the critical current with increasing negative gate bias $V_g$, accompanied by a corresponding increase of $R_N$, is plotted in Fig. 7.4. Here, a steep increase of $I_c$ with $V_g$ is observed around a gate bias of $-0.7$ V, whereas $I_c$ tends to saturate towards zero bias.

In order to describe the dependence of the critical current on the gate voltage, the expression derived by van Dover et al. [181] is frequently used. For a superconductor/normal-conductor/superconductor junction in the limit $\xi_N \ll L$, the critical current is given by

$$I_c = R_N^{-1} \frac{\pi \Delta_0^2}{2ek_B T_c} \frac{\varrho_N m_e}{\varrho_S m_N^*} A^2 f^2 \frac{L}{\xi_N} e^{-L/\xi_N} . \tag{7.1}$$

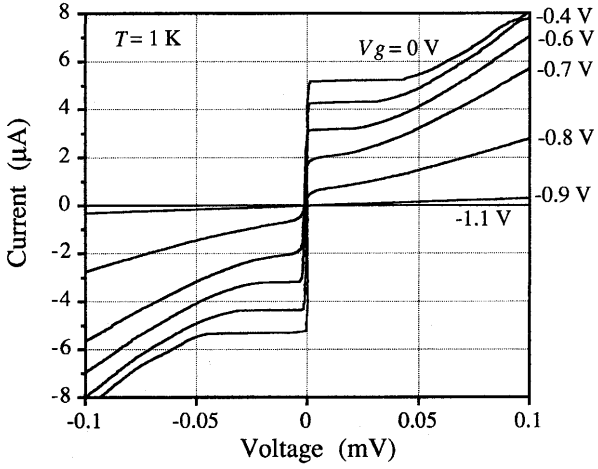


**Fig. 7.3.** Current–voltage characteristics of an InAs inserted-channel InAlAs/InGaAs heterojunction JoFET for successively increasing gate bias from 0 to −1.1 V [11]

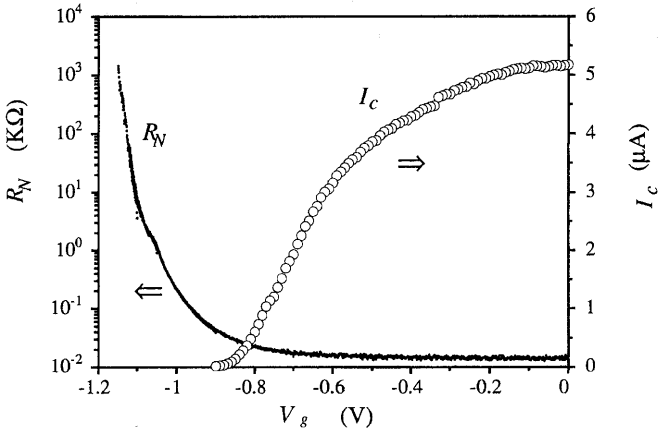


**Fig. 7.4.** Critical current $I_c$ and normal resistance $R_N$ as a function of applied gate bias at $T = 1$ K. The slope of the $I_c$ vs. $V_g$ curve is the superconducting transconductance $g_m^s$ [11]

Here, $\varrho_S$ and $\varrho_N$ are the resistivities in the superconductor and normal conductor, respectively, and $f$ is the ratio of the order parameter at the interface to its bulk value. The factor by which the order parameter changes on crossing the interface is described by $A$. Strictly speaking, (7.1) is only valid near $T_c$ since it is derived from the Ginzburg–Landau theory; however, in most practical cases it also applies at lower temperatures [182]. If no Schottky

barrier is present at the interface, as for InAs, $A^2$ is given by $\varrho_S m_N^*/\varrho_N m_e$, which simplifies (7.1) [182]. However, if a Schottky barrier has to be taken into account, as for Si or GaAs, $A$ is proportional to the tunneling probability through the interface barrier [182].

In (7.1) $R_N$ and $\xi_N$ depend on the carrier concentration $n_{2D}$. For the dirty-limit case, the coherence length is given by

$$\xi_N^d = \sqrt{\frac{\hbar \mathcal{D}_N}{2\pi k_B T}} = \sqrt{\frac{\hbar^3 \mu}{2m^* e k_B T}} \sqrt{n_{2D}} \,, \tag{7.2}$$

while the coherence length in the clean limit can be expressed as

$$\xi_N^c = \frac{\hbar v_F}{2\pi k_B T} = \frac{\hbar^2 \sqrt{2\pi}}{2\pi m^* k_B T} \sqrt{n_{2D}} \,. \tag{7.3}$$

In both cases the coherence length is proportional to $\sqrt{n_{2D}}$. Since $n_{2D} \propto V_g - V_t$, where $V_t$ is the threshold voltage, the coherence length is proportional to $\sqrt{V_g - V_t}$. Kleinsasser et al. [182] analyzed the gate voltage dependence of $I_c$ of an $Si/SiO_2$ JoFET fabricated by Nishino et al. [9]. A very good agreement with the experimental data was obtained by using (7.1), with $A$ determined by the Schottky barrier transparency. For a JoFET with an InAs inserted channel, a transition between the clean and the dirty limit was observed when the carrier concentration in the channel was decreased by applying a negative gate voltage [180]. As mentioned above, (7.1) is strictly valid only in a limited temperature range close to $T_c$. For long contacts ($L > \xi_N$), Kresin [147] developed a model for the critical current as a function of $n_{2D}$ in the clean and in the dirty limit. Within this model, the different effective masses and the potential step between the superconductor and the semiconductor were considered, whereas the barrier at the interface was omitted. For the clean-limit case, a barrier was taken into account in the model presented by Chrestin et al. (see Sect. 6.1.3) [148]. Volkov and Takayanagi [183] analyzed the dependence of $I_c$ on $n_{2D}$ for a JoFET in the dirty limit, where a gate length shorter than the channel length was taken into account. A comparison with experimental data on an InAs-based JoFET [184] confirmed the validity of the model.

One parameter which characterizes the device performance of a JoFET is the superconducting transconductance $g_m^s$, defined as [11]

$$g_m^s = dJ_c/dV_g \,, \tag{7.4}$$

where $J_c$ is the critical current for a width of 1 mm. From the $I_c$ vs. $V_g$ curve in Fig. 7.4, a maximum $g_m^s$ of 350 μS/mm is found at a gate bias of −0.7 V, which is considerably larger than the $g_m^s$ values obtained for JoFET structures with an $SiO_2$ insulation layer [11].

With regard to voltage gain, one of the crucial parameters concerning any possible application in electronic circuits, the JoFET has some important limitations. This has to do with the fact that a gate bias of the order of at

least one volt has to be applied, while the output voltage between the source and drain contacts is of the order of $\Delta_0/e$. Of course the output voltage swing can be increased, but then the superconducting properties of the JoFET are not taken advantage of, so that the device is operated more as a conventional field effect transistor [179]. The voltage gain $G^V$ is defined as the voltage ratio between the output voltage and the gate voltage swing. For an inverter circuit with a load resistance $R_\mathrm{L}$, the voltage gain is given by [185]

$$G^V = \frac{|V^\mathrm{on} - V^\mathrm{off}|}{|V_\mathrm{g}^\mathrm{on} - V_\mathrm{g}^\mathrm{off}|} = \frac{I_\mathrm{c}^\mathrm{on} R_\mathrm{L} R_\mathrm{N}^\mathrm{off}}{(R_\mathrm{L} + R_\mathrm{N}^\mathrm{off})|V_\mathrm{g}^\mathrm{on} - V_\mathrm{g}^\mathrm{off}|} \,. \tag{7.5}$$

Here $I_\mathrm{c}^\mathrm{on}$ and $V_\mathrm{g}^\mathrm{on}$ refer to the superconducting "on" state, while $R_\mathrm{N}^\mathrm{off}$ and $V_\mathrm{g}^\mathrm{off}$ are the normal resistance and the gate voltage in the resistive state ("off" state) of the junction. Owing to the superconducting "on" state of the JoFET, $V^\mathrm{on}$ is zero (Fig. 7.1). For the transistor shown in Fig. 7.2, a voltage gain of the order of one could be obtained since relatively small gate voltages ($V \sim 1$ V) were sufficient to deplete the drain–source channel [11]. Nevertheless, a relatively large load resistance $R_\mathrm{L}$ had to be chosen in order to obtain $G > 1$. This has a negative effect on the maximum operation frequency, which is determined by $R_\mathrm{L}$ and the gate capacitance $C_\mathrm{g}$. For a real application of a JoFET in an electronic circuit, one of the major tasks is to increase $G^V$ by increasing $I_\mathrm{c}$ [11].

## 7.2 Interference Effects

Besides its potential use as an electronic device, a JoFET structure is also very interesting for studying interference effects. In the clean-limit regime Fabry–Pérot-like interference patterns can be found in the critical current, while in the dirty limit localization effects and mesoscopic fluctuations are observed in the critical current.

### 7.2.1 Critical-Current Oscillations

If the superconductor/2DEG interfaces of a JoFET are nonideal so that normal reflection can occur, a JoFET can serve as a resonator similar to a Fabry–Pérot resonator in optics. Fabry–Pérot-like oscillations in a Josephson junction were first discussed by Gudkov et al. [12] in conjunction with the interpretation of three-dimensional Nb/$\alpha$-Si junctions. For a junction with a two-dimensional electron gas as a normal conductor, oscillations due to interference effects were discussed by Chrestin et al. [148], while critical-current oscillations in a one-dimensional junction were investigated theoretically by Rittenhouse and Graybeal [13] and by Tang et al. [144].

In order to discuss the origin of the interference effects in a superconductor/2DEG junction, (6.27) and (6.28), derived by Chrestin et al. [148],

can be referred to. Here, the first two terms in $f(k_y, \omega_n)$ can be attributed to an electron Andreev-reflected as a hole at the superconductor/2DEG interface and vice versa. The remaining two terms in (6.28), leading to the critical-current oscillations, arise when normal reflection is involved in addition. One of the processes contributing to the oscillations is sketched in Fig. 7.5, where two Andreev reflections and two normal reflections occur. If the carrier concentration is changed, thus changing the electron and hole wave vectors, resonant states within the S/2DEG/S cavity arise, leading to a maximum in the critical current.

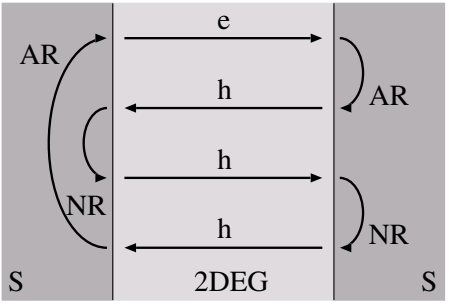


**Fig. 7.5.** One of the processes contributing to the oscillations of the critical current. This process contains two Andreev reflections (AR) and two normal reflections (NR)

The oscillations of the critical current as a function of the carrier concentration, calculated from (6.27), are shown in Fig. 7.6 for a 2DEG in an InAs inversion layer contacted to Nb electrodes. Two features can be made out. First, the oscillation amplitude increases with increasing barrier strength $Z$ at the Nb/InAs interface. For $Z = 0$ only weak oscillations are found, while for finite $Z$ parameters more pronounced oscillations occur owing to the increased normal-reflection probability. Second, for $Z = 0$ the oscillations almost disappear at an electron concentration of $n \approx 1.2 \times 10^{12}$ cm$^{-2}$. This is due to the fact that at this particular electron concentration, the Fermi velocities of the superconductor and the 2DEG are equal, so that even the usual normal reflection due to the Fermi velocity mismatch is suppressed.

The local maxima of the critical current as a function of the carrier density $n_{2D}$ can be approximated by [148]

$$n_{2D,\max} = \frac{\pi}{2L} N^2 \,, \tag{7.6}$$

where $L$ is the length of the junction and the integer $N$ equals half the number of quasiparticle states with resonant values of $k_y$, defined by the maxima of $\cos\left(2\sqrt{k_{FN}^2 - k_y^2}L\right)$; $k_y$ is the wave number perpendicular to the current direction.

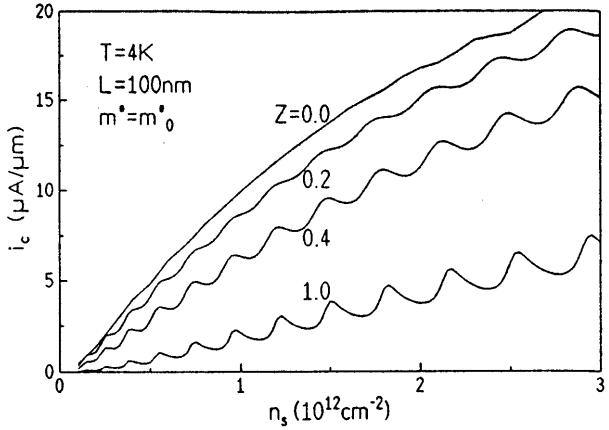


**Fig. 7.6.** Critical current as a function of the carrier concentration $n_s$ for various barrier strengths $Z$ [148]

Initial experiments showing critical-current oscillations as a function of the carrier concentration were reported by Takayanagi et al. [27]. However, in these JoFET structures the Nb electrodes were deposited on top of the InAs channel of the heterostructure shown in Fig. 3.4a, so that the Nb/2DEG interface was not defined sharply. Consequently, the oscillation amplitude of $I_c$ was relatively small. In addition, the junction length $L$ deduced from (7.6) did not fit well to the geometrical Nb electrode separation. A much stronger oscillation amplitude was found for the improved JoFET structure shown in Fig. 7.2 [186]. Here, the Nb electrodes are contacted to the 2DEG at the mesa edge, so that the geometry of the resonator is well defined. The measured oscillations of $I_c$ as a function of the carrier concentration underneath the gate electrode are shown in Fig. 7.7. Since the gate does not cover the complete 2DEG area between the Nb electrodes, the electron and hole wave vectors are only altered in the area underneath the gate. The $I_c$ peak positions calculated taking account of this effect, marked by arrows, show a reasonable agreement with the experimental values.

### 7.2.2 Mesoscopic Fluctuations and Localization Effects

Localization effects and universal conductance fluctuations (UCFs) are two remarkable phenomena in mesoscopic physics, which directly demonstrate the wave nature of the electrons in the conductor [149]. In addition to such effects in purely metallic or semiconducting systems, both effects have been predicted and experimentally observed in the Josephson supercurrent of superconductor/2DEG junctions.

With regard to universal conductance fluctuations, Al'tshuler [187] and Lee and Stone [188] showed, for a disordered wire, that the mesoscopic fluc-

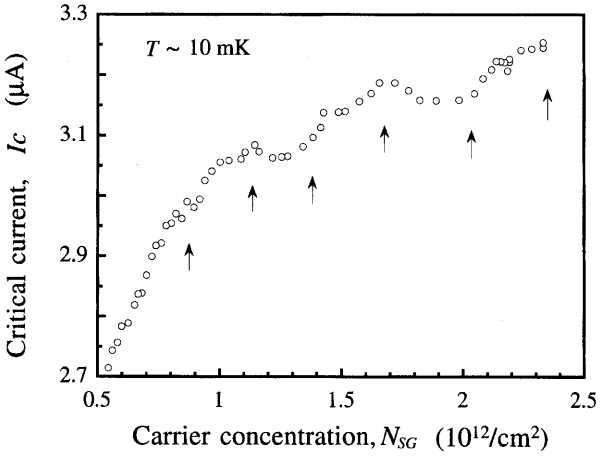


**Fig. 7.7.** Critical current as a function of the carrier concentration underneath the gate electrode. The *arrows* indicate the calculated peak positions [186]

tuations in the conductance $G$ at zero temperature have a root mean square value of $rmsG \equiv \sqrt{\langle G^2\rangle - \langle G\rangle^2} \simeq e^2/h$. Since this value is independent of the wire length and the elastic mean free path, these fluctuations are called "universal". Universal conductance fluctuations manifest themselves as sample-to-sample fluctuations. However, owing to the ergodic property, changing the Fermi Energy $E_\mathrm{F}$ or the magnetic field $B$ is equivalent to averaging $G$ over an ensemble of samples. For a given sample, the fluctuations as a function of $E_\mathrm{F}$ or $B$ are sample-specific and also reproducible, provided that the sample is kept at low temperature. One can say that each sample possesses its own "fingerprint".

From the theoretical point of view, fluctuations in superconductor/2DEG Josephson junctions have been treated in two limits. Al'tshuler and Spivak [189] discussed a junction which was long compared with the elastic mean free path and with the superconducting coherence length in the dirty limit ($L \gg \xi_\mathrm{N}^\mathrm{d}, l_\mathrm{el}$). Their result for the fluctuations in the critical current $rmsI_\mathrm{c} \equiv \sqrt{\langle I_\mathrm{c}^2\rangle - \langle I_\mathrm{c}\rangle^2}$, expressed for a two-dimensional system, can be written as [190]

$$rmsI_\mathrm{c} \approx 2.2\frac{e\mathcal{D}}{L^2}\sqrt{\frac{W}{L}} \tag{7.7}$$

for $L \ll W$ and $T \ll T_\mathrm{N} \equiv \hbar\mathcal{D}/2k_\mathrm{B}L^2$. In order for one to be able to observe these mesoscopic fluctuations, the correlation energy $E_\mathrm{c} = \hbar\pi^2\mathcal{D}/L^2$ must be larger than $k_\mathrm{B}T$ so that thermal smearing is prevented. As can be seen in (7.7), the fluctuations in $I_\mathrm{c}$ depend on the sample length $L$ as well as on the elastic mean free path $l_\mathrm{el}$, since $\mathcal{D}$ depends on $l_\mathrm{el}$. Consequently, these

fluctuations cannot be regarded as "universal" in the spirit of the universal conductance fluctuations.

Universal fluctuations of the critical current were predicted by Beenakker [191] for the case when the junction length is much shorter than the superconducting coherence length. In this short-junction regime,

$$rmsI_c \approx e\Delta_0/\hbar \tag{7.8}$$

for $T \ll T_c$. This result was obtained by relating the Josephson supercurrent to the scattering matrix of the normal region of an SNS junction. As for the theory of UCFs, the statistical properties of the scattering matrix were used to obtain (7.8).

In order for one to observe fluctuations in $I_c$, the transport in the junction must be diffusive so that $l_{el} \ll L$ is fulfilled. Consequently, the first critical-current fluctuations were found in a junction based on an inversion-layer two-dimensional electron gas in p-InAs [190], where the ionized impurities and the rough interface lead to a sufficiently large number of elastic scattering events. For the superconducting electrodes, Nb was employed.

With regard to UCFs, an external magnetic field is often used in order to trace the fluctuations in $G$. Since in spatially extended superconductor/semiconductor junctions the supercurrent is very sensitive to $B$, it is in this case more appropriate to change the Fermi energy $E_F$ by using a gate electrode on top of the semiconductor bridge. As can be seen in Fig. 7.8, the critical current fluctuates if the gate voltage is changed. Furthermore, $I_c$ follows precisely the fluctuations of the differential normal conductance $G_N$. A detailed analysis of the experimental data showed that the sample satisfied the conditions of the theory of Al'tshuler and Spivak [189], since $\xi_N^d$ and $l_{el}$ were much smaller than the separation of the superconducting electrodes.

In the diffusive transport regime the elastic mean free path $l_{el}$ is much shorter than the sample length, and thus the electrons undergo many scattering events while passing through the sample. At some locations multiple scattering leads to the situation that the electrons are moving in closed loops. In these closed loops the electrons can move in two opposite, time-reversed directions. Since the phase accumulations of the electron waves are identical in both directions, a constructive interference occurs, leading to a localization of the electron within the loop. In transport measurements this localization results in an additional contribution to the resistance. If a magnetic field is applied, the time-reversed paths acquire opposite additional phase shifts due to the vector potential $\boldsymbol{A}$. This destroys the constructive interference and reduces the sample resistance. The same effect is obtained by increasing the temperature.

Similarly to the decrease of the normal conductance of a metal due to localization, a reduction of the critical current in a superconductor/dirty-two-dimensional-metal Josephson junction was predicted by Fukuyama and Maekawa [192, 193]. In their theory the diffusion constant $\mathcal{D}$ is modified by

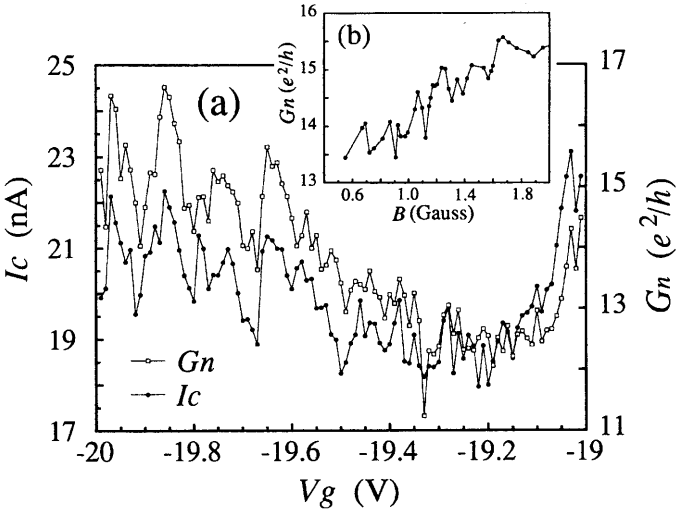


**Fig. 7.8.** (**a**) Critical current $I_c$ and differential normal conductance $G_N$ as a function of the gate voltage. (**b**) Fluctuations of $G_N$ as a function of $B$ for a fixed gate voltage [190] (© (1995) by the American Physical Society)

localization. As can be seen in (7.2), this directly affects the coherence length $\xi_N^d$ and the critical current $I_c$ (7.1).

Verifying localization effects in superconducting junctions faces the same problem as does the detection of fluctuations in $I_c$; a magnetic field cannot be employed, owing to the strong dependence of $I_c$ on $B$. Therefore, $I_c$ was measured as a function of temperature (Fig. 7.9) [184]. Here, the inversion layer in p-type InAs was used as the normal-conducting bridge between the superconducting Nb electrodes. By applying an appropriate gate voltage, the 2DEG channel can be adjusted to the weak (higher electron concentration) or strong (lower electron concentration) localization regime. The localization manifests itself in a saturation of $I_c$ at low temperatures.

As can be seen in Fig. 6.11 for a junction in the clean limit, a saturation of $I_c$ at low temperature does not always mean that localization effects occur. For junction with $\xi_N^d(T_c) \gg L$ and a constant $R_N$, the critical current usually shows a saturation at $T \leq 0.2T_c$ [1]. It was shown that for the junction used for the measurements depicted in Fig. 7.9, this condition was not fulfilled. This proves that the saturation must be due to localization.

## 7.3 Superconducting Quantum Point Contacts

In a two-dimensional electron gas, the free motion of the carriers is restricted to a plane. One can proceed one step further and allow transport in only

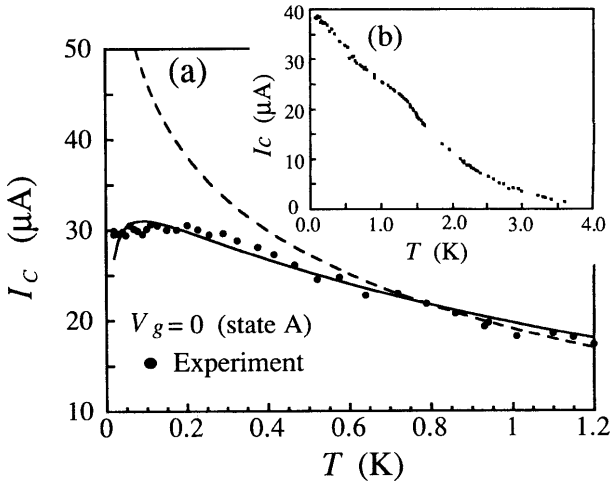


**Fig. 7.9.** (**a**) Critical current of an Nb/p-type InAs/Nb junction as a function of temperature. The *solid* and *dotted lines* show the calculated $I_c$ vs. $T$ curves with and without localization effects. In (**b**) the temperature dependence of a reference junction in the clean limit with an InAs inserted channel (see Fig. 3.4b) is shown for comparison [184] (© (1995) by the American Physical Society)

one direction. This can be obtained by using a split-gate geometry, where a small opening is defined by two gates, separated by a few hundreds of nanometers. If a sufficiently large negative gate voltage is applied, the two-dimensional electron gas underneath the gate is depleted, leaving only a small opening for the electrons to pass through. Since the Fermi wavelength $\lambda_F$ of a 2DEG in a semiconductor heterostructure is comparable to the width of the point contact defined by the split gate, the transverse momentum is quantized. In ballistic structures, where the channel is shorter than $l_{el}$, quantized conductance in units of $2e^2/h$ can be observed [194, 195].

The following question arises: is it possible to observe a quantization of the supercurrent if two superconducting electrodes are connected by a point contact? This problem was addressed theoretically by Furusaki et al. [25, 196, 197] and by Beenakker and van Houten [24, 198]. Here, the latter approach, which applies to a short adiabatic constriction, will be discussed briefly.

The geometry of the constriction is shown in Fig. 7.10. It widens from a minimum width of $S_{min}$ to $S_{max}$, with $S_{max} \gg S_{min}$, at both sides. The length $L$ is assumed to be much shorter than the coherence length $\xi_0 = \hbar v_F/\pi\Delta_0$. The number of modes propagating through the constriction is given by $N \simeq S_{min}/\lambda_F$. Adiabatic propagation, and thus no scattering between the modes, is assumed, which requires $L \gg \lambda_F$. As depicted in Fig. 7.10, the pair potential at both ends of the constriction is approximated by $\Delta_0 \exp(-i\phi_0/2)$ for $x < -L/2$ and by $\Delta_0 \exp(i\phi_0/2)$ for $x > L/2$. The Bogoliubov equation (2.1) for the constriction is solved by expanding the eigenfunction

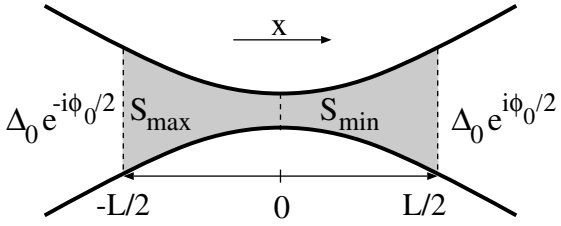


**Fig. 7.10.** Schematic illustration of a constriction between two superconducting reservoirs (after [24])

$$\psi(x,y) = \sum_n \begin{pmatrix} v_n(x) \\ u_n(x) \end{pmatrix} \varphi_n(x,y) \tag{7.9}$$

into transverse modes $\varphi_n(x,y)$, which are the eigenfunctions of the Hamiltonian $-(\hbar^2/2m_e)\partial^2/\partial y^2 + U(x,y)$. The corresponding eigenvalue for the mode $n$ at the position $x$ is $E_n(x)$. In order find the solutions for the propagation along the constriction, the WKB method [199] is used. Owing to this approach only the discrete solutions $|E| \leq \Delta_0$ contribute to the Josephson current [24]. In the short-junction limit ($L \ll \xi_0$) the normalized wave function is given by

$$\begin{aligned} \psi_\pm(x) &= \left(\frac{m_e}{2\hbar^2}\right)^{1/2} (\Delta_0 - E^2)^{1/4} k_0(x)^{-1/2} \begin{pmatrix} 1 \\ 1 \end{pmatrix} \\ &\quad \times \exp\left(\pm i \int_0^x k(x')\,dx'\right) , \end{aligned} \tag{7.10}$$

where $k_0(x) = \{2m_e[\mu - E_n(x)]/\hbar^2\}^{1/2}$. For $\Delta_0 \ll \mu - E_n(x)$, the wave vector $k(x)$ in the integral can be approximated by

$$k(x) = k_0(x)\left(1 - \frac{i|\Delta(x)|}{2[\mu - E_n(x)]} \sin\phi(x)\right) , \tag{7.11}$$

where $\phi(x)$ is the superconducting phase within the junction. In contrast to the one-dimensional case discussed in Sect. 6.1.1, the wave vector does change along the constriction owing to the quantization in the transverse direction. Since $\psi_\pm(x)$ must decrease exponentially for $|x| < L/2$, the wave function $\psi_+(x)$ corresponds to $0 < \phi_0 < \pi$, whereas $\psi_-(x)$ is appropriate to the solution for $-\pi < \phi_0 < 0$. In the limit $L/\xi_0 \to 0$, the Andreev bound-state energy is given by

$$\arccos(E/\Delta_0) = \pm\frac{1}{2}\phi_0 , \tag{7.12}$$

which corresponds to the solution of a one-dimensional junction in the short limit (6.7). It should be stressed that, for a constriction in the short limit

as discussed here, the Andreev bound-state energy is identical for all propagating modes $n$. From the normalized wave function (7.10), the supercurrent per mode can be calculated, which is

$$I_n = \frac{e}{\hbar}\Delta_0 \sin\phi_0/2 \tag{7.13}$$

at $T = 0$. Since all modes contribute by the same amount to the supercurrent the critical current for $N$ occupied modes is given by

$$I_\mathrm{c} = N\frac{e\Delta_0}{\hbar}\ . \tag{7.14}$$

If the number of channels $N$ is increased, the critical current increases stepwise. The steps have a constant height of $e\Delta_0/\hbar$, which is determined solely by fundamental constants and the bulk pair potential $\Delta_0$.

The result that the critical current of a superconducting point contact is independent of the parameters of the junction holds only for a short junction in the adiabatic approximation. Furusaki et al. [25] treated the more general case beyond this limitation for various geometries of the constriction.

For a long constriction in the adiabatic approximation, $L \gg \xi_0$ Furusaki et al. arrived at the following expression for the critical current at zero temperature:

$$I \approx \frac{e}{\pi L}\sum_n^\mathrm{N} v_n\phi_0\ . \tag{7.15}$$

Here the velocity of the $n$th mode is defined as

$$v_n = \left(\frac{1}{L}\int_0^L \mathrm{d}x \frac{m_\mathrm{e}}{\hbar k_n(x)}\right)^{-1}\ , \tag{7.16}$$

where $k_n = \{2m_\mathrm{e}\mu/\hbar^2 - [n\pi/S(x)]^2\}^{1/2}$. $S(x)$ is the width of the constriction at position $x$. In contrast to a constriction in the short limit, the critical current for $L \gg \xi_0$ depends on the junction parameters such as $L$ and $v_n$. For the simplest adiabatic constriction with a constant width $S(x) = S_0$, the velocity of the $n$th mode is given by $v_n = [2\mu/m_\mathrm{e} - (n\pi\hbar/S_0m_\mathrm{e})^2]^{1/2}$. This implies that an increase of the width $S_0$ of the constriction would lead to a smooth increase of $v_n$. Thus no sharp steps, as in the short limit, are expected. In addition, the step height depends on the width of the constriction. In contrast to the adiabatic approximation, where the junction length is much larger than $\lambda_\mathrm{F}$, in constrictions with sudden changes of width, mode mixing and reflection can occur. As a result the critical current as a function of the constriction width can show additional features, i.e. resonant structures [25].

A superconducting quantum point contact can be realized by placing a split gate between two closely spaced superconducting electrodes (Fig. 7.11). In order to operate the structure in the ballistic regime, a high-mobility two-dimensional electron gas in a semiconductor heterostructure has to be chosen. If a sufficiently large negative bias voltage is applied to the split gate, the

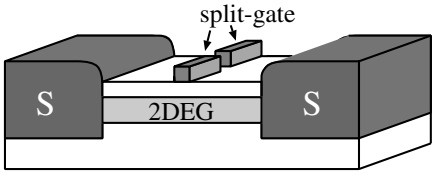


**Fig. 7.11.** Schematic drawing of a split-gate superconducting point contact

electron gas underneath the gate can be depleted. The opening width of the point contact can be adjusted by the gate voltage.

The quantization of the critical current was demonstrated by Takayanagi et al. [26]. Figure 7.12 shows the conductance and $I_c$ as a function of the voltage applied to the split gate. The conductance $G$ of the constriction measured

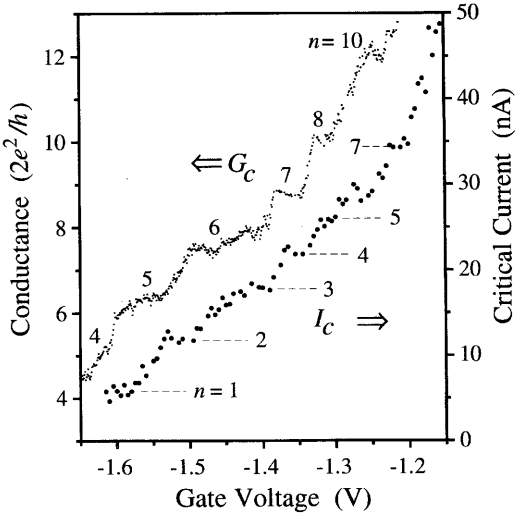


**Fig. 7.12.** Conductance of the constriction and the critical current as a function of the gate voltage [26] (© (1995) by the American Physical Society)

at a small magnetic field shows clear steps. From theory it is predicted that for an ideal point contact, facing two superconducting interfaces, the conductance should be quantized in units of $4e^2/h$ owing to Andreev reflection [200]. Although a quantization in steps of $4e^2/h$ was not obtained, the conductance steps are larger than $2e^2/h$. The latter step size is expected for a completely normal-conducting quantum point contact [26]. It can thus be concluded, at least, that Andreev reflection processes are involved in the carrier transport through the constriction.

The steps in the critical current $I_c$ follow the steps of the conductance $G$, as can be seen in Fig. 7.12. The step height in $I_c$ is considerably smaller than predicted by the theory of Furusaki et al. [25, 196]. This might be due to the fact that in the theoretical model no normal reflection was included. As we already know from the Josephson junctions discussed in Sect. 6.1.2, a finite barrier at the interface or a mismatch of the Fermi velocities can lead to a decrease of the critical current. One discrepancy, which has not been explained up to now, is the reduced number of steps in $I_c$ compared with the number of steps in $G$ (Fig. 7.12). This result implies that some one-dimensional channels do not contribute to the superconducting transport.

# 8. Nonequilibrium Josephson Current

Control of a supercurrent in weak-link Josephson junctions can be realized by two alternative methods. The first approach, which was described in the preceding chapter, is to control the carrier concentration in the semiconductor with a gate electrode. A typical example of this kind of structure is the Josephson field effect transistor. In this chapter we shall discuss how a Josephson supercurrent can be controlled by injecting nonequilibrium carriers. As explained in Sect. 6.1, the net supercurrent is partially determined by the occupation of Andreev bound states located energetically within the superconductive gap. If carriers are injected, the occupation of these Andreev levels is altered. This directly affects the net supercurrent in the junction. In the first part of this chapter the underlying theoretical models will be discussed in detail, while in the second part the corresponding experiments are described.

## 8.1 Supercurrent Control by Nonequilibrium Carriers: Theoretical Concepts

The concept of coupling a normal reservoir to a ballistic SNS junction in order to control the Josephson supercurrent by applying a bias voltage to the normal electrode was first proposed by van Wees et al. [15]. These authors could show that the coupling to the normal reservoir has two effects. First, the Andreev resonances are broadened owing to phase-breaking processes. This leads to a decrease of the critical current even for zero bias voltage. Second, if an appropriate voltage is applied to the normal reservoir, the occupation of the Andreev levels is altered, which directly affects the supercurrent in the junction. Since the current direction changes sign for energetically neighboring Andreev bound states, even a reversal of the supercurrent was predicted for certain ranges of bias voltages. The injection of hot carriers into ballistic junctions of various lengths was investigated by Chang et al. [17]. By taking the scattering phases at the connection point between the junction and the injector into account, Samuelsson et al. [18, 201, 202] were able to show that for a one-dimensional structure, an additional nonequilibrium current contribution has to be considered. The mechanisms described here can in principle

Thomas Schäpers: Superconductor/Semiconductor Junctions, STMP 174, 111–132 (2001)
© Springer-Verlag Berlin Heidelberg 2001

be used for a superconducting device where the supercurrent is controlled by an injection current. From a fundamental point of view, a three-terminal structure could even be useful as a spectrometer in order to resolve single Andreev levels [202, 203]. The finite phase difference between the two electrodes of a Josephson junction under supercurrent flow was studied theoretically by Nakano and Takayanagi [204] in an interferometer setup. Here, the phase difference was employed to control the conductance of a normal-conducting Y-shaped beam splitter, which was attached to both superconducting electrodes.

For the diffusive case, Volkov [16] was able to show that in this regime a reversal of the supercurrent can also be expected. Furthermore, the results of Wilhelm et al. [205] and Yip [19] have demonstrated that the spectral supercurrent $i(E)$ oscillates as a function of energy. This directly implies that the supercurrent can be reversed if a certain bias voltage is exceeded.

### 8.1.1 Carrier Injection in a Three-Terminal Structure

In order to discuss the effect of carrier injection on the Josephson supercurrent in detail, we follow the approach of Samuelsson et al. [18, 202]. Here, a three-terminal junction, as depicted in Fig. 8.1, is considered, where the two superconducting electrodes are connected by a superconducting ring. By threading a magnetic field through the loop, the phase difference $\phi$ can be adjusted independently. Additional carriers are injected from a normal reservoir biased at a voltage $V$. The superconducting loop is at ground potential.

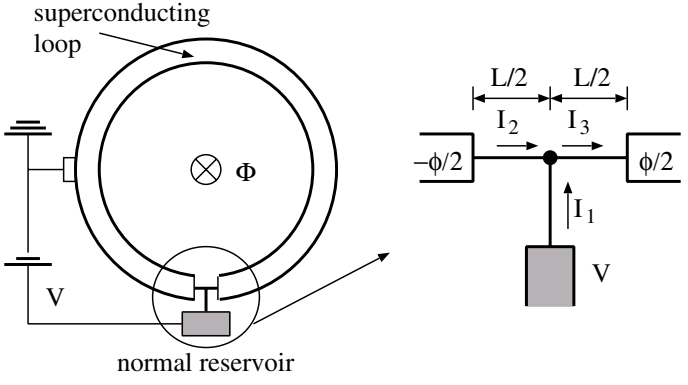


**Fig. 8.1.** Schematic illustration of a three-terminal junction, where the phase difference can be controlled by a magnetic field threading the superconducting loop. The normal conductor is connected to the grounded loop via a voltage source biased at $V$. The sketch on the *right* shows a detail of the junction area with the directions of the current flow in each lead (after [202], © (2000) by the American Physical Society)

The transport is considered to be one-dimensional, and the normal conductor is connected halfway between the superconducting electrodes (see detail in Fig. 8.1). The ingoing and outgoing waves $\Psi_{\rm in}$ and $\Psi_{\rm out}$ at the connection point are related by a scattering matrix $\mathbf{S}$ [15, 18, 202]:

$$\Psi_{\rm out} = \mathbf{S}\,\Psi_{\rm in}\ , \tag{8.1}$$

where

$$\mathbf{S} = \begin{pmatrix} \sqrt{1-2\varepsilon} & \sqrt{\varepsilon} & \sqrt{\varepsilon} \\ \sqrt{\varepsilon} & r & d \\ \sqrt{\varepsilon} & d & r \end{pmatrix}\ . \tag{8.2}$$

Here, $r$ and $d$ are the reflection and transmission amplitudes for the scattering between leads 2 and 3; we define $D = |d|^2$ and $R = |r|^2$. $\sqrt{\varepsilon}$ $(0 \le \varepsilon \le 0.5)$ is the scattering amplitude from the injection lead 1 to lead 2 or 3, where $D+R = 1-\varepsilon$ and $\mathrm{Re}(rd^*) = \varepsilon/2$. Moreover, $\mathrm{Im}(rd^*) = \sigma\sqrt{RD-\varepsilon^2/4}$, where $\sigma = \pm 1$ depending on the phase of the scatterer. Maximum coupling of the normal reservoir is achieved for $\varepsilon = 0.5$, while the reservoir is completely decoupled for $\varepsilon = 0$. Normal reflection at the SN interface is neglected.

When the dwell time of the Andreev resonances in the junction is smaller than the inelastic scattering time, the quasiparticle distribution in the normal region is determined by the Fermi distribution function of the normal reservoir. Under this condition, the currents in the leads $j = 2$ and 3 resulting from the injected particles can be written as

$$I_j = \int_{-\infty}^{+\infty} \mathrm{d}E(i_j^{\rm e} f_{\rm e} + i_j^{\rm h} f_{\rm h} + i^{\rm s} f_0)\ , \tag{8.3}$$

where $i^{\rm e,h}$ are the current densities of injected electrons and holes and $f_{\rm e,h} = f_0(E \pm eV)$ are the corresponding Fermi distribution functions in the normal reservoir. The last term in (8.3) is the contribution of the quasiparticles injected from the superconductor.

In order to obtain the currents in the different leads, the scattering states in the three normal regions have to be calculated by employing the Landauer–Büttiker scattering approach [206, 207]. The plane waves in the different regions of the normal conductor, as well as in the superconducting electrodes, are similar to (2.10) and (2.11) in Sect. 2.2.2, but now we must take both directions of wave propagation into account. The matrix $\mathbf{S}$, as defined in (8.2), is used to describe the scattering of the plane waves at the junction point. The resulting current densities in leads 2 and 3 are given by [202]

$$\begin{aligned} i_2^{\rm e,h} = &- \frac{e}{\hbar}\frac{\varepsilon}{\Gamma}\{2D\sin\phi\sin 2\theta \pm (4\sigma\sqrt{RD-\varepsilon^2/4}\sin\phi\sin^2\theta) \\ &+ 2\varepsilon\sin^2\theta(1+\cos\phi)\}\ , \end{aligned} \tag{8.4a}$$

$$\begin{aligned} i_3^{\rm e,h} = &- \frac{e}{\hbar}\frac{\varepsilon}{\Gamma}\{2D\sin\phi\sin 2\theta \pm (4\sigma\sqrt{RD-\varepsilon^2/4}\sin\phi\sin^2\theta) \\ &- 2\varepsilon\sin^2\theta(1+\cos\phi)\}\ , \end{aligned} \tag{8.4b}$$

where the superscripts e and h are related to the + and – signs, respectively, and where $\theta$ is defined as

$$\theta = \arccos(E/\Delta_0) - EL/(\hbar v_\mathrm{F}) \,. \tag{8.5}$$

$\Gamma$ is given by

$$\Gamma = [(1-\varepsilon)\cos 2\theta - R - D\cos\phi]^2 + \varepsilon^2 \sin^2 2\theta \,. \tag{8.6}$$

In order to separate the different contributions resulting from the coupling of the normal conductor, the currents in leads 2 and 3, as given in (8.3), can be rewritten as [202]

$$I_j = \int_{-\infty}^{+\infty} \mathrm{d}E \left( \frac{i_j^+}{2}(f_\mathrm{e} + f_\mathrm{h}) + \frac{i_j^-}{2}(f_\mathrm{e} - f_\mathrm{h}) + i^\mathrm{s} f_0 \right) \,, \tag{8.7}$$

where $i_j^+ = i_j^\mathrm{e} + i_j^\mathrm{h}$ and $i_j^- = i_j^\mathrm{e} - i_j^\mathrm{h}$. In equilibrium ($V = 0$) the current through the junction is simply given by

$$I_\mathrm{eq} = \int \mathrm{d}E \, (i^+ + i^\mathrm{s}) f_0 \,, \tag{8.8}$$

where

$$i^+ = i_2^+ = i_3^+ = -\frac{e}{\hbar}\frac{\varepsilon}{\Gamma} D \sin\phi \sin 2\theta \,. \tag{8.9}$$

The resulting current density for a short junction is shown in Fig. 8.2. Owing

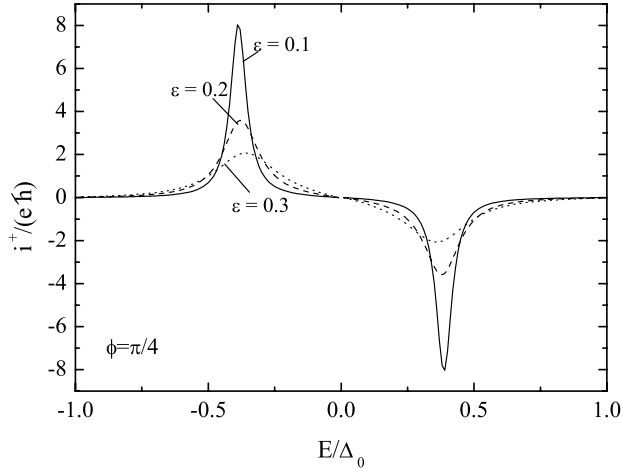


**Fig. 8.2.** Charge current density $i^+/(e\hbar)$ as a function of the energy $E/\Delta_0$ for a junction in the short limit ($L = 0$). The coupling strength $\varepsilon$ is varied as a parameter from 0.1 to 0.3. The transmission and reflection probabilities were calculated according to $D = (\sqrt{1-2\varepsilon} - 1)^2/4$ and $R = (\sqrt{1-2\varepsilon} + 1)^2/4$

to the coupling to the normal reservoir ($\varepsilon > 0$), the charge current density is now extended over a broad energy range. This is in contrast to the case where the junction is decoupled from the reservoir. For the latter case, only a sharp current density peak at

$$E_{\mathrm{B}}^{\pm} = \pm\Delta_0\sqrt{1 - D\sin^2(\phi/2)} \tag{8.10}$$

is found. The broadening of the current density spectrum for finite values of $\varepsilon$ results in a rounding of the current–phase relation $I(\phi)$ and thus to a decrease of the critical current [15, 17].

Part of the nonequilibrium current ($V \neq 0$) can be associated with the nonequilibrium population of the resonant Andreev states that exist:

$$I_{\mathrm{r}} = \int \mathrm{d}E \left(\frac{i^+}{2}(f_{\mathrm{e}} + f_{\mathrm{h}} - 2f_0)\right) . \tag{8.11}$$

The current contributions $I_{\mathrm{eq}}$ and $I_{\mathrm{r}}$ are both related to the current density $i^+$, which is equal in both leads. However, the difference current densities $i_j^-$ are not equal in leads 2 and 3, as can be seen by comparing (8.4a) and (8.4b). Nevertheless, the second terms of the two expressions are identical and, in addition, this contribution survives even in the limit of $\varepsilon \to 0$. The corresponding current density contribution of $i^- = i^{\mathrm{e}} - i^{\mathrm{h}}$, defined as the anomalous current density $i_{\mathrm{a}}$, is given by

$$i_{\mathrm{a}} = -\sigma\frac{8e}{h}\frac{\varepsilon}{\Gamma}\left(\sqrt{RD - \varepsilon^2/4}\sin\phi\sin^2\theta\right) , \tag{8.12}$$

resulting in an anomalous current

$$I_{\mathrm{a}} = \int \mathrm{d}E \left(\frac{i_{\mathrm{a}}}{2}(f_{\mathrm{e}} - f_{\mathrm{h}})\right) . \tag{8.13}$$

The anomalous current is due to the important modifications of the Andreev states caused by the open normal lead. This situation is depicted in Fig. 8.3. Owing to the coupling to the normal reservoir, the electron and hole current densities $i^{\mathrm{e}}$ and $i^{\mathrm{h}}$ differ. This leads to a finite difference current $i^-$, which has the same sign for both resonances.

The contributions to $i_2^-$ and $i_3^-$, which are different in leads 2 and 3, originate from the current density $i_{\mathrm{inj}}$ injected into lead 1:

$$i_{\mathrm{inj}} = i_3^- - i_2^- = \frac{4e}{h}\frac{\varepsilon^2}{\Gamma}\sin^2\theta(1 + \cos\phi) . \tag{8.14}$$

The corresponding injection current in lead 1 is

$$I_1 = I_{\mathrm{inj}} = \int \mathrm{d}E \left(\frac{i_{\mathrm{inj}}}{2}(f_{\mathrm{e}} - f_{\mathrm{h}})\right) . \tag{8.15}$$

For a short junction ($L = 0$), only two resonant Andreev states exist for $|E| \leq \Delta_0$ and the continuous current is zero (see, e.g., Fig. 6.5). At zero temperature and for $\varepsilon \ll 1$ only the lower one of these levels is populated.

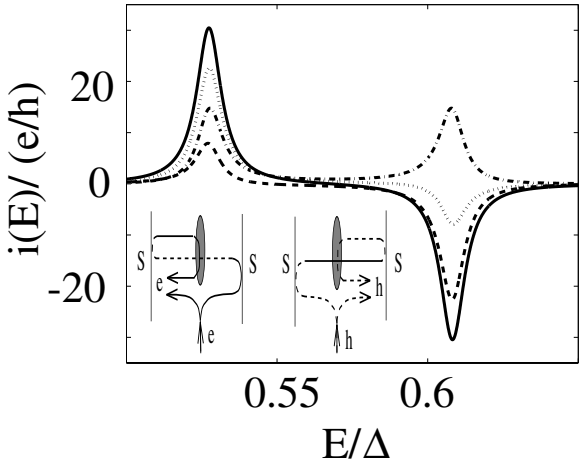


**Fig. 8.3.** The charge current density for two resonant Andreev levels for injected electrons $i^{\mathrm{e}}$ (*dotted line*) and holes $i^{\mathrm{h}}$ (*dashed line*); $i^{+}$ (*solid line*) and $i^{-}$ (*dash-dotted line*) are the sum and difference current densities, respectively. The difference current has the same sign for both resonances. The *inset* shows the corresponding current paths for an injected electron (*solid line*) and a hole (*dashed line*) at resonance [202] (© (2000) by the American Physical Society)

If a voltage is applied ($V > 0$), the electron and hole populations are shifted upwards and downwards, respectively, in energy. For a voltage that reaches the upper Andreev level ($E_{\mathrm{B}}^{+}$), this level becomes populated and the current in the junction jumps abruptly, as shown in Fig. 8.4. The contribution of $I_{\mathrm{eq}}$ is totally compensated by the regular current $I_{\mathrm{r}}$, so that $I_{\mathrm{eq}} + I_{\mathrm{r}}$ is zero for $eV > E_{\mathrm{B}}^{+}$. This cancellation can be understood as a result of the occupation of two resonant Andreev levels with opposite current directions (see Fig. 8.2). The anomalous current $I_{\mathrm{a}}$ jumps by the amount [202]

$$\delta I_{\mathrm{a}} = \sigma \frac{e\Delta_0}{2\hbar} \frac{\sqrt{R}D \sin\phi |\sin(\phi/2)|}{1 - D\sin(\phi/2)} \tag{8.16}$$

and is thus the only remaining current for $eV > E_{\mathrm{B}}^{+}$ (Fig. 8.4).

In a long junction with $L \gg \xi_0$, several resonant Andreev levels are found within the gap ($|E| \leq \Delta_0$), as can be seen, for example, in Fig. 6.2. Each of these Andreev levels carries a supercurrent in the opposite direction to its neighboring states. As a consequence, most of the current is compensated in equilibrium. If an increasing voltage is applied to the normal lead the current $I_{\mathrm{eq}} + I_{\mathrm{r}}$ reverses sign each time a further Andreev level is reached by $eV$, as shown in Fig. 8.5. In contrast to the current reversal due to the oscillating contribution of $I_{\mathrm{r}}$, the anomalous currents $I_{\mathrm{a}}$ add up with the same sign for all levels, as can be seen in Fig. 8.6. The corresponding current–voltage characteristic of the anomalous current contribution has a staircase-like shape.

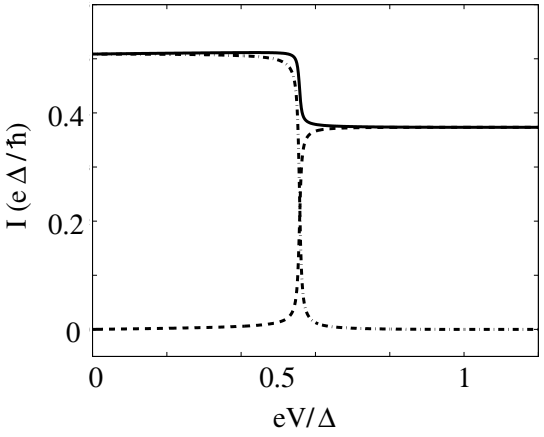


**Fig. 8.4.** The sum of the equilibrium and regular currents $I_{\rm eq} + I_{\rm r}$ (*dash-dotted line*) and the anomalous current $I_{\rm a}$ (*dashed line*) as a function of the applied voltage $eV/\Delta_0$ for a short junction with $L = 0$, for $D = 0.8$, $\phi = 3\pi/4$, $\varepsilon = 0.01$ and $\sigma = -1$ at $T = 0$. $I_{\rm eq} + I_{\rm r}$ jumps to zero if the applied voltage reaches the upper Andreev level. The remaining total current $I_{\rm eq}+I_{\rm r}+I_{\rm a}$ (*solid line*) is in this regime exclusively carried by the anomalous current [202] (© (2000) by the American Physical Society)

In principle, this anomalous nonequilibrium Josephson current is expected to be observable even when the equilibrium supercurrent or the regular current is exponentially small at finite temperature. However, since the anomalous current is a quantum interference term, this contribution depends very sensitive on the scattering phases. Thus, for junctions which are extended in two dimensions, the scattering phases for different modes will be different and on average will roughly be zero [208]. Under these conditions, $I_{\rm r}$ would be the only observable nonequilibrium current contribution at sufficiently low temperatures.

### 8.1.2 Carrier Injection in a Four-Terminal Junction

In the treatment above, a three-terminal configuration was assumed. A four-terminal junction, with two normal electrodes on each side of the junction, has the advantage that a symmetric injection condition can be obtained by biasing one normal electrode at $V/2$ and the opposite one at $-V/2$. The extension to a four-terminal structure in the fully ballistic regime was discussed theoretically by Ilhan and Bagwell [209] and by Samuelsson et al. [202]. Here, we shall consider an alternative concept of a four-terminal junction, where the normal-conducting part of the superconductor is found in the center part of a diffusive normal-conducting wire. This configuration was chosen by Wilhelm et al. [205] in order to model a diffusive junction with two long diffusive wires

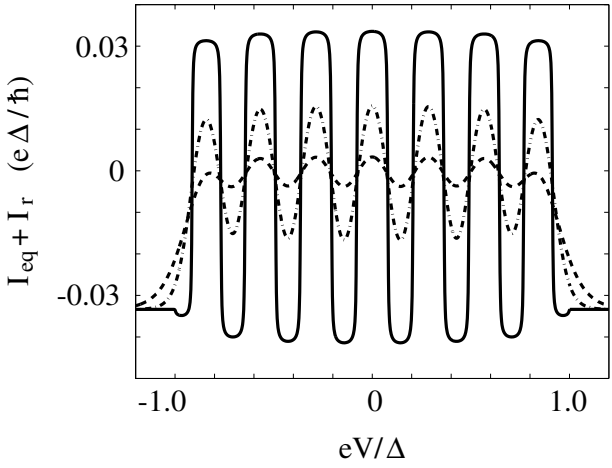


**Fig. 8.5.** The equilibrium current $I_{eq}$ plus the regular nonequilibrium current $I_r$ as a function of the applied voltage $eV/\Delta_0$ at $T = 0$ (*solid line*), $k_BT = 0.04\Delta_0$ (*dash-dotted line*) and $k_BT = 0.07\Delta_0$ (*dashed line*). The following parameters were used: $L = 10\,\xi_0$, $\phi = \pi/2$, $D = 0.8$ and $\varepsilon = 0.05$. For $eV > \Delta_0$ the current corresponds to the continuous current [202] (© (2000) by the American Physical Society)

connected to normal reservoirs. Here, we shall discuss the case of diffusive normal-conducting wires attached to a junction in the ballistic regime [210]. This condition is fulfilled if the length $L_w/2$ of each piece of wire is much longer than the elastic mean free path $l_{el}$ but the junction length $L$, which is equal to the wire width, is smaller than $l_{el}$. The junction itself is regarded as one-dimensional.

If we assume that the two ends of the normal reservoirs are connected by a sufficiently long wire, with a total length $L_w$ smaller than the inelastic scattering length $l_{in}$, then, according to Pothier et al. [211, 212], the distribution function along the wire can be expressed as

$$f(E) = (1 - y/L_w) f_0(E - eV/2) + (y/L_w) f_0(E + eV/2)\,. \tag{8.17}$$

Here, $f_0(E \pm eV/2)$ are the distribution functions of the normal reservoirs shifted by $\pm eV/2$ with respect to the chemical potential of the superconductive electrodes. Let us assume a short one-dimensional junction located in the middle of the wire ($y = L_w/2$), then the distribution function at the position of the junction has a double-step shape, as depicted in Fig. 8.7. The supercurrent in such a short junction, with $\delta$ barriers at the SN interfaces, can be obtained by inserting the modified occupation of $E_B^{\pm}$ into (6.26) [210]:

$$\begin{aligned} I_{dis}(\phi) &= \frac{e\Delta_0}{\hbar} \frac{\sin\phi}{4\sqrt{[\cos^2(\phi/2) + 4Z^2](1 + 4Z^2)}} \\ &\quad \times \left( \tanh \frac{E_B^+ - eV/2}{2k_BT} + \tanh \frac{E_B^+ + eV/2}{2k_BT} \right). \end{aligned} \tag{8.18}$$

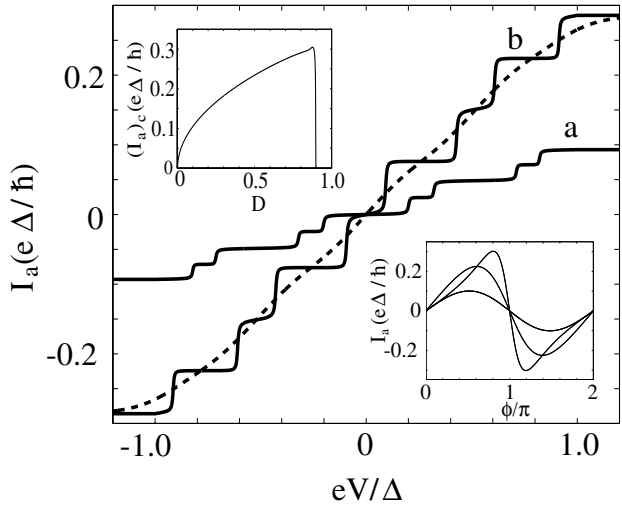


**Fig. 8.6.** The anomalous current as a function of the applied voltage $eV/\Delta_0$ for (*curve a*) $\phi = \pi/4$ and (*curve b*) $\phi = 3\pi/4$ for a junction with the following parameters: $L = 10\xi_0$, $\phi = \pi/2$, $D = 0.8$ and $\varepsilon = 0.05$. At zero temperature (*solid line*) steps are found, which are averaged out if $T$ is increased to $0.1\,\Delta_0/k_B$ (*dashed line*). The *upper inset* shows the critical anomalous current at $eV = \Delta_0$ as a function of the transparency $D$ for $\varepsilon = 0.1$. The *lower inset* shows the anomalous current $I_a(eV = \Delta_0, k_B \gg \hbar v_F/L)$ as a function of the phase difference for $D = 0.1,\ 0.5,$ and 0.9 [202] (© (2000) by the American Physical Society)

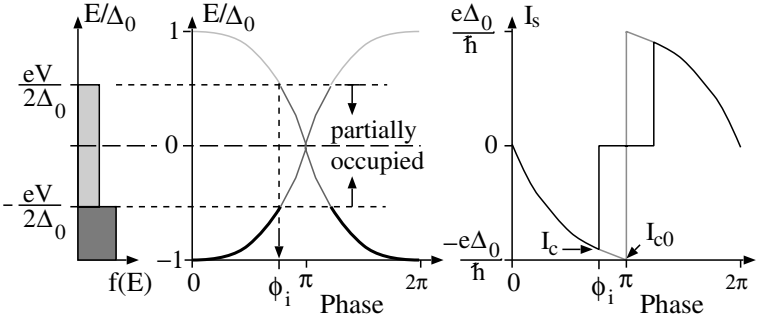


**Fig. 8.7.** Decrease of the critical current due to nonequilibrium carriers. The partial filling of the Andreev levels for energies $-eV/2 < E < eV/2$ leads to a cancellation of the supercurrents carried by the two Andreev levels. As a consequence the critical current is reduced from $I_{c0}$ to $I_c$

The effect of a nonequilibrium distribution function on a short junction at $T = 0$ with no barriers ($Z = 0$) is depicted in Fig. 8.7. Owing to the voltage $V$ applied between the ends of the normal-conducting wire, the An-

dreev levels in the energy interval $[-eV/2, eV/2]$ are only halffilled because of the modified distribution function $f(E)$. As a consequence the supercurrent $I_{\rm dis}(\phi)$ switches to zero when the phase difference $\phi$ lies in the interval $[\phi_{\rm i},\, 2\pi - \phi_{\rm i}]$ (see Fig. 8.7). Here $\phi_{\rm i}$ is the phase where the upper step of $f(E)$ matches the upper Andreev level. Consequently, the critical current, which was originally found at $\phi = \pi$ with a value of $I_{\rm c0} = e\Delta_0/\hbar$, is now reduced to a lower value $I_{\rm c}$. This effect can be used as a control mechanism, since by changing the applied voltage $V$ on the normal conductor, the critical current can be adjusted.

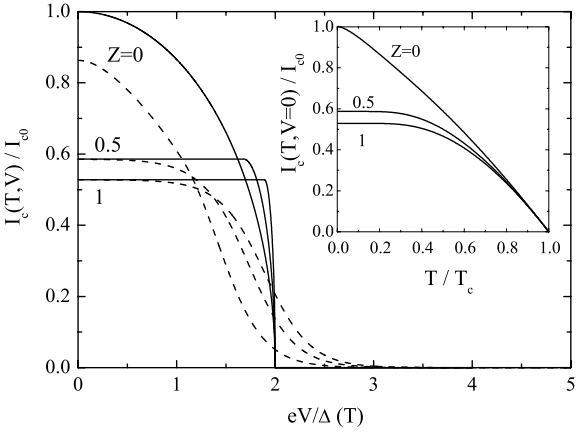


**Fig. 8.8.** Critical current as a function of the applied voltage for various values of the $Z$ parameter at $T = 0$ (*solid lines*) and $T = 0.2T_{\rm c}$ (*dashed lines*). The *inset* shows the normalized critical current $I_{\rm c}(T, V = 0)/I_{\rm c0}$ vs. $T$ for the corresponding $Z$ parameters [210]

In Fig. 8.8 the critical current, calculated from (8.18), is plotted as a function of the applied voltage. In case of no barrier at the interface ($Z = 0$) the critical current decreases immediately at $T = 0$, as well as at $T = 0.2\,T_{\rm c}$ if a voltage $V$ is applied. This behavior can be understood by considering the Andreev-level spectrum sketched in Fig. 8.7. Even a small voltage leads to a rearrangement of the Andreev-level filling in the vicinity of a phase difference $\pi$. The situation changes completely if a barrier is present at the interface ($Z > 0$), since now a gap appears in the Andreev -level spectrum (see Fig. 6.5). Here, a finite bias voltage is necessary to cause the upper Andreev level to be occupied. Consequently, up to bias voltages $eV < E_{\rm gap}$, no influence on the critical current is expected at $T = 0$; a plateau develops. Increasing the temperature leads to a shortening of this plateau owing to the thermal smearing of the nonequilibrium distribution function.

## 8.2 Supercurrent Control by Nonequilibrium Carriers: Experiments

Concerning the experimental realization of Josephson junctions which can be controlled by injected carriers, two type of structures will be introduced. First, an InAs step edge junction is discussed, where the carriers are injected from a $\delta$-doped layer into the channel along the step. In the remaining part of this section it will be shown how carrier injection can be utilized in junctions with a buried two-dimensional electron gas in a heterostructure.

### 8.2.1 Carrier Injection in an InAs Step Junction

An InAs step edge junction, as depicted in Fig. 3.5a, has the advantage that the channel length is simply defined by the depth of the step. Furthermore, the characteristics of the junction can be modified by using an epitaxially grown layer system. In Fig. 8.9 such a type of InAs step edge junction is shown, where an inserted p-type $\delta$-doped layer is introduced, in order to control the two-dimensional channel along the step. The conductive $\delta$-doped layer is contacted by an additional Au electrode. The underlying idea of this kind of structure is that a barrier is formed in the two-dimensional channel owing to the pn junction at the intersection between the p-type $\delta$-doped layer and the surface channel. This barrier determines the coupling $\varepsilon$ to the junction. By applying an appropriate voltage to the control electrode, the barrier height can be controlled by changing the space charge area. Owing to the relatively high transparency of the barrier formed by the pn junction, hot-carrier injection is a major contribution to the characteristics of the structure.

In order to obtain isolation between the different terminals of the structure, an InGaAs barrier combined with an InGaAs cap layer was grown in addition [32]. Only on those areas where this bilayer was removed by wet chemical etching was the InAs surface two-dimensional electron gas recovered. This was done before the two Nb electrodes were deposited, as shown in Fig. 8.9.

A typical set of current–voltage characteristics of an InAs step junction with a $\delta$-doped layer as an injector is shown in Fig. 8.10a. For zero voltage applied to the control electrode, the junction has a critical current $I_c$ of 320 μA and a normal resistance $R_N$ of 1.6 Ω at 4.2 K, thus yielding an $I_cR_N$ product of 510 μV. When a voltage is applied to the control electrode, the width of the superconducting state in the characteristic is reduced. This can be seen better in Fig. 8.10b, where the difference $2I_c = I_{c+} - I_{c-}$ between the positive value $I_{c+}$ and the negative value $I_{c-}$ of the critical current is plotted. For negative control voltages the double critical current $2I_c$ is reduced from an initial value of 640 μA to a value below 500 μA at a control voltage of −500 mV. A maximal superconducting transconductance $g_m^s$, as defined in (7.4), of 12 mS/mm was obtained for the control voltage interval [−200 mV,

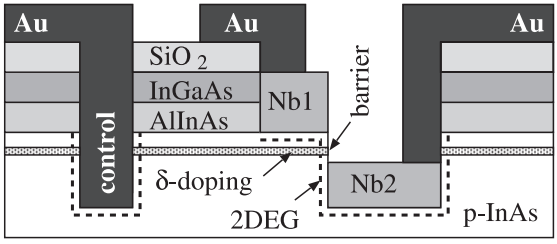


**Fig. 8.9.** Schematic illustration of an InAs step junction. The supercurrent flows in the surface two-dimensional electron gas along the step between the two Nb electrodes. The junction has a length of 120 nm and a width of 20 μm. The InAlAs and InGaAs layers serve as a barrier and a cap layer, respectively. Control of the junction is obtained by injecting carriers via the p-type δ-doped layer. The $SiO_2$ layer is used to prevent leakage currents from the Au electrodes

−100 mV], which is larger than the values obtained for JoFET structures [11]. For positive voltages applied to the control electrode, $2I_c$ first increases slightly and then decreases for $V_g > 200$ mV.

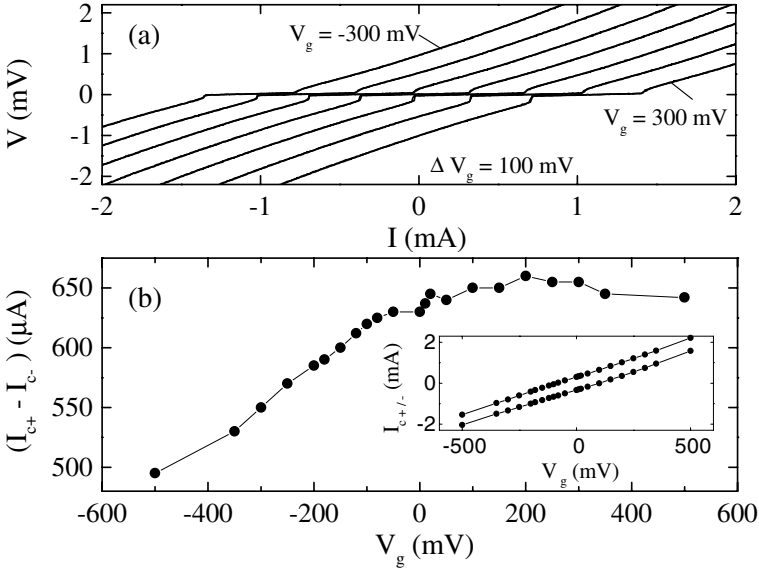


**Fig. 8.10.** (**a**) Current–voltage characteristics of an InAs step edge junction at 4.2 K controlled by a current injected from a δ-doped layer. From *left* to *right*, voltages $V_g$ of −300, −200, ..., 200 and 300 mV were applied between the control electrode and the upper Nb electrode. (**b**) The difference between the positive value ($I_{c+}$) and the negative value ($I_{c-}$) of the critical current ($2I_c = I_{c+} - I_{c-}$) as a function of $V_g$. The *inset* shows the positive value ($I_{c+}$) and negative value ($I_{c-}$) of $2I_c$ [20]

The observed shift of the current–voltage characteristic (Fig. 8.10) when a control voltage is applied indicates that a considerable amount of carriers are injected from the $\delta$-doped layer into the channel. The shift is due to the fact that this current is superimposed on the current flowing between the two superconducting Nb electrodes. The large injection current indicates that the barrier formed by the pn junction is relatively transparent.

The asymmetry shown in Fig. 8.10b can be explained by the pn junction at the intersection between the p-type $\delta$-doped layer and the n-type surface two-dimensional channel. As mentioned above, owing to this pn junction a barrier arises between these two degenerate sections [77]. If a negative control voltage is applied, the barrier height is increased and the carrier concentration is reduced owing to pinning at the surface. The resulting higher resistance of the channel leads to the observed reduction of the critical current. If a positive voltage is applied, the barrier in the channel is lowered, leading to an increase of $I_c$. Comparison with the theoretical models in the preceding section shows that in this structure it is possible to control the coupling strength $\varepsilon$ with the applied voltage. The reduction of $I_c$ for higher positive control voltages can be attributed to heating effects. Owing to high transparency of the barrier, a considerable current flows from the $\delta$-doped layer into the two-dimensional channel. At zero bias a low $\mathrm{d}V/\mathrm{d}I$ value of 140 $\Omega$ was observed. Thus the large current injected from the $\delta$-doped layer into the channel leads to a heating and thus to a broadening of the Fermi distribution function. As explained in the preceding section, this leads to a rearrangement of the occupation of the Andreev bound states in the junction. The net supercurrent decreases owing to the occupation of Andreev states carrying a supercurrent in the opposite direction.

When the p-type $\delta$-doped layer was replaced by an n-type $\delta$-doped layer, a reduction of the critical current was observed as well, but now almost symmetrically with respect to the polarity of the control voltage or current [32]. In this case no barrier is formed between the two-dimensional channel at the step edge and the $\delta$-doped layer. The change in the supercurrent is in this case solely due to carrier injection effects, without any change of the coupling of the injector to the channel. The resulting heating of the carriers by hot-carrier injection results in a reduction of the critical current.

### 8.2.2 Multiterminal Josephson Junctions

In order to feed an additional current through the buried 2DEG located between the superconducting electrodes, ohmic contacts have to be fabricated in addition. A top view of a typical junction with normal-conducting 2DEG leads is shown in Fig. 8.11, while a detail of the junction is depicted in Fig. 8.12. For the InGaAs/InP heterostructures, an Ni/Au:Ge/Ni layer system was used. The four ohmic contact areas are connected to the junction via two-dimensional-electron-gas leads. As an alternative to structures based on an InGaAs/InP layer system, an $Al_{0.2}Ga_{0.8}Sb$/InAs heterostructure grown

by molecular beam epitaxy can also be used as a 2DEG [85]. The ohmic contacts for the corresponding Nb–AlGaSb/InAs–Nb junctions were fabricated by using a Pd/Au layer system [23].

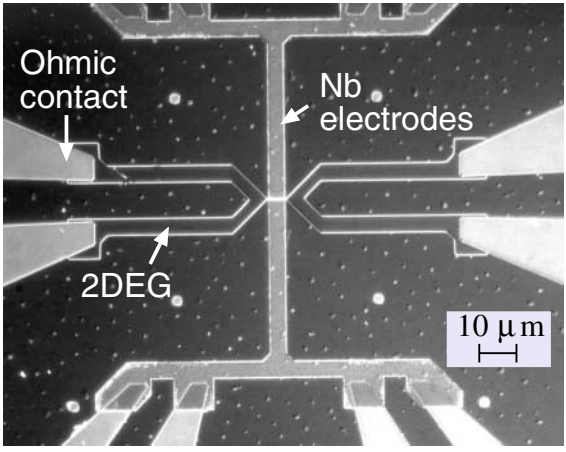


**Fig. 8.11.** Top view of an Nb–InGaAs/InP–Nb junction with additional ohmic contacts to the normal-conductive area of the junction

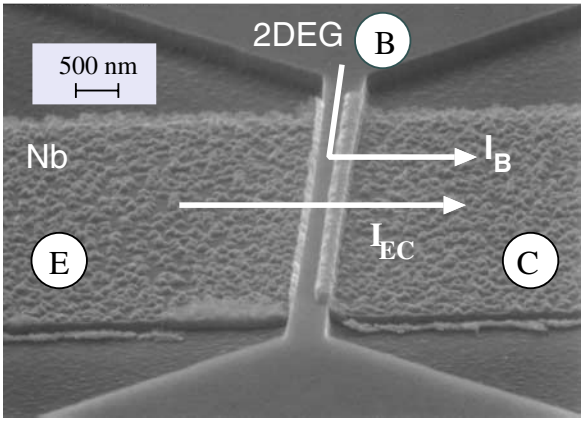


**Fig. 8.12.** Scanning electron micrograph of an Nb–InGaAs/InP junction. The normal-conductive area of the junction is connected on both sides to ohmic contacts so that a current $I_B$ can be injected into the junction. The separation of the superconducting electrodes shown is 400 nm, while the width of the Nb electrodes is 6 µm. The *arrows* indicate the flow of the bias current $I_{EC}$ and the injection current $I_B$

The fact that an injection current $I_B$ can be utilized to control a Josephson junction is demonstrated in Fig. 8.13. Referring to the measurement setup shown in Fig. 8.14, the control current is fed from terminal B into the Nb electrode C, which serves as a common ground for this circuit. For small control currents ($I_B < 50$ nA) a strong effect on the junction $I$–$V$ characteristic is observed, while for larger values of $I_B$ the effect on the characteristic is smaller. A closer inspection of the curves in Fig. 8.13 shows that the $I$–$V$ characteristics are slightly shifted upwards for reverse control currents ($I_B < 0$) and downwards for the forward control currents. Therefore the switching of the junction into the resistive state in the forward direction $I_{c+}$ and in the reverse direction $I_{c-}$ was plotted as two separate lines in Fig. 8.15 for the following analysis.

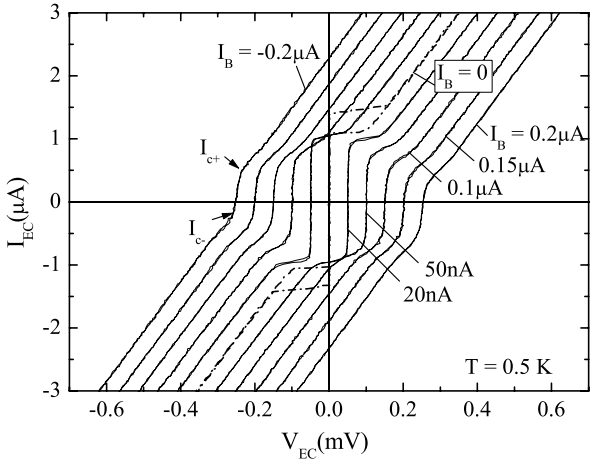


**Fig. 8.13.** Current–voltage characteristics for different injection currents, varied as a parameter. The curves for reverse ($I_B < 0$) and forward ($I_B > 0$) control currents are shifted in steps of 50 μV [22]

The critical current $I_c = (I_{c+} - I_{c-})/2$ and the offset current $I_{offset} = (I_{c+} + I_{c-})/2$ can be determined from $I_{c-}$ and $I_{c+}$ (Fig. 8.15). The offset current is due to the fact that in the superconducting state of the junction both Nb electrodes are at the same electrical potential. Therefore, part of the injection current flows first into the opposite electrode E, as depicted in Fig. 8.14. Subsequently, this current component is transferred into electrode C as a supercurrent. Owing to this current contribution, the threshold of $I_{EC}$ for switching into the resistive state is shifted. In fact, in this particular junction the current contribution which flows first into E is even larger than the contribution which directly flows into C, since the $I_{offset}(I_B)$ curve has a slope of $-0.7$, instead of the value of $-0.5$ for symmetric injection. The asymmetric injection is due to different interface transparencies on the two

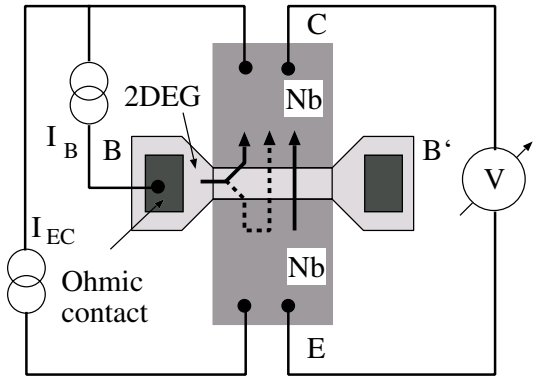


**Fig. 8.14.** Schematic illustration of the setup for a three-terminal measurement. Contact C is used as a common ground. The *arrows* show the current paths in the junction. The *broken arrow* represents the injection current which flows first into the opposite electrode E

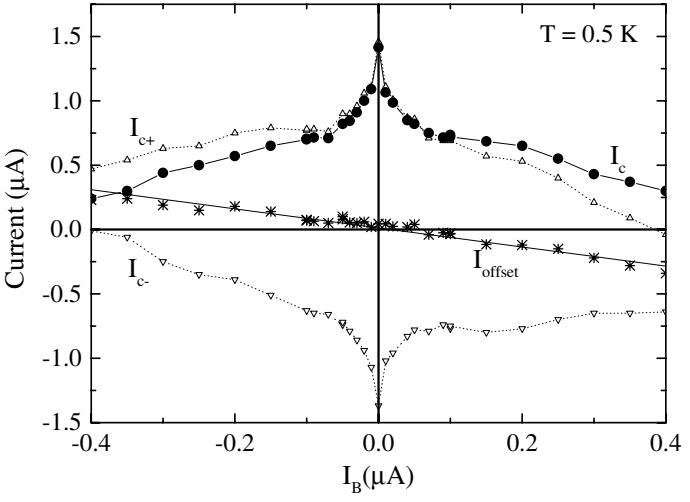


**Fig. 8.15.** Upper critical current $I_{c+}$ ($\triangle$) and lower critical current $I_{c-}$ ($\triangledown$) as a function of the injection current $I_B$. The critical current $I_c$ ($\bullet$) and the offset current $I_{offset}$ ($*$) were determined from $I_{c\pm}$ [22]

sides of the junction. For this sample, the resistance from B to E was higher by 20 Ω than the resistance from B to C.

As noted above, for small injection currents ($I_B \leq 50$ nA) a very strong effect on the critical current $I_c$ is observed, e.g. $I_B = 50$ nA is sufficient to reduce the initial critical current of 1.48 μA by 43%. As can be seen in

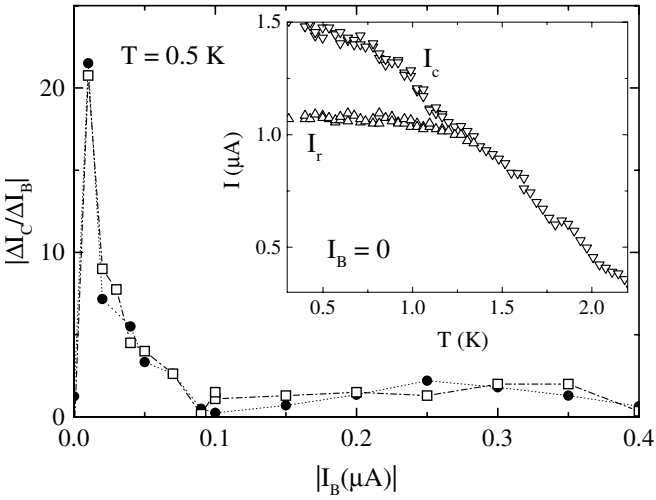


**Fig. 8.16.** $|\Delta I_c/\Delta I_B|$ as a function of the injection current. The *inset* shows $I_c$ ($\bigtriangledown$) and $I_r$ ($\bigtriangleup$) vs. temperature [22]

Fig. 8.16, a ratio of critical current to control current $|\Delta I_c/\Delta I_B|$ as large as 20 was observed at low values of $|I_B|$. For larger injection currents the decrease of $I_c$ is slower.

The model describing the effect of nonequilibrium carriers on the Josephson effect introduced in Sect. 8.1 can be utilized to explain the measured data. The condition that the junction should be in the short limit is fulfilled, since only two Andreev bound states are present below $\mu$ (see Fig. 6.6). Nevertheless, some differences have to be considered. First, in the experiment a current $I_B$ was injected into the junction, while in the theoretical model a voltage was applied to the normal leads. Second, the junction discussed in the model was one-dimensional, whereas the measured junction has a width of 6 μm. Concerning the first statement, the injection of a current into the normal-conducting region of the junction is of course accompanied a voltage drop between the semiconductor and the superconductor. However, the voltage drop is not constant but, rather, decreases from the entrance point of the junction to the opposite side. Typical values for the voltage drop at the Nb/2DEG interface were 0.18 mV at the injection point and 5 μV at the other end for an injection current of $I_B = 0.1$ μA. Consequently, in a more elaborate model an averaging along the junction would be desirable.

Comparing the theoretical results plotted in Fig. 8.8 with the experimental $I_c$ vs. $I_B$ values shows that the plateau predicted in the model for a finite $Z$ parameter is not observed in the experiment. Nevertheless, since the temperature dependence of the critical current tends to saturate at low temperatures in accordance with the finding discussed in Sec. 6.2.1, a barrier must be

present at the interface and thus a finite $Z$ parameter can be assumed. One possible reason for the absence of the plateau in the $I_c(I_B)$ measurements is the two-dimensional character of the junction, which implies that the gap in the Andreev-level spectrum is lowered owing to wave vectors with a component parallel to the Nb/2DEG interface. In addition, Ilhan and Bagwell [209] showed that even if the supercurrent switches abruptly as a function of the injection voltage, the supercurrent changes only slowly as a function of the injection current.

As demonstrated by Morpurgo et al. [21], an injection current can lead to a heating of the normal-conductive region of the junction up to an effective temperature $T^*$ [211]. In this model, the broadening of the distribution function $f(E)$ due to electron–electron scattering processes leads to a decrease of the net supercurrent. However, as explained below, in contrast to the results obtained on Nb/Au junctions [21], it is not possible to explain the sharp decrease of the critical current in the Nb/2DEG structures solely by heating.

For the following discussion we shall refer to experiments on Nb–AlGaSb/InAs–Nb junctions [23, 107]. During these measurements the injection current $I_{B,B'}$ was driven through the 2DEG from the ohmic contact B on one side of the junction to the contact B′ on the opposite side (Fig. 8.14). In accordance with the results in Fig. 8.15, the critical current first decreases strongly for smaller injection currents, while a slower decrease is observed for larger injections currents (Fig. 8.17). From the voltage drop $V_{inj}$ measured between the two ends of the control line, the effective temperature $T^*$ was determined by using the following expression [211]:

$$T^*(y) = \sqrt{T^2 + (y/L_w)(1 - y/L_w)(3e^2/\pi^2 k_B^2)V_{inj}^2}\,. \tag{8.19}$$

For the analysis, the effective temperature $T^*(y = L_w/2)$ at the center of the junction, with $T = 0.6$ K, was taken as an average value. In Fig. 8.17 (inset) the critical current is plotted as a function of $T$ and $T^*$. Obviously, the $I_c(T^*)$ curve beginning at $T = 0.6$ K decreases considerably more steeply than the $I_c(T)$ curve; only at higher temperatures $T$, $T^*$ do both curves merge.

From the difference between the two curves at low temperatures it can be concluded that, at least at low injection currents, different mechanisms are responsible for the steep decrease of $I_c$ with $I_B$ and with $T^*$. In order to obtain a broadening of the distribution function, which can be interpreted as a higher effective temperature $T^*$, electron–electron scattering processes are necessary. By using the formula of Giuliani and Quinn [213], the inelastic scattering length $l_{in,ee}$ can be estimated for typical injection energies. For an excess energy of 2 meV and a Fermi energy of 30 meV, $l_{in,ee} \approx 7\mu$m. This result shows that even for injection energies where the critical current is almost completely suppressed, the inelastic scattering length is larger than the width of the junction. This result leads us to the conclusion that the distribution resembles more a step-like distribution function, as in the model introduced in Sect. 8.1.2, than a broadened distribution function. This statement holds for

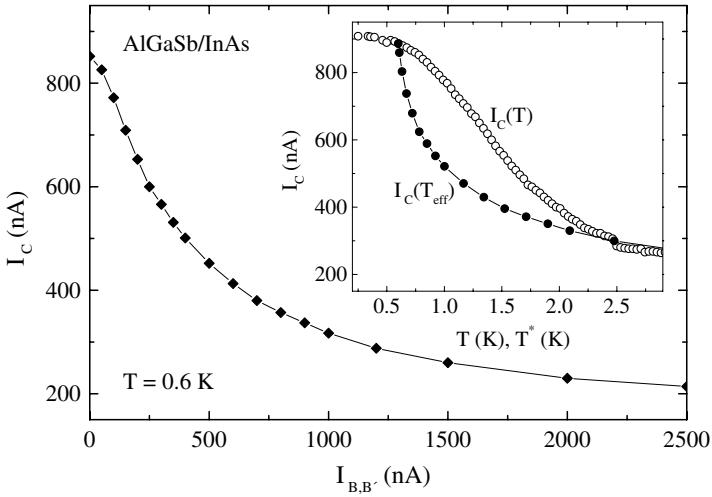


**Fig. 8.17.** Critical current vs. injection current $I_{\mathrm{B,B'}}$ fed from terminal B to terminal B′ for an AlGaSb/InAs-based junction. The *inset* shows $I_{\mathrm{c}}$ as a function of the bath temperature $T$ and effective temperature $T^*$ [210]

the AlGaSb/InAs-based junction as well as for the Nb–InGaAs/InP–Nb junction. However, for larger injection currents heating effects due to electron–electron scattering will at least partially contribute to the reduction of $I_{\mathrm{c}}$, which can be concluded from the fact that both curves in Fig. 8.17 (inset) merge for larger temperatures $T$, $T^*$.

Morpurgo et al. [214, 215, 216] used a junction connected to a superconducting ring, similar to the configuration shown in Fig. 8.1, in order to detect the discrete Andreev levels in the junction formed by the two superconducting terminals of the ring and the 2DEG in between. For an increasing magnetic field, the differential resistance $\mathrm{d}V/\mathrm{d}I$ of this structure showed an oscillation pattern with a period of the flux quantum threaded through the ring. If now an injection voltage was applied, a change of the $\mathrm{d}V/\mathrm{d}I(B)$ oscillation amplitude, accompanied by a phase shift, was observed. By using a microscopic model, based on an analysis of the interference processes occurring within the junction, Morpurgo et al. could explain the modification of the oscillation pattern by the presence of discrete Andreev bound states.

In contrast to junctions with a semiconducting channel, a reversal of the supercurrent, as discussed in Sect. 8.1, was observed by Baselmans et al. [217, 218] in a purely metallic four-terminal Nb/Au junction. The observed effects could be explained consistently by the model in the diffusive regime of Wilhelm et al. [205].

By employing superconducting aluminum electrodes as injectors, Kutchinsky et al. [219] obtained an enhancement of the critical current in an Al/n-type GaAs/Al Josephson junction when the injection voltage reached $\Delta_0/e$.

This effect can be explained by the peak of the density of states in the superconducting injectors at $\Delta_0$. If this singularity in the density of states of the injectors matches the chemical potential of the junction, the critical current is enhanced.

### 8.2.3 Local Suppression of the Josephson Current

Depending on the width of the structure, carrier injection from one side or the other into the junction is not always sufficient to suppress the Josephson supercurrent completely. This can be seen in Fig. 8.18, where the critical current of the junction is plotted for different modes of carrier injection. In the case of a carrier injection from either contact A or contact B into S1, a finite critical current is found even for large injection currents. In contrast, if the injection current is fed from contact A to B a complete suppession is possible.

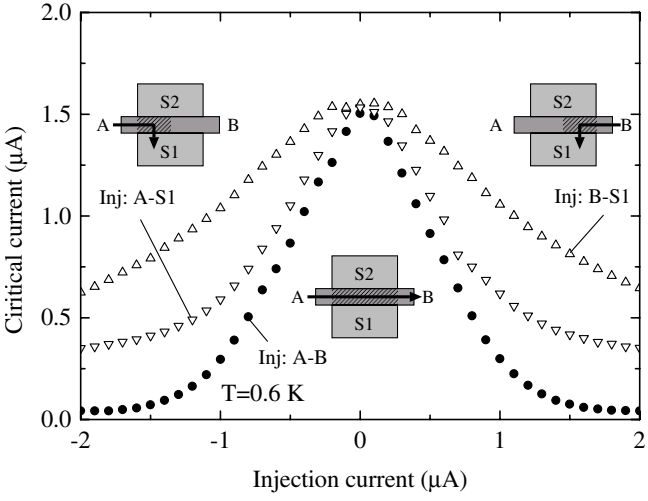


**Fig. 8.18.** Critical current as a function of the injection current for three different configurations for carrier injection. Contacts A and B are normal-conducting terminals. The critical current was determined for the junction formed by the superconducting electrodes S1 and S2 with the two-dimensional channel in between. The results of injection from either A or B into S1, as well as for a control current passing from A directly into B, are plotted

The partial suppression can be explained by the fact that for injection from A or B into S1 only part of the normal-conducting area between the superconducting electrodes is affected. This is depicted in the schematic illustration attached to the curves in Fig. 8.18. As can be seen here, the injection

current affects only the junction area in the vicinity of the injection point, whereas the area on the opposite side is more or less unaffected. Owing to the S/2DEG interface, which is not perfectly homogeneous, the efficiency of the supercurrent suppression differs according to whether the current is injected from A or B. In the case of injection from A through the normal region of the junction into B a complete suppression is observed, which shows that in this case the whole 2DEG area of the junction is affected.

More detailed information about how the injection current influences the supercurrent distribution can be gained with the help of a magnetic field. In Sect. 6.2.2 it was demonstrated that by analyzing the interference pattern of the critical current as a function of an external magnetic field, information about the supercurrent distribution in the junction area can be extracted. This method can now be employed in order to trace the region where the injection current affects the supercurrent flow.

In Fig. 8.19 the $I_c(\Phi/\Phi_0)$ interference pattern of an AlGaSb/InAs-based junction, which will serve as a reference, is plotted [23]. Here, no current is

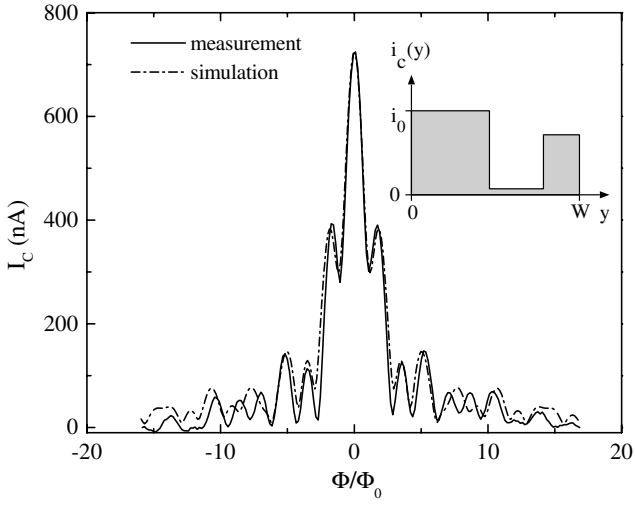


**Fig. 8.19.** $I_c(\Phi/\Phi_0)$ pattern of an AlGaSb/InAs-based junction without injection current (*solid line*) and a fit using the distribution in the *inset* (*dash-dotted line*) [23] (© (1999) by the American Physical Society)

injected from a normal lead. By using a generalized form of (6.34), the current distribution in the junction can be simulated. As can be seen in Fig. 8.19, the supercurrent distribution is largest at the left side, while almost no current is flowing in the middle. The higher current densities at the edges of the contacts can be explained by the fact that this junction can be regarded as being in the intermediate range between a short and a long Josephson junction ($W \simeq \lambda_j$,

where $\lambda_j$ is the Josephson penetration depth). The asymmetry is presumably due to inhomogeneities at the superconductor/2DEG interface.

The effect of an injection current on the supercurrent distribution in the junction is visualized in Fig. 8.20. The upper graph shows the $I_c$ vs. $\Phi/\Phi_0$

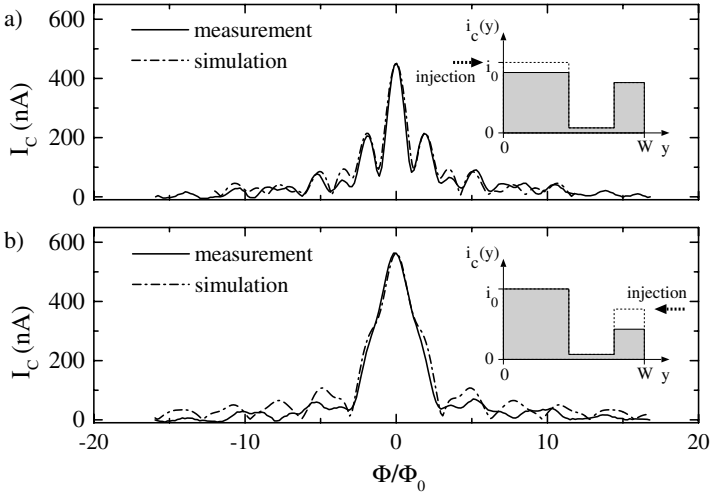


**Fig. 8.20.** (**a**) $I_c(\Phi/\Phi_0)$ for an injection current of 500 nA from the left-hand side (*solid line*) and a simulation (*dash-dotted line*) for the modified supercurrent distribution shown in the *inset*. The side of the current injection is marked by an *arrow*. (**b**) Corresponding measurement and simulation for injection from the opposite side [23] (© (1999) by the American Physical Society)

characteristic for the case where a current of 500 nA is injected from the left. Here, a three-terminal configuration as depicted in Fig. 8.14 was used. The experimental interference pattern was fitted as described above by assuming a step-like supercurrent distribution. Now, the best fit is obtained for a distribution where the supercurrent density is reduced on the left, as shown in Fig. 8.20 (inset). The interference pattern calculated using this modified current distribution matches well to the experimental curve. Since now the current distribution is more balanced, the interference pattern resembles the shape corresponding to a superconducting quantum interference device.

Analogously to the case of injection from the left-hand side, an injection current from the right-hand side leads to a decrease of the supercurrent density on this side, as shown in Fig. 8.20. Owing to the lowering of the supercurrent in the area where the current is injected, the dominant contribution to the supercurrent is now found on the opposite side. As a result, the interference pattern has approximately the shape corresponding to a shorter junction.

# 9. Conclusion

In this book the properties of superconductor/III–V semiconductor hybrid structures with a two-dimensional electron gas as a conducting channel have been reviewed. A crucial parameter for all of these structures is the transparency of the superconductor/two-dimensional-electron-gas interface. Optimizing the transparency is of course mainly a technological challenge but, as was shown, a detailed understanding of the transport processes is necessary in order to assess the experimental results obtained. At present, argon sputtering is the best-established interface-cleaning technique and is used in many laboratories. However, there is still room for further improvement. In this respect He plasma cleaning seems to be a promising method, since here the semiconductor crystal is not degraded by the sputtering process.

Comparing Josephson junctions that contain an inversion layer with junctions based on a buried two-dimensional electron gas in a heterojunction shows that the former type of structure has some advantages concerning a large characteristic voltage, which is an important parameter with respect to possible applications. However, if more fundamental questions about the transport mechanisms are to be addressed, the latter structures based on heterojunctions are almost ideal model systems, since here the transport can be regarded as ballistic. In this regime the transport processes can be described by relatively simple models.

Control of the critical current by light exposure is a typical example of how specific properties of semiconductors, in this case persistent photoconductance, can be employed. Another rather unique property is the large Fermi wavelength of the semiconductor, which is of the order of the feature size accessible by electron beam lithography. Owing to this large Fermi wavelength, remarkable quantum effects, such as the quantization of the critical current, can be observed very clearly.

In principle, a Josephson element with a semiconductor bridge between two superconducting electrodes can serve as a basis for a three-terminal electronic device, since the electron concentration of the semiconductor can be controlled easily by a gate. However, the performance of the Josephson field effect transistors obtained so far shows that, owing to many technological problems, it is questionable whether this concept will find its way into real electronic circuits.

Thomas Schäpers: Superconductor/Semiconductor Junctions, STMP 174, 133–134 (2001)
© Springer-Verlag Berlin Heidelberg 2001

Control of the Josephson current can also be obtained by injecting nonequilibrium carriers via an additional ohmic contact into the normal-conductive area of the junction. This effect can be explained theoretically within the framework of a nonequilibrium occupation of phase-coherent Andreev bound states. Currently these kinds of multiterminal structures are being intensively studied, theoretically as well as experimentally. Here, one aspect is their potential application as a transistor-like device.

Regarding future research on superconductor/two-dimensional-electron-gas structures, it will be very interesting to study the Andreev reflection process in large magnetic fields. Owing to the Landau quantization so-called edge states are formed in the two-dimensional electron gas, which couple to the superconductor. In order to preserve the superconductive state in a magnetic field, different electrode materials, e.g. NbN, have to be employed. Initial steps in this direction have been taken already [220, 221]. Another field of interest is the coupling of superconducting electrodes to a semiconductor quantum dot. Concerning theory, many effects have been predicted already [222, 223, 224, 225], but experiments on hybrid quantum dot structures are still lacking.

# References


1. K.K. Likharev: Rev. Mod. Phys. **51,** 101 (1979) 1, 105
2. A.W. Kleinsasser, W.J. Gallagher, "Three-terminal devices". In *Superconducting Devices*, ed. by S.T. Ruggiero, D.A. Rudman (Academic Press, Boston, 1990) pp. 325–372 1
3. T.M. Klapwijk: Physica B **197,** 481 (1994) 1
4. C.W.J. Beenakker: "Quantum transport in semiconductor-superconductor microjunctions". In *Mesoscopic Quantum Physics*, ed. by E. Akkermanns, G. Montambaux, J.-L. Pichard (North-Holland, Amsterdam, 1994) pp. 5–50 1
5. B.J. van Wees, H. Takayanagi, "The superconducting proximity effect in semiconductor–superconductor systems: ballistic transport, low-dimensionality and sample specific properties". In *Mesoscopic Electron Transport*, ed. by L.L. Son, L.P. Kouwenhoven, G. Schön, (Kluwer Academic Publishers, Dordrecht, 1997) pp. 469–501 1
6. K.K. Likharev: Phys. World, May, 39 (1997) 1
7. T.D. Clark, R.J. Prance, A.D.C. Grassie: J. Appl. Phys. **51,** 2736 (1980) 1, 95, 96
8. H. Takayanagi, T. Kawakami: Phys. Rev. Lett. **54,** 2449 (1985) 1, 2, 24, 27, 78, 96
9. T. Nishino, M. Miyake, Y. Harada, U. Kawabe: IEEE Electron Device Lett. **6,** 297 (1985) 1, 2, 96, 99
10. Z. Ivanov, T. Claeson: Jpn. J. Appl. Phys. (Suppl. 26-3) **26,** 1617 (1987) 1, 96
11. T. Akazaki, H. Takayanagi, J. Nitta, T. Enoki: Appl. Phys. Lett. **68,** 418 (1996) 1, 97, 97, 97, 98, 98, 99, 99, 100, 100, 122
12. A.L. Gudkov, M.Yu. Kupriyanov, K.K. Likharev: Zh. Éksp. Teor. Fiz. **94,** 319 (1988) [Sov. Phys. JETP **68**, 1478 (1988)] 1, 100
13. G.E. Rittenhouse, J.M. Graybeal: Phys. Rev. B **49,** 1182 (1994) 1, 66, 100
14. H. Takayanagi: Physica B **227,** 224 (1996) 1, 2, 27, 29
15. B.J. van Wees, K.-M. Lenssen, C.J.P.M. Harmans: Phys. Rev. B **44,** 470 (1991) 1, 111, 113, 115
16. A.F. Volkov: Phys. Rev. Lett. **74,** 4730 (1995) 1, 112
17. L.-F. Chang, P.F. Bagwell: Phys. Rev. B **55,** 12678 (1997) 1, 111, 115
18. P. Samuelsson, V.S. Shumeiko, G. Wendin: Phys. Rev. B **56,** 5763 (1997) 1, 111, 112, 113
19. S.-K. Yip: Phys. Rev. B **58,** 5803 (1998) 1, 112
20. S.G. Lachenmann, A. Kastalsky, A. Förster, D. Uhlisch, K. Neurohr, T. Schäpers: J. Appl. Phys. **83,** 8077 (1998) 1, 27, 122
21. A.F. Morpurgo, T.M. Klapwijk, B.J. van Wees: Appl. Phys. Lett. **72,** 966 (1998) 1, 128, 128


Thomas Schäpers: Superconductor/Semiconductor Junctions, STMP 174, 135–142 (2001)
© Springer-Verlag Berlin Heidelberg 2001

22. T. Schäpers, J. Malindretos, K. Neurohr, S.G. Lachenmann, A. van der Hart, G. Crecelius, H. Hardtdegen, H. Lüth, A.A. Golubov: Appl. Phys. Lett. **73,** 2348 (1998) 1, 1, 125, 126, 127
23. K. Neurohr, T. Schäpers, J. Malindretos, S. Lachenmann, A.I. Braginski, H. Lüth, M. Behet, G. Borghs, A.A. Golubov: Phys. Rev. B **59,** 11197 (1999) 1, 25, 124, 128, 131, 131, 132
24. C.W.J. Beenakker, H. van Houten: Phys. Rev. Lett **66,** 3056 (1991) 1, 2, 73, 106, 107, 107
25. A. Furusaki, H. Takayanagi, M. Tsukada: Phys. Rev. B **40,** 10563 (1992) 1, 2, 106, 108, 108, 110
26. H. Takayanagi, T. Akazaki, J. Nitta: Phys. Rev. Lett. **75,** 3533 (1995) 1, 2, 109, 109, 109
27. H. Takayanagi, T. Akazaki, J. Nitta: Phys. Rev. B **51,** 1374 (1995) 2, 92, 102
28. G. Bastian, E.O. Göbel, A.B. Zorin, H. Schulze, J. Niemeyer, T. Weimann, M.R. Bennett, K.E. Singer: Phys. Rev. Lett. **81,** 1686 (1998) 2, 25, 62, 62, 64
29. A. Chrestin, U. Merkt: Appl. Phys. Lett. **70,** 3149 (1997) 2, 27, 78, 79, 80
30. S.G. Lachenmann, A. Kastalsky, I. Friedrich, A. Förster, D. Uhlisch: J. Low Temp. Phys. **106,** 321 (1997) 2, 27, 27, 33, 78
31. S.G. Lachenmann, I. Friedrich, A. Förster, D. Uhlisch, A.A. Golubov: Phys. Rev. B **56,** 14108 (1997) 2
32. S.G. Lachenmann, I. Friedrich, A. Förster, T. Schäpers, A. Kastalsky: J. Appl. Phys. **85,** 8242 (1999) 2, 24, 121, 123
33. A. Kastalsky, A.W. Kleinsasser, L.H. Green, R. Bhat, F.P. Milliken, J.P. Harbison: Phys. Rev. Lett. **67,** 3026 (1991) 2, 31
34. K.-M. Lenssen, M. Matters, C.J.P.M. Harmans, J.E. Mooij, M.R. Leys, W. van der Vleuten, J.H. Wolters: Appl. Phys. Lett. **63,** 2079 (1993) 2
35. A.M. Marsh, D.A. Williams, H. Ahmed: Physica B **203,** 307–309 (1994) 2, 25, 30
36. C. Nguyen, J. Werking, H. Kroemer, E.L. Hu: Appl. Phys. Lett. **57,** 87 (1990) 2, 25, 62
37. J. Nitta, T. Akazaki, H. Takayanagi, K. Arai: Phys. Rev. B **46,** 14286 (1992) 2, 81
38. L.C. Mur, C.J.P.M. Harmans, J.E. Mooij, J.F. Carlin, A. Rudra, M. Illgems: Phys. Rev. B **54,** 2327 (1995) 2, 29, 30, 80, 81, 83
39. H. Hardtdegen, R. Meyer, H. Løken-Larsen, J. Appenzeller, T. Schäpers, H. Lüth: J. Crystal Growth **116,** 521 (1992) 2, 26, 32
40. H. Hardtdegen, R. Meyer, M. Hollfelder, T. Schäpers, J. Appenzeller, H. Løken-Larsen, T. Klocke, C. Dieker, B. Lengeler, H. Lüth, W. Jäger: J. Appl. Phys. **73,** 4489 (1993) 2, 26, 32
41. M.F. Tietze, T. Schäpers, J. Appenzeller, G. Engels, M. Hollfelder, B. Lengeler, H. Lüth: J. Appl. Phys. **79,** 871 (1996) 2
42. J.-O. Wesström, K. Hieke, B. Stalnacke, T. Palm, B. Stoltz: Appl. Phys. Lett. **70,** 1302 (1997) 2
43. T. Schäpers, J. Appenzeller, H. Hardtdegen, H. Lüth: J. Appl. Phys. **83,** 2360 (1998) 2
44. K. Kajiyama, Y. Mizushima, S. Sakata: Appl. Phys. Lett. **23,** 458 (1973) 2
45. K. Neurohr, A.A. Golubov, T. Klocke, J. Kaufmann, T. Schäpers, J. Appenzeller, D. Uhlisch, A.V. Ustinov, M. Hollfelder, H. Lüth, A.I. Braginski: Phys. Rev. B **54,** 17018 (1996) 2, 14, 31, 33, 34, 34, 35, 35, 36, 36, 36, 37, 37
46. G.E. Blonder, M. Tinkham, T.M. Klapwijk: Phys. Rev. B **25,** 4515 (1982) 5, 9, 12, 12, 12, 34, 46, 66
47. J. Bardeen, L.N. Cooper, J.R. Schrieffer: Phys. Rev. **108,** 1175 (1957) 5

48. P. DeGennes, *Superconductivity of Metals and Alloys* (Benjamin, New York, 1993) 6
49. A.F. Andreev: Zh. Éksp. Teor. Fiz. **46,** 1823 (1964) [Sov. Phys. JETP **19**, 1228 (1964)] 8
50. A.V. Zaitsev: Zh. Éksp. Teor. Fiz. **86,** 1742 (1984) [Sov. Phys. JETP **59**, 1015 (1984)] 9, 77
51. G.B. Arnold: J. Low-Temp. Phys. **59,** 143 (1985) 9
52. G.E. Blonder, M. Tinkham: Phys. Rev. B **27,** 112 (1983) 12
53. A.A. Golubov, M.Yu. Kupriyanov: Physica C **259,** 27 (1996) 13, 17, 54
54. R. Hoonsawat, I.M. Tang: Phys. Lett. A **127,** 441 (1988) 13, 53
55. N.A. Mortensen, K. Flensberg, A.-P. Jauho: Phys. Rev. B **59,** 10176 (1999) 13
56. M. Kupka: Physica C **221,** 346 (1994) 13
57. J. Sánchez-Cañizares, F. Sols: Phys. Rev. B **55,** 531 (1997) 13
58. B.A. Aminov, A.A. Golubov, M.Yu. Kupriyanov: Phys. Rev. B **53,** 365 (1996) 14, 17, 17, 18, 47, 54, 54, 54, 55, 59, 61
59. A. Chrestin, T. Matsuyama, U. Merkt: Phys. Rev. B **55,** 8457 (1997) 14, 27, 61, 61, 62
60. W.L. McMillan: Phys. Rev. **175,** 559 (1968) 14
61. K. Usadel: Phys. Rev. Lett. **25,** 507 (1970) 14
62. G. Eilenberger: Z. Phys. **214,** 195 (1968) 14, 15
63. M.Yu. Kupriyanov, V.F. Lukichev: Zh. Éksp. Teor. Fiz. **94,** 139 (1988) [Sov. Phys. JETP **67**, 1163 (1988)] 15
64. G.M. Eliashberg: Sov. Phys. JETP **34,** 668 (1971) [Zh. Éksp. Teor. Fiz **61**, 1254 (1971)] 15
65. A.I. Larkin, Yu.N. Ovchinnikov: Zh. Éksp. Teor. Fiz. **68,** 1915 (1975) [Sov. Phy. JETP **41** 960 (1975)] 15
66. W. Belzig, C. Bruder, G. Schön: Phys. Rev. B **54,** 9443 (1996) 16
67. A.A. Golubov, M.Yu. Kupriyanov: Pis'ma Zh. Éksp. Teor. Fiz. **61,** 830 (1995) [JETP Lett. **69**, 855 (1995)] 17, 54
68. G. Kieselmann: Phys. Rev. B **35,** 6762 (1987) 19
69. P.C. van Son, H. van Kempen, P. Wyder: Phys. Rev. B **37,** 5015 (1988) 19
70. T. Ando, A.B. Fowler, F. Stern: Rev. Mod. Phys. **54,** 437 (1982) 21, 24, 75
71. J.J. Harris, J.A. Pals, R. Woltjer: Rep. Prog. Phys. **52,** 1217 (1989) 21
72. H. Lüth, *Surfaces and Interfaces of Solid Materials* (Springer, Berlin, Heidelberg, 1996) 22
73. D.C. Tsui: Phys. Rev. Lett. **24,** 303 (1970) 22
74. E. Yamaguchi: Phys. Rev. B **32,** 5280 (1985) 22, 24, 24
75. A.G. Milnes, A.Y. Polyakov: Mater. Sci. Eng. B **18,** 237 (1993) 22
76. U. Schüssler, R. Kümmel: Phys. Rev. B **47,** 2754 (1993) 23, 66
77. R. Scharnweber, T. Matsuyama, U. Merkt: Supercond. Sci. Technol. **7,** 141 (1994) 24, 123
78. R. Dingle, H. Störmer, A.C. Gossard, W. Wiegman: Appl. Phys. Lett. **33,** 665 (1978) 25
79. L. Pfeiffer, K.W. West, H.L. Sörmer, K.W. Baldwin: Appl. Phys. Lett. **55,** 1888 (1989) 25
80. C.T. Foxon, J.J. Harris, D. Hilton, J. Hewitt, C. Roberts: Semicond. Sci. Technol. **4,** 582 (1989) 25
81. A.M. Marsh, D.A. Williams, H. Ahmed: Phys. Rev. B **50,** 8118 (1994) 25, 30
82. D.A. Williams: Superlatt. Microstruc. **25,** 701 (1999) 25
83. G. Tuttle, H. Kroemer, J.H. English: J. Appl. Phys. **65,** 5239 (1989) 25

84. G. Tuttle, H. Kroemer, J.H. English: J. Appl. Phys. **67,** 3032 (1990) 25, 25
85. M. Behet, S. Nemeth, J.D. Boeck, G. Borghs, J. Tümmler, J. Woitok, J. Geurts: Semicond. Sci. Technol. **13,** 428 (1998) 25, 124
86. C. Nguyen, H. Kroemer, E.L. Hu: Appl. Phys. Lett. **65,** 103 (1994) 25, 31
87. J.P. Heida, B.J. van Wees, T.M. Klapwijk, G. Borghs: Phys. Rev. B **57,** 5618 (1998) 25, 85, 85, 86, 86
88. C. Nguyen, B. Brar, H. Kroemer, J.H. English: Appl. Phys. Lett. **60,** 1854 (1992) 26
89. T. Akazaki, J. Nitta, H. Takayanagi, T. Enoki, K. Arai: Appl. Phys. Lett. **65,** 1263–1265 (1994) 26, 26
90. A. Richter, M. Koch, T. Matsuyama, C. Heyn, U. Merkt: Appl. Phys. Lett. **77,** 3227 (2000) 26
91. A. Richter, M. Koch, T. Matsuyama, U. Merkt: Supercond. Sci. Technol. **12,** 874 (1999) 27
92. S.G. Lachenmann, A. Kastalsky, I. Friedrich, A. Förster, A.V. Ustinov, D. Uhlisch: Czech. J. Phys. **46,** 659 (1996) 27, 78
93. A. Serfaty, J. Aponte, M. Octavio: J. Low Temp. Phys. **63,** 23 (1986) 27
94. J.H. Kaufmann: "Elektrische Transportmessungen an Supraleiter/Halbleiter/Supraleiterstrukturen im Materialsystem Nb/(InGaAs/InP)/Nb". Ph.D. Thesis, Technical University Aachen (RWTH), Ber. des Forschungszentrums Jülich, Jül-3276 (1996) 28, 29
95. S. Valeri, M. Lolli, G. Ottaviani: Vacuum **41,** 643 (1990) 29, 33, 36, 40
96. S. Valeri, M. Lolli: Surf. Interf. Anal. **16,** 59 (1990) 29, 33, 36
97. D. Uhlisch: "Ladungstransport an Grenzflächen zwischen Supraleitern und hochbeweglichen zweidimensionalen Elektronengasen". Ph.D. Thesis, Technical University Aachen (RWTH), Ber. des Forschungszentrums Jülich, Jül-3490 (1998) 29
98. J.P. Heida, B.J. van Wees, T.M. Klapwijk, G. Borghs: Phys. Rev. B **60,** 13135 (1999) 29, 30, 81
99. D.R. Heslinga, S.E. Shafranjuk, H. van Kempen, T.M. Klapwijk: Phys. Rev. B **49,** 10484 (1994) 31, 43
100. P.H.C. Magnée, N. van der Post, P.H.M. Kooistra, B.J. van Wees, T.M. Klapwijk: Phys. Rev. B **50,** 4594 (1994) 31
101. A. Kastalsky, L.H. Greene, J.B. Barner, J.P. Harbison: Phys. Rev. Lett. **64,** 958 (1990) 31
102. A.W. Kleinsasser, A. Kastalsky: Phys. Rev. B **47,** 8361 (1993) 31
103. J.R. Gao, J.P. Heida, B.J. van Wees, S. Bakker, T.M. Klapwijk: Appl. Phys. Lett. **63,** 334–336 (1993) 31
104. B.J. van Wees, A. Dimoulas, J.P. Heida, T.M. Klapwijk, W. van der Graaf, G. Borghs: Physica B **203,** 285 (1994) 31
105. D. Uhlisch, A.A. Golubov, M. Hollfelder, K. Neurohr, A.V. Ustinov, A.I. Braginski, H. Lüth: Czech J. Phys., Suppl. S2 **46,** 657 (1996) 33
106. S.J. Pearton, U.K. Chakrabarti, A.P. Perley: J. Appl. Phys. **68,** 2760 (1990) 33, 36
107. K. Neurohr: "Ballistische Tieftemperatur-Josephson-Kontakte auf der Basis hoch_beweglicher zweidimensionaler Elektronengase". Ph.D. Thesis, Technical University Aachen (RWTH), Ber. des Forschungszentrums Jülich, Jül-3607 (1998) 33, 128
108. J. Halbritter: Appl. Phys. A **43,** 1 (1987) 35
109. M.Y. Kupriyanov, V.F. Lukichev: Trudy FIAN **14,** 160 (1988) 35
110. M. Gurvitch, M.A. Washington, H.A. Huggins, J.M. Rowell: IEEE Trans. Magn. **MAG-19,** 791 (1983) 36
111. A.F. Volkov, A.V. Zaitsev, T.M. Klapwijk: Physica C **210,** 21 (1993) 36

112. A. Kaluza: "Untersuchungen an Supraleiter/Halbleiter/Supraleiter Strukturen im Materialsystem Niob-InGaAs/InP im Hinblick auf Oberflächenreinigung und Transporteigenschaften". Diploma Thesis, Technische Hochschule Aachen (RWTH) (1996) 37, 38
113. A.B. Pippard: *Magnetoresistance in Metals* (Cambridge University Press, Cambridge, 1989) 39, 39
114. S. Valeri, A. di Bona, E. Engeli, S. Bordiga, A. Piccirillo: Thin solid films **197,** 179 (1991) 40
115. J. Knoch, J. Appenzeller, B. Lengeler: J. Appl. Phys. **88,** 3522 (2000) 41
116. D. Gallet, G. Hollinger, P. Vikorovitch, D. Bonnevie, L. Goldstein, B.J. Robinson, D.A. Thompson, P. Hofstra: "Effect of surface pre-treatments on carrier depletion at growth-interrupted p-type InP interfaces for laser structures grown by GSMBE". In *Fourth International Conference on InP and Related Materials*, Cat. No. 92CH3104-7 (IEEE, New York, 1992), pp. 125–137 41, 42
117. C.M. Rouleau, R.M. Park: Appl. Phys. Lett. **73,** 4610 (1993) 41
118. G. Bruno, M. Losurdo, P. Capezzuto, V. Capozzi, T. Trovato, G. Perna, G.F. Lorusso: Appl. Phys. Lett. **69,** 685 (1996) 41, 41, 42
119. T. Schäpers, R.A. Müller, G. Crecelius, H. Hardtdegen, H. Lüth: J. Appl. Phys. **88,** 4440 (2000) 42, 43, 44
120. M. Jakob, H. Stahl, J. Knoch, J. Appenzeller, B. Lengeler: Appl. Phys. Lett. **76,** 1152 (2000) 44, 45, 45, 46
121. A.A. Golubov, F.K. Wilhelm, A.D. Zaikin: J. Low Temp. Phys. **106,** 297 (1997) 46
122. J. Appenzeller, M. Jakob, H. Stahl, J. Knoch, B. Lengeler: Appl. Phys. Lett. **77,** 549–551 (2000) 46
123. G. Bastian, H. Takayanagi: Physica C **352**, 219–222 (2001) 46
124. R. Kümmel, U. Gunsenheimer, R. Nicolsky: Phys. Rev. B **42,** 3992 (1990) 47, 47, 48, 49, 49, 57, 87
125. M. Octavio, M. Tinkham, G.E. Blonder, T.M. Klapwijk: Phys. Rev. B **27,** 6739–6746 (1983) 47, 51, 52
126. I.O. Kulik: Zh. Éksp. Teor. Fiz. **57,** 1745 (1969) [Sov. Phys. JETP **30**, 944 (1970)] 49, 65, 65, 66, 67, 68
127. L.A.A. Pereira, R. Nicolsky: Physica C **282–287,** 2411 (1997) 49
128. L.A.A. Pereira, A.M. Luiz, R. Nicolsky: Physica C **282–287,** 1529 (1997) 49
129. U. Gunsenheimer, A.D. Zaikin: Phys. Rev. B **50,** 6317 (1994) 49
130. J.M. Picard, internal report: Ecole Polytechnique, Paris, and Forschungszentrum Jülich (1998) 50
131. T.M. Klapwijk, G.E. Blonder, M. Tinkham: Physica B **109–110,** 1657 (1982) 52, 53, 59
132. K. Flensberg, J.B. Hansen, M. Octavio: Phys. Rev. B **38,** 8707 (1988) 52, 59, 82
133. M. Hurd, S. Datta, P.F. Bagwell: Phys. Rev. B **54,** 6557 (1996) 53, 59
134. U. Zimmermann, S. Abens, D. Dikin, K. Keck, V.M. Dmitriev: Z. Phys. B **97,** 59 (1995) 53, 59
135. W.M. van Huffelen, T.M. Klapwijk, D.R. Heslinga, M.J. de Boer, N. van der Post: Phys. Rev. B **47,** 5170 (1993) 53, 57
136. M. Kuhlmann, U. Zimmermann, D. Dikin, S. Abens, K. Keck, V.M. Dmitriev: Z. Phys. B **96,** 13 (1994) 53
137. D.R. Heslinga, W.M. van Huffelen, T.M. Klapwijk: IEEE Trans. Magn. **27,** 3264 (1991) 53
138. D. Uhlisch, J. Appenzeller, M.F. Tietze, T. Schäpers, M. Hollfelder, H. Lüth: Phys. Rev. B **57,** 1834 (1998) 57

139. R. Kürsten, T. Matsuyama, U. Merkt, private communication 59
140. S.G. Lachenmann, A. Förster, D. Uhlisch, T. Schäpers, A. Kastalsky, A.A. Golubov: Appl. Supercond. **6,** 681 (1999) 61, 63, 78, 79
141. C. Ishii: Prog. Theor. Phys. **5,** 1525 (1972) 65
142. J. Bardeen, J.L. Johnson: Phys. Rev. B **5,** 72 (1971) 65
143. P.F. Bagwell: Phys. Rev. B **46,** 12573 (1992) 65
144. H.X. Tang, Z.D. Wang, Y. Zhang: Z. Phys. B **101,** 359 (1996) 65, 68, 70, 100
145. R. Waung, S. Feng: Appl. Phys. Lett. **61,** 2458 (1992) 66
146. A.F. Morpurgo, F. Beltram: Phys. Rev. B **50,** 1325 (1994) 66
147. V.Z. Kresin: Phys. Rev. B **34,** 7587 (1986) 66, 75, 99
148. A. Chrestin, T. Matsuyama, U. Merkt: Phys. Rev. B **49,** 498 (1994) 66, 75, 76, 76, 82, 82, 92, 99, 100, 100, 101, 102
149. C.W.J. Beenakker H. van Houten: "Semiconductor Heterostructures and Nanostructures", In *Solid State Physics*, Vol. 44, ed. by H. Ehrenreich, D. Turnbull (Academic Press, New York, 1991) pp 1-228 69, 102
150. C.W.J. Beenakker: Rev. Mod. Phys. **69,** 731 (1997) 69
151. P.W. Brouwer, C.W.J. Beenakker: Chaos, Solitons Fractals **8,** 1249 (1997) 69
152. I.O. Kulik, A.N. Omel'yanchuk: Fiz. Nizk. Temp. **3,** 945 (1977) [Sov. J. Low Temp. Phys. **3**, 459 (1977)] 73, 77, 77, 78, 78
153. V. Ambegaokar, A. Baratoff: Phys. Rev. Lett. **10,** 486 (1963) 73, 77
154. A. Brinkman, A.A. Golubov: Phys. Rev. B **61,** 11297 (2000) 76, 76
155. I.O. Kulik, A.N. Omel'yanchuk: Fiz. Nizk. Temp. **4,** 296 (1978) [Sov. J. Low Temp. **4**, 142 (1978)] 77
156. A.A. Golubov, M.Yu. Kupriyanov, "Current-voltage characteristics of ScNS junctions with dirty NS electrode". In *Extended abstracts of the 5th International Superconductivity Electronics Conference*, Nagoya, pp. 135–137 (1995) 77, 77, 78
157. T. Schäpers, A. Kaluza, K. Neurohr, J. Malindretos, G. Crecelius, A. van der Hart, H. Hardtdegen, H. Lüth: Appl. Phys. Lett. **71,** 3537 (1997) 80, 81, 82
158. A.B. Zorin: Rev. Sci. Instrum. **66,** 4296–4300 (1995) 80
159. H. Takayanagi, T. Akazaki: Solid State Commun. **96,** 815 (1995) 83
160. C.W.J. Beenakker, B. Rejaei, J.A. Melsen: Phys. Rev. Lett **72,** 2470 (1994) 83
161. Y.V. Nazarov: Phys. Rev. Lett. **73,** 134 (1994) 83
162. A. Barone G. Paterno, *Physics and Application of the Josephson Effect* (Wiley, New York, 1982) 83, 83, 86
163. J.M. Rowell: Phys. Rev. Lett. **11,** 200 (1963) 83
164. J. Gu, W. Cha, K. Gamo, S. Namba: J. Appl. Phys. **50,** 6437 (1979) 85
165. T. Schäpers, K. Neurohr, J. Malindretos, A. Kaluza, J.-M. Picard, H. Lüth: Superlatt. and Microstruc. **25,** 851 (1999) 29, 86, 87, 88, 89
166. W.C. Steward: Appl. Phys. Lett. **12,** 277 (1968) 86
167. D.E. McCumber: J. Appl. Phys. **39,** 3113 (1968) 86
168. J.P. Heida: "Josephson currents in two-dimensional mesoscopic ballistic conductors". Ph.D. Thesis, Rijksuniversiteit Groningen, The Netherlands (1998) 86, 89
169. I. Giaever: Phys. Rev. Lett. **20,** 1286 (1968) 89
170. F. Andreozzi, A. Barone, M. Russo, G. Paterno, R. Vaglio: Phys. Rev. B **18,** 6035 (1978) 89
171. S. Takaoka, Y. Nakao, T. Kousai, K. Haruta, L. Oto, K. Murase, K. Gamo: Jpn. J. Appl. Phys. **34,** 5585–5587 (1995) 89
172. H.P. Wei, D.C. Tsui, M. Razeghi: Appl. Phys. Lett. **45,** 666 (1984) 90
173. S. Müller, J. Pillath, W. Bauhofer, A. Kohl, K. Heime: Appl. Phys. Lett. **67,** 1603–1605 (1995) 90

174. T. Schäpers, R.A. Müller, A. Kaluza, H. Hardtdegen, H. Lüth: Appl. Phys. Lett. **75,** 391 (1999) 90, 90, 91, 92
175. M.J. Kane, D.A. Anderson, L.L. Taylor, S.J. Bass: J. Appl. Phys. **60,** 657 (1986) 91, 91
176. G. Bastian, E.O. Göbel, J. Schmitz, M. Walther, J. Wagner: Appl. Phys. Lett. **75,** 94 (1999) 93, 94, 94, 94
177. C. Gauer, J. Scriba, A. Wixforth, J.P. Kotthaus, C. Nguyen, G. Tuttle, J.H. English, H. Kroemer: Semicond. Sci. Technol. **8,** S137 (1993) 93
178. T. Nishino, E. Yamada, U. Kawabe: Phys. Rev. B **33,** 2042 (1986) 96
179. A.W. Kleinsasser, T.N. Jackson, D. McInturff, F. Rammo, G. Pettit, J.M. Woodall: Appl. Phys. Lett. **55,** 1657 (1989) 96, 100
180. H. Takayanagi, T. Akazaki, J. Nitta, T. Enoki: Jpn. J. Appl. Phys. **34,** 1319 (1995) 97, 99
181. R.B. van Dover, A. de Lozanne, M.R. Beasley: J. Appl. Phys. **52,** 7327 (1981) 97
182. A.W. Kleinsasser, T.N. Jackson: Phys. Rev. B **42,** 8716 (1990) 98, 99, 99, 99
183. A.F. Volkov, H. Takayanagi: Phys. Rev. B **53,** 15162 (1996) 99
184. H. Takayanagi, J.B. Hansen, J. Nitta: Phys. Rev. Lett. **74,** 162 (1995) 99, 105, 106
185. A.W. Kleinsasser, T.N. Jackson: IEEE Trans. Magn. **25,** 1274 (1989) 100
186. H. Takayanagi, T. Akazaki: Jpn. J. Appl. Phys. (Part 1) **34,** 4552 (1995) 102, 103
187. B. Al'tshuler: Pis'ma Zh. Éksp. Teor. Fiz. **41,** 530 (1985) [JETP Lett. **41**, 648 (1985)] 102
188. P. Lee, A. Stone: Phys. Rev. Lett. **55,** 1622 (1985) 102
189. B. Al'tshuler, B. Spivak: Zh. Éksp. Teor. Fiz. **92,** 609 (1987) [Sov. Physics-JETP **65**, 343 (1987)] 103, 104
190. H. Takayanagi, J.B. Hansen, J. Nitta: Phys. Rev. Lett. **74,** 166 (1995) 103, 104, 105
191. C.W.J. Beenakker: Phys. Rev. Lett **67,** 3836 (1991) 104
192. H. Fukuyama, S. Maekawa: J. Phys. Soc. Jpn. **55,** 1814 (1986) 104
193. H. Fukuyama: "Proximity effect and Anderson localization". In *Novel Superconductivity. Proceedings of the International Workshop on Novel Mechanisms of Superconductivity*, (Plenum, New York, 1987) pp. 51–60 104
194. B.J. van Wees, H. van Houten, C.W.J. Beenakker, J.G. Willamson, L.P. Kouwenhoven, D. van der Marel, C.T. Foxon: Phys. Rev. Lett. **60,** 848 (1988) 106
195. D.A. Wharam, T.J. Thornton, R. Newbury, M. Pepper, H. Ahmed, J.E.F. Frost, D.G. Hasko, D.C. Peacock, D.A. Ritchie, G.A.C. Jones: J. Phys. C **21,** L209 (1988) 106
196. A. Furusaki, H. Takayanagi, M. Tsukada: Phys. Rev. Lett. **67,** 132 (1991) 106, 110
197. A. Furusaki: Superlatt. Microstruc. **425,** 809 (1999) 106
198. H. van Houten C.W.J. Beenakker: Physica B **175,** 187 (1991) 106
199. J. Bardeen, R. Kümmel, A.E. Jacobs, L. Tewordt: Phys. Rev. **187,** 556 (1969) 107
200. C.W.J. Beenakker: Phys. Rev. B **46,** 12841 (1992) 109
201. G. Wendin, V.S. Shumeiko, P. Samuelsson: Superlatt. Microstruct. **25,** 983 (1999) 111
202. P. Samuelsson, J. Lantz, V.S. Shumeiko, G. Wendin: Phys. Rev. B **62,** 1319 (2000) 111, 112, 112, 112, 113, 113, 114, 116, 116, 117, 117, 118, 119
203. H.T. Ilhan, H.V. Demir, P.F. Bagwell: Phys. Rev. B **58,** 15120 (1998) 112
204. H. Nakano, H. Takayanagi: Phys. Rev. B **47,** 7986–7994 (1993) 112

205. F.K. Wilhelm, G. Schön, A.D. Zaikin: Phys. Rev. Lett. **81,** 1682 (1998) 112, 117, 129
206. R. Landauer: IBM J. Res. Devel. **1,** 223 (1957) 113
207. M. Büttiker: Phys. Rev. Lett. **57,** 1761 (1986) 113
208. P. Samuelsson, A. Ingerman, V.S. Shumeiko, G. Wendin: Physica C **352,** 82 (2001) 117
209. H.T. Ilhan, P.F. Bagwell: J. Appl. Phys. **84,** 6758 (1998) 117, 128
210. A.A. Golubov, K. Neurohr, T. Schäpers, M. Behet, H. Lüth: Superlatt. Microstruc. **25,** 1033 (1999) 118, 118, 120, 129
211. H. Pothier, S. Guèron, N.O. Birge, D. Esteve, M. Devoret: Z. Phys B: Cond. Matt. **104,** 178 (1997) 118, 128, 128
212. H. Pothier, S. Guèron, N.O. Birge, D. Esteve, M. Devoret: Phys. Rev. Lett. **79,** 3490 (1997) 118
213. G.F. Giuliani, J.J. Quinn: Phys. Rev. B **26,** 4421 (1982) 128
214. A.F. Morpurgo, B.J. van Wees, T.M. Klapwijk, G. Borghs: Phys. Rev. Lett. **79,** 4010 (1997) 129
215. A.F. Morpurgo, B.J. van Wees, T.M. Klapwijk, G. Borghs: Physica B **249–251,** 458 (1998) 129
216. A.F. Morpurgo, J.J.A. Baselmans, B.J. van Wees, T.M. Klapwijk: J. Low Temp. Phys **118,** 637 (2000) 129
217. J.J.A. Baselmans, A.F. Morpurgo, B.J. van Wees, T.M. Klapwijk: Nature **397,** 43 (1999) 129
218. J.J.A. Baselmans, A.F. Morpurgo, B.J. van Wees, T.M. Klapwijk: Superlatt. Microstruc. **25,** 973 (1999) 129
219. J. Kutchinsky, R. Taboryski, C.B. Sørensen, J.B. Hansen, P.E. Lindelof: Phys. Rev. Lett. **83,** 4856 (1999) 129
220. H. Takayanagi, T. Akazaki: Physica B **249–251,** 462 (1998) 134
221. D. Uhlisch, S.G. Lachenmann, T. Schäpers, A.I. Braginski, H. Lüth, J. Appenzeller, A.A. Golubov, A.V. Ustinov: Phys. Rev. B **61,** 12463 (2000) 134
222. N.R. Claughton, M. Leadbeater, C.J. Lambert: J. Phys: Cond. Matt. **7,** 8757 (1995) 134
223. A.L. Yeyati, J.C. Cuevas, A.L. Davalos, A. Rodero: Phys. Rev. B **55,** 6137 (1997) 134
224. H. Schomerus, C.W.J. Beenakker: Phys. Rev. Lett. **82,** 2951 (1999) 134
225. Q.F. Sun, J. Wang, T.H. Lin: Phys. Rev. B **62,** 648 (2000) 134

# Index


AC Josephson effect, 88
adiabatic approximation, 106
Andreev bound-state, 107
Andreev ladder, 47, 48
Andreev-level spectrometer, 112
Andreev-level spectrum, 120
Andreev-level spectrum, continuous, 66
Andreev-level spectrum, discrete, 66
Andreev reflection, 8, 44
Andreev reflection coefficient, 12
Andreev reflection, angle dependence, 13
Andreev resonance, 111
anodic oxidation, 27
anomalous current, 116
anomalous current density, 115
$Ar^+$ sputtering, 28
atomic force microscope, 42

ballistic superconductor/2DEG structure, 25
band profile, 93
Bardeen–Cooper–Schrieffer theory, 5
Blonder–Tinkham–Klapwijk model, 9
Bogoliubov equation, 6
Boltzmann equation, 51
bound states, 67
bypass channel, 40, 91, 92

carrier injection, 112
characteristic voltage, 77–80
chemical etching, 33
clean limit, 14, 99
coherence length, 14, 99
conductance, 12
conductance, negative, 86
conduction band, 21
confinement energy, 23
constriction, 17
control current, 125
Cooper pair, 5
Cooper pair condensate, 6
Cooper pair density, 16
critical current, 73, 78
critical-current enhancement, 129
critical-current oscillations, 102
current density distribution, 83
current–voltage characteristic, 78

degeneracy of eigenvalues, 68
degraded semiconductor layer, 38
$\delta$-doped layer, 121
$\delta$-shaped barrier, 9
differential conductance, 31
differential conductance, negative, 57, 87
differential resistance, 58
diffusive interface scattering, 39, 58
diffusive normal conductor, 79
dirty limit, 14, 99
discrete Andreev states, 66
distribution function, 113, 118
drain contact, 96
drain–source resistance, 96

effective electron mass, 7, 32
elastic mean free path, 14, 24
electrical filtering, 80
electrochemical potential, 7
electron beam evaporation, 33
electron cyclotron resonance plasma cleaning, 41
electron–electron scattering, 128
electron-like excitation, 6
electron-like particles, 70
electron–phonon interaction, 5, 6
energy dispersion, 23
energy gap, 6, 73
excess current, 12, 49, 82
extended Andreev states, 66

Fabry–Pérot-like oscillations, 100
Fermi velocity mismatch, 12, 34
Fermi wave vector, 6, 23


Thomas Schäpers: Superconductor/Semiconductor Junctions, STMP 174, 143–145 (2001)
© Springer-Verlag Berlin Heidelberg 2001

Fermi wavelength, 22
focusing factor, 84
four-terminal junction, 117
Fraunhofer interference pattern, 83

GaSb/AlSb/InAs heterostructure, 93
gate capacitance, 100
gate electrode, 95
Gaussian wave packet, 47
Green's function, 15, 18, 77
group velocity, 7

heating effects, 129
helium plasma, 42
heterojunction, 24
hole, 8
hole-like excitation, 6
hole-like particles, 70
hot-carrier injection, 111
hysteresis, 49, 79, 82, 86

$I_cR_N$ product, 77
illumination, continuous, 92
illumination, pulsed, 91
inelastic mean free path, 36
inelastic scattering, 36, 48
inelastic scattering length, 45, 118
infrared light illumination, 93
interface transparency, 25, 31
interference effects, 100
inversion layer, 22
inverter circuit, 100
ion sputter cleaning, 33
ionized-impurity scattering, 24

Josephson field effect transistor, 95
Josephson supercurrent, 65

Kümmel–Gunsenheimer–Nicolsky model, 47
Kümmel–Gunsenheimer–Nicolsky model, modified, 49

Landauer–Büttiker scattering approach, 113
light exposure, 89
load resistance, 96
localization, 102, 104
localization effect in the critical current, 104
London penetration depth, 85

magnetic flux quantum, 83
magnetoresistance, 39
magnetotransport measurement, 38
Matsubara frequency, 15, 76
mesoscopic fluctuations, 103
modulation doping, 25

nonequilibrium carriers, 111, 127
nonequilibrium current, 115
nonequilibrium distribution, 52, 119, 120
nonequilibrium population, 115
nonequilibrium supercurrent, 111
normal conductor/superconductor interface, 8, 9
normal reflection, 9
normal reservoir, 112
normal-reflection coefficient, 12
normal-state resistance, 12, 78, 79

Octavio–Tinkham–Blonder–Klapwijk model, 51
offset current, 125
ohmic contact, 123
one-dimensional junction, ideal, 66

p-doped InAs, 22
pair-breaking parameter, 15
persistent photoconductance, 90
photogenerated carriers, 90
plasma cleaning, 33
pn junction, 123
point contact, 43
point contact spectroscopy, 44
potential barrier, 9, 123
probability current, 12
proximity effect, 14
proximity layer, 61

quantized conductance, 106
quantum Hall effect, 32
quantum well, 24, 66
quasiparticle density of states, 15
quasiparticle injection, 113
quasiparticle interference effects, 63

reactive ion etching, 28
reflection amplitude, 113
resistive state, 125
resistively capacitively shunted junction model, 86
resonant states, 101
retroreflection, 8, 44
return current, 79

scattering matrix, 113
Schottky barrier, 25, 96
Schrödinger equation, 22
self-aligned process, 28

semiconductor wire structure, 38
short-junction limit, 107
Shubnikov–de Haas effect, 32
Shubnikov–de Haas measurements, 91
SN/c/NS model, 54
source contact, 96
spacer layer, 25
specular reflection, 44
split gate, 106, 108
sputter cleaning, 36
sputter deposition, 33
step edge junction, 27, 78, 121
subgap peak, 61
subharmonic gap structures, 52, 57
superconducting pair potential, 7
superconducting quantum point contact, 106
superconducting transconductance, 99
superconductive ground state, 6
superconductor/normal-conductor interferometer, 112
supercurrent, 65
supercurrent distribution, 83, 131
supercurrent, reversal, 129
suppression parameter, 15
surface cleaning, 33
surface degradation, 36
surface roughness, 40
surface roughness scattering, 24
surface states, 22

temperature, effective, 128
three-terminal junction, 112
transfer matrix, 70
transmission amplitude, 113
transmission coefficient, 70
transmission matrix method, 68
triangular quantum well, 24
two-dimensional electron gas, 21

universal conductance fluctuations, 102
universal critical-current fluctuations, 104

valence band, 22
voltage gain, 99

wet chemical cleaning, 33
WKB method, 107

$Z$ parameter, 10
$Z$ parameter, angle-dependent, 52
$Z$ parameter, effective, 12
zero-field resistance, 39